KENS REPORT-V

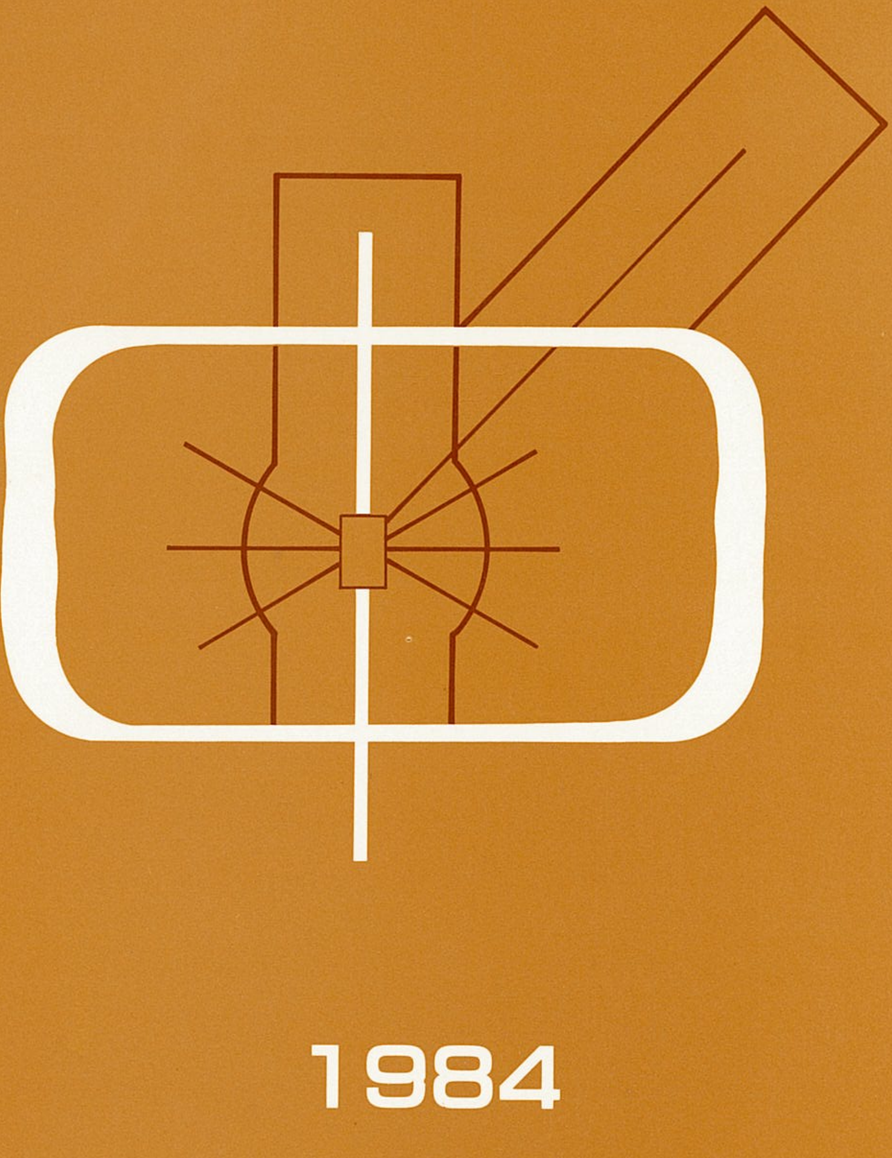

1984

NATIONAL LABORATORY FOR HIGH ENERGY PHYSICS, KEK

KENS REPORT-V

Edited by

Y. ISHIKAWA

N. NIIMURA

M. MISAWA

KEK Progress Report 84- 2

KEK Reports are available from:

Technical Information Office
National Laboratory for High Energy Physics
Oho-machi, Tsukuba-gun
Ibaraki-ken, 305
JAPAN

Phone: 0298-64-1171
Telex: 3652-534 (Domestic)
(0)3652-534 (International)
Cable: KEKOHO

PREFACE

The present report follows a previous issue, KENS Report IV published in August 1983. This volume collects the summaries of the works performed at KENS during the 1983 fiscal year. I feel sorry that the publication of this report is substantially delayed. The main reason was that I was absent abroad between April and September and N. Watanabe who was arranged to take my place could not find a time because of his full occupation to the U target job.

We regret, first of all, that our neutron source is completely shut down this year because of construction of a big tunnel for TRISTAN. We expect that the beam experiments will be restarted from next June. We are glad, however, to inform that our KENS-I' project is steadily in progress in this period. We plan to replace our target from W to U in the next summer, and an H^- injection system as well as a new 40 MeV proton LINAC injector will also be accomplished or in great progress until this time. Therefore the neutron intensity would be increased substantially from the next fall.

Although the numbers of papers submitted in the report did not exceed those of the previous year, I believe that the quality of each paper is much improved. One of the highlight of last year's researches was the successful observation of the Bose-condensation in the liquid ^{4}He by the resonance detector spectrometer RAT. The detection of very early stage of the spinodal decomposition in Fe-Cr and Al-Zn alloys by SAN, which became possible by virtue of the potential of SAN for the wide Q measurements, gave a promissing aspect of SAN for this kind of study. The TOP and LAM-80 spectrometers have also provided other examples of the potentials of the cold pulsed neutron source.

Two powder diffractometers, MRP (Medium Resolution machine) and HRP (High Resolution machine) are new spectrometers installed in the last fiscal year. Some results obtained with them are reported in this volume. We are proud of observing a beautiful powder pattern with more than 200 diffraction lines by HRP. We display in Fig. 1 the recent layout of the KENS facility, which shows that we have already no vacant beam hole. WIT on the H2 beam hole is another small angle scattering machine which is now under construction. The photographs of the recent experimental halls, full of spectrometers, are also shown in the next page.

Finally we should also mention that our next goal, KENS-II project has been discussed extensively the last year. The result of the design study of the proton accelerator GEMINI is reported in this volume. The details of the discussions concerning the project are summarized in a proceedings which will appear soon an a KEK Report.

October 24, 1984

Editor in Chief : Y. Ishikawa

KENS NEUTRON SCATTERING FACILITY

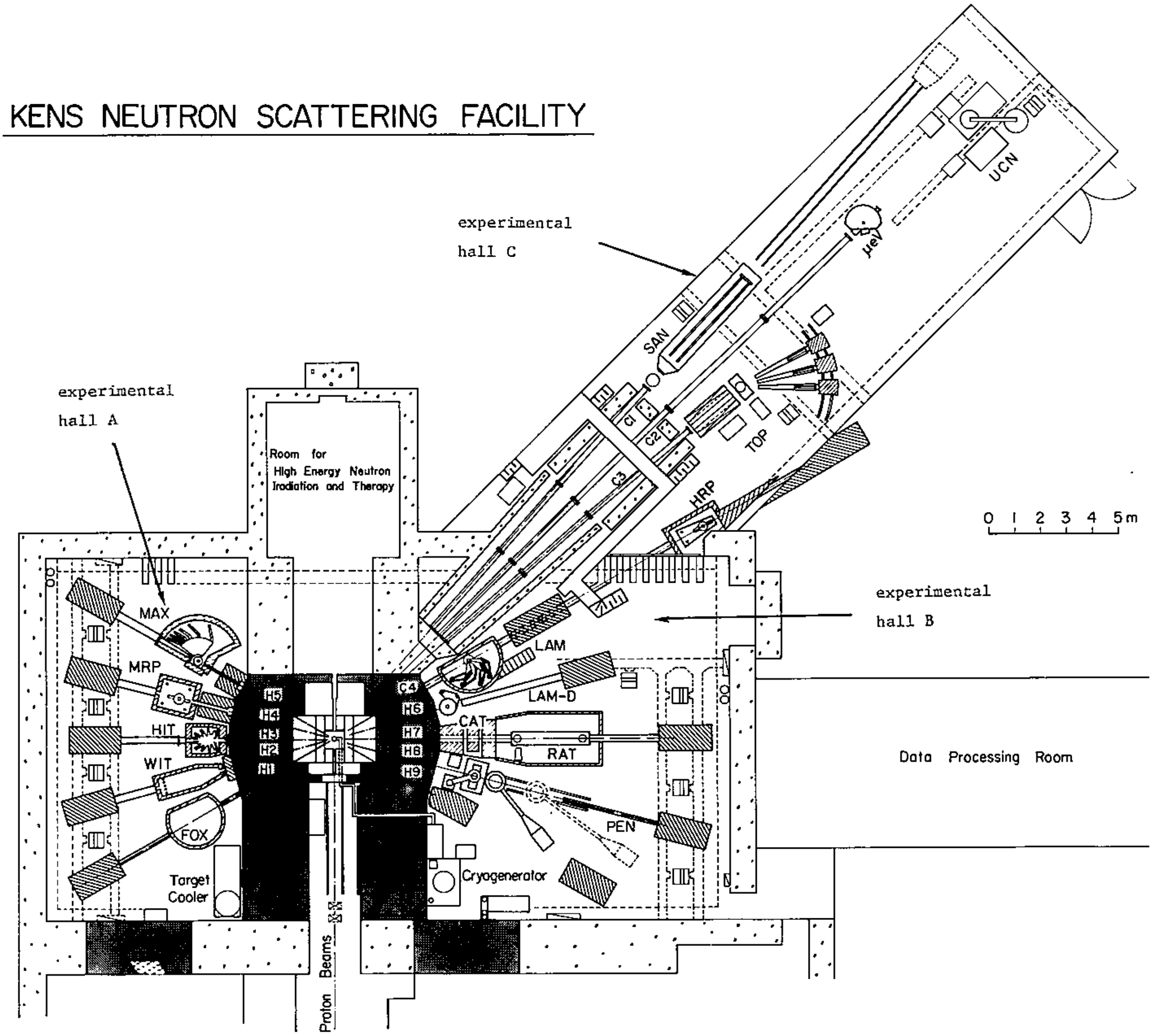

Fig. 1. The recent layout of the KENS facility.
H1 ∿ H9 : thermal and epithermal neutron beam holes.
C1 ∿ C4 : cold neutron beam hole and guiders.

H1 : Single crystal diffractometer (FOX).
H2 : Thermal neutron small angle instrument (WIT), under construction.
H3 : Liquid and amorphous spectrometer (HIT).
H4 : Medium resolution powder diffractometer (MRP).
H5 : Multi-analyzer crystal spectrometer (MAX).
H6 : Molecular spectrometer (LAM-D).
H7 : eV-spectrometer (RAT).
Crystal spectrometer for high energy incoherent scattering (CAT).
H8: Polarized epithermal neutron spectrometer (PEN).

C1 : Small angle instrument (SAN).
C2 : High resolution quasi-elastic spectrometer (LAM-80).
Spin echo μeV spectrometer prototype (μeV), under construction.
Ultra cold neutron generator test machine (UCN).
C3: Polarized cold neutron spectrometer (TOP).
C4: Medium resolution quasi-elastic spectrometer (LAM-40).
High resolution powder diffractometer (HRP).

experimental
hall A

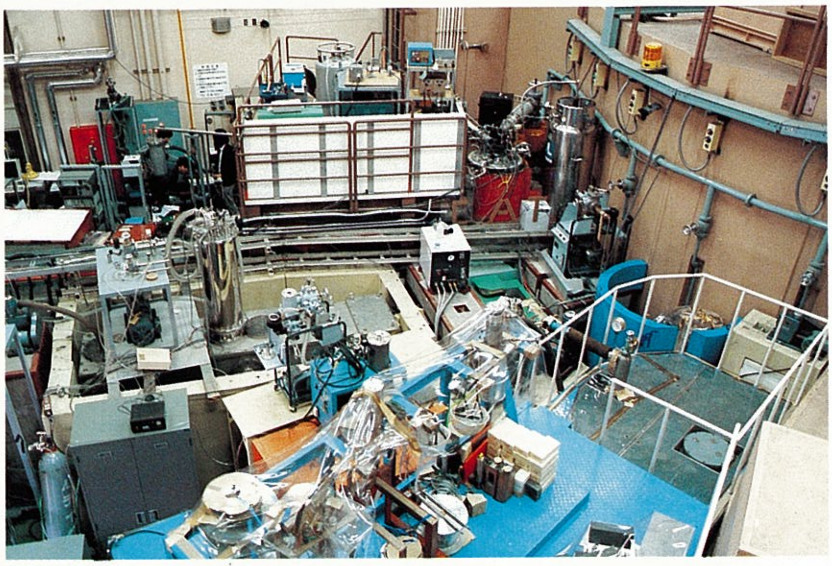

experimental
hall B

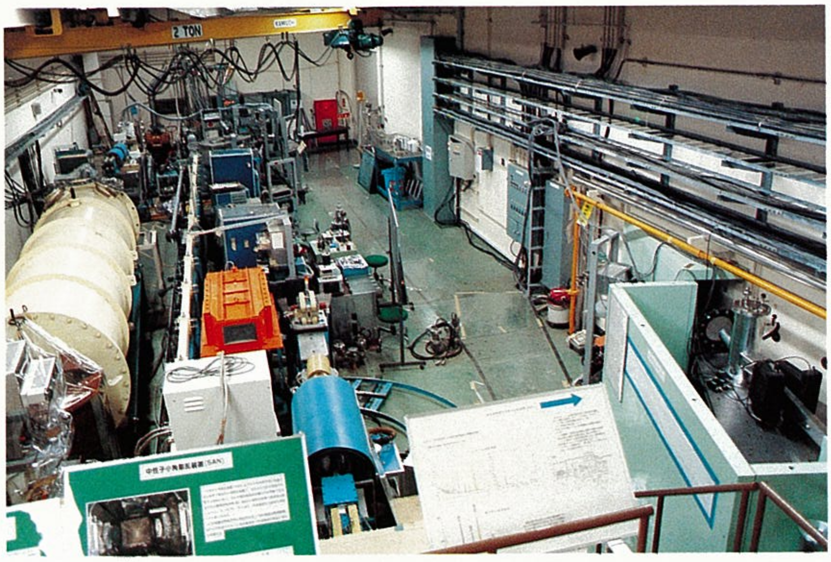

experimental
hall C

The recent experimental halls

CONTENTS

Page

I ACCELERATOR

II EXPERIMENTAL RESULTS AND INSTRUMENTAL DEVELOPMENTS

HIT

SAN

FOX

HRP/MRP

LAM

MAX

RAC

TOP

PEN

UCN

Summary of BSF Operation

Toshikazu ADACHI, Yoshiro IRIE, Naokatsu KANEKO,
Masayuki MIKI, Yoshiharu YANO and Hiroshi SASAKI

National Laboratory for High Energy Physics
Oho-machi, Tsukuba-gun, Ibaraki-ken, 305, Japan

The summary of BSF operation in the FY 1983 and the average beam intensity and transmission data in each operation period are shown in Tables 1 and 2, respectively. The beam time used for the BSF operation amounts to 2789.1 hours, which correspond to 76.0 % of the PS operation time, 3666.7 hours. This percentage is 12 % lower than that of FY 1982, because the PS operation in September and October was devoted to the accelerator study of H^- injection and polarized beam acceleration. On January 10 to 13, the booster synchrotron was operated additionally for Particle Radiation Medical Science Center. The beam time for medical use has increased by 2.4 times compared with that of FY 1982. To utilize the booster beam more

Table 1 Summary of BSF operations since April 1982 through February 1983. (units are "hours", unless otherwise specified)

	Neutron Experiment	Meson Experiment	Biomedical Research	Total	Ratio
BEAM UTILITY					
BEAM ON	1117.4	1115.5	417.2	2650.1	95.0 %
REJECT	1.0	1.8	0.3	3.1	0.1
BEAM LINE TROUBLE	2.4	10.3	2.1	14.8	0.5
ACCELERATOR TROUBLE	26.5	48.5	12.5	87.5	3.1
OTHERS	2.0	2.1	0	4.1	0.2
BEAM LINE TUNING				29.5	1.1 %
SUMMATION	1149.3	1178.2	432.1	2789.1	100.0 %

Table 2 Beam Intensity and Transmission.

	Neutron		Meson		Biomedical Use	
	Average Intensity (10^{11}ppp)	Transmission	Average Intensity (10^{11}ppp)	Transmission	Average Intensity (10^{11}ppp)	Transmission
1983 April - July	4.6	0.91	4.6	0.90	5.3	0.98
1983 November - December	4.6	0.81	4.3	0.78	4.5	0.79
1984 January - February	4.8	0.82	4.9	0.86	4.7	0.84

(Transmission includes the beam extraction efficiency of the booster synchrotron)

efficiently, interlock system was reinforced so that neutron or meson experiments can be done during the setting time of the patients in the medical treatment room. Regarding Table 2, beam intensity was measured on the 500 MeV beam line nearest to the targets or the energy degrader. Transmission is defined as the ratio of the beam intensity measured this way to the booster intensity displayed on CATV. The beam intensity integration system was replaced by a new version which consists of CAMAC ADC, timing modules and a micro-computer. This new system has come into operation since the first operation cycle of November and shows good stability.

Small deviation of the primary proton beam in the horizontal direction gives rise to the enormous decrease of the surface muon production rate and of the secondary proton beam intensity after passing through the small aperture energy degrader. An auto-beam- steering system was installed in the middle point of the beam line to compensate such deviations. Figure 1 shows the schematic view of this system. A pair of steering magnets HS2-A and HS2-B is controlled automatically by a micro-computer to restore beam positions at the beam profile monitors PR-5 and PR-7, respectively when the beam center was shifted from the originally optimized position. The beam profile monitor is composed of 32 by 32 horizontal and vertical tungsten meshes at 2.5 mm intervals. Figure 2 shows the results of the test of this auto-steering system. Beam deviation in the upstream was simulated by adjusting the bending angle of PHB1 magnet, which switches the beam pulse from the main ring injection line to the BSF beam line. PR-12 and PR-13 are those nearest to the meson production target. The recovery times of beam positions and surface muon production rate are less than ten minutes as is seen from the figure.

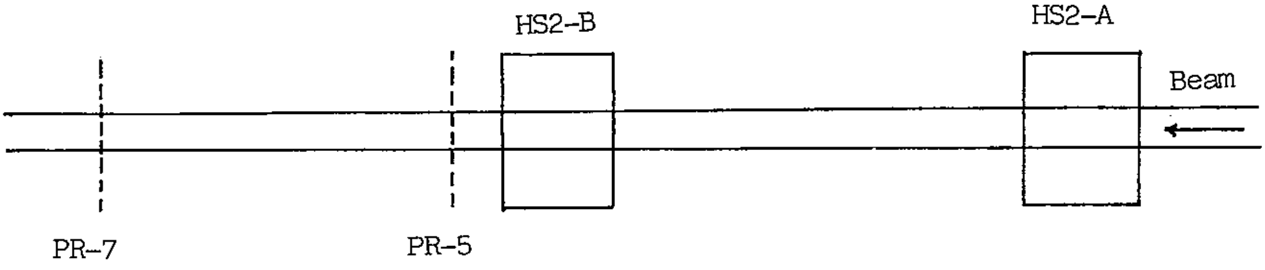

Fig. 1 Schematic view of auto-beam-steering system.

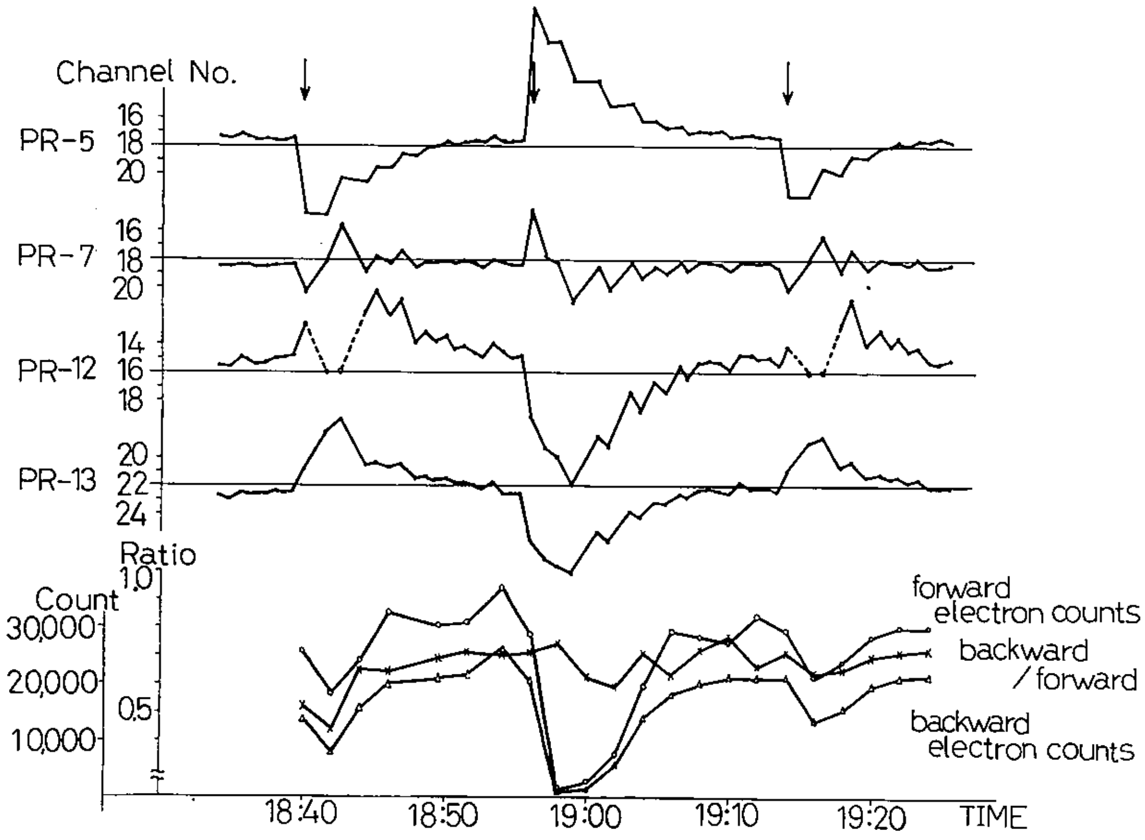

Fig. 2 Test of the auto-beam-steering system. Bending angle of PHB1 was changed intensionally at arrow points. Channel division is 2.5 mm.

Preamplifiers which are placed close to the profile monitor heads are easily damaged by the radiation along the beam line and their maintenance is really a tedious work. Every mesh of 30 μm tungsten wire on the monitor head is replaced by a couple of 50 μm tungsten wires to increase the S/N ratio and thus to enable to keep the preamplifier away from the beam line as far as possible. Figure 3 shows the comparison of output signals between the cases of single and a couple of tungsten wires mesh. In the latter case the preamplifier is placed in a cable pit which is 60 m away from the monitor head. The beam profile can be clearly seen even though the beam shape shows broad peak. Study to replace the tungsten wires by wider and thinner strips is now in progress.

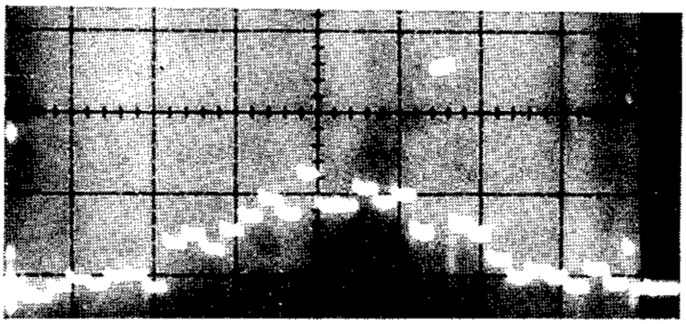

(a) 30 μm tungsten wire.

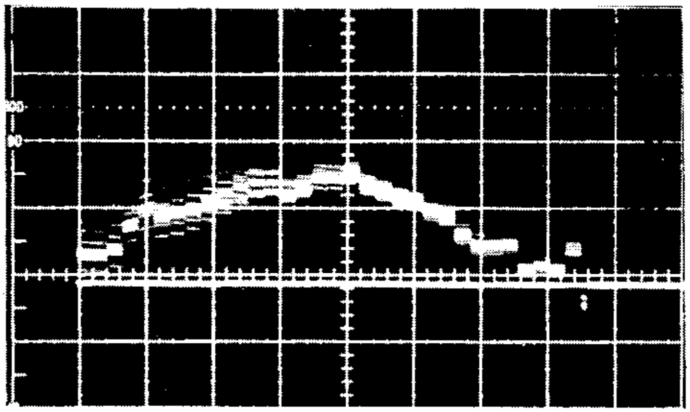

(b) a couple of 50 μm tungsten wires. Preamplifier is placed 60 m away from the monitor head.

Fig. 3 Comparison of the beam profile singals.

Accelerator Project GEMINI for Intense Pulsed Neutron and Meson Source at KEK

H. SASAKI and GEMINI Study Group*

National Laboratory for High Energy Physics
Oho-machi, Tsukuba-gun, Ibaraki-ken, 305, Japan

Abstract

A rapid-cycling synchrotron is designed for the intense pulsed neutron and meson source at KEK. This 800 MeV accelerator aims to deliver proton beams of 500 μA in time average. This paper describes conceptual design of the accelerator and also the present status of R & D for some technical problems.

Introduction

Five hundred MeV Booster Synchrotron at KEK, which is delivering 2 μA proton beam in time average, is used as a pulsed neutron and meson source of Booster Synchrotron Utilization Facility (BSF) as well as an injector for 12 GeV Proton Synchrotron in a time-shared mode. Since commissioning of BSF in 1980, a long-term future program of BSF has been discussed1). This is the construction of an intense pulsed neutron source (KENS-II program) and the extension of the present meson science experimental facility BOOM (Super-BOOM project). The most important part of this program is the construction of a high intensity proton accelerator. An accelerator system for KENS-II and Super-BOOM is named GEMINI, which is abbreviation of "a generator of meson-intense and neutron-intense beam". This is an 800 MeV rapid-cycling synchrotron aiming to deliver the proton beam of 500 μA in time average. Unlike the present meson factories or spallation neutron sources worldwide except those in BSF, GEMINI should deliver equally the

---

* T. Adachi, H. Baba, S. Inagaki, Y. Irie, N. Kaneko, T. Kawakubo, M. Kumada, S. Matsumoto, M. Miki, I. Sakai, H. Someya and Y. Yano.

pulsed proton beams to each of the meson and neutron experimental facility. In BSF, the unique features of the 70 nsec pulsed proton beam are effectively used for the time-of-flight technique in the neutron scattering experiments and for the studies on the relaxation phenomena of condensed matters with μSR. In GEMINI, it is also required that a single bunched beam is simultaneously supplied to each of the neutron and meson experimental facility. Particularly, some kinds of μSR experiment ask a single short bunched beam less than 30 nsec in bunch length even at the sacrifice of beam intensity.

Accelerator System

The parameters of GEMINI are listed in Table 1. The accelerator will consist of an H^- ion source, RFQ, 100 MeV Alvarez-type linac, and 800 MeV rapid-cycling synchrotron. A highly symmetric lattice with high tunes was chosen for the synchrotron lattice; 24 equal FBDO cells with a phase advance of about 90° per cell set the betatron tunes around 7. The layout of the accelerator is shown in Fig. 1.

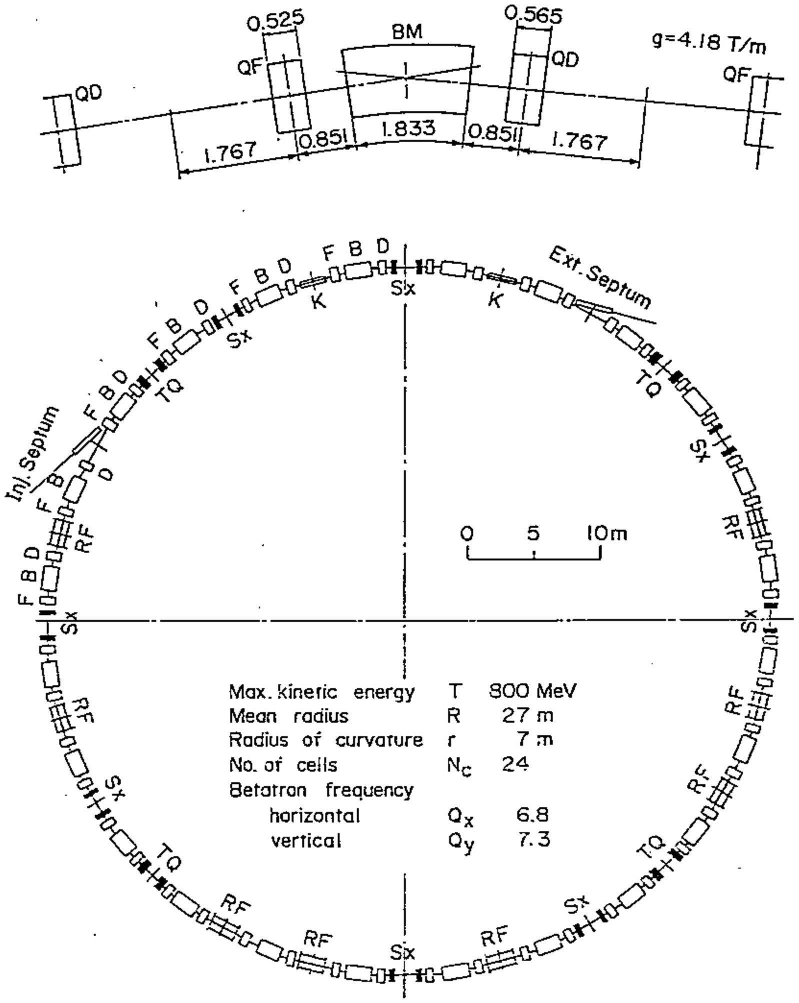

Fig. 1 GEMINI Layout

Table 1 A New Pulsed Neutron and Meson Source GEMINI

Maximum kinetic energy	800 MeV
Maximum intensity	6×10^{13} p/p
Repetition rate	50 Hz (100/3 Hz & 100 Hz)
Average beam current	500 μA
Injection energy	100 MeV
Injected H^- beam current	30 mA
Number of turns of injected beam	>240
Beam pulse width of injected beam	>330 μs
Magnet radius	7.00 m
Average radius	27.00 m
Number of period	24
Length of straight section	3.008 m
Structure	FBDO
Betatron frequency per revolution	
Horizontal	6.8
Vertical	7.3
Revolution frequency	0.757 - 1.489 MHz
Maximum beta-function	
Horizontal	12.4 m
Vertical	12.9 m
Momentum compaction factor	2.71×10^{-2}
Transition energy/rest energy	6.07
Beam emittance	
800 MeV	0.29 x 0.16 (mm rad)^2
100 MeV	0.97 x 0.52 (mm rad)^2
Number of bending magnets	24
Length of bending magnets	1.833 m
Length of quadrupole magnets	
Focussing magnet	0.525 m
Defocussing magnet	0.565 m
Bending magnet field	
800 MeV	0.697 T
100 MeV	0.212 T
Quadrupole magnet peak field gradient	4.18 T/m
Peak energy gain per turn	90.6 keV (60.4 keV)
Harmonic number	2
RF frequency	1.513 - 2.978 MHz
Maximum RF voltage	214 kV (166 kV)
RF bucket area	1.89 eV•sec
Number of RF stations	8
Incoherent space charge limit	7.2×10^{13} protons

Injector Linac[2)]

100 MeV linac with a 30 mA H^- ion beam is assumed as an injector to the synchrotron. The accelerating structure of this injector system is divided into three stages: 50 ∿ 100 keV H^- ion source, 1 MeV RFQ or APF and 100 MeV Alvarez linac. 1 MeV injection energy enables us to use klystron working around 400 MHz as RF power source for the 100 MeV linac. This will simplify the power system of the linac. If the Alvarez linac is excited at 400 MHz, the diameter of cavity is reduced nearly to a half of the present proton linac at KEK. Table 2 shows accelerating energy by each cavity, cavity length, number of cells contained in a cavity and RF power for 6 partitions at the average accelerating voltage of 3.5 MV/m.

Table 2 Features of 100 MeV Injector Linac

Cavity Number	Energy (MeV)	Length (m)	Number of cells	Power (MW) Cavity	Beam	Total
1	18.37	7.267	81	0.852	0.521	1.373
2	35.57	7.136	41	0.835	0.516	1.351
3	52.68	7.305	33	0.870	0.513	1.383
4	69.93	7.483	29	0.911	0.517	1.428
5	85.38	7.180	25	0.898	0.464	1.362
6	100.39	7.458	25	0.929	0.450	1.379

Injection and Extraction

Beam injection will be carried out in horizontal plane. In order to store the number of protons of 6×10^{13} into the synchrotron with a 30 mA H^- ion beam, injection would occur at least over 240 turns requiring 330 μsec. For the purpose of filling the horizontal phase space, injection starts with a horizontal bump orbit, which coincides with the injection orbit of the H^- ion beam at the exit of a focussing quadrupole magnet as shown in Fig. 2. The density distribution of the beam after injection is regulated by choosing a proper decay waveform of the bump field.

Beam extraction is performed by the horizontal single-turn extraction. The emittance of the extracted beam is assumed to be twice of the expected one from adiabatic damping of the initial emittance. Figure 3 shows the extraction trajectory of beam. The deflection by the kicker magnet is

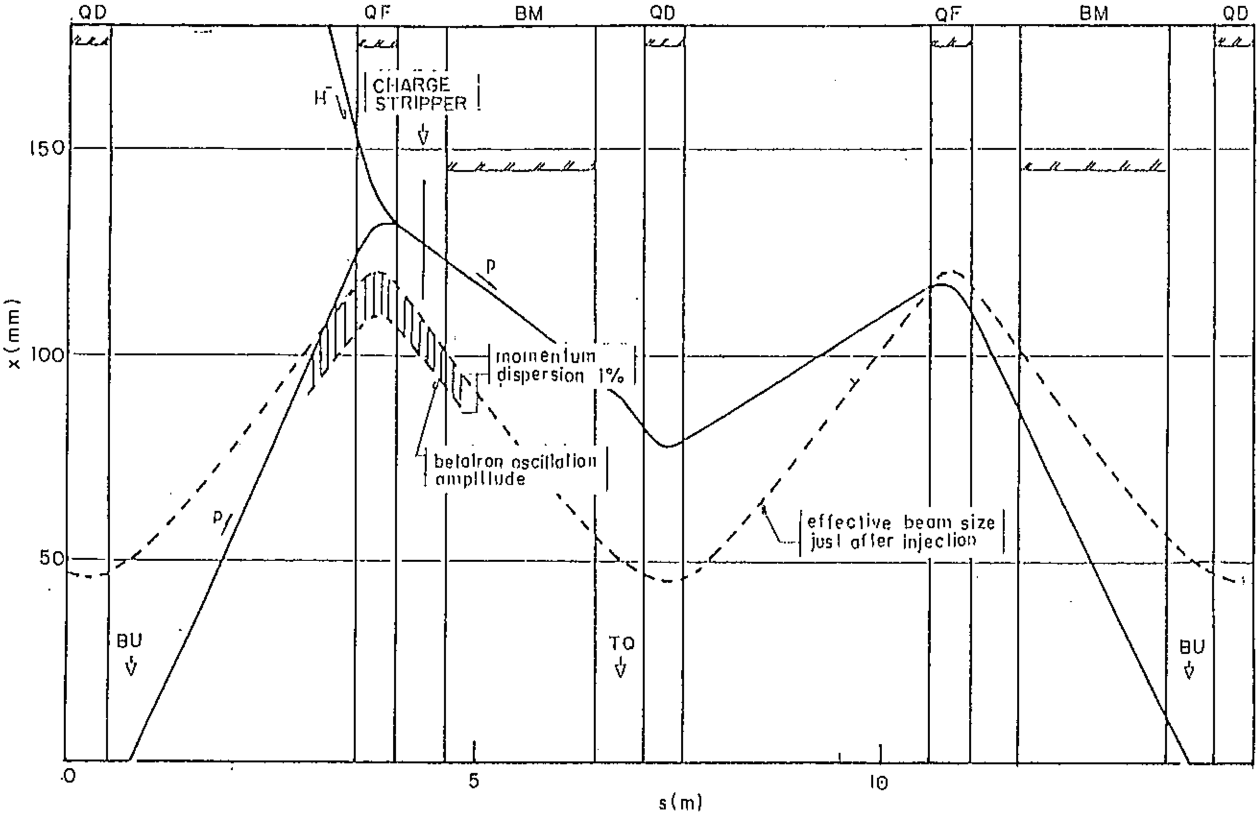

Fig. 2 Injection Optics

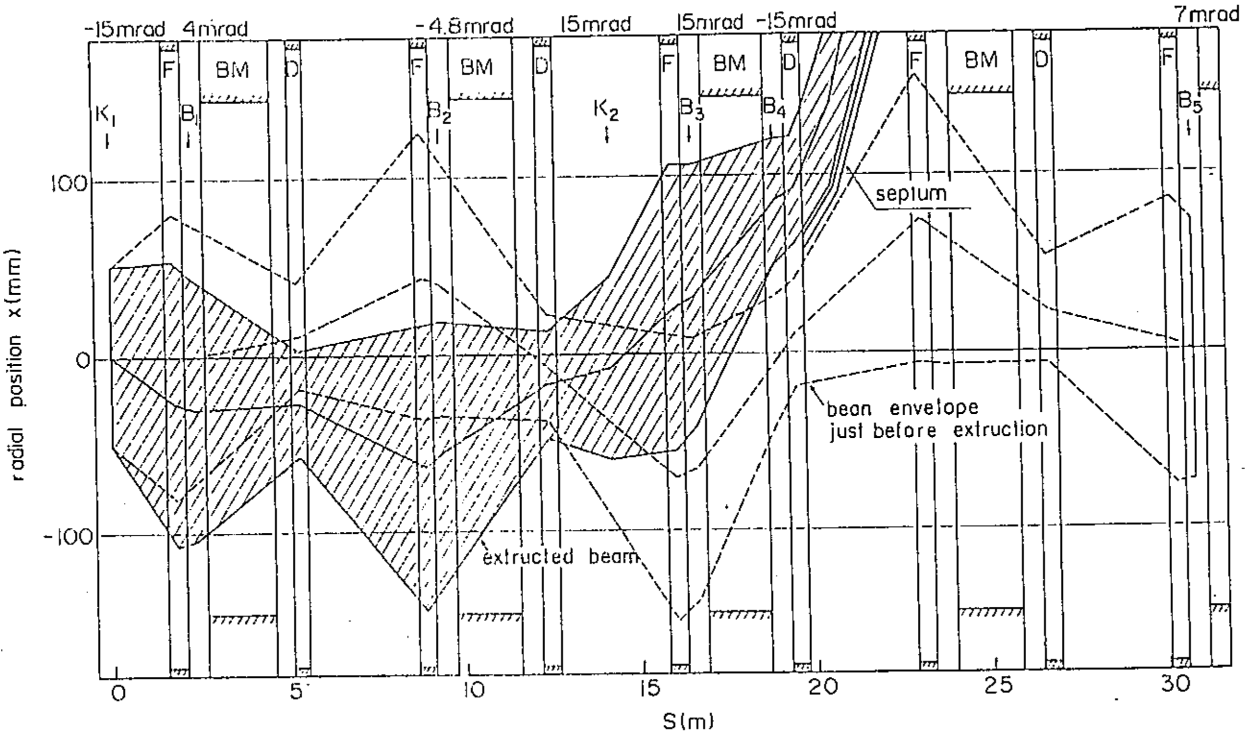

Fig. 3 Extraction Optics

15 mrad for the first and second magnet. The septum magnet is divided into two parts, each of which deflects the beam by 150 and 225 mrad, respectively. These bends provide a separation of 80 cm between the central orbit and the central line of the extracted beam at the exit of the septum magnet. This distance is long enough for the extracted beam to clear the yoke of the quadrupole magnet following the septum magnet.

Ring Magnets

The accelerator ring is made of 24 bending and 48 quadrupole magnets. The required semi-aperture of good-field region is 11.5 cm x 7.4 cm and 13.5 cm x 9.0 cm in the bending and quadrupole magnet respectively. For the vacuum chamber, it is necessary to add 3 and 4 cm in horizontal aperture of the bending and quadrupole magnet respectively to allow the room for injection and extraction of beam. The cross-section of the ring-magnet is shown in Fig. 4.

The ring magnet is excited with a repetition rate of 50 Hz. All of the bending and quadrupole magnets are divided into twelve groups. These are connected in series through resonant capacitors and forms a ring circuit. The dc bypass of the capacitors for the dc bias current is provided by installing chokes in parallel to the capacitors. In order to reduce the RF accelerating voltage, the magnet system would be excited by a dual-frequency system with resonant frequency of 100/3 and 100 Hz as proposed by M. Foss and W. Praeg at ANL$^{3)}$. This reduces the peak RF voltage of 214 kV to 166 kV.

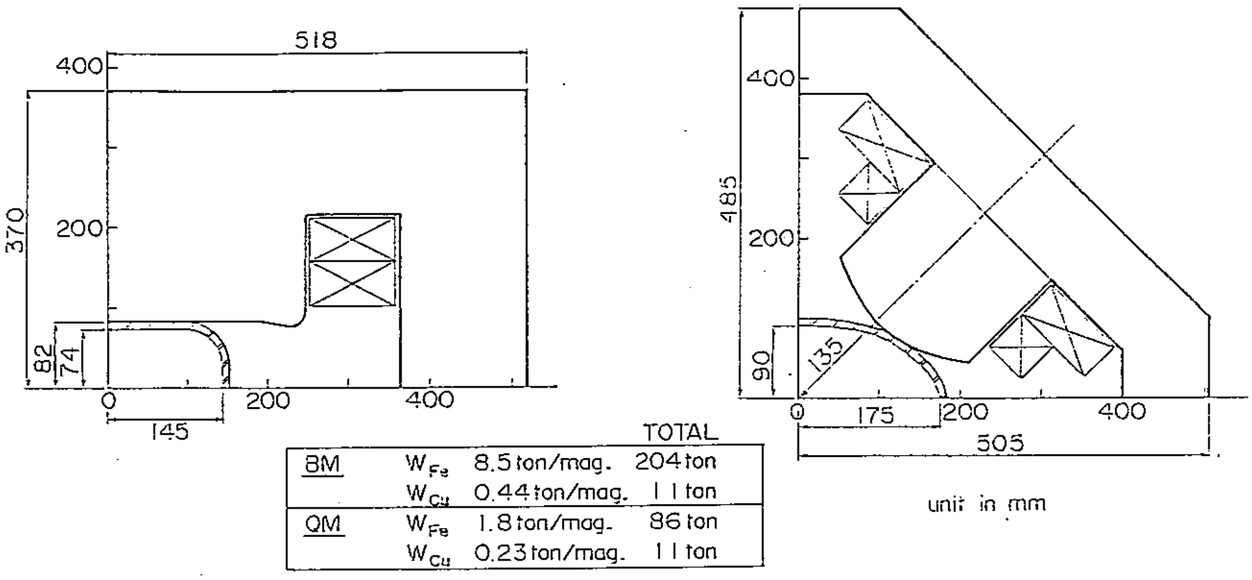

			TOTAL
BM	W_{Fe}	8.5 ton/mag.	204 ton
	W_{Cu}	0.44 ton/mag.	11 ton
QM	W_{Fe}	1.8 ton/mag.	86 ton
	W_{Cu}	0.23 ton/mag.	11 ton

Fig. 4 Gap and Core Geometry of Ring Magnet

RF Acceleration

We assume a 100 MeV injected beam with an effective full momentum spread of 0.75 %. If the RF bucket area has to be twice of the injection beam emittance, the required peak RF voltage through the acceleration period is 166 kV in the 100/3 Hz operation of the guide field magnet. The RF voltage program and relevant parameters of RF bucket are shown in Fig. 5. The required RF voltage will be provided with eight RF stations, each of which is installed in a 3 m long straight section and consists of two reentrant ferrite-loaded cavities. A low impedance cathode-follower is proposed as a final-stage power amplifier in order to compensate for a large beam loading.

Vacuum Chamber

The vacuum chamber will be made from about 300 mm long sections of pure alumina, which are joined by metallizing the ends and brazing in vacuum. The lengths of vacuum chamber to be manufactured are within the limits of joining in this method, which enables us to attach directly metal flange at the end of the chamber.

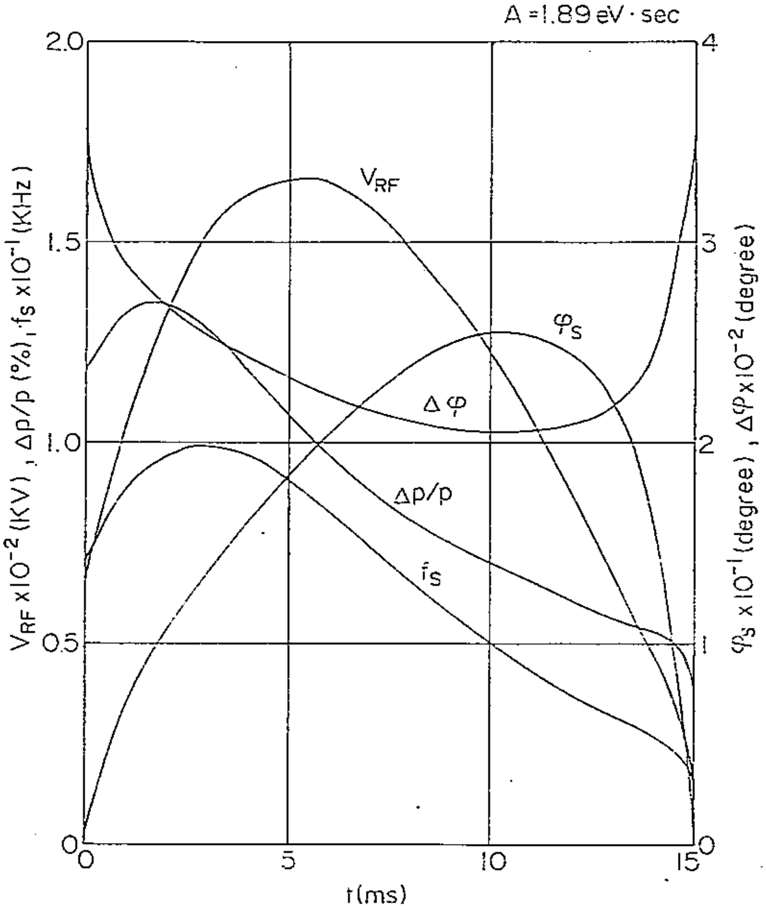

Fig. 5 RF Voltage Program and Relevant Parameters of RF Bucket

Research and Development

R & D for some technical problems is in progress:

1) Prototype of the permanent quadrupole magnet for the linac drift tube. A few kinds of the permanent quadrupole magnet made of samarium cobalt were fabricated. The maximum field gradient of 16.1 and 12.8 kG/cm was realized with a segmented ring quadrupole and an ordinary quadrupole magnet of 6 mm in bore radius, respectively.

2) Beam chopper. In GEMINI using the H^- charge-exchange injection scheme, the most likely beam loss at around injection will result from the inefficiency of the beam trapping in the longitudinal phase space. A chopper synchronizing with the RF accelerating voltage will be introduced into the beam line following the preaccelerator. With a 20 % chopped beam, the inefficiency of the adiabatic trapping is estimated to be less than 1 %. Electronic test of such a chopper is under way.

3) Application of GTO thyristor to the dual frequency mode operation of the ring magnet$^{4)}$. The switching system of the resonant capacitor will be more simplified by replacing ordinary thyristor originally proposed at ANL with GTO thyristor. The test to confirm the switching behavior of the GTO thyristor is under way with a small scale resonant network.

4) Application of stranded cable to the exciting coil of the ring magnet. The power loss due to eddy current in the GEMINI magnet amounts to one third of the total a.c. power consumption of the magnet system by using copper hollow conductor. In order to reduce the eddy-current power loss, aluminum stranded cable containing a stainless steel water-cooling pipe is under development.

5) A prototype of the bending magnet and a small scale model of the RF power amplifier system are under construction.

And also experiments such as the beam bunch shortening test will be carried out by practical use of the existing accelerator and experimental facilities.

References

1) T. Adachi (Ed.), Proc. of the Meeting on BSF Future Prospects, KEK Int. 82-6 (1982).
T. Adachi and Y. Masuda (Ed.), Proc. of the Meeting on BSF Future Prospects-II, KEK Int. 83-7.

2) S. Inagaki et al., Proc. of 7th Meeting on Linear Acceleraters, KEK 82-14, 110 (1982).

3) M. Foss and W. Praeg, IEEE Trans. Nucl. Sci. NS-28, 2856 (1982).

4) H. Someya, et al., Proc. of 4th Symp. on Accelerator Science and Technology at RIKEN, Japan, 317 (1982).

Photostructural Change in As_2S_3 Glass Observed by the Neutron Diffraction

S. Hatta, T. Mizoguchi and N. Watanabe*

Faculty of Science, Gakushuin University, Mejiro,
Tokyo 171, JAPAN

*National Laboratory for High Energy Physics,
Oho-machi, Tsukuba-gun, Ibaragi 305, JAPAN

It is well known that some chalcogenide glasses such as As_2S_3, $GeSe_2$ etc. show the shift of optical absorption edge$^{1)}$ and the volume expansion$^{2)}$ by light exposure. Such phenomena are based on photostructural change, which is characteristic in the glassy structure, without observing it in the corresponding crystals. The photostructural change was partially observed by Hamanaka et al$^{3)}$, who found the reversible change of the first peak located at about 1 $Å^{-1}$ in the interference function S(Q) of As_2S_3 glass by the light exposure ,using X ray diffraction$^{3)}$. However, the change of structure by the exposure in the real space over a wide range has been scarcely studied for As_2S_3 glass.

In the present work, by using the neutron scattering, a total radial distribution function affected by the light exposure is reported, and its photostructural change in the real space is described.

Samples used in this work were prepared by the rapid quenching technique from the molten state of As_2S_3 in Ar atmosphere. Different from many of amorphous alloys, our glassy sample is not any continuous ribbon, but broken pieces with 40~60 μm in thickness. The pre-annealing was done at 170°C for 2h in Ar gas flow. After this annealing, the sample pieces were exposed to the light of a halogen lamp in Ar atmosphere for 10h at room temperature, inserting a water filter between the sample and the lamp. Considering the absorption coefficient of As_2S_3 glass in a visible light region, the sample pieces are enough thin for the light to affect the structure, with illuminating the both surfaces of each sample piece. The pulse neutron scattering experiment was carried out by a high intensity total scattering spectrometer (HIT) at the National Laboratory for High Energy Physics (KEK). Since the photostructural change is cancelled by annealing below the melting temperature (Tm=310°C), the same sample pieces of As_2S_3 glass were heated at 180°C for 1h in Ar atmosphere and were used again for the second neutron diffraction experiment.

With an appropriate correction with respect to absorption, multiple scattering and incoherent nuclear scattering, two interference functions S(Q) were obtained up to 50 A^{-1}, as shown in Fig. 1a. The decrease of the first peak height of S(Q) by the light exposure has been reconfirmed, as reported by Hamanaka et al.3) This means that the interlayer correlation, which is characteristic to the chalcogenide glasses, is decreased by the light exposure. Additionally, a small phase shift of the oscillation in S(Q) can be observed. The difference in $S(Q)_1$(exposed) and $S(Q)_2$(annealed) of As_2S_3 glass is also shown in Fig. 1b. By the Fourier transformation of S(Q) up to 36 A^{-1}, two reduced radial distribution function, $G(r)_1$ (exposed) and $G(r)_2$ (annealed) were obtained. The first peak of each G(r) is not so sharp as that of Ge-Se glass4). This may be due to the difference in the coordination number and the chemical bonding property. Although there exists the difference in S(Q), As_2S_3 glass has indicated relatively small photostructural change in real space, as seen in Fig. 2a. The difference of two G(r)s, which was calculated from ΔS(Q) in Fig. 1b by the Fourier transformation, is emphasized in Fig. 2b. The first peak height in $G(r)_1$ is increased, while a shoulder beside the first peak and the second peak become comparatively small to $G(r)_2$. From the result, the light exposure is thought to make the bond length more rigid and to let the bond angle more random. Both the first and the second peak in $G(r)_1$ seem to be very slightly shifted to the right, however, this change is just close to the resolution limit(~0.02A) in these diffraction experiments. This expansion might be correspondent to the increase of As_2S_3 film thickness (0.5%) by the light exposure, as reported by Tanaka2). In crystalline As_2S_3, the mean bond lengths of As-S and As-As (or S-S) are 2.24A and 3.41A, respectively5). As shown in Fig. 2a, these bond lengths of crystalline As_2S_3 are clearly smaller than those of the glass by about 4%.

References

1)K. Tanaka :Appl. Phys. Lett. 26 (1975) 243
2)K. Tanaka :J. Non-crystalline Solids 35,36 (1980) 1023
3)H. Hamanaka, K. Tanaka and S. Iizima
:Solid State Commun. 23 (1977) 63
4)S. Hatta, S. Yoda, T. Mizoguchi and N. Watanabe
:KENS REPORT IV (1983) 26
5)A. F. Wells ;"Structural Inorganic Chemistry"
Oxford University Press (1962) 682

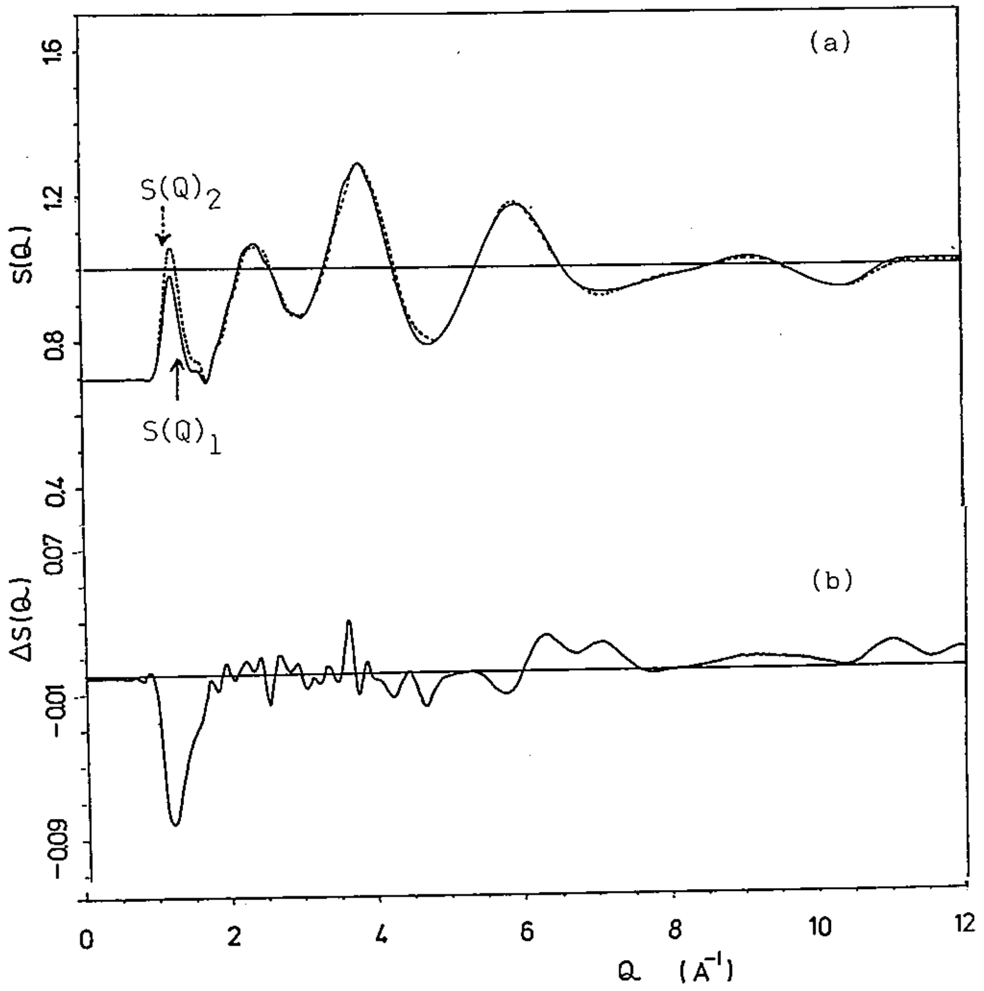

Fig. 1a Two interference functions, $S(Q)_1$(exposed) and $S(Q)_2$ (annealed) of As_2S_3 glass.

Fig. 1b $\Delta S(Q)$; the difference of $S(Q)_1$ and $S(Q)_2$ $(S(Q)_1-S(Q)_2)$.

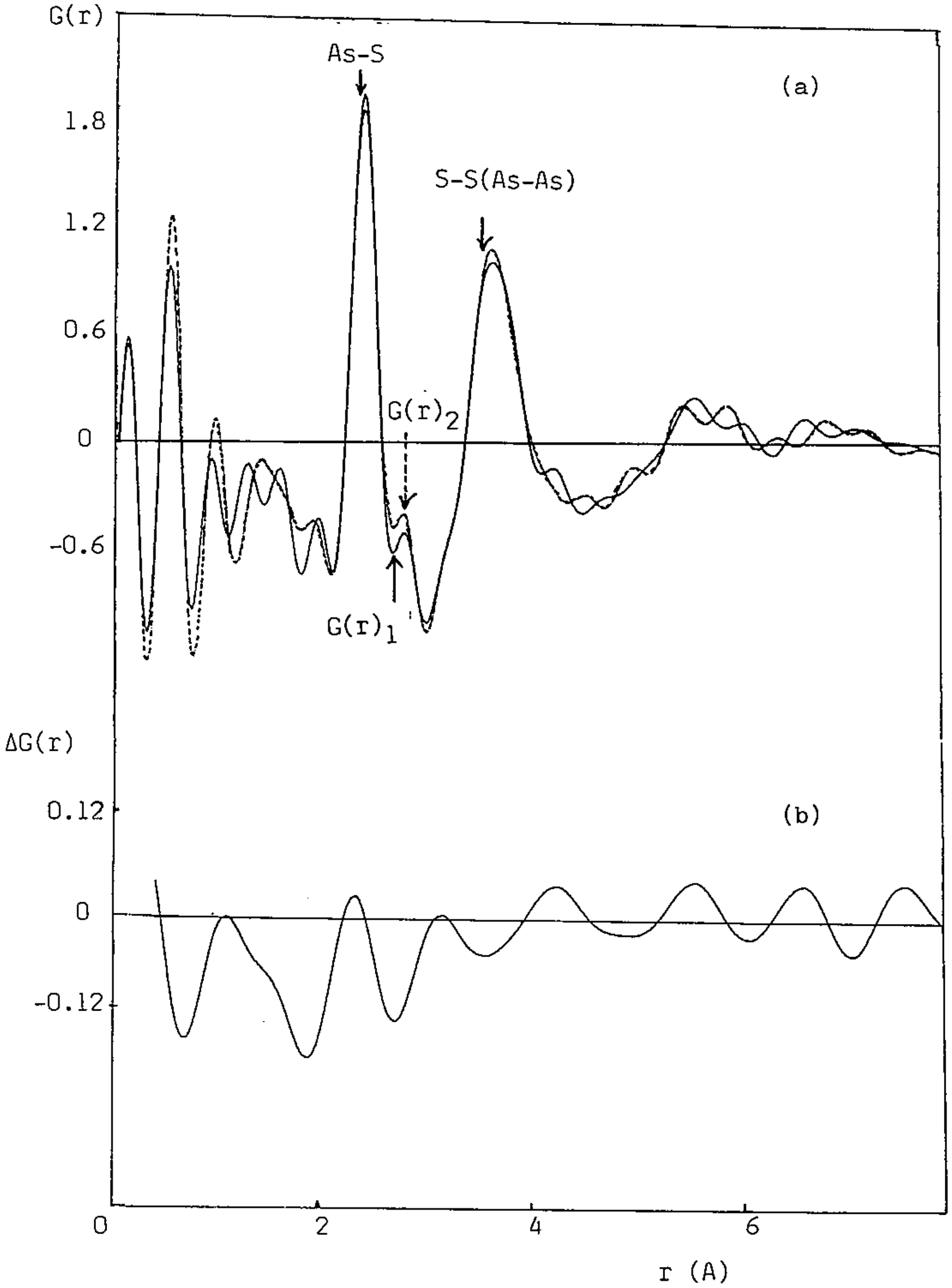

Fig. 2a Two reduced radial distribution functions $G(r)_1$ (exposed) and $G(r)_2$(annealed) of As_2S_3 glass. The arrows show the crystalline bond length of As_2S_3.

Fig. 2b $\Delta G(r)$;the difference of $G(r)_1$ and $G(r)_2$. $\Delta G(r)$ was obtained from $\Delta S(Q)$ by the Fourier transformation.

Direct Observation of Ni-Ni Correlation Function in Ni-42at%V Amorphous Alloy

Toshiharu FUKUNAGA, Shigeo URAI*, Noriyuki HAYASHI,
Noboru WATANABE** and Kenji SUZUKI

The Research Institute for Iron, Steel and Other Metals, Tohoku University, Sendai 980, Japan

*Toyama Technical College, Toyama 930-11, Japan

**National Laboratory for High Energy Physics, Oho-machi, Tsukuba-gun Ibaraki 305, Japan

Partial atomic structures provide more detailed information of the chemical and topological short-range structure in metal-metalloid and metal-metal alloy glasses. Many attempts have been made to evaluate the partial atomic structures of binary alloy glasses using various experimental techniques such as X-ray anomalous scattering, isotope substitution for neutron scattering and combination of different radiations. However, it is very difficult to obtain the partial atomic structure factors without enhancement of experimental errors involved in the total structure factors in solving mathematically the linear simultaneous equations. In this paper we attempt to obtain directly the partial structure of Ni-Ni atom correlation in Ni-42at%V amorphous alloy by neutron diffraction technique.

A thick plate(20mm x 20mm x 0.43mm) of Ni-42at%V amorphous alloy was prepared by using a high rate triode DC sputter deposition apparatus. The measurement of the neutron scattering intensity from this amorphous alloy was carried out at room temperature in vacuum by using the High Intensity Total scattering spectrometer(HIT).

The total structure factor S(Q) of Ni-42at%V amorphous alloy observed by neutron diffraction is shown in Fig. 1 together with the S(Q) observed by X-ray diffraction. The S(Q) can be divided into three atomic partial structure factors $S_{NiNi}(Q)$, $S_{NiV}(Q)$ and $S_{VV}(Q)$ as follows:

$$S(Q) = \frac{C_{Ni}^2 b_{Ni}^2}{\langle b\rangle^2} S_{NiNi}(Q) + \frac{2C_{Ni}C_V b_{Ni} b_V}{\langle b\rangle^2} S_{NiV}(Q) + \frac{C_V^2 b_V^2}{\langle b\rangle^2} S_{VV}(Q) \quad , \tag{1}$$

where b_i and C_i are the coherent scattering length and the concentration of component Ni and V atom respectively and $\langle b\rangle = C_{Ni}b_{Ni} + C_V b_V$. For neutron scattering the coherent scattering length of V atom is very small($b_V=-0.0382 \times 10^{-12}$cm) in comparison with that of Ni atom($b_{Ni}=1.03 \times 10^{-12}$cm). Therefore, the total S(Q) for neutron scattering is rewritten by using numerically calculated weighting factors of the partial atomic structure factors:

$$\begin{aligned} S(Q) &= 1.056\ S_{NiNi}(Q) - 0.057\ S_{NiV}(Q) + 0.0008\ S_{VV}(Q) \\ &\simeq 1.056\ S_{NiNi}(Q) \quad . \end{aligned} \tag{2}$$

Since the weighting factors of Ni-V and V-V correlations are much smaller than that of Ni-Ni correlation, the S(Q) of Ni-42at%V amorphous alloy observed by neutron diffraction is almost equal to the $S_{NiNi}(Q)$. As shown in Fig. 1 the large pre-peak located at $Q \simeq 1.9\ A^{-1}$ was observed in $S_{NiNi}(Q)$ of Ni-42at%V amorphous alloy, which has been also observed in $S_{NiNi}(Q)$'s for Ni-60at%Ti$^{1)}$ and Ni-50at%Zr$^{2)}$ alloy glasses. The small pre-peak at $Q \simeq 1.9\ A^{-1}$ observed in the X-ray S(Q) is certainly originated from the large pre-peak at $Q \simeq 1.9\ A^{-1}$ in the $S_{NiNi}(Q)$.

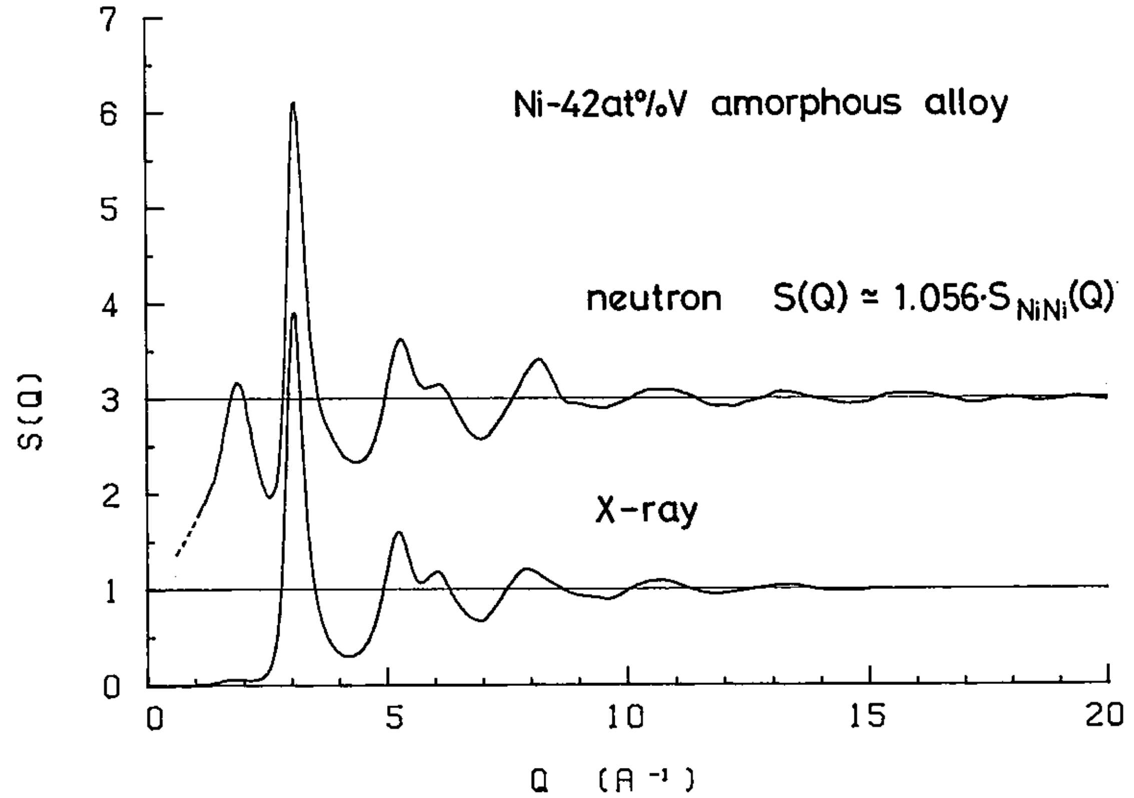

Fig. 1. Total structure factors S(Q) of Ni-42at%V amorphous alloy by neutron and X-ray diffraction. S(Q) obtained by neutron diffraction gives directly the partial $S_{NiNi}(Q)$.

Figure 2 shows the partial radial distribution function(RDF) of Ni-Ni correlation defined as the Fourier transforms of $S(Q) \simeq 1.056\ S_{NiNi}(Q)$ truncated at Q_{max}=20, 18, 16, 14, 12 A^{-1}. The coordination number and the first neighbor distance of Ni atoms around a Ni atom calculated from the first peak area and position in RDF were about 5.3 atoms and 2.485 A. In the case of a statistically random distribution of the total coordination number of 12 atoms, the coordination number of Ni atoms around a Ni atom is about 6.9 atoms. The coordination number of Ni atoms around a Ni atom of Ni-42at%V amorphous alloy is much smaller than that of the random distribution alloy. This indicates the preference of Ni-V unlike atom pair in the nearest neighbor at the distance r_p=2.485 A. We conclude that the chemical short-range order apparently exists in Ni-42at%V amorphous alloy.

References

1) T. Fukunaga, N. Watanabe and K. Suzuki, J. Non-cryst. Solids 61 & 62 (1984) 343.

2) N. Hayashi, T. Fukunaga, N. Watanabe and K. Suzuki, in this Report.

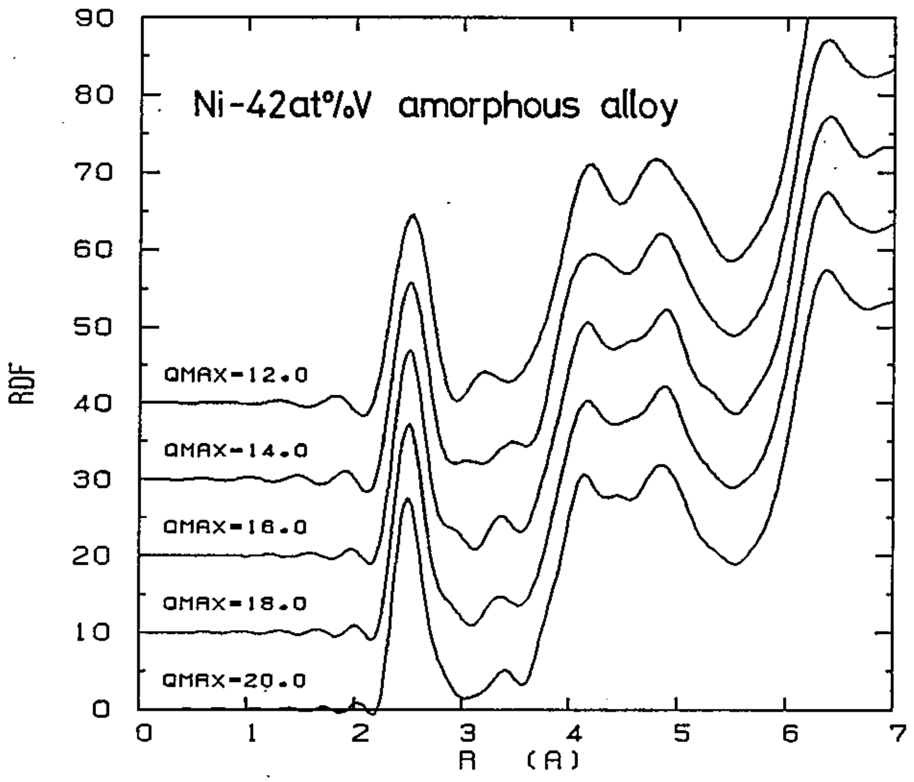

Fig. 2. Radial distribution functions as the Fourier transforms of $S(Q) \simeq 1.056\ S_{NiNi}(Q)$ for Ni-42at%V amorphous alloy.

Partial Structure Functions of NiZr Alloy Glass

Noriyuki HAYASHI, Toshiharu FUKUNAGA, Noboru WATANABE* and Kenji SUZUKI

The Research Institute for Iron, Steel and Other Metals, Tohoku
University, Sendai 980, Japan

*National Laboratory for High Energy Physics, Oho-machi, Tsukuba-gun,
Ibaraki 305, Japan

There are increasing interests in the chemical short-range structure of metal-metal alloy glasses as well as of metal-metalloid alloy glasses. Therefore, the partial structure of binary alloy glasses has been intensively studied by many researchers.

In this paper we distinguish the three atomic partial structure factors of NiZr alloy glass from the total structure factors measured by pulsed neutron total scattering using isotope substitution method. The ^{60}Ni-isotope content in NiZr alloy glass is adjusted so that the weighting factors for unlike-atom partial structure factor $S_{NiZr}(Q)$ have nearly the same contribution in the three total structure factors S(Q). Therefore, the derivation of remaining like-atom partial structure factors $S_{NiNi}(Q)$ and $S_{ZrZr}(Q)$ becomes reasonably simple, because the contribution of $S_{NiZr}(Q)$ to S(Q) is automatically cancelled.

Three kinds of NiZr alloy glass substituted by ^{60}Ni isotope metal were prepared by rapid quenching from the molten state using single roll technique under Ar-gas atomosphere. The measurements of the neutron scattering intensity from these alloy glasses were carried out at room temperature in vacuum by using the High Intensity Total scattering spectrometer(HIT).

The three total structure factors S(Q) for ^{n}NiZr, $^{n+60}$NiZr and ^{60}NiZr alloy glasses observed by neutron total scattering are shown in Fig. 1. S(Q) of ^{n}NiZr alloy glass shows a pre-peak located at $Q \simeq 1.9$ A^{-1}, which has been observed in S(Q) of $^{n}Ni_{35}Zr_{65}$ alloy glass$^{1)}$, too. Such a distinct pre-peak does not appear in S(Q)'s of ^{60}NiZr and $^{n+60}$NiZr alloy glasses. Profiles of the second peak drastically change with increasing ^{60}Ni-isotope content.

Figure 2 shows $S_{NiNi}(Q)$, $S_{NiZr}(Q)$ and $S_{ZrZr}(Q)$ for NiZr alloy glass. $S_{NiNi}(Q)$ has a large pre-peak located at $Q \simeq 1.9$ A^{-1}, which has been also

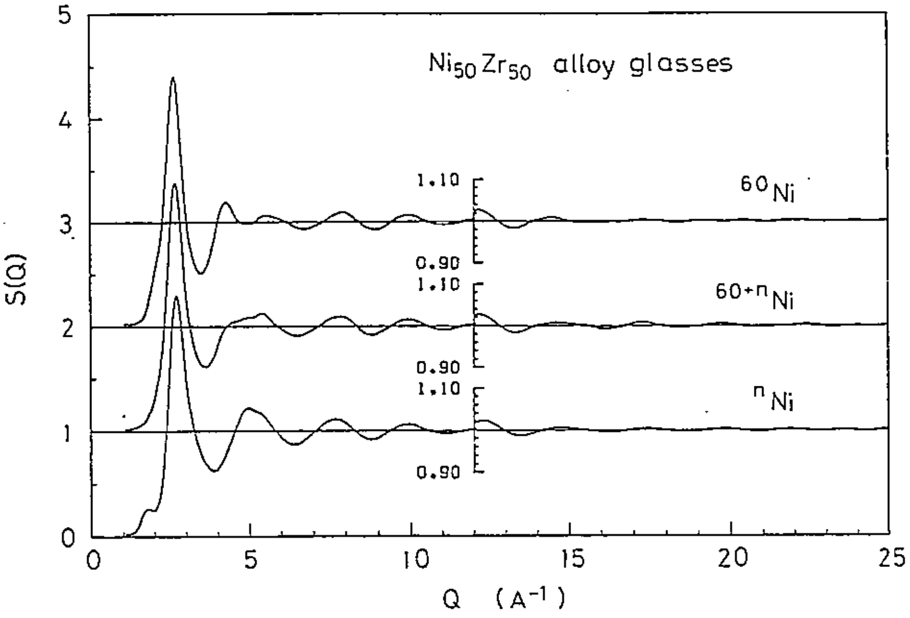

Fig. 1. Total structure factors of ^{n}NiZr, $^{n+60}$NiZr and ^{60}NiZr alloy glasses.

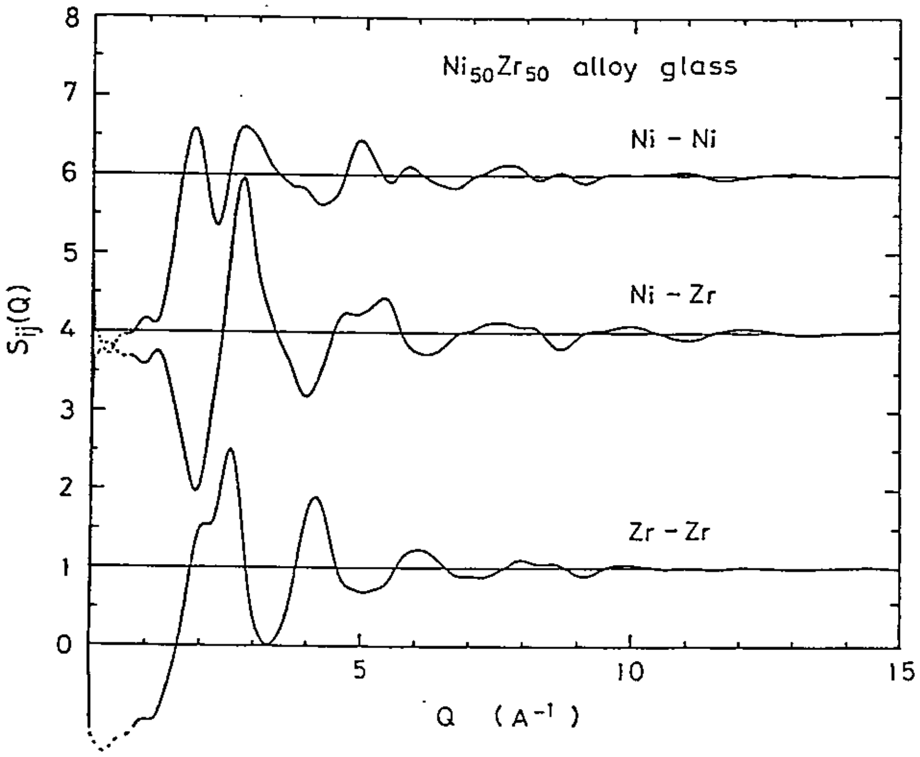

Fig. 2. Partial atomic structure factors $S_{NiNi}(Q)$, $S_{NiZr}(Q)$ and $S_{ZrZr}(Q)$ of NiZr alloy glass.

observed in $S_{NiNi}(Q)$'s for $Ni_{40}Ti_{60}$ 2) and $Ni_{35}Zr_{65}$ 1) alloy glasses. Overall feature of $S_{NiNi}(Q)$ of NiZr alloy glass is very similar to that of $Ni_{40}Ti_{60}$ alloy glass. In $S_{ZrZr}(Q)$ a shoulder is observed at the low Q side of the first peak. The asymmetric first peak extended toward low Q region in $S_{TiTi}(Q)$ of $Ni_{40}Ti_{60}$ alloy glass well corresponds to the shoulder in $S_{ZrZr}(Q)$. Now, we can assign that the small peak appearing in S(Q) of n_{NiZr} alloy glass is certainly originated from the large pre-peak at $Q \simeq 1.9$ A^{-1}in $S_{NiNi}(Q)$. Furthermore, it is concluded that no pre-peak in S(Q)'s of $^{n+60}$NiZr and ^{60}NiZr alloy glasses is due to the compensation between the large pre-peak at $Q \simeq 1.9$ A^{-1} in $S_{NiNi}(Q)$ and the negative peak $Q \simeq 1.9$ A^{-1} in $S_{NiZr}(Q)$.

Figure 3 shows the partial atomic pair reduced distribution functions $G_{NiNi}(r)$, $G_{NiZr}(r)$ and $G_{ZrZr}(r)$ defined as the Fourier transforms of $S_{NiNi}(Q)$, $S_{NiZr}(Q)$ and $S_{ZrZr}(Q)$ truncated at $Q_{max}=15$ A^{-1}. The interatomic distances and coordination numbers of the nearest neighbor correlation for NiZr alloy glass are listed in Table 1, together with those of NiZr crystalline compound 3). The nearest interatomic distances of Ni-Ni, Ni-Zr and Zr-Zr correlation are about 2.63 A, 2.73 A and 3.32 A respectively. It is noticeable that the Ni-Ni and Zr-Zr interatomic distances in Ni-Zr alloy glass are smaller than those in NiZr crystalline compound, but larger than Ni and Zr atomic diameter

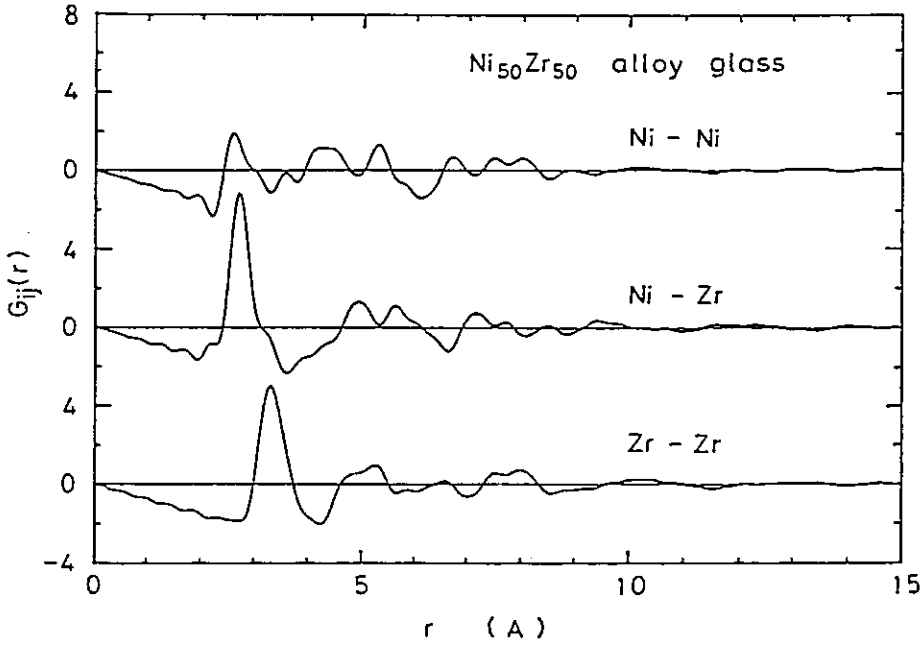

Fig. 3. Partial atomic pair reduced distribution functions $G_{NiNi}(r)$, $G_{NiZr}(r)$ and $G_{ZrZr}(r)$ of NiZr alloy glass.

(D_{Ni}=2.48 A and D_{Zr}=3.20 A). The Ni-Zr interatomic distance in NiZr alloy glass is rather close to that in NiZr crystalline compound, but much smaller than the mean value of the Ni and Zr atomic diameters. The coordination numbers of Ni-Ni, Ni-Zr and Zr-Zr correlations in NiZr alloy glass are slightly less than those in NiZr crystalline compound. However, the chemical short-range structures are almost similar between NiZr alloy glass and crystalline compound.

Table 1. Interatomic distances(r) and coordination numbers(n) of the nearest neighbor Ni-Ni, Ni-Zr and Zr-Zr correlations of NiZr alloy glass and NiZr crystalline compound.

atomic pair	NiZr glass		NiZr crystal		
	r(A)	n(atoms)	r(A)	n(atoms)	
Ni-Ni	2.63	3.3	2.49 3.26	2 2	(4)
Ni-Zr	2.73	6.7	2.66 2.70 2.87	2 4 1	(7)
Zr-Zr	3.32	7.8	3.26 3.41 3.46	2 4 2	(8)

References

1) T. Fukunaga, N. Watanabe and K. Suzuki, J. Non-cryst. Solids 61 & 62 (1984) 343.

2) A. Lee, G. Etherington and C. N. J. Wagner, J. Non-cryst. Solids 61 & 62 (1984) 349.

3) W. L. Korst, J. Phys. Chem. 66 (1962) 370.

Neutron Diffraction Study of Chemical Short Range Order in $Ni_{60}Nb_{40}$ Amorphous Alloy

M.SAKATA , S.HASHIBA , N.AKUTSU* and T.MIZOGUCHI*

Applied Physics Department, Nagoya University, Nagoya, 464, Japan

*Faculty of Science, Gakushuin University, Tokyo, Japan

The preference of unlike atoms as the first nearest neighbours in amorphous system is called chemical short range order(CSRO) and the existence of CSRO is believed to be one of the key factor to enhance the thermal stability of the amorphous alloy1). It is a very easy work to observe CSRO of a binary amorphous alloy directly by a diffraction experiment as long as the atomic scattering factor of the two composition atoms are greatly different from each other. A neutron diffraction experiment for some alloy glasses like CuTi and NiTi is one of these easy works because of a negative atomic scattering length of Ti atoms. The direct observation of CSRO becomes, however, a extremely difficult work for the system of which components have the similar atomic scattering factor. Hence there remains often some ambiguity of the existence of CSRO. $Ni_{60}Nb_{40}$ is one of these cases for which there is a controversy on the existence of CSRO.2)3) The aim of this work is to investigate the local density and concentration fluctuation in order to examine the existence of CSRO in $Ni_{60}Nb_{40}$ amorphous alloy.

Thin ribbons of three different isotope composition $Ni_{60}Nb_{40}$ amorphous alloys, i,e, $^{Nat}Ni_{60}Nb_{40}$, $(^{Nat}Ni_{58}\,^{60}Ni_{42})_{60}Nb_{40}$ and $^{60}Ni_{60}Nb_{40}$(the latter two are abbreviated as $^{Mix}Ni_{60}Nb_{40}$ and $^{Iso}Ni_{60}Nb_{40}$, respectively), have bean prepared by a single roll melt spinning method under Ar atomosphere. For $^{Mix}Ni_{60}Nb_{40}$, only the structure factor of density fluctuation, Snn(Q) should be observed where Q represents scattering vector. The total neutron scattering was measured at room temperature up to $Q=24A^{-1}$ with High Intensity Total scattering spectrometer(HIT) installed at KENS, National Laboratory for High Energy Physics, Tsukuba. In order to attain experimental condition as unchanged as possible for each measurement, the height and radius of the sample cell and vanadium rod which was used for intensity normalization were kept constant, i,e, h(height)=4.0cm and R(radius)=0.4cm.

The total structure factors S(Q) for the three specimens are shown in Fig. 1 with the structure factor of concentration fluctuation, Scc(Q), which was derived from these three S(Q) using Bhatia-Thornton[4] type partial structure factor expression. Under the first peak $(Q \approx 3A^{-1})$ of the total structure factors, Scc(Q) is not shown because of the great errors.

The RDFs(radial distribution functions) for them are shown in Fig.2. Some structural parameters obtained from RDF and S(Q) are listed in Table 1 where the first and second neighbour distance r_1 and r_2, their ratio, coordination number n, Warren-Cowley's order parameter α and the ratio of pre-peak and the 1st peak position Q_p/Q_1 in Q space are given. Those of $Cu_{66}Ti_{34}$ amorphous alloys for which CSRO is undoubtedly observed are also included in the table for the comparison. The table clearly shows that structures of $Ni_{60}Nb_{40}$ and $Cu_{66}Ti_{34}$ amorphous alloys are quite similar. It should be emphasized that not only α is negative but also the ratio of r_1/r_2 is very close to that of Q_p/Q_{1st} in $Ni_{60}Nb_{40}$ amorphous alloy. These experimental results support the interpretation that the origin of the pre-peak is due to CSRO. It would be interesting to note that the expected value of ratio of r_1/r_2 and n for dense random packing of hard spheres model(DRPHS) (0.61 and 12, respectively) are also very similar to those listed in the table. This seems to suggest that the structure of transition metal-transition metal amorphous alloy was represented by the DRPHS with some CSRO as a first approximation.

Table 1 Some structural parameters of $Ni_{60}Nb_{40}$ and $Cu_{66}Ti_{34}$ metallic glasses

	r_1	r_2	r_1/r_2	n	α	Q_p/Q_1
$Ni_{60}Nb_{40}$	2.61	4.55	0.57	12.5	-0.3	0.60
$Cu_{66}Ti_{34}$	2.64	4.51	0.58	11.9	-0.2	0.62

References

1) M.Sakata, N.Cowlam and H.A.Davies : Proc. 4th Int. Conf. Rapidly Quenched Metal p327 (1982)

2) M.Sakata, N.Cowlam and H.A.Davies : J. Non-Cryst. Solids 46 (1981) 329

3) H.Ruppersburg and G.N.J.Wagner : J. Non-Cryst. Solids 55 (1983) 165

4) A.B.Bhatia and D.E.Thornton, Phys. Rev., B2 (1970) 3004

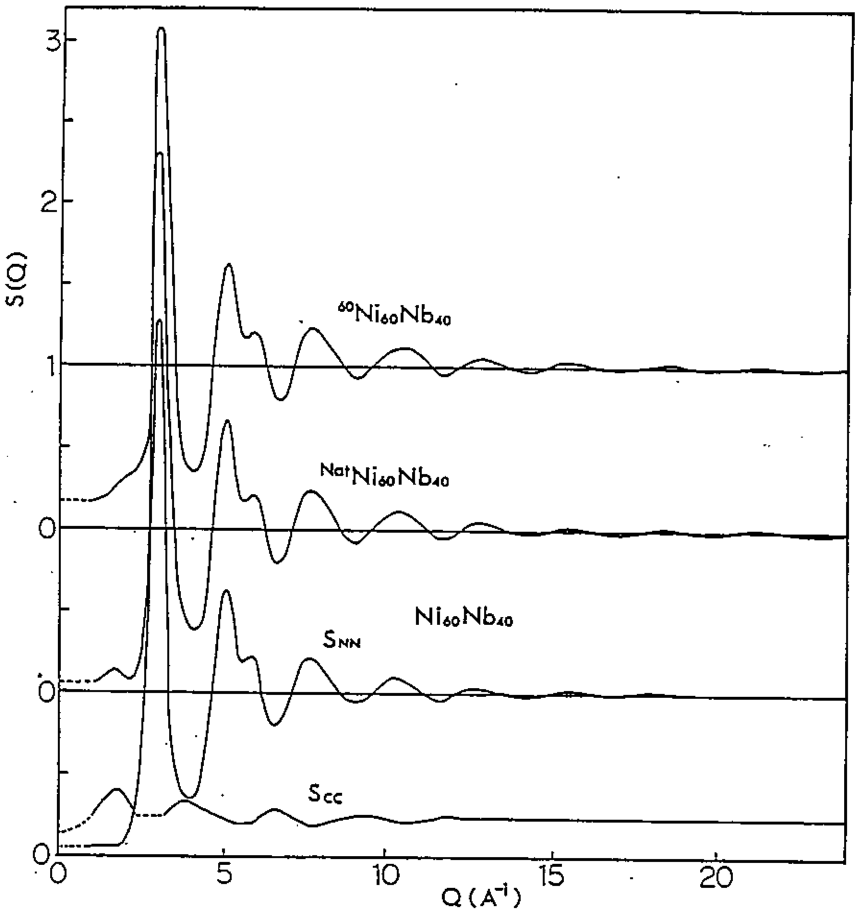

Fig.1.
The observed total structure factors S(Q) of $Ni_{60}Nb_{40}$ amorphous alloys of three different isotope compositions by time of flight neutron scattering and the structure factor due to concentration fluctuation Scc(Q) derived from them.

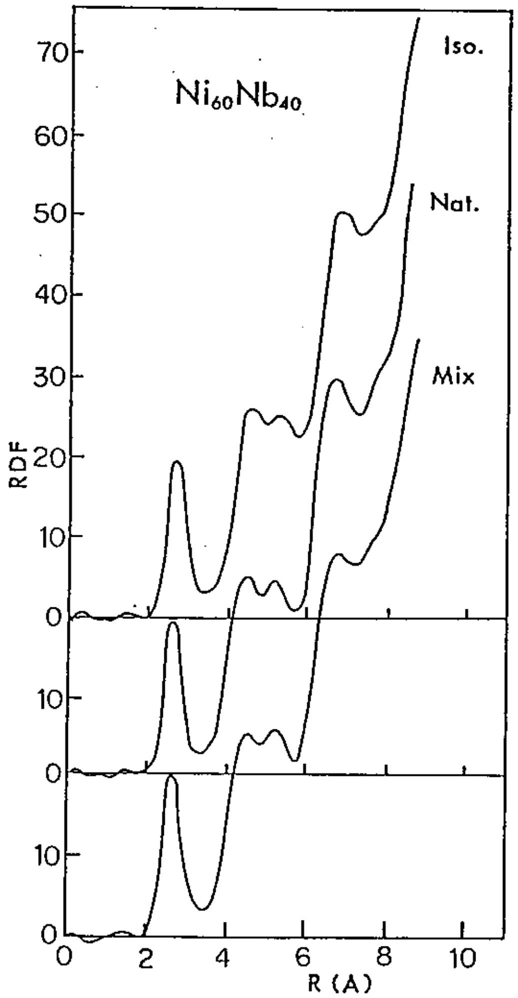

Fig.2.
The radial distribution function of $Ni_{60}Nb_{40}$ amorphous alloys of three different isotope compositions.

The Comparison of Structures between Amorphous Ni-Zr and Ni-Hf Alloys

+Toshio Kudo, Toshiharu Fukunaga* and Noboru Watanabe**

The Research Development Corporation of Japan
5-2, Nagata-cho 2-chome, Chiyoda-ku, Tokyo 100, Japan

*The Research Institute for Iron, Steel and Other Metals,
Tohoku University, Sendai 980, Japan

**National Laboratory for High Energy Physics, Oho-machi,
Tsukuba-gun, Ibaraki 305, Japan

The isomorphous replacement method, substituting Hf for Zr in the amorphous alloy $Ni_{35}Zr_{65}$, has been used to evaluate the partial structure factors in amorphous $Ni_{35}(Zr\text{-}Hf)_{65}$ alloys by Wagner and Lee1). In this method, it has been tacitly assumed that this substitution of atoms does not change the structure of the amorphous alloy. In spite of the samples being noncrystalline, the assumption is based on the crystallographical fact that the crystalline compound of $NiHf_2$ is isostructural with the one of $NiZr_2$2).

In order to confirm whether the assumption holds or not in the amorphous alloy, the experiment of pulsed neutron scattering was carried out with the high intensity total scattering spectrometer (HIT), selecting the two amorphous samples of $Ni_{36}Zr_{64}$ and $Ni_{36}Hf_{64}$.

The amorphous samples were prepared from the molten alloys by the melt spinning method. The as-quenched ribbons were finely cut and each piece was packed into a vanadium holder. A hafnium metal contains originally a small amount of Zr as an impurity, and so the nominal compositions, $Ni_{36}Zr_{64}$ and $Ni_{36}Hf_{64}$, are revised by the result of chemical and spectrochemical analysis as follows: $Ni_{35.9}Zr_{64.1}$ and $Ni_{35.7}Hf_{59.0}Zr_{5.3}$. The density of the amorphous Ni-Zr alloy is 7.14 g/cm^3, while the one of the amorphous Ni-Hf-Zr alloy is 11.92 g/cm^3. Calculating the number of atoms per unit volume from the values of density, each is 0.0541 A^{-3} for the binary Ni-Zr

---

+Present address: Research & Development Division, CASIO COMPUTER CO., LTD 2951-5, Ishikawa-cho Hachioji-city, Tokyo 192, Japan alloy and 0.0542 A^{-3} for the ternary Ni-Hf-Zr alloy, and the two values of the mean atomic density are almost equal.

In the case subtracting the one from the other between two stucture factors, it is essential to evaluate the weighting factors W_{ii}, W_{ij}, W_{jj} in the structure factor, $S(Q)=\sum_{ij} W_{ij} S_{ij}(Q)$. Here the weighting factors of the ternary Ni-Hf-Zr alloy are calculated as a quasi-binary Ni-(Hf-Zr) alloy which consists of Ni atoms and the composition average atoms of Hf and Zr. As shown in Table 1, the differences of the values of W_{ii}, W_{ij}, W_{jj} between the Ni-Zr alloy and the Ni-Hf-Zr alloy are negligibly small. Therefore the pair of two amorphous samples is an ideal case to verify an isomorphous structure in amorphous alloys.

The observed structure factors are compared each other in Fig. 1. To analyze quantitatively a difference between the two structure factors, the S(Q) of the amorphous Ni-Zr alloy is subtracted from the one of the amorphous Ni-Hf-Zr alloy and the difference $\Delta S(Q)$ is shown in Fig. 2. There is especially a big difference around the first peak of S(Q) and an oscillation in $\Delta S(Q)$ persists to $Q \simeq 20\ A^{-1}$. Being difficult to surmise directly a structure in a real space from $\Delta S(Q)$, the subtraction $\Delta S(Q)$ is converted by Fourier transformation. The distribution function $\Delta g(r)$ obtained as the Fourier transform of $\Delta S(Q)$ is equivalent to subtracting the pair distribution function g(r) of the Ni-Zr alloy from that of the Ni-Hf-Zr alloy. A conspicuous difference of structure exists mainly at the nearest neighbor coordination as shown in Fig. 3. Therefore it is proved that the structures of the amorphous Ni-Zr and Ni-Hf-Zr alloys are not strictly isomorphous. The positions, which correspond to two maxima and a minimum of $\Delta g(r)$ at $r \simeq 2.5 \sim 3.1$ A, are compared to the interatomic distances of nearest neighbor pairs, that is, Ni-Ni, Zr-Zr and Ni-Zr pairs, in the crystalline $NiZr_2$. The values 2.60 A, 3.08 A and 2.78 A of two maximum and one minimum positions in $\Delta g(r)$ are marverously located close by the distances 2.62 A, 3.07 A and 2.76 A of Ni-Ni, Zr-Zr and Ni-Zr pairs in the crystalline $NiZr_2$ 2). The origin of this structure change by the substitution of Hf atoms for Zr atoms is ascribed to a preference formation for like atom pairs or unlike atom pairs in the nearest neighbor atoms. To put it more concretely, the like atom pairs such as Ni-Ni and Hf-Hf pairs are more preferentially formed in the Ni-Hf amorphous alloy than the Ni-Ni and Zr-Zr like atom pairs in the Ni-Zr amorphous alloy. On the contrary, the formation of Ni-Zr unlike atom pairs is in preference to that of Ni-Hf unlike atom pairs.

References

1) C. N. J. Wagner and D. Lee, J. Physique 41 (1980) C 8-242.

2) M. E. Kirkpatrick, D. M. Bailey and J. F. Smith, Acta Crys. 15 (1962) 252.

Table 1. Weighting factors W_{ii}, W_{ij}, W_{jj} of amorphous Ni-Zr and Ni-(Hf-Zr) alloys.

$Ni_{35.9}Zr_{64.1}$	W_{NiNi}	$2W_{NiZr}$	W_{ZrZr}
	0.199	0.494	0.307
$Ni_{35.7}Hf_{59.0}Zr_{5.3}$	W_{NiNi}	$2W_{Ni(HfZr)}$	$W_{(HfZr)(HfZr)}$
	0.183	0.490	0.327

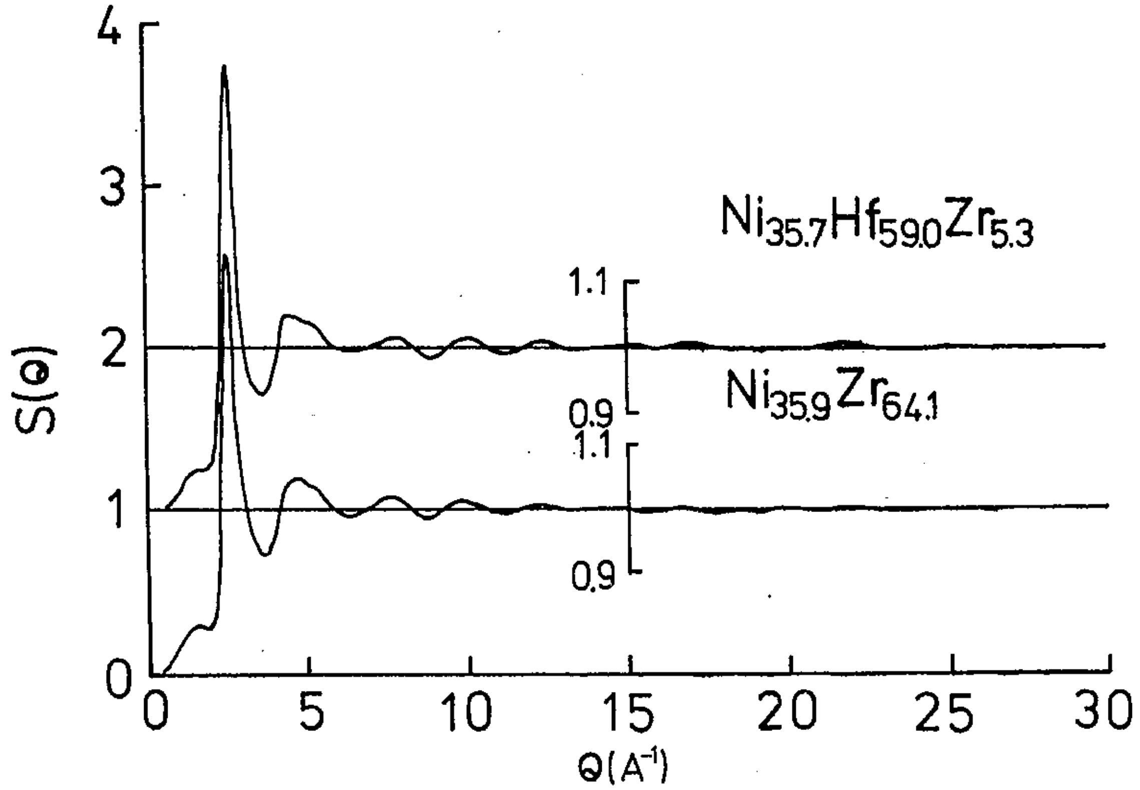

Fig. 1. Structure factors of amorphous $Ni_{35.9}Zr_{64.1}$ and $Ni_{35.7}Hf_{59.0}Zr_{5.3}$ alloys.

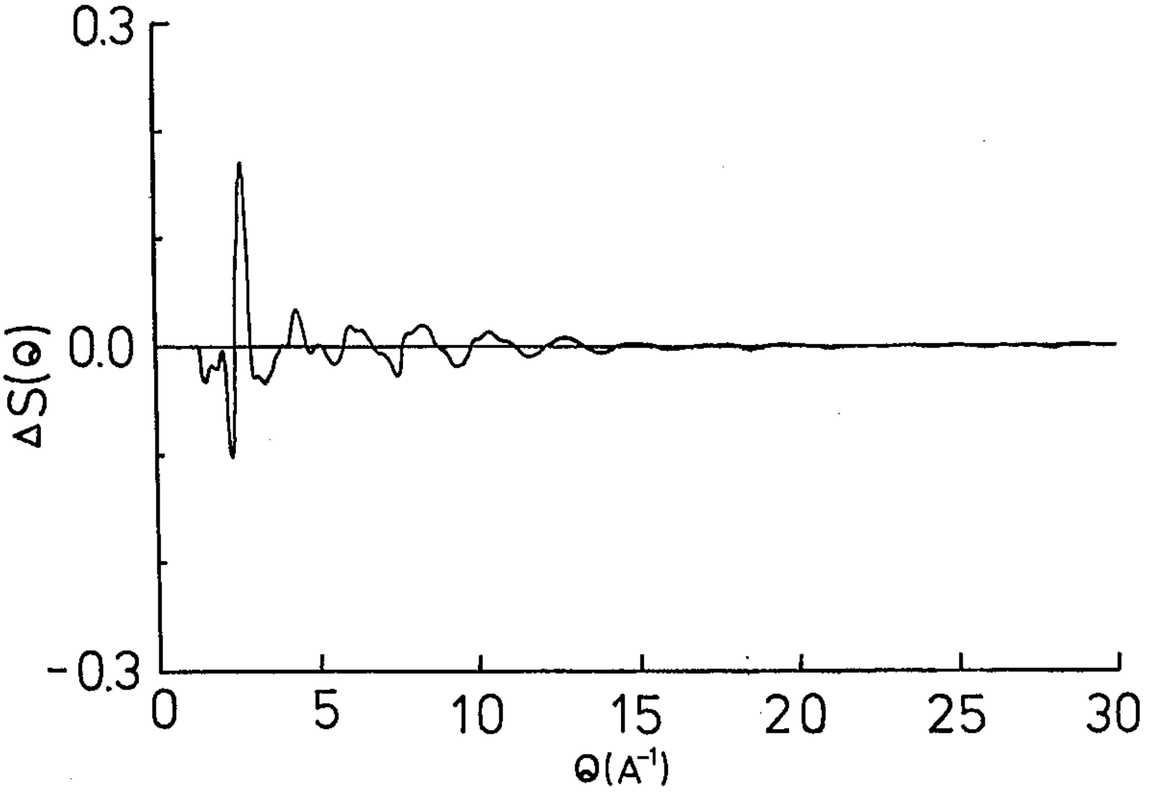

Fig. 2. The subtraction, ΔS(Q), of the S(Q) of the amorphous Ni-Zr alloy from that of the amorphous Ni-Hf-Zr alloy.

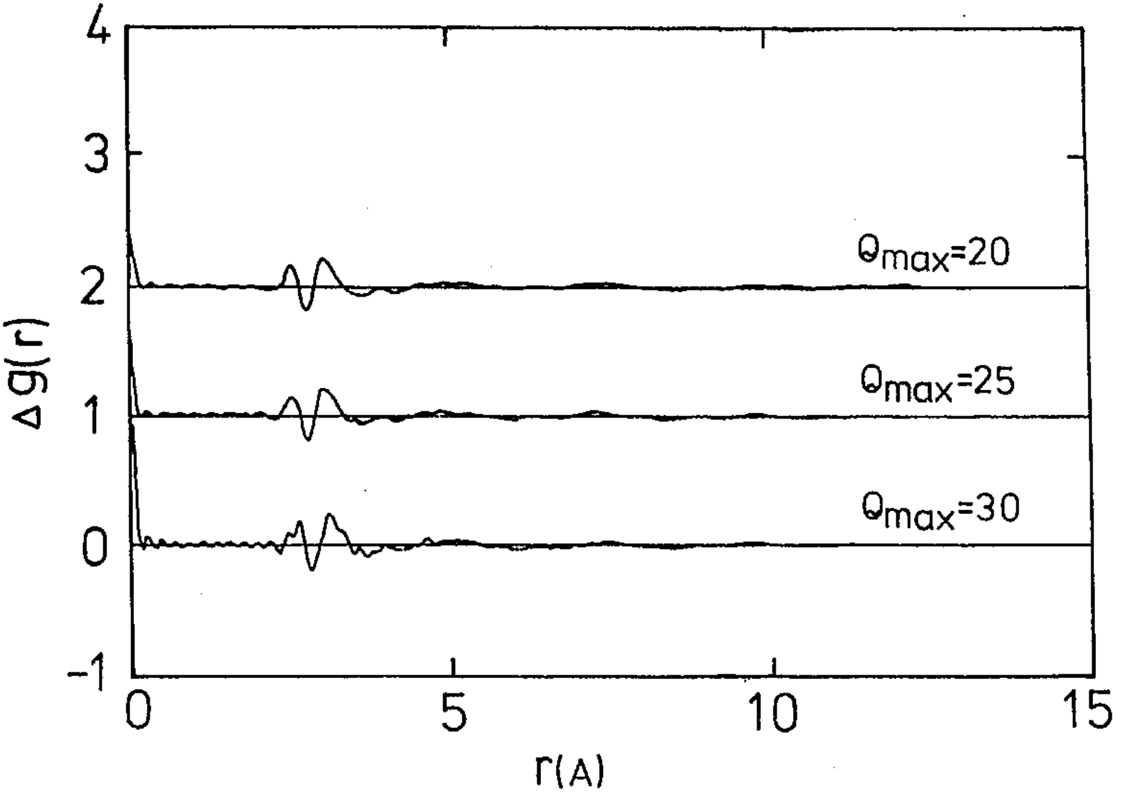

Fig. 3. The distribution function Δg(r) obtained by the Fourier transformation of ΔS(Q).

Neutron Diffraction of amorphous $Tb_{72}Fe_{28}$ Alloy

S. Hatta, T. Mizoguchi and N. Watanabe>

Faculty of Science, Gakushuin University, Mejiro,
Tokyo 171, JAPAN

>National Laboratory for High Energy Physics
Oho-machi, Tsukuba-gun, Ibaragi 305, JAPAN

Previously Rhyne et al investigated amorphous structure of $TbFe_2$ alloy by conventional neutron diffraction using a reacter, but the result was slightly obscure$^{1)}$. Subsequently, O'Leary obtained the three partial correlation functions of Fe-Fe, Tb-Fe and Tb-Tb pairs$^{2)}$, where the nuclear and magnetic data by neutron scattering of a-$TbFe_2$$^{1)}$ had been used together with the interference function S(Q) of a-$GdFe_2$ by an X ray diffraction$^{3)}$. In order to determine the structure of amorphous Tb-Fe alloys more directly, TOF pulse neutron scattering experiment for a-$Tb_{72}Fe_{28}$ was done by a high intensity total scattering spectrometer (HIT) at the National Laboratory for High Energy Physics (KEK). Amorphous alloy ribbon samples were prepared by a rapid quenching method from the molten alloy in Ar atmosphere. Diffraction experiment was carried out at room temperature above the ferrimagnetic Curie temperature (Θ_f= 160K). The experimental data were appropriately corrected with respect to absorption, multiple scattering and incoherent nuclear scattering. In an obtained spectrum, an overwhelming paramagnetic scattering was observed together with the coherent nuclear scattering, as shown in Fig. 1. The cross section of paramagnetic scattering is

$$\left(\frac{d\sigma}{d\Omega}\right)_{para} = \frac{2}{3}\left(\frac{\gamma_N e^2}{mc^2}\right)^2 \left\langle \frac{g^2 J(J+1)}{4} f^2(Q) \right\rangle \quad (1)$$

where γ_N is the ratio of the neutron magnetic moment to the nuclear Bohr magneton and f(Q) is a magnetic form factor, m is the electron mass, e is the electron charge and c is the light velocity. < > represents the compositional average of the alloy. Fe moment is assumed to have $g_{Fe}=2$, $J_{Fe}=1$ with considering the results of the calculation by Gangulee et al4). For Tb atom, there exists a definite moment with $g_{Tb}=1.5$ and $J_{Tb}=6$. f(Q) was calculated by a polynomial approximation, by use of the data listed in 5) and 6). In the paramagnetic scattering of a-$Tb_{72}Fe_{28}$, the contribution of Fe is very small below 3%. By subtracting the paramagnetic scattering term from the spectrum, the interference function S(Q) (Fig. 2) was obtained. By the Fourier transformation of S(Q) up to 36 A^{-1}, the radial distribution function, G(r), was calculated. As seen in Fig. 3, the first peak of G(r) indicates the clear splitting into three subpeaks. They are located at 2.48, 3.01, 3.52 A, which correspond to Fe-Fe, Fe-Tb, Tb-Tb atomic pairs, respectively, as the sum of the Goldschmidt atomic radii. These results are different from those by O'Leary2), who reported that in a-$TbFe_2$ the estimated atomic radii are non-additive, and that the Tb-Fe distance is rather greater than the average of the Fe-Fe and Tb-Tb distances. This would imply that the short range order depends on the alloy composition in amorphous alloys of binary constituents with different atomic size. All results are listed in Table 1.

Table 1

	Rhyne et al1)	O'Leary2)	Present work
Tb-Tb	~ 3.5A	3.42	3.52
Tb-Fe	~ 2.9	3.2	3.01
Fe-Fe	~ 2.6	2.55	2.48

References

1)J. J. Rhyne, S. J. Pickart and H. H. Alperin
:AIP Conf. Proc. No 18 (1974) 563

2)W. P. O'Leary :J. Phys. F, Metal Phys. 5 (1975) L175

3)G. S. Cargil Ⅲ :AIP Conf. Proc. No 18 (1974) 631

4)A. Gangulee and R. C. Taylor
:J. Appl. Phys. 49 (3) (1978) 1762

5)Y. A. Izyumov and R. P. Ozerov
:" Magnetic Neutron Diffraction" Plenum (1970) 363

6)M. Blume, A. J. Freeman and R. E. Watson
:J. Chem. Phys. 37 (1962) 1245

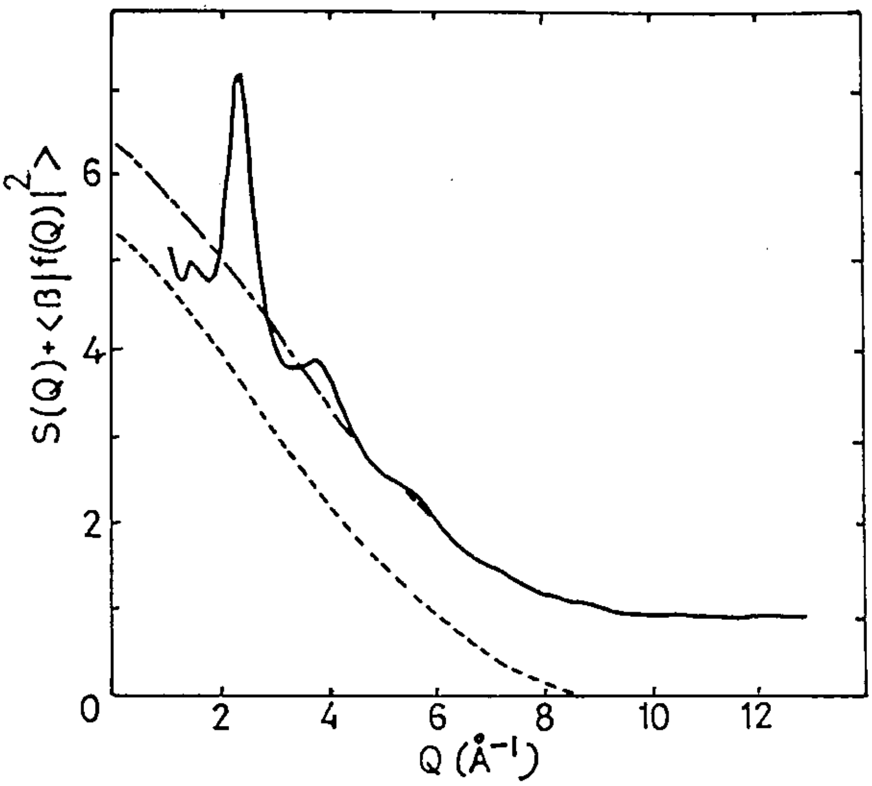

Fig. 1 The spectrum of the neutron scattering of a-$Tb_{72}Fe_{28}$. The broken line represents $\langle\beta f(Q)^2\rangle$ and the chain shows $\langle\beta f(Q)^2\rangle+1$, here $\beta = \frac{1}{\langle b^2\rangle}\frac{2}{3}\left(\frac{\gamma_N e^2}{mc^2}\right)^2 \cdot \frac{g^2 J(J+1)}{4}$

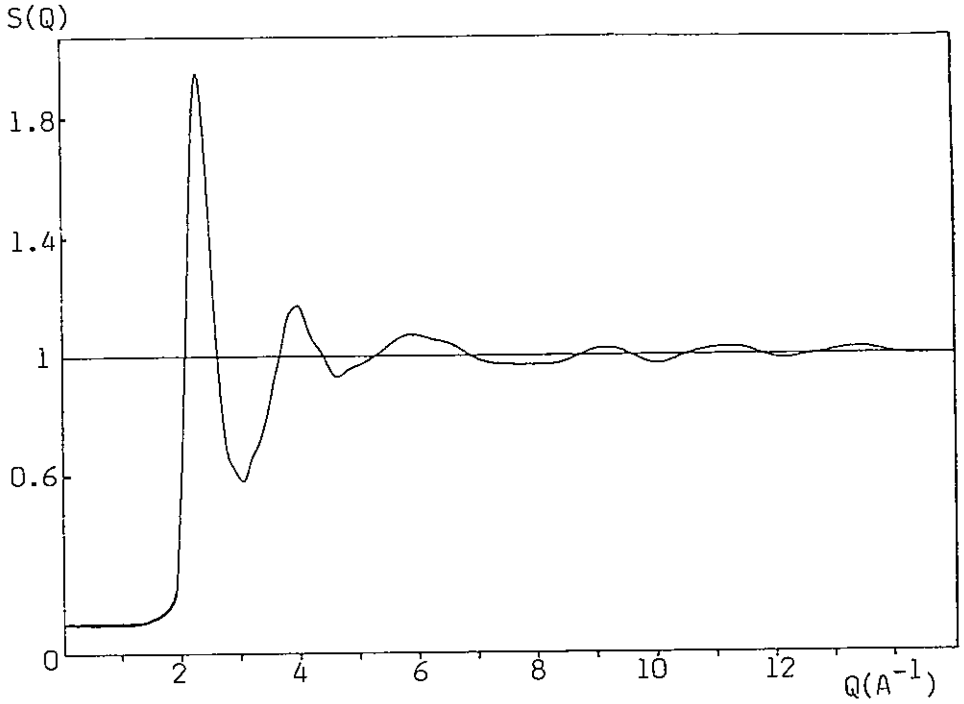

Fig. 2 S(Q) of a-$Tb_{72}Fe_{28}$. This is obtained by subtracting the paramagnetic scattering contribution from the spectrum in Fig. 1.

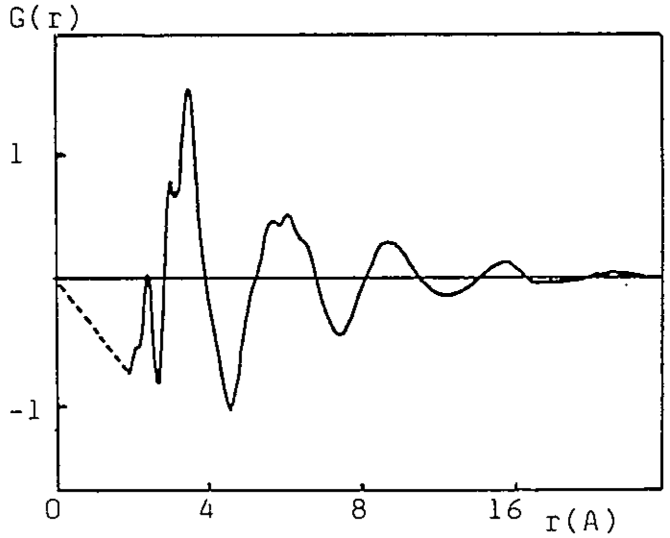

Fig.3
The reduced RDF vs. r for a-$Tb_{72}Fe_{28}$

Short Range Structure of Y-Al-D Amorphous Alloys

Noriyuki HAYASHI, Toshiharu FUKUNAGA, Noboru WATANABE*
and Kenji SUZUKI

The Research Institute for Iron, Steel and Other Metals,
Tohoku University, Sendai 980, Japan

*National Laboratory for High Energy Physics, Oho-machi,
Tsukuba-gun, Ibaraki 305, Japan

The aim of this study is to examine what kind of atomic sites in $Y_{.50}Al_{.50}$ and $Y_{.67}Al_{.33}$ amorphous alloys are occupied by hydrogen atoms through the high resolution observation of radial distribution function (RDF). Total structure factors S(Q) for $Y_{.50}Al_{.50}D_X$(X = 0, 0.09, 0.15 0.20, 0.30, 0.54 and 0.56) and $Y_{.67}Al_{.33}D_X$(X = 0, 0.10, 0.17, 0.25, 0.49, 0.70, 0.80 and 1.07) were measured with a High Intensity Total scattering spectrometer (HIT) installed at KEK.

Amorphous alloys were prepared into a form of thin ribbons with about 1 mm in width and 20 μm in thickness by rapid quenching from melts using single roll method under Ar-gas atomosphere. Deuterium atoms were absorbed into the amorphous ribbons by a gas-charge method under ~20kg/cm^2 pressure at 230°C ($Y_{.50}Al_{.50}D_X$) and 160°C ($Y_{.67}Al_{.33}D_X$). Deuterium content absorbed was controlled by measuring the change in D_2-gas pressure during absorption and in sample weight, and then analyzed by Ar-gas carrier chromatography.

The total structure factors S(Q) of $Y_{.50}Al_{.50}D_X$ amorphous alloys obtained in this study are shown in Fig. 1. With increasing D concentration the height of the first peak in S(Q) decreases, while that of the second one drastically increases. The position of the first peak in S(Q) is almost constant, while that of the second one shifts toward lower Q. The S(Q) oscillates untill about Q = 20 A^{-1}. Small angle scattering appears gradually with increasing D concentration. In the case of the S(Q) of Ni-Ti-D$^{1)}$, Pd-Zr-D$^{2)}$ and Ni-Zr-D$^{3)}$ amorphous alloys the small angle scattering does not appear.

Figure 2 shows the radial distribution functions RDF of $Y_{.50}Al_{.50}D_X$ amorphous alloys obtained as the Fourier transforms of S(Q) truncated at

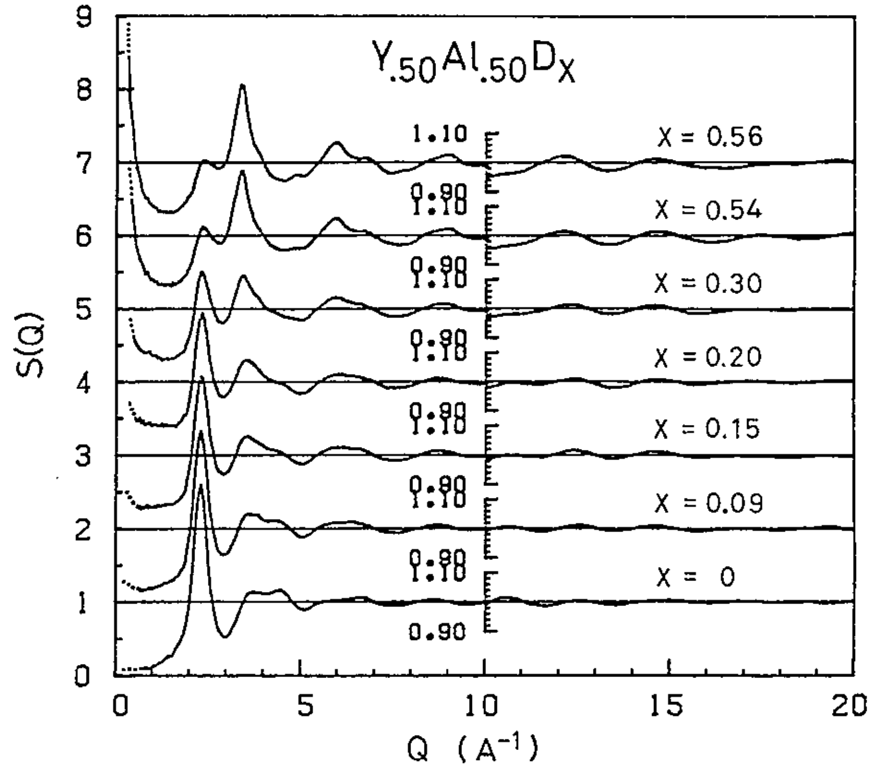

Fig. 1. Total Structure Factors of $Y_{.50}Al_{.50}D_X$ amorphous alloys.

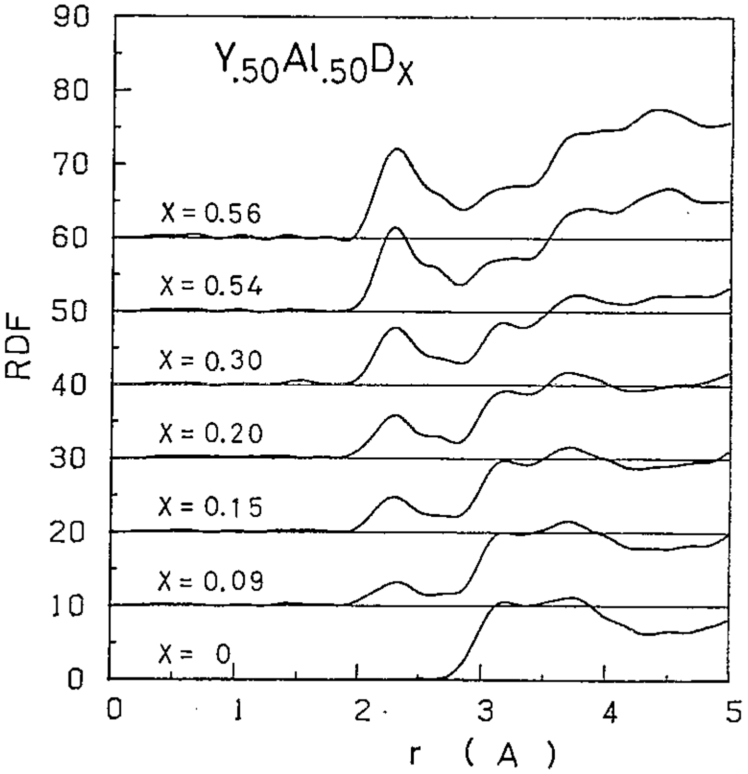

Fig. 2. Radial distribution functions of $Y_{.50}Al_{.50}D_X$ amorphous alloys obtained by Fourier transforming the S(Q) (Q_{max}=20 A^{-1}).

$Q_{max} = 20\ A^{-1}$. A new peak appears at lower r side of the first peak in RDF. The peak height increases with increasing D concentration. The positions of the peak and shoulder are fixed at r ~2.3 A and r ~2.6 A respectively.

Such a characteristic behavior indicated in Figs. 1 and 2. is found in the case of $Y_{.67}Al_{.33}D_X$ amorphous alloys too.

The atomic distances for D-Y and D-Al pairs, when D atoms are absorbed into YAl crystal[4)], are expected to be r_{D-Y} ~2.3 A and r_{D-Al} ~2.0 A.

Figure 3 shows the nearest neighbor coordination numbers of Y atoms arround a D atom ($n_{D \rightarrow Y}$) obtained by a two Gaussian curves-fitting for the radial distribution functions of Y-Al-D amorphous alloys. The two Gaussian curves-fitting was performed on the condition that the two peaks are located at r ~2.3 A and r ~2.6 A respectively. The former peak corresponds to only D-Y correlation, while the latter one consists of D-Al or/and D-D correlations. Only the D-Y correlation is discussed in this paper. In both of $Y_{.50}Al_{.50}D_X$ and $Y_{.67}Al_{.33}D_X$ amorphous alloys, a D atom is surrounded by more than 4Y atoms in the low D concentration range of $X \lesssim 0.30$. The coordination number of Y atoms around a D atom may be extrapolated to 6 with approaching the zero D content. On the other hand, a D atom is surrounded by about 4Y atoms over the all D concentration range of $X \gtrsim 0.50$. These results mentioned above mean that D atoms initialy prefer to sit in the octahedral site consisting of 4Y atoms in Y-Al-D amorphous alloys, when D concentration is gradually increased. In YH_X crystalline system, a O-site to T-site occupation ratio is 0.352 at X = 0.20[5)], but 0.0256 at X = 1.99[6)], at room temperature. This result is quite suggestive of understanding the present observation on the deuterium atom environment in Y-Al-D amorphous alloys.

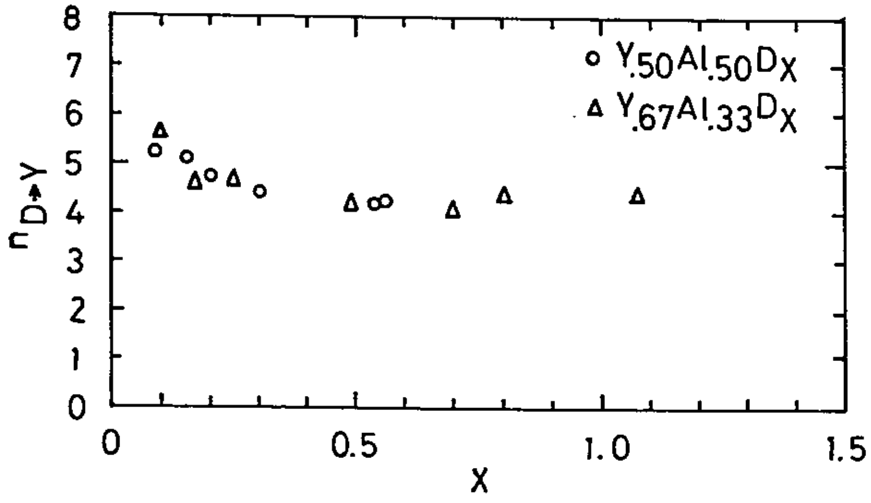

Fig. 3. Nearest neighbor coordination numbers of Y atoms around a D atom ($n_{D \rightarrow Y}$) in Y-Al-D amorphous alloys.

Existence of the small angle scattering indicates some contributions from the fluctuation of D atom distribution in Y-Al-D amorphous alloys because of no small angle scattering in X-ray diffraction measurement.

References

1) K. Kai, T. Fukunaga, N. Hayashi, N. Watanabe and K. Suzuki, KENS Report IV, KEK Internal (1983) p.54-56.

2) K. Kai, T. Fukunaga, T. Nomoto, N. Watanabe and K. Suzuki, in T. Masumoto and K. Suzuki (eds.), Proc. 4th Int. Conf. on Rapidly Quenched Metals, Sendai, August 1981, Vol. 2, Japan Institute of Metals, Sendai, 1982, p.1609-1612.
K. Kai, T. Fukunaga, N. Watanabe and K. Suzuki, KENS Report III, KEK Internal (1982) p.14-16.

3) K. Kaneko, T. Kajitani, M. Hirabayashi, M. Ueno and K. Suzuki, J. Less-Common Met., 89 (1983) p.237-241.
N. Hayashi, Y. Tomitsuka, T. Fukunaga, N. Watanabe and K. Suzuki, KENS Report IV, KEK Internal (1983) p.50-53.
K. Suzuki, N. Hayashi, Y. Tomitsuka, T. Fukunaga, K. Kai and N. Watanabe, J. Non-Cryst. Solids, 61 & 62 (1984) p.637-642.

4) T. Dagerhamn, Akiv. Kemi, 27 (1967) p.363-380.

5) J. E. Bonnet, S. K. P. Wilson and D. K. Ross, in Electronic Structure and Properties of Hydrogen in Metals, (NATO Conference Series, Series VI : Materials Science, Vol. 6) ed. by P. Jena and C. B. Satterthwaite, (Plenum Press, New York, 1983) p.183-188.

6) J. A. Goldstone, J. Eckert, E. L. Venturini and P. M. Richards, ibid., p.169.

Structural Anisotropy of Sputter-deposited Ni-42at%V Amorphous Alloy

Toshiharu FUKUNAGA, Shigeo URAI*, Noriyuki HAYASHI,
Noboru WATANABE** and Kenji SUZUKI

The Research Institute for Iron, Steel and Other Metals, Tohoku
University, Sendai 980, Japan

*Toyama Technical College, Toyama 930-11, Japan

**National Laboratory for High Energy Physics, Oho-machi, Tsukuba-gun,
Ibaraki 305, Japan

Some amorphous alloys have been reported to have magnetic anisotropies. For example, electro-deposited Co-P alloys$^{1)}$ have weak perpendicular easy-axis magnetic anisotropy and sputtered amorphous ferrimagnetic Gd-Co alloys$^{2)}$ have much larger magnetic anisotropy. The anisotropy of amorphous films is certainly induced by deposition-growth condition. In fact, the magnetic anisotropy constant of bias sputter-deposited Gd-Co film increases with increasing bias voltage. The origin of these anisotropic properties in amorphous alloys is thought to come from the anisotropies in the topological or chemical atomic scale structure.

In this paper we measure two kinds of the structure factor S(Q) of sputter-deposited Ni-42at%V amorphous alloy with the scattering vector($\vec{Q}$) parallel to the sample plane($\vec{a}$) ($\vec{Q}/\!/\vec{a}$) and with the scattering vector perpendicular to the sample plane ($\vec{Q}\perp\vec{a}$) to get the information of the structural anisotropy.

A plate specimen(0.43mm thick x 20mm long x 20mm wide) of Ni-42at%V amorphous alloy was prepared by using a high rate triode DC sputter deposition apparatus. The measurement of the neutron scattering intensity from this amorphous alloy was carried out at room temperature in vacuum by using the High Intensity Total scattering spectrometer(HIT). The plate sample was mounted at 45° to the incident neutron beam so that ^{3}He-counters located at scattering angle $2\theta=\pm 90°$ recorded the $S_{/\!/}(\vec{Q})$ with $\vec{Q}/\!/\vec{a}$ at $2\theta=+90°$ and the $S_\perp(Q)$ with $\vec{Q}\perp\vec{a}$ at $2\theta=-90°$ simultaneously as shown in Fig. 1.

For Ni-42at%V amorphous alloy we can observe only the anisotropy of Ni-Ni atom correlation aligned perpendicular and parallel to the film plane, because the contribution of the partial $S_{NiV}(Q)$ and $S_{VV}(Q)$ to the total $S(Q)$ is very small due to the small neutron coherent scattering length of V atom(b_V=-0.0382 x 10^{-12}cm) and so the total $S(Q)$ observed by neutron scattering is almost equal to the partial $S_{NiNi}(Q)$ ($S(Q) \simeq 1.056\ S_{NiNi}(Q)$)3).

Figure 2 shows the $S_{//}(Q)$ ($\vec{Q}//\vec{a}$) and $S_{\perp}(Q)$ ($\vec{Q}\perp\vec{a}$) of Ni-42at%V amorphous alloy. Pre-peaks located at $Q \simeq 1.9$ A^{-1} are observed in both $S_{//}(Q)$ and $S_{\perp}(Q)$. The first large peak at $Q \simeq 3.2$ A^{-1} of $S_{\perp}(Q)$ is located on lower Q side than that of $S_{//}(Q)$. FWHM of the first peak of $S_{\perp}(Q)$ is wider than that of $S_{//}(Q)$. The split of the second peak and the amplitude over the range of $Q \simeq 12 \sim 16$ A^{-1} are different between $S_{//}(Q)$ and $S_{\perp}(Q)$.

These results obviously suggest that Ni-Ni atom arrangement are different between the perpendicular and the parallel axis to the film plane in Ni-42at%V amorphous alloy. The anisotropies in the magnetic and mechanical properties of amorphous alloys are expected to be originated from the anisotropy of the atomic structure observed in this study.

Further careful data analysis is in progress to elucidate the atomic arrangement aligned perpendicular and parallel to the film plane.

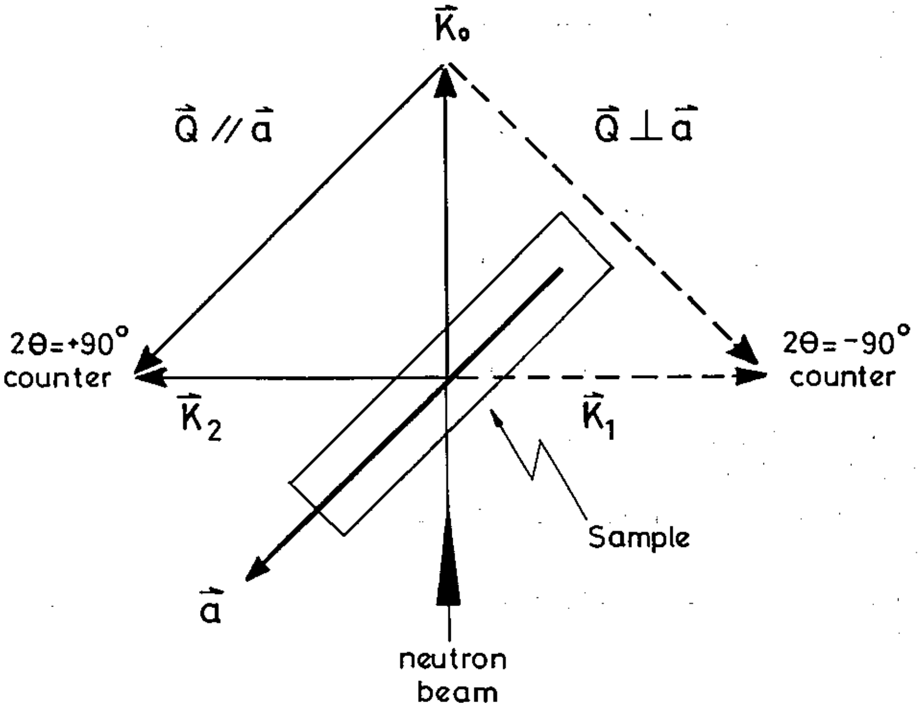

Fig. 1. Schematic diagram to measure the structure factors $S(Q)$ with $\vec{Q}//\vec{a}$ and $\vec{Q}\perp\vec{a}$, where $\vec{Q}$ is the scattering vector and $\vec{a}$ is the direction parallel to the sample plane.

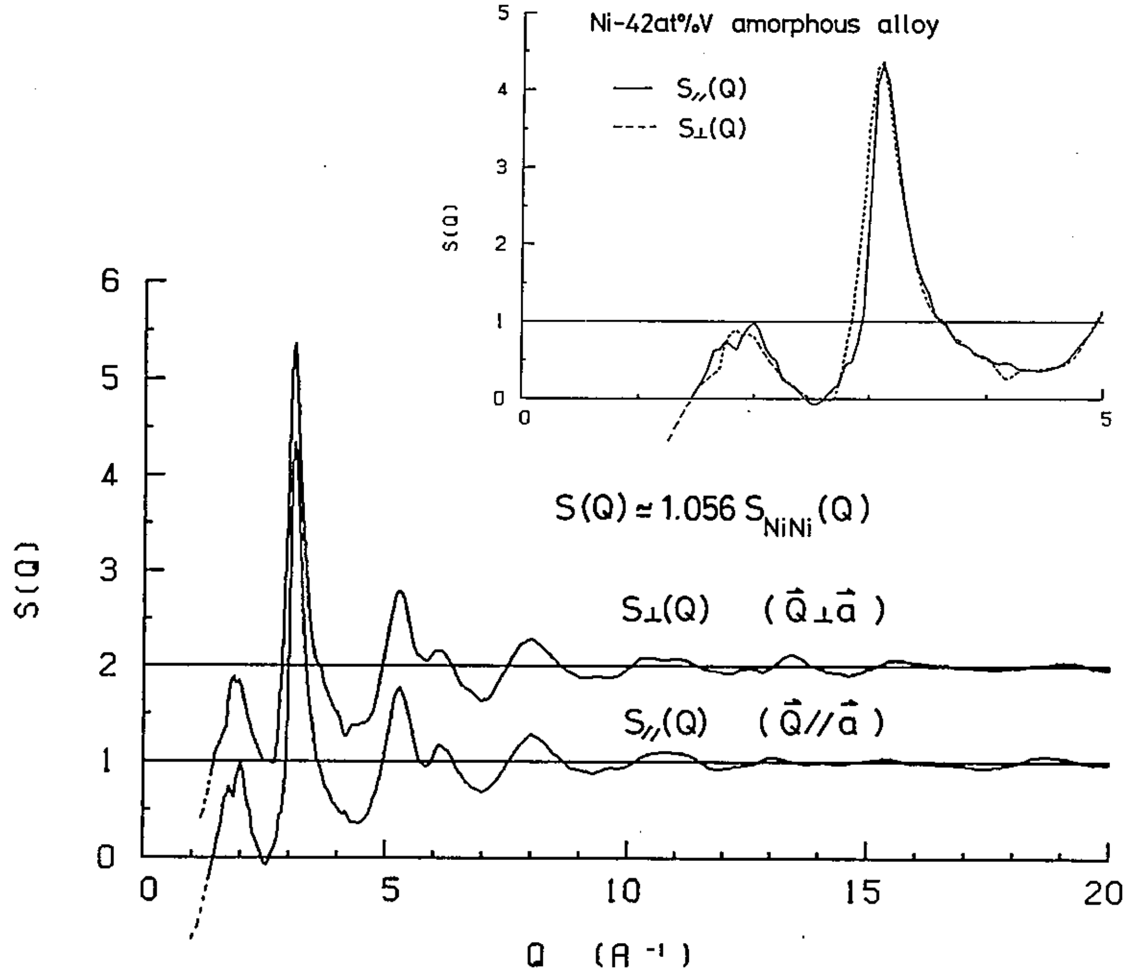

Fig. 2. Anisotropy in neutron structure factor S(Q) of Ni-42at%V amorphous alloy with $\vec{Q}//\vec{a}$ and $\vec{Q}\perp\vec{a}$.

References

1) G. S. Cargill III, R. J. Gambino and J. J. Cuomo, IEEE Trans. Mag. MAG-10 (1974) 803.

2) R. J. Gambino, P. Chaudhari and J. J. Cuomo, AIP Conf. Proc. 18 (1974) 578.

3) T. Fukunaga, S. Urai, N. Hayashi, N. Watanabe and K. Suzuki, in this Report.

Glass transition of B_2O_3 glass

Masakatsu MISAWA

National Laboratory for High Energy Physics
Oho-machi, Tsukuba-gun, Ibaraki-ken, 305, Japan

In a previous paper$^{1)}$, structural study of the glass transition of a P_2Se_3 glass by means of neutron total scattering was reported. Abnormal temperature dependence of the first peak of the structure factor S(Q) of the glass was found in that experiment. The interpretation of this experimental finding, however, is in controversy, because the structure of the P_2Se_3 glass is not fully understood. In this report a B_2O_3 glass, one of the most widely investigated glasses, was chosen to study the glass transition, because its structure seems to be better understood than the P_2Se_3 glass.

The B_2O_3 glass enriched with ^{11}B to 99.35 % was prepared from its melt. The S(Q) measurements were carried out at 25, 106, 180, 250, 280, 300, 330 and 360°C on heating and 250 and 40°C on cooling by using the High Intensity Total Scattering Spectrometer (HIT). The exposure time was about 2 hours at each temperature. The glass transition temperature of the B_2O_3 glass, Tg, is reported to be about 275°C by specific volume measurement$^{2)}$ (see Fig. 3).

The preliminary results of the S(Q) of the B_2O_3 glass observed at 25, 250 and 360°C are shown in Fig. 1. No drastic change in S(Q) seems to occur. But one can find a significant difference in a low Q part of the S(Q) curves as demonstrated in Fig. 2 where two S(Q)'s observed at 25 and 360°C are compared with each other. The first peak of S(Q) shifts toward the lower Q side and the height of the peak increases with increasing temperature, which have the similar characteristics as previously observed in P_2Se_3 glass.

It is hard to determine a position of the first peak of the S(Q), Q_1 precisely because of an asymmetric shape of the peak. Here, Q_1 is defined arbitrarily as a center of the width of the peak at S(Q) = 1.5 above which the S(Q) curve seems to be symmetric. Figure 3 shows the plots of Q_1 defined above as a function of temperature. The open circles show the values of Q_1 obtained on heating, while the closed circles show those on

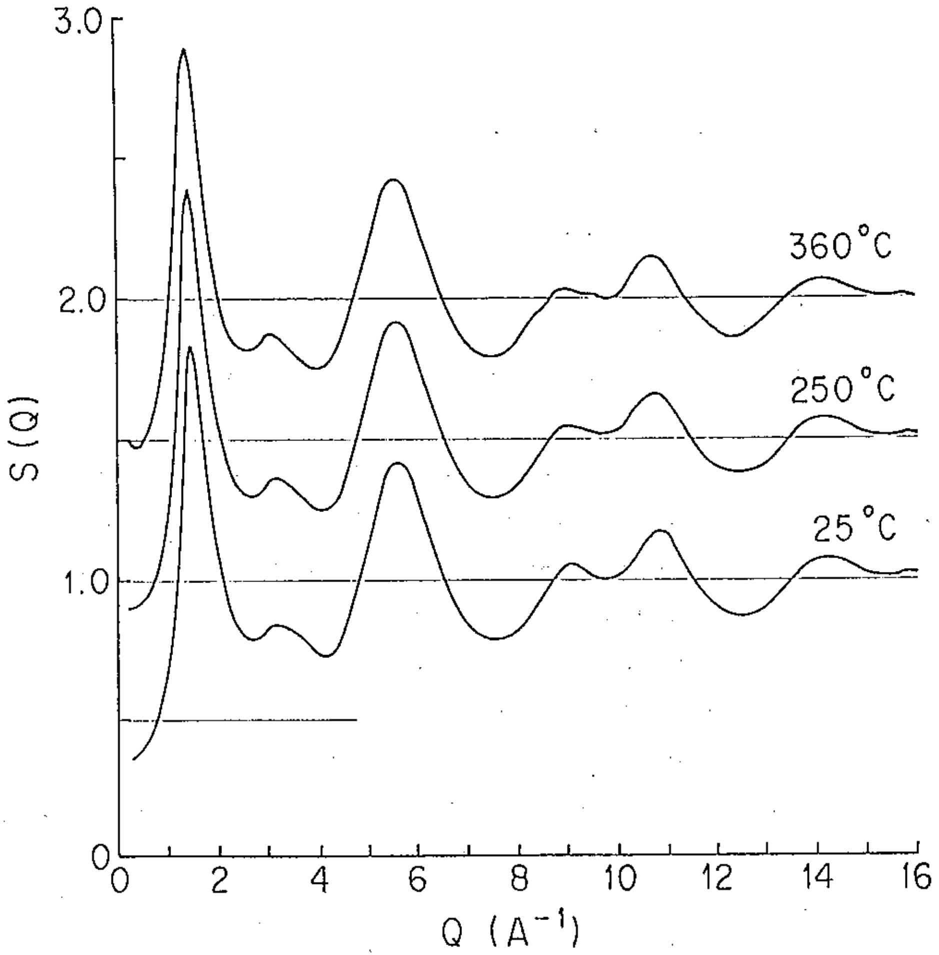

Fig. 1 Structure factors S(Q) of B_2O_3 glass observed at 25 and 250°C and of the supercooled melt at 360°C.

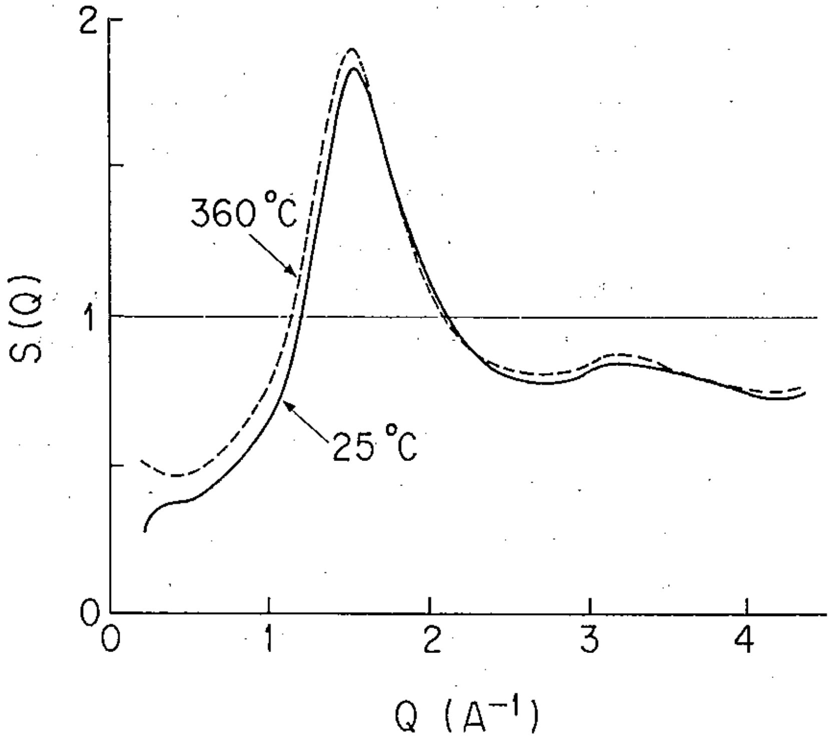

Fig. 2 Comparison of the structure factor S(Q) of B_2O_3 glass (25°C) and that of the supercooled melt (360°C).

cooling. Both results agree with each other within an experimental error, indicating that the shift of the first peak of the S(Q) is reversible. The Q_1 data exhibit an abrupt change in slope near Tg. This characteristic temperature dependence of the Q_1 data coincides with that of the specific volume as shown in Fig. 3.

The fractional change of the specific volume between 25 and 360^0C is about 6.0 %, while that of the Q_1 in the same temperature range is 2.1 % which is just one third of the volume change described above, suggesting that the volume change in the region near Tg may be isotropic even in a microscopic scale. Further data analysis is in progress.

The author would like to thank all members of HIT group for their help in carrying out the experiment.

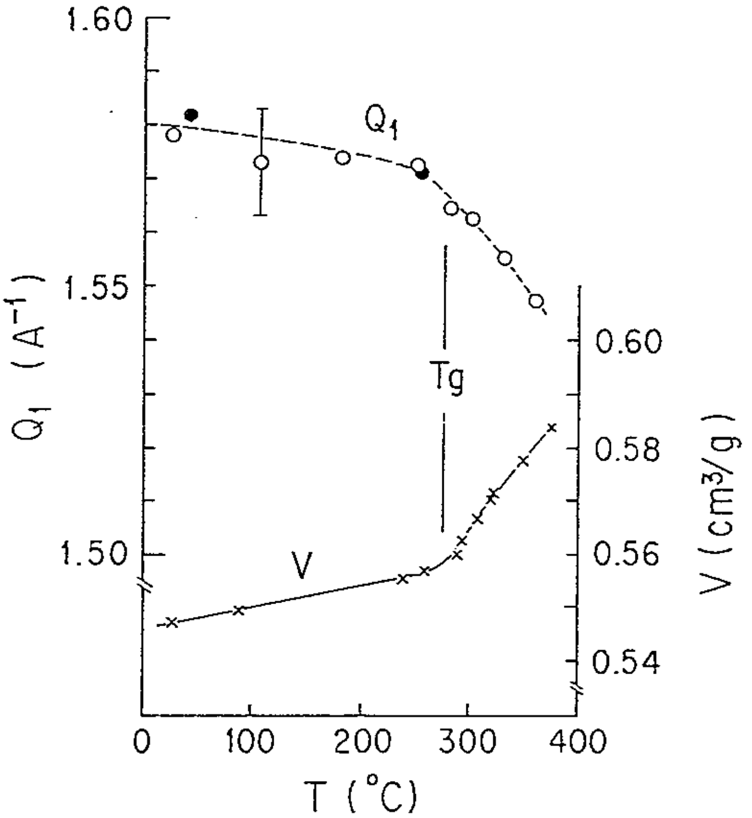

Fig. 3 Position of the 1st peak of S(Q), Q_1 and specific volume, V as a function of temperature.

References

1) M. Misawa and N. Watanabe, KENS REPORT-IV, KEK Internal 83-4 (Sept. 1983) 18.

2) P. B. Macedo, W. Capps and T. A. Litovitz, J. chem. Phys. 44 (1966) 3357.

Structure of Some Univalent Metal Nitrate Melts by Means of Pulsed Neutron Diffraction

Toshio YAMAGUCHI, Yusuke TAMURA, Isao OKADA, Hitoshi OHTAKI,
Masakatsu MISAWA* and Noboru WATANABE*

Department of Electronic Chemistry, Tokyo Institute of Technology,
Nagatsuta, Midori-ku, Yokohama 227, Japan

*National Laboratory for High Energy Physics, Oho-machi, Tsukuba-gun,
Ibaraki 305, Japan

The structure of molten univalent metal nitrates and the nature of the M^+-NO_3^- interaction have been investigated by various methods. Raman and infrared spectra have been interpreted in terms of a specific ionic association between cations and nitrate ions$^{1)}$ and formation of quasi-crystalline aggregates.$^{2)}$ From a neutron diffraction study of a series of metal nitrate melts, Suzuki and Fukushima$^{3)}$ have found two different O-O distances within a nitrate ion having the C_{2v} symmetry in molten $LiNO_3$, $AgNO_3$ and $TlNO_3$ owing to specific M^+-NO_3^- interactions. In an X-ray diffraction study of molten $AgNO_3$, Holmberg and Johansson$^{4)}$ have reported that four nitrate ions coordinate to an Ag^+ and have claimed that the nitrate ions must be shared with Ag ions and hence a definite symmetry of the nitrate ions should hardly be detected by the diffraction method.

In the present study, we have measured neutron scattered intensities from molten $LiNO_3$, $RbNO_3$, $AgNO_3$ and the 1:1 $LiNO_3$ - $RbNO_3$ mixture in order to determine the structure of nitrate ions and M^+-NO_3^- interactions in the melts.

Commercial metal nitrates of reagent grade were dried in a vacuum oven overnight and then sealed in vacuo in a quartz tube with an inner diameter of 10 mm. Neutron scattering measurements of the melts were performed by using the High Intensity Total scattering spectrometer (HIT). The furnace consisted of two infrared lamps facing each other, between which the sample was placed.

Figure 1 shows the structure functions $i(Q)$ (= $S(Q) - 1$) multiplied by the momemtum transfer Q for the melts. The radial distribution functions (RDFs) were obtained by conventional Fourier transformation of the $Q\cdot i(Q)$ values and shown in Fig. 2. The first peak observed at 1.25 Å for all the melts corresponds to the expected N-O distance within nitrate ions. The second peak appearing around 2.2 Å for the melts except the molten $AgNO_3$ was assignable to the O-O contacts within the nitrate ions. In the RDF of the $AgNO_3$ melt the second peak could be resolved into two centered at 2.2 Å and 2.4 Å. The former peak is ascribed to the O-O interactions within nitrate ions as seen in other melts. It has been found that the shortest Ag-O distances between an Ag^+ and nitrate ions have been observed at 2.4 - 2.5 Å in structure determinations of an $AgNO_3$ melt$^{4)}$ and solid silver compounds,$^{5)}$ in which nitrate ions coordinate to silver ions. Thus, we assigned the 2.4 Å peak to the Ag-O interactions.

In order to analyze the scattering data quantitatively, a least-squares fitting procedure was applied to the structure functions $Q\cdot i(Q)$, where the minimum of a function $U = \Sigma Q^2\{i(Q)_{obs} - i(Q)_{mod}\}^2$ was searched with the distance r_{ij}, the mean square variation $2\gamma_{ij}$ to r_{ij} and the number of interactions n_{ij} as variables. Theoretical structure function $i(Q)_{mod}$ based on a model adopted is calculated by using the function $\langle b_i\rangle^{-2}\Sigma\Sigma n_{ij}b_ib_j\sin(Qr_{ij})/(Qr_{ij})\exp(-\gamma_{ij}Q^2)$. In the case of the molten $AgNO_3$ and $LiNO_3$ we examined two models for the structure of nitrate ions; (A) D_{3h} symmetry and (B) C_{2V} symmetry. In the case of the $AgNO_3$ melt, the Ag-O interactions were taken into account as well as the N-O and O-O interactions within the nitrate ions.

Final results are listed in Table 1, together with the results given in Ref. 3. From the agreement factor R defined as $[\Sigma Q^2\{i(Q)_{obs} - i(Q)_{mod}\}^2/\Sigma Q^2 i(Q)_{obs}^{\,2}]^{1/2}$, the D_{3h} symmetry model is preferred for the nitate ion in the $LiNO_3$ and $AgNO_3$ melts. In the $AgNO_3$ melt, about four nitrate ions are bound to an Ag^+ as monodentate ligands, and the result agrees well with that found in the X-ray diffraction study of $AgNO_3$ melt.$^{4)}$

The orientation of nitrate ions and the cations was difficult to be determined only from the present diffraction data, since the M^+-N and M^+-O peaks found in the RDF were not well resolved. The cation distribution around a nitrate ion has been demonstrated by molecular dynamics simulations based on the present neutron and X-ray scattering data for molten $LiNO_3$, $RbNO_3$ and 1:1 $LiNO_3$ - $RbNO_3$ mixture, and the results will be described elsewhere.

References

1) S. C. Wait, Jr., A. T. Ward and G. J. Janz, J. Chem. Phys. 45 (1966) 133.
2) D. W. James and W. H. Leong, J. Chem. Phys. 51 (1969) 640.
3) K. Suzuki and Y. Fukushima, Z. Naturforsch. A37 (1983) 367.
4) B. Holmberg and G. Johansson, Acta Chem. Scand. A37 (1983) 367.
5) P. Meyer, A. Rimsky and R. Chevalier, Acta Cryst. B32 (1976) 1143.

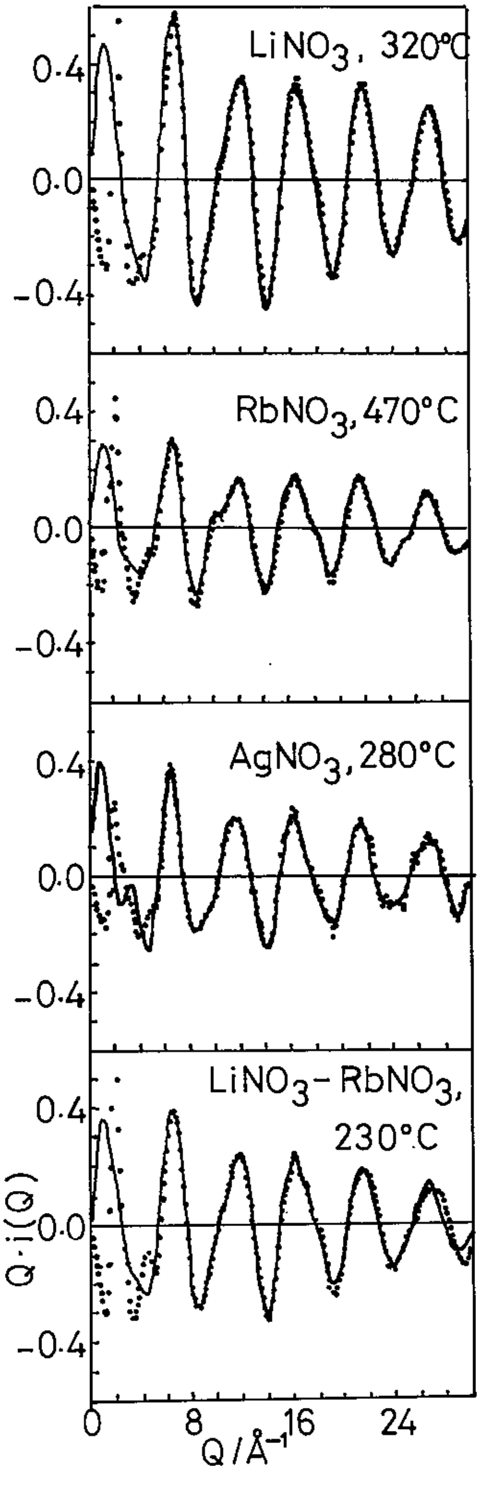

Fig. 1 Structure functions Q·i(Q) for the melts. Experimental (···) and model (—)

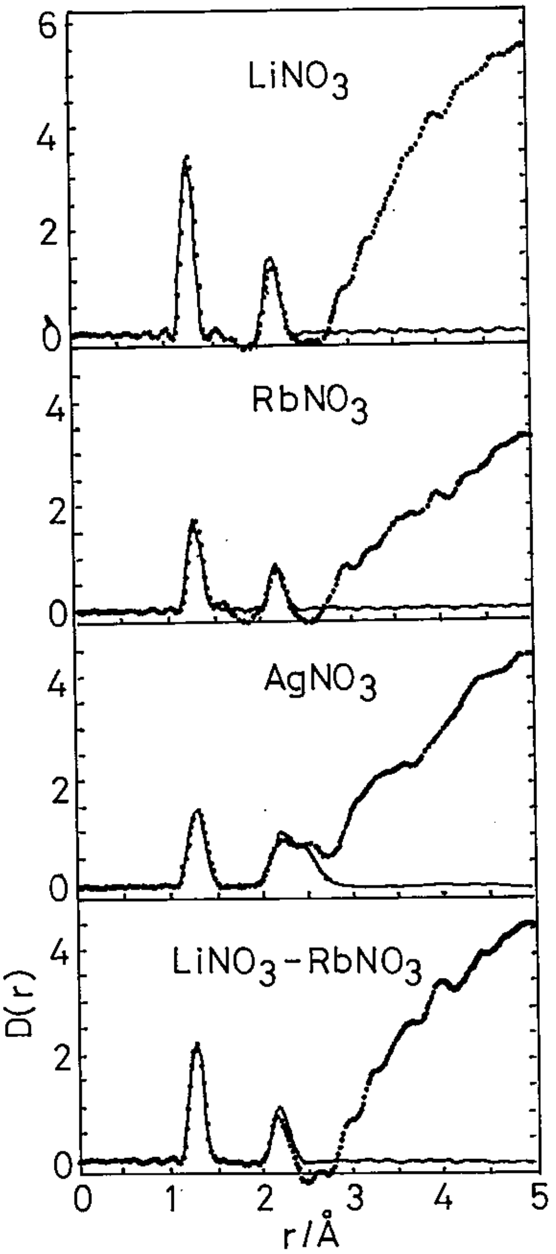

Fig. 2 Radial distribution functions of the melts. Experimental (···) and model (—)

Table 1. Results of the least-squares refinement of the $Q \cdot i(Q)$ curve for the distance r_{ij}(Å), the temperature coefficient γ_{ij}(Å^2), the number of interactions n_{ij} and the agreement factor R*. The values in parentheses are their estimated standard deviations. The values in brackets are those reported by Suzuki and Fukushima[3)]

		Q-range	r_{N-O}	γ_{N-O}	n_{N-O}	r_{N-O}	γ_{O-O}	n_{O-O}	r'_{O-O}	γ'_{O-O}	n'_{O-O}	r_{M-O}	γ_{M-O}	n_{M-O}	R
$LiNO_3$	A	15 - 30	1.250(1)	0.0008(1)	3	2.155(4)	0.0029(2)	3							0.087
	B	15 - 30	1.251(1)	0.0008(1)	3	2.09(1)	0.001(1)	1	2.196(1)	0.001	2				0.138
		5 - 20	1.250	0.0008	3	2.155	0.0029	3				1.89(2)	0.0016(5)	3.2(9)	0.078
		[9 - 20	1.26	0.0014	3	2.09	0.0025	1	2.21	0.0025	2]				
$RbNO_3$		9 - 30	1.255(1)	0.0011(1)	3	2.161(3)	0.0025(2)	3							0.189
		[9 - 20	1.25	0.0010	3	2.17	0.0027	3]							
$AgNO_3$	A	20 - 30	1.249(1)	0.0010(1)	3	2.149(5)	0.0019(2)	3							0.248
	B	20 - 30	1.255(1)	0.0010(1)	3	2.11(1)	0.001(1)	1	2,205	0.001	2				0.364
		5 - 20	1.249	0.0010	3	2.149	0.0019	3				2.393(8)	0.008(1)	4.3(5)	0.174
		[9 - 20	1.27	0.0016	3	2.10	0.0025	1	2.22	0.0025	2]				
$LiNO_3$-$RbNO_3$		5 - 30	1.249(1)	0.0012(3)	3	2.167	0.0032(2)	3				1.93(2)	0.003(2)	4(1)	0.183

$$^{*}R = \left[\Sigma Q^2 \{ i(Q)_{obs} - i(Q)_{mod} \}^2 / \Sigma Q^2 \cdot i(Q)_{obs}^{\ 2} \right]^{1/2}$$

Structure of Liquid N,N-Dimethylformamide by Pulsed Neutron Diffraction

Toshio YAMAGUCHI, Yusuke TAMURA, Hitoshi OHTAKI, Masakatsu MISAWA* and Noboru WATANABE*

Department of Electronic Chemistry, Tokyo Institute of Technology,
Nagatsuta, Midori-ku, Yokohama 227, Japan

*National Laboratory for High Energy Physics, Oho-machi, Tsukuba-gun,
Ibaraki 305, Japan

Liquid N,N-dimethylformamide (later abbreviated as DMF) is one of the commonly used solvents in many chemical reactions. Structural investigations have been carried out by using NMR,1) Raman and infrared methods,2) which have brought forward discussions about cluster formation of DMF molecules in the liquid state. Theoretical calculations previously reported3),4) have been limited to a monomer DMF molecule. A recent X-ray diffraction study on liquid DMF5) has indicated that the intermolecular arrangement of DMF molecules is very disordered and hence no appreciable DMF cluster is formed. Weak hydrogen bonds between DMF molecules have also been supported by ab initio molecular orbital calculations on aggregates of DMF molecules.5) The neutron diffraction method is especially useful for studying formation of hydgrogen-bonds because the method can observe locations of hydrogen atoms in molecules.

The aim of the present study is to determine the molecular structure of liquid DMF and also to investigate the presence of hydrogen-bonds between DMF molecules by using deuterated DMF.

Deutrated liquid DMF, $(CD_3)_2NCDO$, with a D content of 99 per cent, was purchased from E. Merck. A quartz cell with an inner diameter of 10 mm and thickness of 0.4 mm was used for the measurements.

Neutron scattered intensities were measured for liquid DMF at room temperature with the High Intensity Total scattering spectrometer (HIT). The observed structure functions i(Q) (= S(Q) − 1) multiplied by the momentum transfer Q is shown in Fig. 1. Figure 2 shows the radial distribution function (RDF) obtained by the Fourier transform of the Q·i(Q) values truncated at $Q_{max} = 28\ \text{Å}^{-1}$.

In the radial distribution function, peaks appear at 1.08 Å, 1.40 Å, 1.72 Å, 2.08 Å, and 2.47 Å. From the structure of the almost planar skeleton of DMF molecule determined by X-ray diffraction$^{5)}$ (Fig. 3), these peaks are ascribed to the following interactions.

1) 1st peak (1.08 Å): C-D such as C2-D21, and C1-O.
2) 2nd peak (1.40 Å): N-C1, N-C2, and N-C3.
3) 3rd peak (1.74 Å): D...D such as D21...D22.
4) 4th peak (2.08 Å): N...D such as N...D21, O...D11, N...D11 and O...N.
5) 5th peak (2.47 Å): C1...C2, C1...C3, C2...C3, and C2...D11.

Besides the above atom pairs, interactions between atoms C1, D11 and O, and methyl D atoms, and between methyl D atoms in different methyl groups are also expected to contribute in part to the 4th and 5th peaks. However, distances of these interatomic interactions vary by rotation of the two methyl groups along each C-N bond. Thus, we examined the following three types of conformation of the methyl groups relative to the N-C1 bond; (A) two methyl groups are in the eclipsed form, (B) two methyl groups are in the staggered form, (C) the methyl group at the trans position is in the eclipsed form, and the other methyl group is in the staggered form, and (D) the opposite case as to model C. All the interatomic distances were taken from Ref. 5 except for the C-D distance = 1.08 Å taken from the position of the 1st peak in the present RDF. Theoretical structure function $i(Q)_{mod}$, which is defined by $\langle b_i \rangle^{-2} \Sigma\Sigma b_i b_j \sin(Qr_{ij})/(Qr_{ij})\exp(-\gamma_{ij}Q^2)$ with the bond distance r_{ij} and the mean square variation $2\gamma_{ij}$ to r_{ij}, was calculated for the above conformations of the methyl groups. However, each model gave similar $i(Q)_{mod}$ values over the Q-range of 6 - 28 $Å^{-1}$. Thus, the conformation of the two methyl groups could not be concluded in the present study.

In order to determine the interatomic distances within a DMF molecule, a least-squares fitting procedure was applied to the structure function $Q\cdot i(Q)$ over the Q range 6 - 28 $Å^{-1}$, where the function $U = \Sigma Q^2\{i(Q)_{exp} - i(Q)_{mod}\}^2$ was minimized with variables r_{ij} and γ_{ij}. The following assumptions were made; i.e. (1) all the non hydrogen atoms are coplanar, (2) the methyl groups have local C_{3V} symmetry and have no tilt, (3) the C-D distances within the methyl groups and the C1-D11 distance are not distinguishable, and (4) the conformation of the methyl groups shown in Fig. 3 (model A) is taken as a model which is suggested from theoretical calculations for a monomer DMF.$^{3),4)}$

The final results are given in Table 1. A good agreement between experimental and model structure functions has been attained in the Q-range of 6 – 28 Å as shown in Fig. 1. Peak shapes for all the intramolecular interactions less than 3.5 Å were calculated using the values given in Table 1 and were subtracted from the original RDF. The result is shown by the dashed line in Fig. 2. As is seen in the residual curve, the intramolecular interactions within the DMF molecule satisfactorily explained the peaks in the range r < 3.2 Å. The presence of hydrogen bonds between the DMF molecules through the carbonyl deuterium - oxygen interaction, if any, might be difficult to be detected because of their small contribution to the RDF. The present study has shown that the spectrometer HIT gives data with good precision to investigate the structure of complex molecular liquids.

Peferences

1) H.-J. Bittrich and D. Kirsch, Z. Phys. Chem. (Leipzig) 257 (1976) 403 and the references therein.

2). G. Fini and P. Mirone, J. Chem. Soc. Faraday Trans. II 70 (1974) 1776.

3) J. F. Yan, F. A. Momany, R. Hoffmann and U. A. Scheraga, J. Phys. Chem. 74 (1970) 420.

4) B. M. Rode and R. Fussenegger, J. Chem. Soc. Faraday Trans. II 71 (1975) 1958.

5) H. Ohtaki, S. Itoh, T. Yamaguchi, S. Ishiguro and B. M. Rode, Bull. Chem. Soc. Jpn. 56 (1983) 3406.

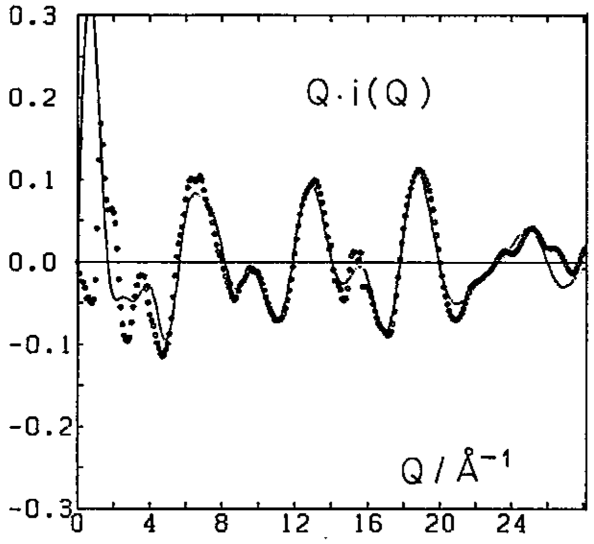

Fig. 1 Structure function Q·i(Q) of liquid DMF. Experimental (•••) and model (—)

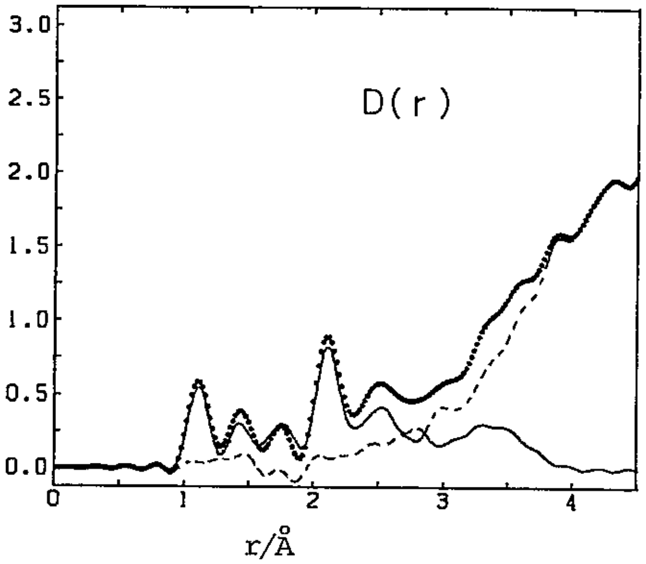

Fig. 2 Radial distribution function of liquid DMF. Experimental (•••) and model (—) and their difference (---)

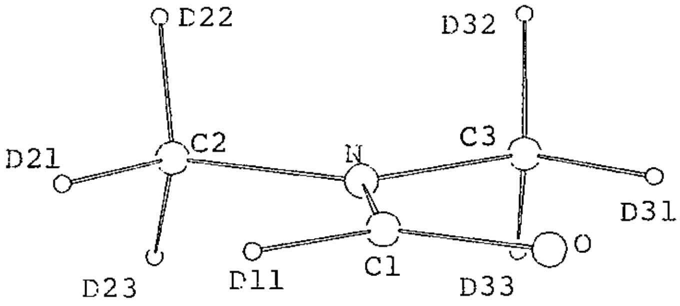

Fig. 3 Molecular structure of liquid DMF

Table 1. Molecular parameters of liquid DMF determined by neutron diffraction method.

	C1-D11 C-D(-CD_3)	C1-O	C1-N	N-C2 N-C3	DCD(°)	DC(2,3)N(°)
r/Å	1.085(4)	1.26(1)	1.37(4)	1.45(1)	107(2)	109(1)
γ/Å^2	0.0011(1)	0.001(1)	0.002(1)	0.003(1)		

A Neutron Diffraction Study of Aqueous LiCl Solutions. A Concentration Difference Method

Toshio YAMAGUCHI, Yusuke TAMURA, Isao OKADA and Hitoshi OHTAKI,
Masakatsu MISAWA* and Noboru WATANABE*

Department of Electronic Chemistry, Tokyo Institute of Technology,
Nagatsuta, Midori-ku, Yokohama 227, Japan

*National Laboratory for High Energy Physics, Oho-machi, Tsukuba-gun,
Ibaraki 305, Japan

Diffraction techniques have played a principal role in determination of the structure of electrolyte solutions. Recently the neutron diffraction method has effectively been used to elucidate the orientation of water molecules around ions dissolved in water.1) Extraction of the contribution of the ion-water interactions from the total scattering data is based on the first-order difference method. This method may be classified into three kinds; i.e. (1) isotopic substitution,1) (2) isomorphous substitution,2) and (3) free water subtraction.3) The former two have essential limiations in application, because suitable pairs of isotope or atoms with similar ionic radii are required. Method (3) is only applicable to solutions containing enough free water.

In the present communication, we will propose a concentration difference method, in which scatterings from solutions with different solute concentrations are compared.

In a solution of MX in D_2O, the total structure factor S(Q) is written by

$$S(Q) = \Sigma c_i b_i^2 + \Sigma\Sigma c_i c_j b_i b_j [S_{ij}(Q) - 1]$$

The second term is separated into two parts, (1) MX-D_2O (M-O, M-D, M-M, X-O, X-D, X-X and M-X), and (2) D_2O (D-O, O-O and D-D). The latter represents D_2O-D_2O interactions in the system, which is a predominant contributor to the total S(Q), and hence should be removed from the total scattering data for the system when one wishes to analyze interactions between the solute and solvated water molecules. If the $S(Q)$ values for two solutions with different MX concentrations are scaled so as to contain equal amount of water molecules in the both systems, the interference term from the water structure may be cancelled by taking the difference of the scaled $S(Q)$ values, $\Delta(Q)$. The $\Delta(Q)$ will be expressed as follows.

$$\Delta(Q) = \Sigma(fc_i^A - c_i^B)b_i^{\,2} + \Sigma\Sigma(fc_i^A c_j^A - c_i^B c_j^B)b_i b_j[S_{ij}(Q) - 1]$$

f is a normalization constant to make the amount of water molecules equal in the both systems.This method holds only for the case in which the hydration structure of the ions and the water structure are very similar in the two solutions to be compared.

We applied this method to 11 mol dm^{-3} and 5 mol dm^{-3} aqueous LiCl-D_2O solutions. The neutron scattering intensities were collected by using the High Intensity Total scattering spectrometer (HIT). The sample solutions were sealed in vacuo into a quartz tube with an inner diameter of 10 mm.

Figure 1 shows the difference structure function $Q\cdot i(Q)$, in which $i(Q)$ is given by $[\Delta(Q) - \Sigma(fc_i^A - c_i^B)b_i^{\,2}]/\Sigma(fc_i^A - c_i^B)b_i^{\,2}$, The corresponding radial distribution function $d(r)$ given by $(2r/\pi)\int Q\cdot i(Q)\sin(Qr)dQ$ is demonstrated in Fig. 2.

Since the scattering length of natural Li has a negative value, the Li-O and Li-D interactions give negative contributions to the RDF. Such curve shapes are seen around 1.93 Å and 2.5 - 2.7 Å, which are consistent with Li-O and Li-D distances, respectively, obtained from the isotopic substitution method (see Fig. 3a).1) The peak observed at 2.2 Å is ascribed to the Cl-D1 distance within hydrated chloride ions (Fig. 3b). The Cl-O and Cl-D2 interactions contribute to the broad peak around 3.0 - 4.0 Å. The results obtained are compared with those determined by the isotopic substitution method1) in Table 1. Both results agree well with each other. The present results may indicate that the orientation of hydrated water molecules around Li^+ and Cl^- ions does not change appreciably with increasing solute concentration.

Since the radial distribution function obtained by the concentration difference method contains the contribution from the hydration structure of both Li^+ and Cl^- ions, the more exact ion-water distance and the hydration number are obtained by a model fitting procedure applied to the structure function $Q\cdot i(Q)$, which is now in progress.

References

1) J. E. Enderby and G. W. Neilson, Rep. Prog. Phys. 44 (1981) 593.

2) J. Newsome, G. W. Neilson and M. Sandström, J. Chem. Soc. Faraday II 77 (1981) 1245.

3) N. Ohtomo, K. Arakawa, M. Takeuchi, T. Yamaguchi and H. Ohtaki, Bull. Chem. Soc. Jpn. 77 (1981) 1314.

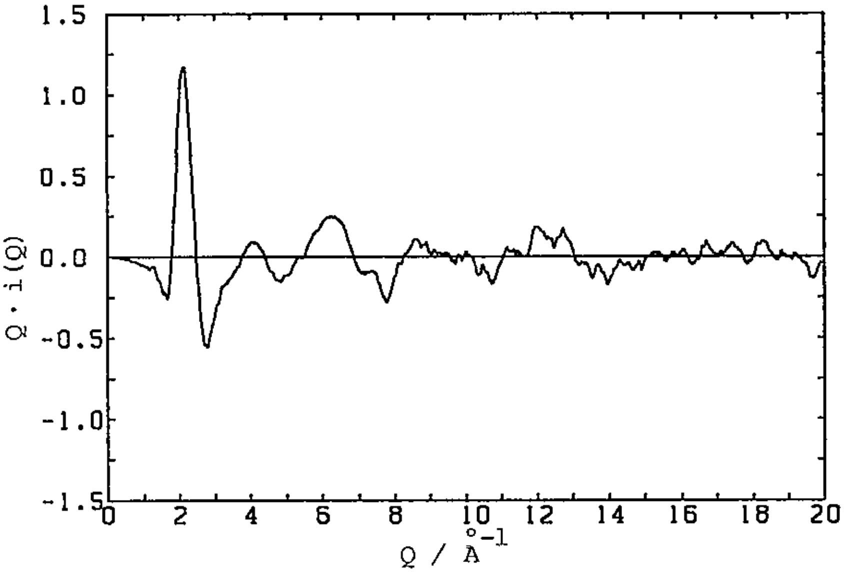

Fig. 1 The structure function $Q \cdot i(Q)$ values for the aqueous LiCl solutions.

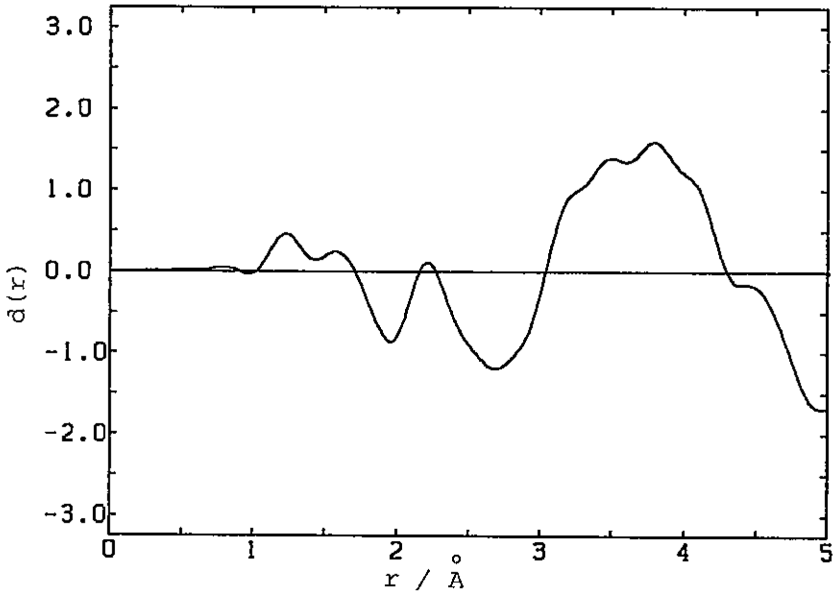

Fig. 2 The radial distribution function for the aqueous LiCl solutions.

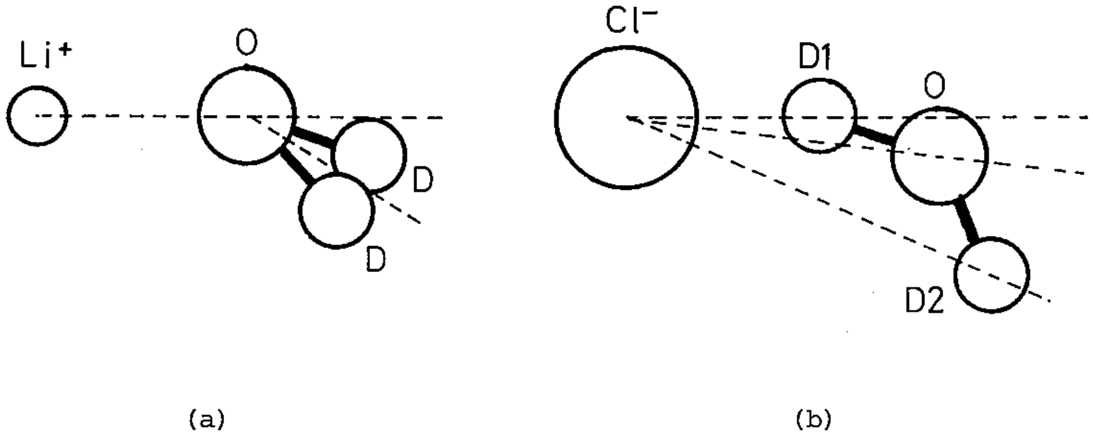

Fig. 3 The orientation of water molecule around the ions.
(a) Li^+ ion, (b) Cl^- ion

Table 1. Comparison of ion-water distances(Å) of hydrated Li^+ and Cl^- ions.

	The concentration difference method	The isotopic substitution method[1)]	
		9.95 mol·dm^{-3}	3.57 mol·dm^{-3}
Li^+-O	1.93	1.95(2)	1.95(2)
Li^+-D	2.5-2.7	2.50(2)	2.55(2)
Cl^--D1	2.19	2.22(2)	2.25(2)
Cl^--O	3.3-4.1	3.29(4)	3.34(4)
Cl^--D2		3.5-3.7	-

Lithium Ions in Incompletely Hydrated Solution

Kazuhiko ICHIKAWA, Yasuo KAMEDA, Takaaki MATSUMOTO*,
Masakatsu MISAWA,** and Noboru WATANABE**

Chemical Department and *Nuclear Department,
Hokkaido University, Sapporo 060, Japan

**National Laboratory for High Energy Physics
Tsukuba-gun, Ibaraki 405, Japan

Introduction

The nature of hydration around Li^+ in aqueous solutions at less than ca. 20 mol% LiCl was investigated by the neutron first-order difference method due to Enderby et al.[1,2] It is clarified that the number of water molecules in the first coordination shell, the angle ϕ between the Li-O axis and the plane of the water molecule, and the lithium-deuterium distance vary with concentration. They observed no direct and indirect interactions between lithium cations and chloride anions in aqueous solutions up to ca. 17 mol% LiCl. To our knowledge no direct evidence for direct and indirect correlation between alkali metal ions and halide ions was observed in the diffraction techniques. From a point of view of complex formation phenomena, concentrated aqueous chloride solutions containing transition metal ions (e.g., Co^{2+}, Ni^{2+}, Cu^{2+} and Fe^{3+}) were examined by the X-ray diffraction method, though the hydrogen atoms cannot be observed with adequate precision.[3]

This paper reports, for the first time, an experimental evidence for direct and indirect interactions between Li^+ and Cl^- by the methods of TOF neutron diffraction and isotopic substitution for incompletely hydrated solutions at larger than 25 mol% LiCl.

Theoretical Formalism

The neutron first-order difference method described by Soper et al.[1] avoids the difficulties associated with the Placzek correction of the observed differential cross-section, because the terms arising from every pair of nuclei involving no lithium nucleus disappear.

Let $\Delta_{Li}(Q)$ represents the algebraic difference between the coherent differential scattering cross-sections scaled by a molecule formulated by $(LiCl)_x(D_2O)_{1-x}$, for two solutions. They are identical in all respects except that samples were isotopically enriched for Li. It follows that

$$\Delta_{Li}(Q) = A[a_{LiO}(Q)-1] + B[a_{LiD}(Q)-1] + C[a_{LiCl}(Q)-1] + D[a_{LiLi}(Q)-1] \quad (1)$$

where $A = 2x(1-x)\ (b_{Li}-b'_{Li})\ b_O$ (2)

$B = 4x(1-x)\ (b_{Li}-b'_{Li})\ b_D$ (3)

$C = 2x^2(b_{Li}-b'_{Li})\ b_{Cl}$ (4)

$D = x^2(b^2_{Li}-b'^2_{Li})$. (5)

Here $E=x(b^2_{Li}-b'^2_{Li})$ was deleted. The first-order difference $\Delta_M(Q)$ (e.g., eqn (1) for n=1) for the $(MX_n)_x(D_2O)_{1-x}$ system can be related to $\Delta^S_M(Q)$ developed by Soper et al. as follows,

$$\Delta_M(Q) = \Delta^S_M(Q)\cdot[(n-2)x + 3]^2 = \Delta^S_M(Q)\cdot y^2 \quad (6)$$

The distribution function $\bar{G}_{Li}(r)$ around Li^+ can be derived from the Fourier transform of $\Delta_{Li}(Q)$, as follows,

$$\bar{G}_{Li}(r) = \frac{1}{2\pi^2\rho_0 r}\int \Delta_{Li}(Q)\cdot Q\sin(Qr)dQ, \quad (7)$$

where ρ_0 is the number density of molelules. From $\Delta_{Li}(Q)$ given in eqn (1) $\bar{G}_{Li}(r)$ can be expressed in terms of the atom pair distribution functions $g_{\alpha\beta}(r)$, namely

$$\bar{G}_{Li}(r)/y = A[g_{LiO}(r)-1]+B[g_{LiD}(r)-1]+C[g_{LiCl}(r)-1]+D[g_{LiLi}(r)-1] \quad (8)$$

and

$$g_{\alpha\beta}(r)-1 \equiv \frac{1}{2\pi^2\rho r}\int [a_{\alpha\beta}(Q)-1]\cdot Q\sin(Qr)dQ. \quad (9)$$

From the definition of $g_{\alpha\beta}(r)$ the number of α atoms around Li^+, $n_{Li\alpha}$ is

$$n_{Li\alpha} = C_\alpha\rho\int 4\pi r^2\ g_{Li\alpha}(r)dr, \quad (10)$$

where C_α stands for atom fraction of an α atom; ρ the number density of atoms.

Experimental

The sample was sealed in a quartz sample cell (10 mm in inner diameter and 0.4 mm in thickness) and the pulsed-neutron diffraction measurement of the two $(LiCl)_{0.331}(D_2O)_{0.669}$ systems with difference in isotopic state of Li($f(^7Li)$=1.0 and f=0.926) was carried out at 130±2°C using the high intensity total scattering spectrometer (HIT).

Results and Discussion

Figures 1a and 1b show the unsmoothed data of two coherent differential scattering cross-section $d\sigma(2\theta,Q)/d\Omega|^{obs}_{coh}$ at 33.1 mol% LiCL and $2\theta=50.6°$. Figure 1c shows the algebraic difference $\Delta^{\circ}_{Li}(Q)$ between figs. 1a and 1b, where the term of $x(b^{2}_{Li}-b'^{2}_{Li})$ was deleted. $\Delta^{\circ}_{Li}(Q)$ is equal to $\Delta_{Li}(Q)$ given by eqn(1), because the Placzek correction is sufficiently small to allow $\Delta_{Li}(Q)$ to be derived from $\Delta^{\circ}_{Li}(Q)$. Since A, B and C are much larger than D for highly concentrated solutions, $\Delta_{Li}(Q)$ is determined by not only a_{LiO} and a_{LiD} but also a_{LiCl}; direct or indirect correlation between Li^{+} and Cl^{-} can be, for the first time, observed.

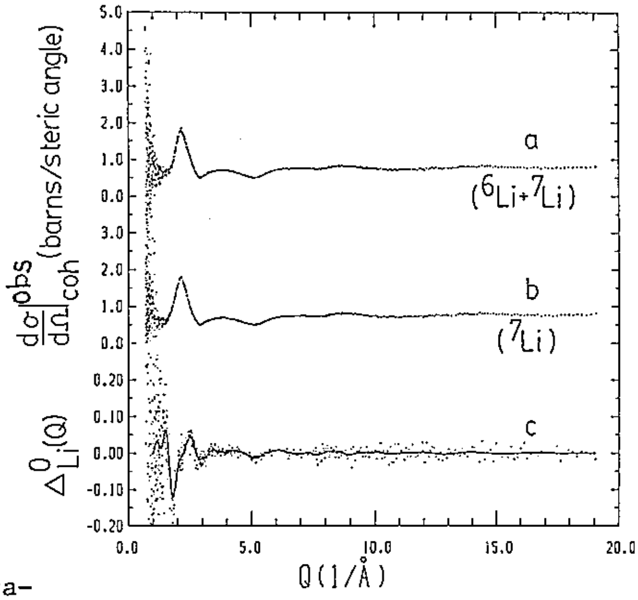

Fig. 1 Observed differential scattering cross sections for two Li-substituted samples and $\Delta^{\circ}_{Li}(Q)$ at 33.1 mol% LiCl, full circles: unsmoothed data points, solid curve: smoothed curve used for the Fourier transform.

In order to study the concentration dependence of the correlation between solute-soluteions and the hydration effects, $\bar{G}_{Li}(r)$ given by eqn (7) was obtained by the Fourier transform using values derived from the smooth curve in $\Delta^{\circ}_{Li}(Q)$ (see fig. 1c). The form of $\bar{G}_{Li}(r)$ shown in fig. 2 indicates (i) the first two peaks at 1.95 Å and 2.31 Å can be identified with Li-O and Li-D correlations, respectively. (ii) The hydration number of 2.3±0.2 was obtained by integrating eqn (10) between 1.8 and 2.6 Å. The hydration number depends on concentration strongly (see fig. 3a) and this number does not support the tetrahedral model.$^{4)}$ (iii) The second two peaks located as 2.76 Å and 3.28 Å are identified as direct

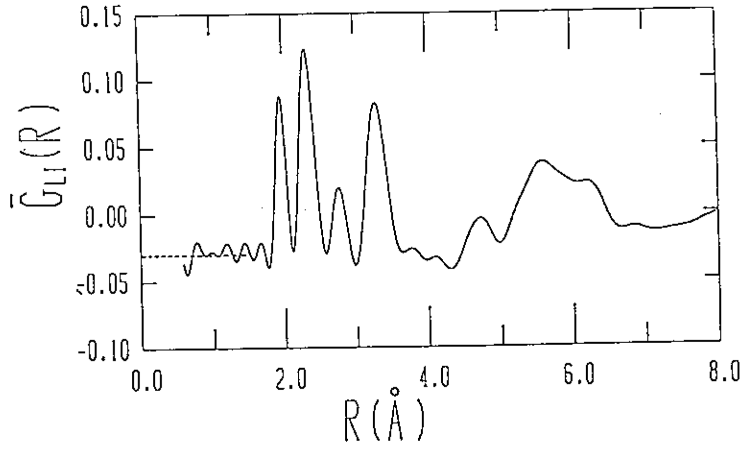

Fig. 2 $\bar{G}_{Li}$ (R) for $(LiCl)_{0.331}(D_2O)_{0.669}$ at 130°C.

and indirect Li-Cl correlations locates nearly across the first hydration shell which is definitely deficient in the number of water molecules hydrated around Li^+ of interest (n_{LiCl}=1.5) and the other Cl^- locates just outside of the first hydration shell (n_{LiCl}=7.4). (iv) The angle $\phi \backsim 75°$ is larger than the lone-pair configuration $\phi \backsim 55°$ and ϕ increases with increasing the LiCl concentration (see fig. 3b). The large value of ϕ observed in incompletely hydrated solution at 33.1 mol% LiCl may arise from the strong interaction between D and Cl^- which is also concerned with direct correlation with Li^+; this reflects the fact that water-bridging between Li^+ and Cl^- is important. (v) According to Newsome et al.[2)] the form of $\bar{G}_{Li}(r)$ for aqueous solutions up to ca. 17 mol% LiCl indicates the stability of the first hydration shell within the range of 3 Å because of $g_{\alpha\beta}(\backsim 3\ \text{Å})=0$ for all the nuclei pairs (see eqn (8)): the form of $\bar{G}_{Li}(r)$ above ca. 25 mol% LiCl insists on the short-range correlations between water molecules and Li^+ as well as between Cl^- and Li^+ within the range of 4 Å because of $g_{\alpha\beta}(\backsim 4\ \text{Å})=0$.

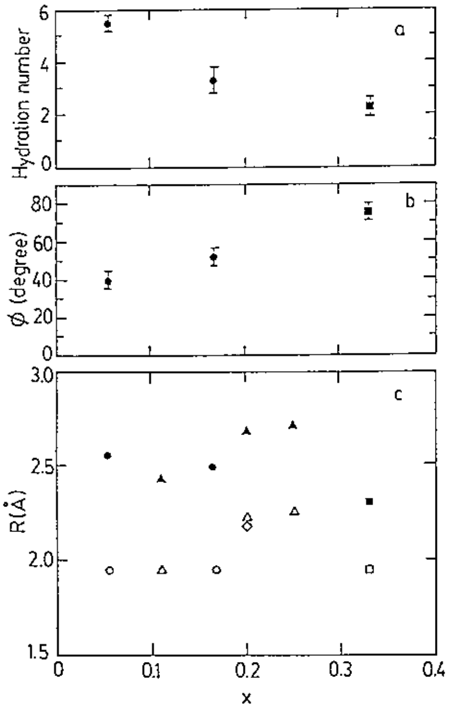

Fig.3 Concentration dependence of a) hydration number of lithium ion, b) ϕ, and c) Li-O(open) and Li-D (solid) distances, □ : this work, ○ : ref. 2, △ : ref. 4, ◇ : ref. 5.

References

1) A. K. Soper, G. W. Neilson, J. E. Enderby, and R. A. Howe, J. Phys. C: Solid State Physics, 10 (1977), 1793.
2) J. R. Newsome, G. W. Neilson, and J. E. Enderby, J. Phys. C: Solid State Physics, 13 (1980), L923.
3) R. Caminiti, P. Cucca, and T. Radnai, J. Phys. Chem., 88 (1984), 2382.
4) A. H. Narten, F. Vaslow, and H. A. Levy, J. Chem. Phys., 58 (1973).
5) I. Okada, Y. Kitsuno, H. G. Lee, and H. Ohtaki, Physical and Theoretical Chemistry (Eds. N. Tanaka et al., Elsevier Sc. Pub., Amsterdam), 27 (1982), 81.

Short range order in a binary critical mixture of perfluoro(methylcyclohexane)—carbon tetrachloride II

Yoshinobu IZUMI, Yasuhiro MIYAKE, Toshiharu FUKUNAGA*, Noriyuki HAYASHI*, Masakatsu MISAWA**, Noboru WATANABE** and Kenji SUZUKI*

Department of Polymer Science, Faculty of Science,
Hokkaido University, Sapporo 060, Japan

*The Research Institute for Iron, Steel and Other Metals,
Tohoku University, Sendai 980, Japan

**National Laboratory for High Energy Physics,
Oho-machi, Tsukuba-gun, Ibaraki-ken 305, Japan

In a previous report[1)], we studied the short range order and its temperature variations of the binary critical mixture of perfluoro(methylcyclohexane)—carbon tetrachloride by a high intensity total scattering spectrometer (HIT) installed at a spallation neutron source of KEK. No apparent change was observed in the profiles of S(Q) and RDF over the Q range examined ($Q<0.6$ Å^{-1}), irrespective that the critical point was approached or not. On the other hand, it has been reported that the S(Q) near the critical point apparently shows "normal" Ornstein-Zernike behavior in a low Q range[2)]. It is therefore suggested that a cut-off Q_c should exist: the critical fluctuation governs the behavior of S(Q) when $Q<Q_c$, while the short range order governs that of S(Q) when $Q>Q_c$. Until now no direct estimation of Q_c has been done, though the Q_c is determined by matching the theory and the experiment based on the critical viscosity[3)].

Present work concerns with the first direct estimation of Q_c from the high Q side ($Q>Q_c$) by HIT. The measurement has been made by using the counters at the lowest scattering angle and by using an improved cell for precise temperature control. The minimum Q value attained is 0.2 Å^{-1} after a smoothing of the profiles of S(Q). The measured tenperatures are $29.0\pm0.5^{\circ}$C($\Delta T=0.4^{\circ}$C), $40.0\pm0.5^{\circ}$C($\Delta T=11.4^{\circ}$C) and $60.0\pm0.5^{\circ}$C($\Delta T=31.4^{\circ}$C).

Fig. 1 shows the plot of S(Q) before the smoothing at three different temperatures. It is noted that no appreciable change is observed in the profiles of S(Q) which reconfirmes the previous result, though the data in a low Q side ($Q<0.3$ Å^{-1}) are influenced by the statistical error. By smoothing the data in the low Q region, we can say that $Q_c<0.2$(or 0.15) Å^{-1}. Further studies at the lower Q region are clearly desirable using neutron small—angle scattering method. As far as we know, such studies have not been made.

References

1) Y.Izumi, Y.Miyake, T.Fukunaga, N.Hayashi, N.Watanabe and K.Suzuki, KENS REPORT—IV, 1983, 65.
2) B.Chu, D.Thiel, W.Tscharnuter, and D.V.Fenby, J.Phys.(France) 33(1972) Cl—111; B.E.Sundquist and R.A.Oriani, J.Chem.Phys. 36(1962) 2604.
3) R.Perl and R.A.Ferrell, Phys.Rev. A6(1972) 2358.

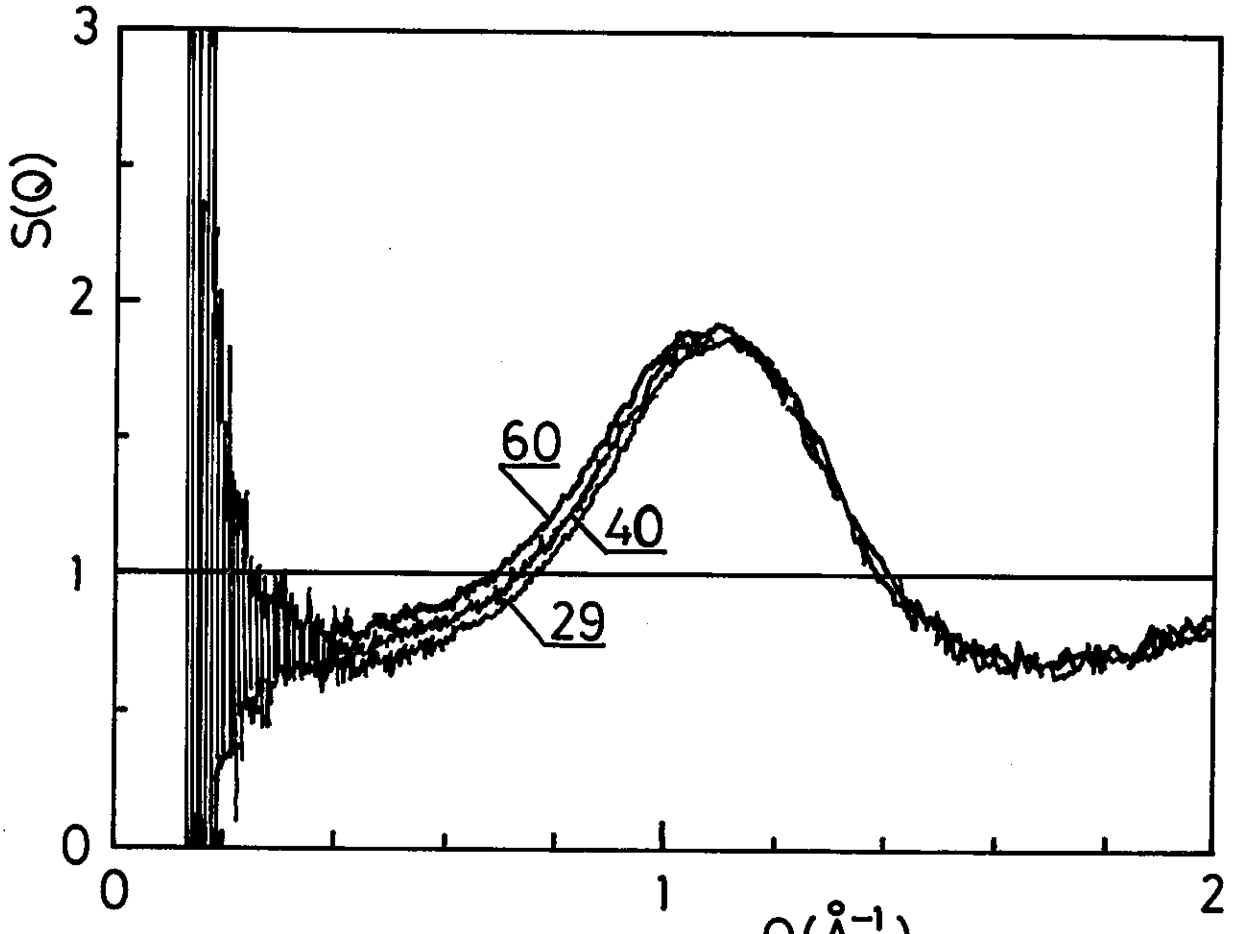

Fig. 1. Structure factors by perfluoro(methylcyclohexane)—carbon tetrachloride mixture at 29.0, 40.0 and 60.0°C.

Early Stages of Phase Separation in an Al-6.8%Zn
Studied by Small Angle Neutron Scattering

Michihiro FURUSAKA, Mitsuru MERA and Yoshikazu ISHIKAWA

Physics Department, Tohoku University, Sendai 980, Japan

It has been established that the scattering function in FeCr alloys at the late stages of phase separation process, scattering function obeys the q^{-4} relation at higher q side of the peak, and the scaling law of the form $F(q/q_1)=q_1^3 \cdot S(q,t)$[1),2)] holds[3)] in the entire q range, where q_1 is the first moment of time dependent scattering function $S(q,t)$. At a very early stage, however, we have shown that the scattering function exhibits rather the q^{-2} relation at higher q side and no scaling law holds. This q^{-2} relation has been predicted[4)] by the non-linear theory of Langer, Bar-on and Miller.[5)] These salient results were obtained by virtue of simultaneous measurements of the wide q range which is an important potential of SAN at KENS.

Quite recently, it was reported that a similar scattering law also holds for an AlZn alloy [6)] at late stages of the phase separation. But, as far as the earlier stages in this alloy are concerned, no definite results have been obtained. One of the reasons is that the atomic diffusion of the sample is rather fast even at room temperature and another is the limitation of the measurement of q range with the small angle scattering instrument at reactor. Therefore, we have undertaken the study of the early stage of the phase separation process of the AlZn alloy with SAN in order to compare with the phase separation process in FeCr alloys.

The sample of AlZn alloy at off critical concentration (6.8at%Zn) was made from 99.999% Al and Zn by induction melting. It was homogenized at 400°C for at least 12 hours in an *in situ* furnace[7)] with a simultaneous measurement of neutron scatering until the small angle scattering intensity from the sample became negligible, followed by quenching by a flash of liquid nitrogen.[7)] The scattering intensity from the as quenched sample was found to be almost the same as the one measured during the homogenizing process.

The scattering function $S(q,t)$ from the sample annealed at 116°C are presented in log-log scale in Fig. 1(a), which shows the q^{-4} relation at the higher q side of the peak and the scaling law also holds as presented in Fig. 2(a) in agreement with the previous observation. At an intermediate temperature (25°C), the shape of the scattering function S(q,t) at higher q side varys from q^{-2} to q^{-4} dependence as the annealing time increases (Fig.1(b)). Figure 2(b) also shows that the scaling law holds at late stages (7~10 minutes), where the scattering function has q^{-4} dependence. But it is not the case for earlier stages, where the scattering function deviates from the q^{-4} relation. In contrast to them, the scattering from the sample annealed at -30°C (Fig. 1(c)) shows the q^{-2} relation, and the scaling law does not hold, just as is the case with FeCr alloys. It should also be noted that even at the very beginning of the phase separation process, exponential divergence of the time evolutions of scattering intensities predicted by the Cahn's theory could not be detected for this sample.

To conclude, the late stages of the phase separation are detected in the sample annealed at 116°C, and 25°C. The existence of the very early stage was found for the sample annealed at -30°C, where the scaling law does not hold and the scattering function shows the q^{-2} relation. It is the first experiment which shows the existence of such a very early stage of the phase separation process, to our knowledge. The close resemblance between the phase separation behavior of the FeCr sample and that of AlZn sample suggests that the early stage of the phase separation process we found is the general characteristic of the separation porcess.

References

1) J. Marrow, J. L. Lebowitz and M. H. Kalos: Phys. Rev. Lett. **43** (1979) 282.
2) H. Furukawa: Phys. Rev. Lett. **43** (1979) 136.
3) M. Furusaka and Y. Ishikawa: KENS REPORT-IV (1983) 84.
4) M. Furusaka: Doctor Thesis, Tohoku Univ (1984). (in Japanese).
5) J. S. Langer, M. Bar-on and H. D. Miller: Phys. Rev. **A11** (1975) 1417.
6) M.Hennion, D. Ronzaud and P. Guyot: Acta Metall. **30** (1982) 599.
7) M. Furusaka, M. Mera and Y. Ishikawa: KENS REPORT-IV (1983) 88.

Fig.1. Log-log plots of scattering functions measured in Al-6.8at%Zn. Annealing temperatures are (a) 116°C, (b) 25°C, (c) -30°C.

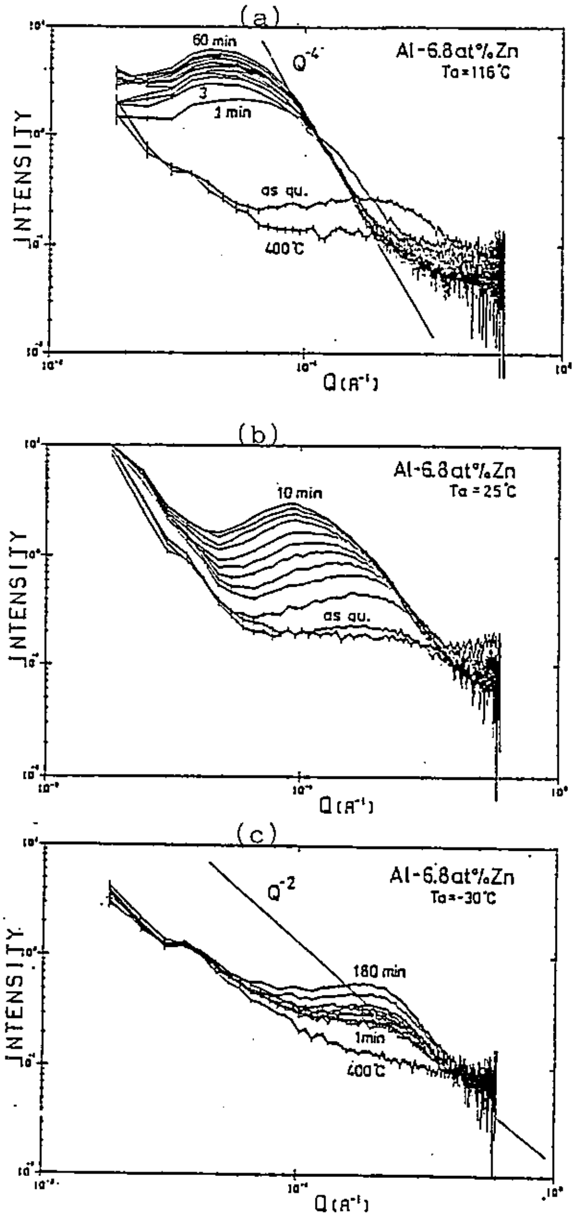

Fig.2. Scaled functions $F(q/q_1)$ for the sample annealed at (a) 116°C, (b) 25°C.

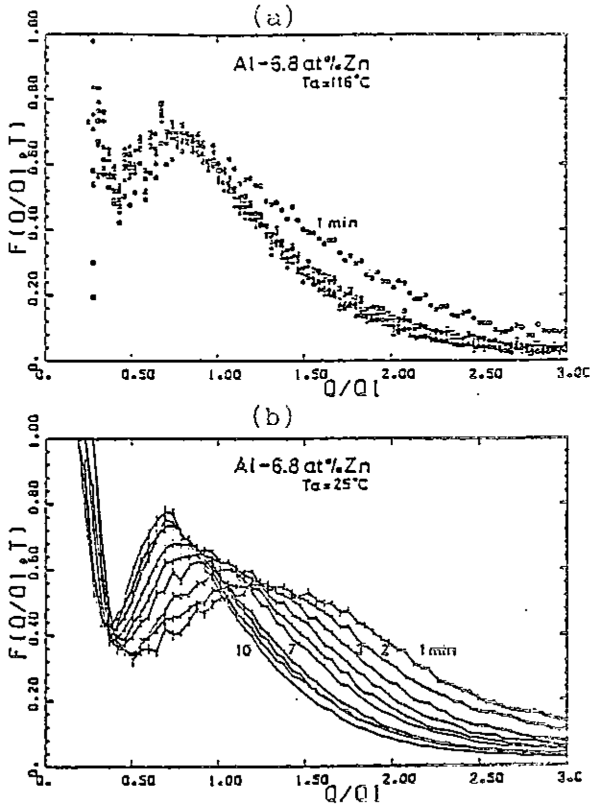

Spin Wave Scattering Measured with a Small Angle Scattering Instrument SAN

Michihiro FURUSAKA, Yoshikazu ISHIKAWA and *Shigehumi ONODERA

Physics Department, Tohoku University, Sendai 980, Japan
**Sendai Radio Technical College, Miyagi 989-31, Japan*

Small angle neutron scattering measurement from Fe_3Pt has been paid an attention in conjunction with the Invar effect of the alloy. There has been a report on this subject,[1) but the results have an ambiguity that the small angle scattering is contaminated with spin wave scattering. Therefore the separation of elastic scattering from inelastic one was performed by applying an external magnetic field which, however, modifies the phenomenon. In this report, we show a possibility of separating spin wave scattering from elastic one by analyzing wavelength dependence of the small angle scattering obtained with SAN at KENS.

If the quadratic dispersion relation holds for the spin wave excitations with a spin wave stiffness constant D, the critical angle θc of the spin wave scattering is given by,[2)

$$\theta c \approx \frac{\hbar^2}{2m} \cdot \frac{1}{D} = \frac{1}{D'}. \qquad (\theta c \ll 1) \qquad (1)$$

No spin wave scattering occurs outside of this angle and it is independent of incident neutron wavelength.

The scattering intensities from an orderd Fe_3Pt measured at 150°C by different wavelengths are plotted against q in Fig.1(a). The estimation of q was performed under an assumption that the scattering was purely elastic. They clearly show the wavelength dependence. In contrast to them, when the scattering functions are plotted against the scattering angle θ, multiplying by k_i^2, they are nearly independent of the incident wavelengths for the θ greater than 0.03rad (Fig.1(b)). For the wavelengths 3~4A, the scattering curves fall on a single line for the θ greater than 0.02rad. Discrepancy at the small θ side of the scattering functions is considered to come from the elastic one.

Since spin wave damping factors of invar alloys are significantly larger than those of non Invar alloys,[3)] life time, energy gap and stiffness constant have been taken into account to calculate the profiles of the small angle spin wave scattering $I(\theta)$. The spin wave scattering cross section $S(q,w)$ was assumed to be,

$$S(q,w) = A(k_i,k_f) \cdot \frac{\hbar w}{1-\exp[-\hbar w/k_B T]} \cdot \frac{1}{K_1{}^2+q^2} \cdot \frac{G \cdot q^2}{(w-w_q)^2 + (G \cdot q^2)^2}, \qquad (2)$$

where, $A(k_i,k_f)$ is a wavelength dependent constant, K_1 the perpendicular component of the inverse correlation length, $\hbar w_q$ the magnon energy and $G \cdot q^2$ the damping factor. The small angle scattering intensity $I(\theta)$ was obtained by integrating $S(q,w)$ with q^z component parallel to the k_i, followed by convolution with the instrument resolution.

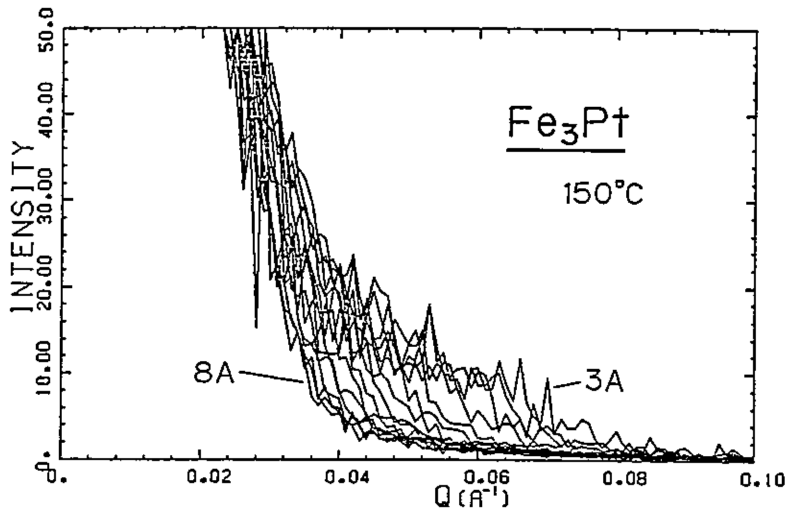

Fig. 1(a). Scattering functions plotted against q, assuming the scatteing to be purely elastic. Sample is Fe_3Pt, measured at 150°C without external magnetic field.

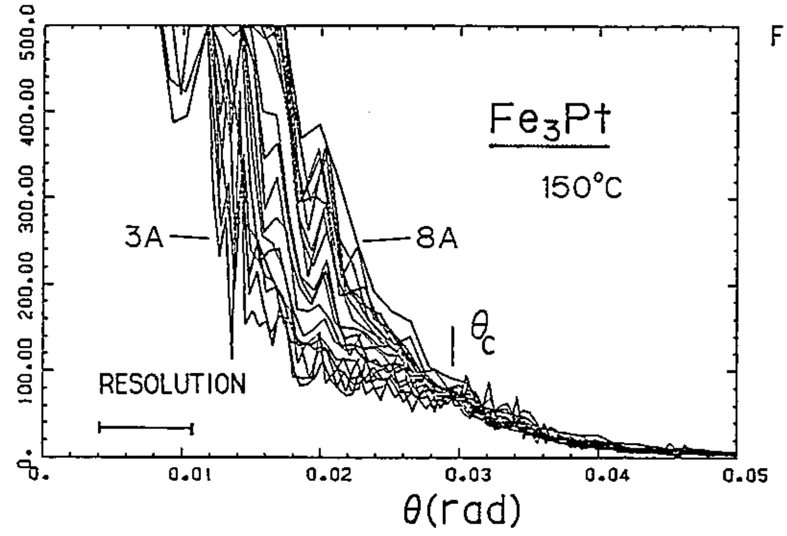

Fig. 1(b). Scattering functions normalized by $k_i{}^2$ plotted against θ, for the same sample.

For the calculation, spin wave parameters determined by triple axis spectrometers in the q regions greater than $0.03 Å^{-1}$ for the same sample were employed. They are, stiffness constant D (85meV·A^2), damping factor coefficient G (6.6meV·A^2) and energy gap E_g (0.04meV). Experimental results (continuous lines) from the sample of Fe_3Pt measured at room temperature as well as calculated ones (broken lines) using these parameters are presented in Fig.2. The experimental results for shorter wavelengths (3~4A) are well reproduced by calculation. Note that the elastic scattering intensity is weak compared with inelastic one in this λ range, because the elastic scattering is limited in small θ range, compared with the scattering measured with longer wavelengths. A little wavelength dependence in the scattering intensities is explained by taking into accout the spin wave life time and the small energy gap. In contrast to them, for longer wavelengths (5A~), the scattering function showed a clear θ dependence. That is due to the elastic scattering by magnetic inhomogenity.

To conclude, our analysis has shown the potential of measurement of spin wave scattering with our small angle scattering instrument SAN. The characteristics of the potential are, (1) the inelastic scattering with very small energy transfers can be detected at very small q (down to 10μV at 0.01A^{-1}), (2) this method has an ability to separate elastic small angle scattering component from inelastic one, and (3) only one measurement is enough for this analysis. This method has been applied to the measurement of small angle scatteing from Fe_3Pt, which enabled us to determine elastic scattering separately. The details will be published elsewhere.

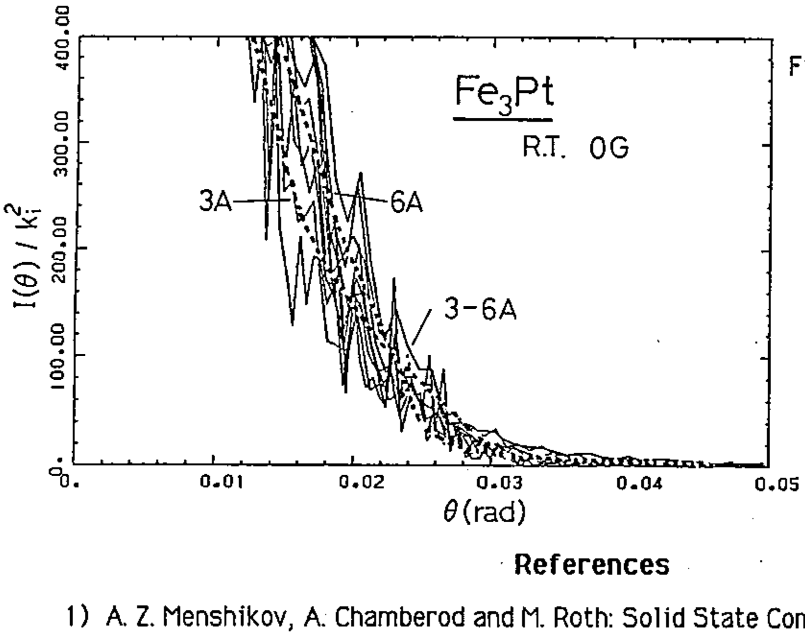

Fig.2. Scattering functions normalized by k_i^2 plotted against θ. Sample is Fe_3Pt measured at room temperature.

References

1) A. Z. Menshikov, A. Chamberod and M. Roth: Solid State Commun, **44** (1982) 243.
2) M. W. Stringfellow, J. Phys. **C2** (1968) 950.
3) Y. Ishikawa, S. Onodera and K. Tajima: J. Magn. & Magn. Mater. **10** (1979) 183.

Small-angle Neutron Scattering from Semi-dilute Polyelectrolyte Solutions

Kimio Kurita, Takahisa Iida, Tsuyoshi Iizuka, Takashi Nakamura,
Eiichi Wada, Koji Okano*, Shinya Nakajima**, Michihiro Furusaka***
And Yoshikazu Ishikawa***

College of Science and Technology, Nihon University, Tokyo 101
*Department of Applied Physics, University of Tokyo, Tokyo 113
**Kanagawa Dental College, Yokosuka 238
***Department of Physics, Tohoku University, Sendai 980

The purpose of the present study is to measure separately the intermolecular and intramolecular parts of the structure factor of SANS by salt free polyelectrolyte solutions thereby clarifying the origin of the broad maximum that appears in the total structure factor.

For this purpose we employed the method by Williams et al$^{1)}$. The aqueous solvent was a mixture H_2O and D_2O, the composition of which was chosen to give zero contrast to the unlabeled (protonated) polyelectrolyte chains. So that for a coherent elastic neutron scattering only the labeled (deuterated) chains were visible. Let the total structure factor S(q) of solutions, in which all the polyelectrolyte chains are labeled, be decomposed into the intramolecular part $S_1(q)$ and intermolecular part $S_2(q)$ as

$$S(q) = S_1(q) + S_2(q) \qquad (1)$$

If, at the same total concentration C, only a few are labeled so that a fraction X of the chains will give rise to a coherent scattering, the structure factor, $S_X(q)$, is given by

$$S_X(q) = XS_1(q) + X^2S_2(q) \qquad (2)$$

We can determine $S_1(q)$ and $S_2(q)$ separately, for each total concentration C, by measuring X dependence of $S_X(q)$.

The samples used were sodium polystyrene sulfonate. They were prepared by sulfonation of a protonated and a deuterated polystyrene, PS_H(Press. Chem., $M_w=0.93\times10^5$, $M_w/M_n \leqq 1.06$) and PS_D(Polym. Lab., $M_w=1.03\times10^5$, $M_w/M_n \leqq 1.06$), by method of Vink$^{2)}$. There were about 93% or more sulfonated styrene per chain. The solvent used was a mixture of 70% H_2O and 30% D_2O. The total concentrations were 0.026, 0.052, 0.103 g/cm^3 which were higher than the cross-over concentration.

The measurements were performed with the KENS-SAN instrument at KEK[3]. The excess scattering intensity of sodium polystyrene sulfonate solution against the solvent was determined after the transmission correction was made both for the solution and solvent. The solvent gave zero contrast for the protonated chains. Solution cell was made of quartz and thickness of the sample liquid was 2mm. Area of the neutron beam at the window was 35x14 mm^2. The incoherent neutron spectrum as well as the detector efficiency of two-dimensional position sensitive detector was corrected by employing the incoherent scattering intensity from water.

Fig.1 shows plots of angular dependence of scattering function with the resolution of dq/q=0.2. One broad maximum of the scattering function, whose position varies with concentration, appears for all concentrations. The q values corresponding to the maximum intensity vary as $C^{1/2}$. Fig.2 shows an example of the q dependence of $S_X(q)/X$. The intrachain $S_1(q)$ and the interchain $S_2(q)$ signals extracted from Fig.2 (X varying between 0.4 and 1.0 for each total concentration C) are shown in Fig.3. The figure shows that the intrachain $S_1(q)$ decreases while the interchain $S_2(q)$ increases monotonically with increasing q. The negative sign of $S_2(q)$ means the repulsive interchain interaction. The both functions do not have any maximum, but the sum(Eq.1) of the two functions gives the above maximum. The q dependences of $S_1(q)$ and $S_2(q)$ at other concentrations are similar to those at 0.103 g/cm^3(Fig.4).

The results shown in Fig.3 decidedly demonstrate that the maximum that appears in the total structure factor S(q) has nothing to do with the Bragg reflection, rather it occurs as a result of a delicate interplay of inter- and intrachain interferences. The whole features of the obtained $S_1(q)$ and $S_2(q)$ are consistent with the theory of French group[4)5)].

According to the simple theory[4)], " the correlation tube effect " is expressed as

$$S_2(q) = -S_1(q) \frac{1}{1 + \xi^2 q^2} \qquad (3)$$

where ξ is roughly the diameter of the correlation tube. We tried to determine the value of ξ for each concentration by fitting the $S_2(q)$ value calculated by means of Eq.(3) together with the experimentally observed $S_1(q)$ to the measured one. The solid lines in Fig.5 show the smoothed curves thus calculated. The concentration dependence of ξ thus determined was plotted in Fig.6. We see that ξ varies roughly as $C^{-1/2}$. Again, this behavior agrees with the theoretical prediction[4)6)].

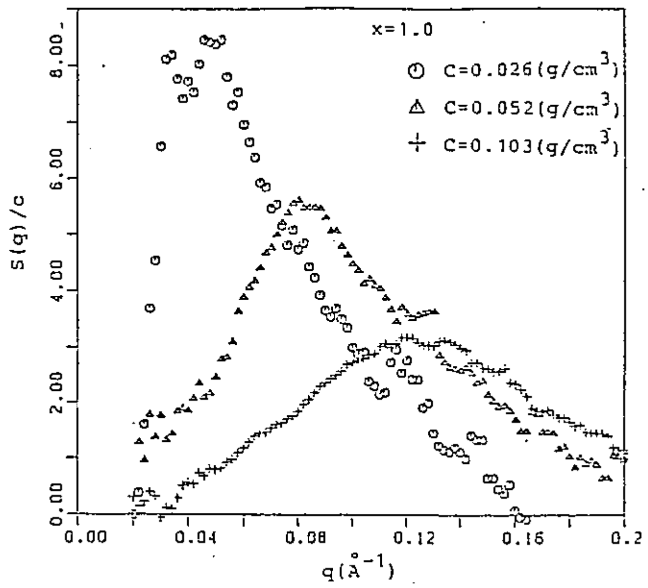

Fig.1

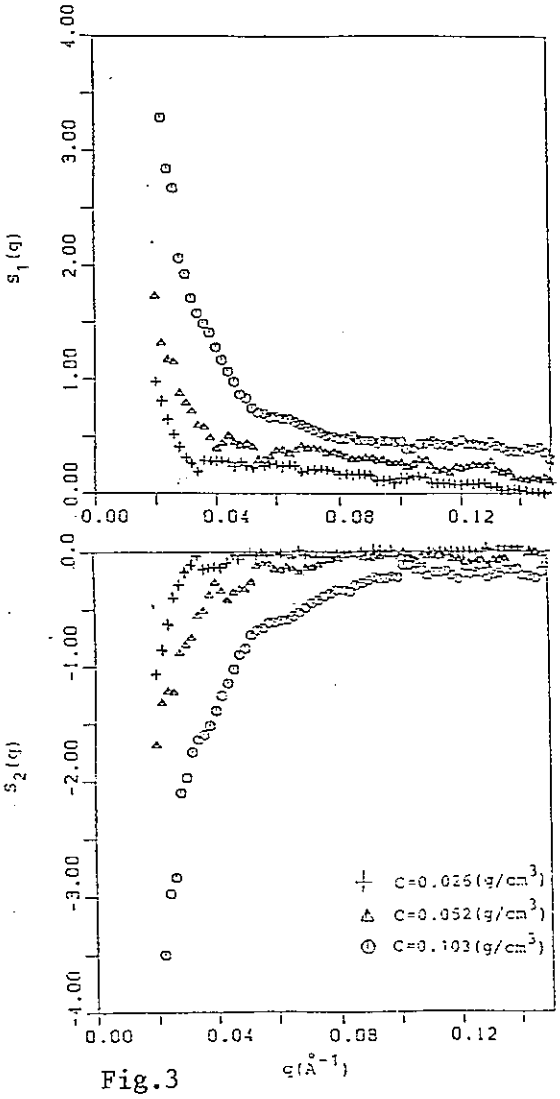

Fig.3

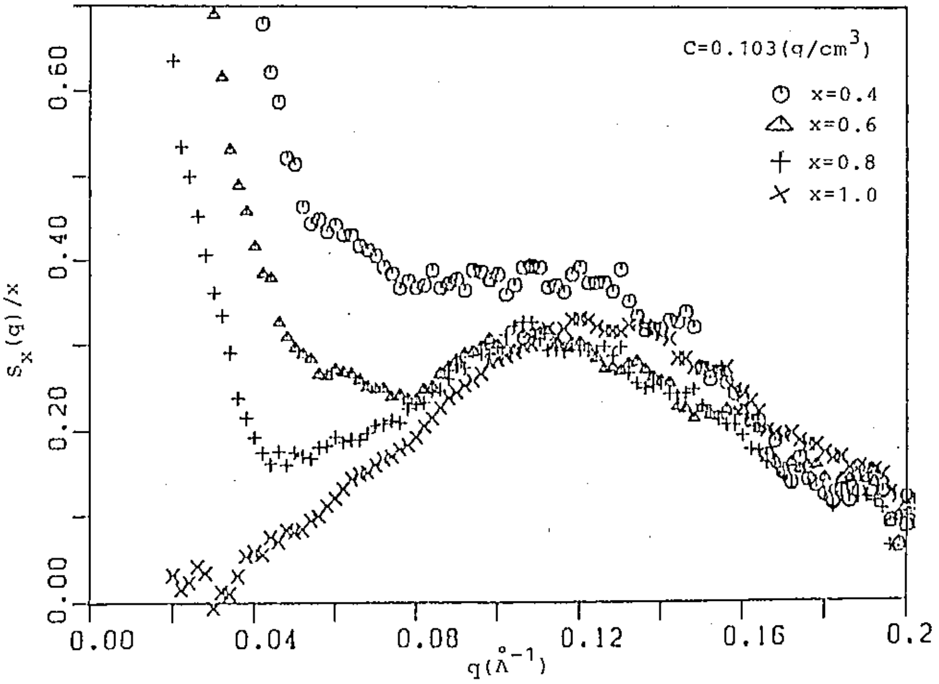

Fig.2

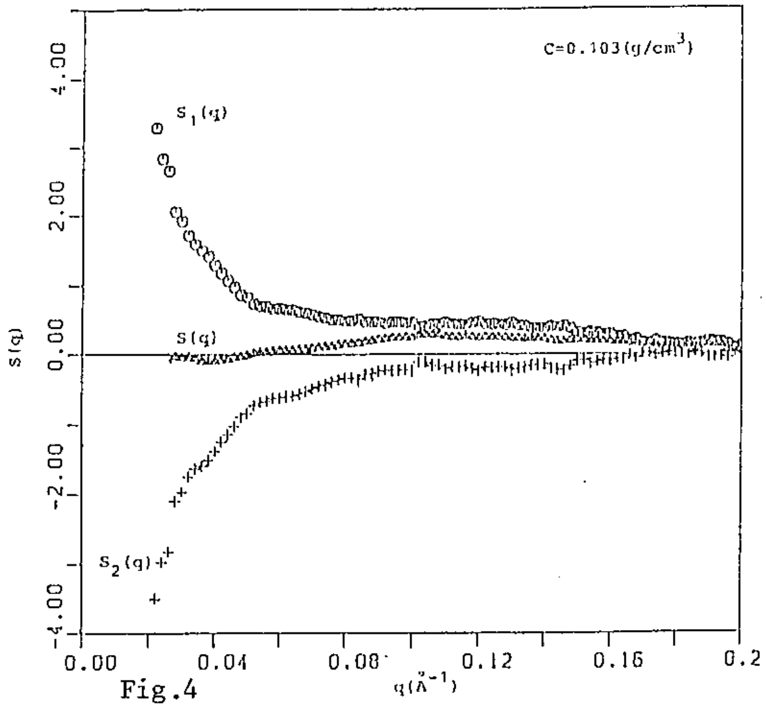

Fig.4

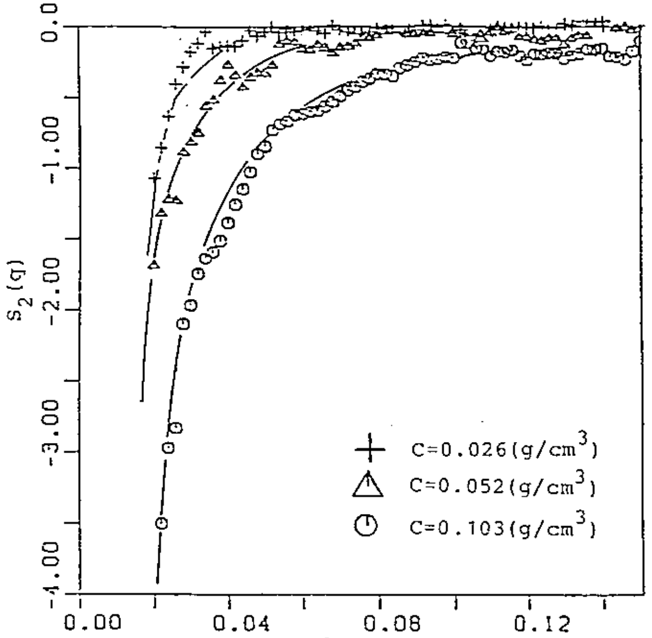

Fig.5

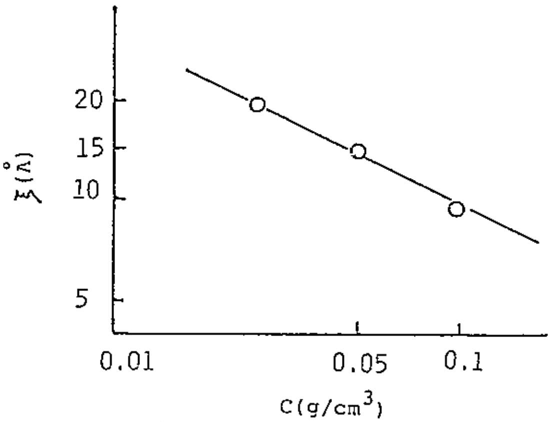

Fig.6

References

1) C.E.Williams, M.Nierlich, J.P.Cotton, G.Jannink, F.Boue, M.Daoud B.Farnoux, C.Picot, P.G.de Gennes, M.Rinaudo, M.Moan, C.Wolff, J. Polym. Sci. Polym. Lett., 17, 379 (1979).

2) H.Vink, Makromol. Chem., 182, 279 (1981).

3) Y.Ishikawa, S.Ikeda, M.Furusaka, N.Niimura, KENS REPORT I, 101 (1980).

4) J.Hayter, G.Janninck, F.Brochard-wyart, P.G.de Gennes, J. Physique, L41, 451 (1980).

5) M.Benmouna, G.Weill, H.Benoit, Z.Akcasu, ibid., 43 1679 (1982).

6) P.G.de Gennes, P.Pincus, R.M.Velasco, F.Brochard, ibid., 37 1461 (1976).

Determination of the D_2O/H_2O ratio in solutions by the use of neutron transmission measurements

M. Hirai*, N. Niimura**, F. Tokunaga*, Y. Ishikawa*,
K. Mita***, M. Zama***, S. Ichimura***

* Physics department, Tohoku University, Sendai, 980
** Laboratory of Nuclear Science, Tohoku University, Sendai, 982
***Division of Chemistry, National Institute of Radiological Sciences, Chiba, 260

The contrast variation method is one of the most attractive applications of neutron diffraction from the solution of biological materials. D_2O/H_2O ratio in the solution and solvent should be exactly the same since the scattering intensity of the solute particles can be obtained by subtraction of the scattering intensity of solvent from that of solution. The neutron transmission measurement with SAN is found to be very useful to determine the D_2O/H_2O ratio in the solution.

The transmission can be written as follows,

$$T = \frac{I}{I_0} = \exp(-\sigma_T - \sigma_{cell}) \qquad (1)$$

where I is the transmitted intensity, and I_0 is the incident intensity and σ_T and σ_{cell} are the total cross sections of the contents and cell itself, respectively. The total cross section σ_T may be written as follows,

$$\sigma_T = k_1 \cdot C \cdot \sigma_{solute} + k_2 \cdot \sigma_{solvent} \cdot f(C) \qquad (2)$$

where k_1 and K_2 are constants, C the concentration of the solute and f(C) comes from the excluded volume effect of the solute. σ_{solute}, the total cross section of the solute, is given by the linear expression of x, D_2O/H_2O ratio.

Though the total cross section of the solvent, $\sigma_{solvent}$ has a non-linear term on x which is deduced from the molecular weights between D_2O and H_2O, this can be given approximately by the linear expression of x. So, it is derived from eq.(1) and (2) that the natural logarithm of the transmission is proportional to the D_2O/H_2O ratio. Fig. 1

indicates the wavelength dependence of the transmission of the standard solvents which is a unique potential of the SAN. From the logarithm plots of Fig. 1, the calibration lines for the determination of the D_2O/H_2O ratio in the solution have been obtained as shown in Fig. 2.

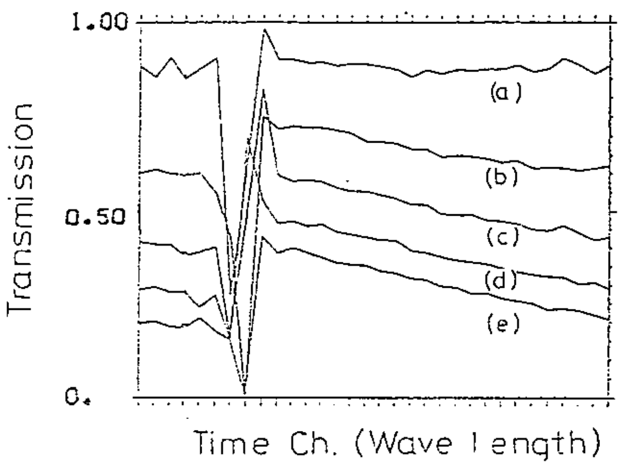

Fig. 1 The wavelength dependence of the transmission of standard solvents. (a): 100% D_2O, (b): 75%D_2O, (c): 50%D_2O, (d): 25%D_2O (e): H_2O

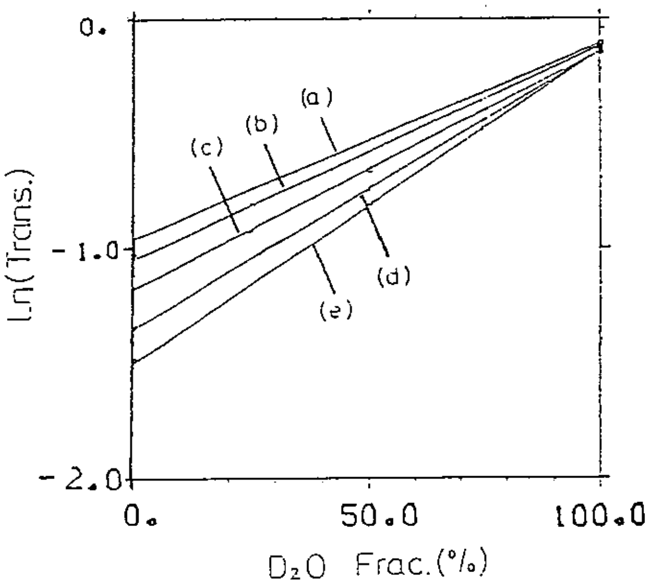

Fig. 2 Calibration lines for the determination of the D_2O/H_2O ratio are obtained by logarithm plots of fig 1. (a): 2.5Å, (b): 3.9Å, (c): 5.3Å, (d): 6.6Å, (e): 8.0Å

Generally, the sample preparation to obtain the solution of the adequate D_2O/H_2O ratio is executed by the use of dialysis against the solvent of the same D_2O/H_2O ratio. In this case it is sometimes difficult to reach the expected ratio of D_2O/H_2O even after a series of dialysis because of the slow rate of exchange between deuterium and hydrogen in the solution. Especially, in the solution containing highly charged particles, for example, nucleosome core particles which might have many hydrated water molecules, it takes scores of hours to exchange D_2O to H_2O. Fig. 3 (a) demonstrates this circumstance. The solution was diluted in the 100%D_2O solvent and condensed several times repeatedly in about 10 hours. The expected ratio was 99.5%D_2O, but 94%D_2O was estimated from the calibration lines in Fig. 2. Fig. 3 (b) shows the transmission profile after matching the D_2O/H_2O ratio of the solvent to that of the solution. The two transmission profiles agree well with each other. This shows that the calibration lines obtained in Fig. 2 are correct and that the transmission matching is performed correctly.

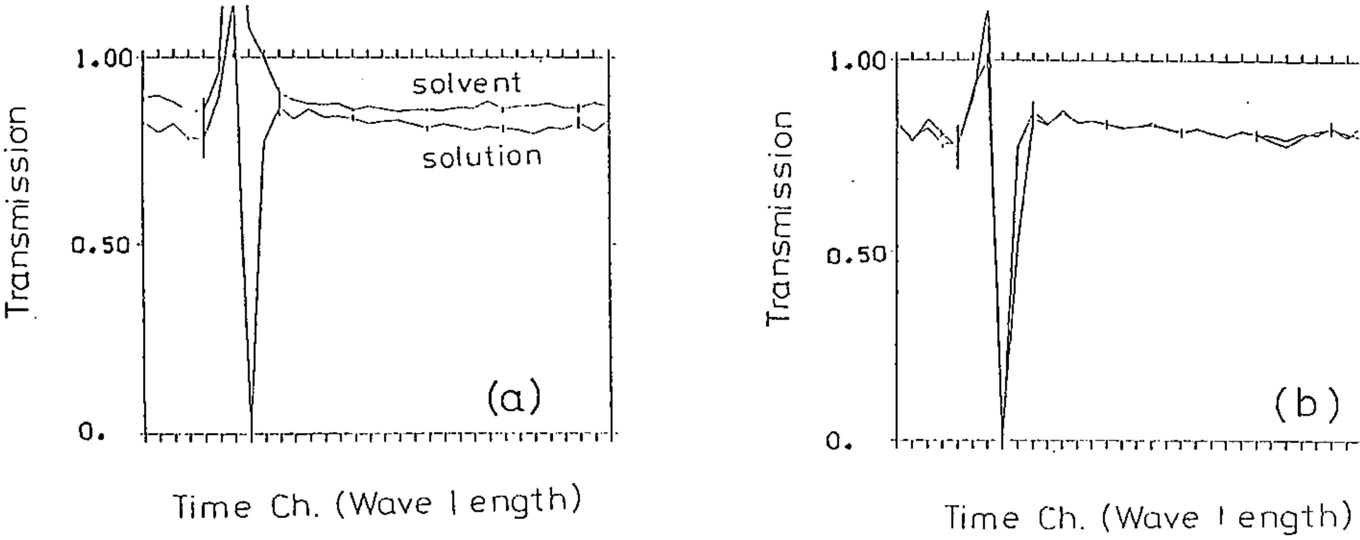

Fig. 3 Transmission profiles of the solvent and solution. (a) and (b) are before and after transmission matching respectively.

There are other methods to determine the D_2O/H_2O ratio. The H-NMR measurement can be used for this purpose, but it is not convenient. Though the infrared absorption analysis is easily applied, the calibration lines deviate from the linearity below 80%D_2O. The density measurement covers the full range of D_2O/H_2O ratio and is more accurate for the solvent. But for the solution, because of the difference of the densities between the solute and solvent and the change of the viscosity, the error of the D_2O/H_2O ratio is estimated to be about 4% for the 1 wt% nucleosome core particle solution. For the same solution the error of the D_2O/H_2O ratio by the use of the neutron transmission measurement is less than 0.4%. Note that our method is the privilege of the SAN which employs the various wavelengths neutrons.

Interparticle Interaction of Nucleosome Core Particle at Low Ionic Strength

M. Hirai*, K. Mita**, M. Zama**, S. Ichimura**,
N. Niimura*** and Y. Ishikawa*.

* Physics Department, Tohoku University, Sendai 980
** Division of Chemistry, National Institute of Radiological Science, Chiba 260
*** Laboratory of Nuclear Science, Tohoku University, Sendai 982

The nucleosome core particle, consisting of 146 base pairs of DNA wrapped around an octamer of two each of inner histones H2A, H2B, H3 and H4, constitutes the first level of DNA packaging in chromatin. The association of conformationally altered core nucleosomes with transcriptionally active genes attracts current interest in the conformational state and transition of the core particle. One way to characterize the ability of nucleosome to unfold has been to examine their response to variations in ionic strength.

In a course of detailed neutron small angle scattering studies of the nucleosome core particles, we have found that the interparticle interaction between nucleosome core particles is changed drastically by variations in ionic strength below 10^{-2} M. At low salt state ($<10^{-3}$ M), a single peak is observed clearly (fig. 1 (a)). As increasing ionic strength by adding salt, this peak decays gradually with broadening of its width (fig. 1 (b)). This tendency doesn't depend on solute concentrations in the range of our measurements (1.0 wt%∿0.6 wt%).

Fig. 2 shows the dependence of the peak positions on solute concentrations. The peak position shifts toward the Q region at low concentration. It is found that the peak is originated from the interparticle interaction. Furthermore, the peaks are located at a little higher Q region than we expected from each solute concentration. It may suggest that the cores are dispersed heterogeneously.

The core particle has totally 146 negative electronic charges. So, at low salt state, the electrostatic shielding by counterions can be weakened and such interaction might be reinforced. We apply the

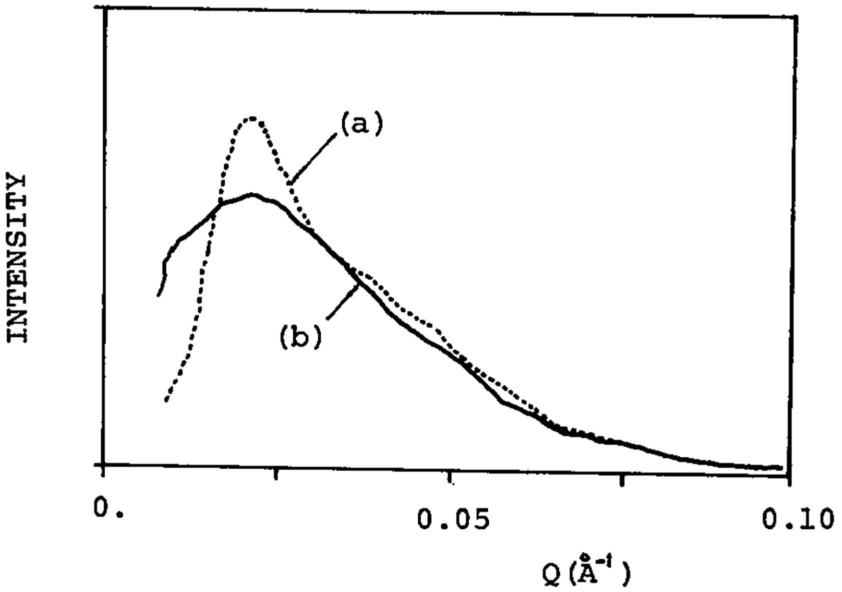

Fig. 1. Neutron scattering profiles of 1.04 wt% nucleosome core particle in D_2O (94%)

(a) in 0.02 mM EDTA (low salt)

(b) in 0.02 mM EDTA + 10 mM NaCl (high salt)

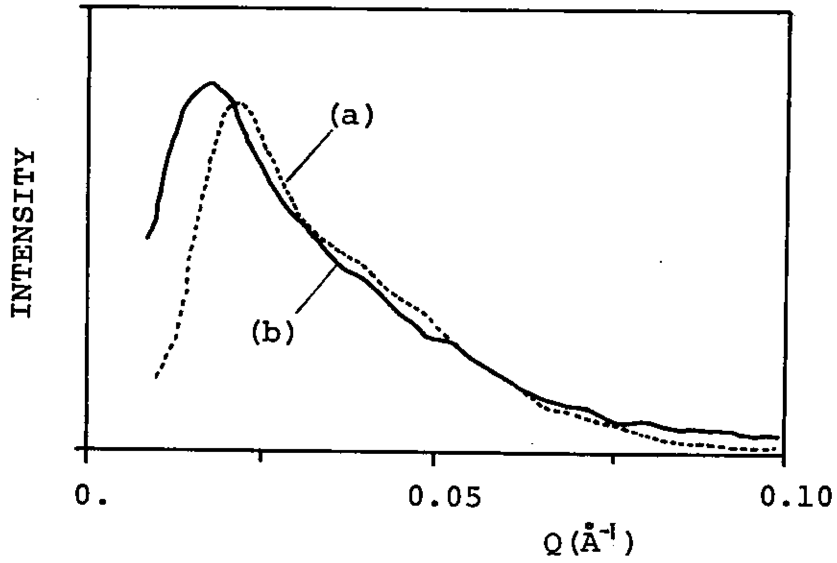

Fig. 2. Neutron scattering profiles of two different concentrations

(a) 1.04 wt% nucleosome core particle in D_2O (94%)

(b) 0.56 wt% nucleosome core particle in D_2O (100%)

treatment given by Hosemann et al.$^{1)}$ to estimate the effect of the interparticle interaction on scattering profiles. Though the models are very simplified, the tendency on variations in ionic strength is very similar to that on variations in g-factor which repesents ordering parameter of cores (fig. 3).

It is difficult to estimate the accurate radius of gyration, R_G, obtained by the use of Guinier plot because of the peak in the Guinier region. We found that it is possible to estimate R_G by using the data outside the peak ($Q > 0.025 \mathring{A}^{-1}$) where the scattering plofile doesn't depend on such interation approximately (shown in fig. 3).

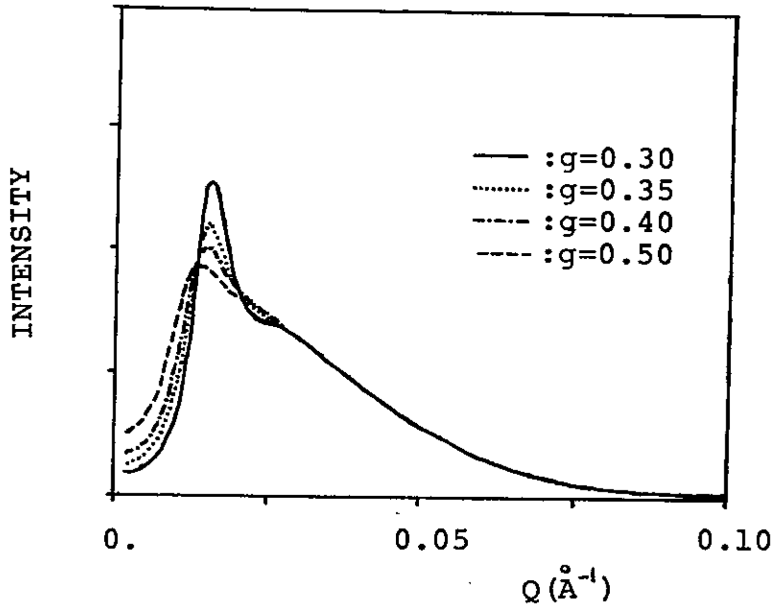

Fig. 3. Simulated scattering profiles on various ordering parameters, g-values where the core particle shape is fixed as a cylinder with 105 Å in diameter, 45 Å in height. The concentration is 0.6 wt%.

The radius of gyration already reported$^{2)}$ has been also estimated by the use of the data of this range. We have a plan of SOR small angle X-ray measurement with the very low concentration solution at low and high ionic strength.

Reference

1) P. H. Lindenmeyer, R. Hosemann : J. Appl. Phys. 34 (1963) 42
2) K. Mita, M. Zama, S. Ichimura, N. Niimura, K. Kaji, M. Hirai, Y. Ishikawa : Physica 120B (1983) 436

Determination of the Histone to Histone Distance in the Nucleosome Core Particle

Mitsuhiro Hirai*, Kazuei Mita**, Mitsuo Zama**, Sachiko Ichimura**,
Koei Hamana***, Nobuo Niimura+, and Yoshikazu Ishikawa*.

* Physics Department, Tohoku University, Sendai, 980
** Division of Chemistry, National Institute of Radiological Science, Chiba, 260
*** College of Medical Care and Technology, Gunma University, Maebashi, 371
\+ Laboratory of Nuclear Science, Tohoku University, Sendai, 982

Reconstituted subunits containing two deuterated proteins in a protonated matrix have been used successfully by Moore and Engelmann[1)] for distance determinations between proteins within the small ribosomal subunit. The design of the experiment is shown in Fig. 1.

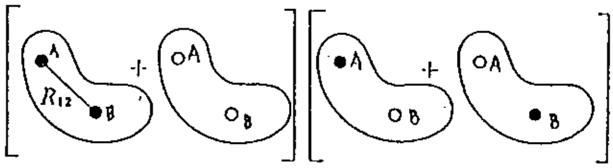

Fig. 1. The design of the experiment for distance determinations between proteins within the small ribosomal subunit.

The first scattering profile (the "signal") is collected on an equimolar mixture of ribosomes containing both of the proteins of a given pair in deuterated form with ribosomes containing the same proteins in the normal hydrogenated form. The second scattering curve (the "noise") is collected using a mixture containing equal amounts of ribosomes containing one deuterated protein and ribosomes containing the other deuterated protein. Since both samples have the same amount of deuterated proteins, hydrogenated proteins and RNA, the only difference between them is the arrangement of the scattering element. The difference curve arises from the fact that the pair of deuterated proteins is held in a fixed spatial relationship in the "signal" sample.

This method can be applied to distance determination between histone proteins in the nucleosome core particle. As to the design of the experiment, however, there is a great difference between ribosomal subunits and nucleosome core particles. In the ribosomal subunit there is no pair of the same proteins, whereas in the nucleosome core particle there are two each of proteins H2A-H2A, H2B-H2B, H3-H3 and H4-H4. This means that the "noise" sample containing one deuterated protein cannot be reconstituted in the nucleosome core particle. The design of the experiment should be modified as shown in Fig. 2; when we want to determine H2B-to-H2B distance for example, the "noise" sample is reconstituted by the use of equal amounts of deuterated and hydrogenated proteins H2B. If there is no special difference between deuterated and hydrogenated proteins as to binding ability, the equal amounts of four kinds of nucleosome core particles as shown in Fig. 2 can be reconstituted.

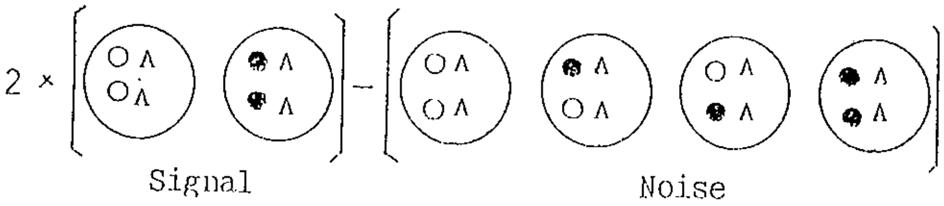

Fig. 2. The design of the experiment for distance determination between proteins within the nucleosome core particle.

The difference curve between the double "singnal" and the "noise" profiles should be able to give the distance between H2B and H2B proteins.

According to this principle, we have tried the distance determination between H2B-H2B proteins. Deuterated histones were isolated from *Saccharomyces cerevisiae* (baker's yeast) growing on media containing $D_2O^{2)}$.

Both samples of the "signal" and the "noise" were reconstituted as mentioned above, and the neutron scattering profiles were measured with SAN. The difference curve is shown in Fig. 3. The figure indicates that there is a significant difference between the signal and noise at low Q side, which is clearly out of the experimental errors. Note, however, that the difference is negative; the noise is larger than the signal although the experiment was repeated with the sample of the same origin, but the same result was obtained. For a moment, we cannot find a reasonable interpretation of the result, but the possibility of the incomplete reconsitution of the signal or/and noise cannot be ignored. We are now checking biochemically the fidelity of the reconstitution. The most important yield of the present study that we found that this type of measurements could be carried out even with SAN with a reasonable resolution.

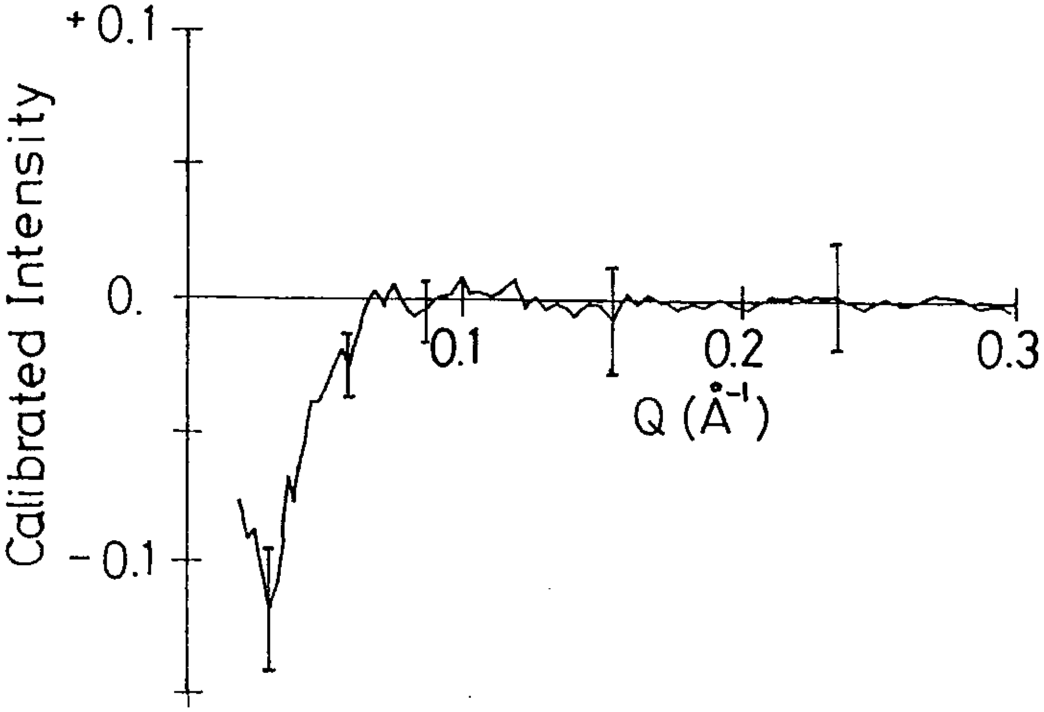

Fig. 3. The observed difference curve between the "signal" and the "noise" samples for H2B-H2B distance determination. The concentration of nucleosome core particles is 2.5 wt%. D_2O/H_2O ratio in the solution is 49%.

References

1) D.M. Engelmann and P.B. Moore : Proc. Natl. Acad. Sci. USA 69 (1972) 1997.

2) K. Hamana, K. Mita, S. Ichimura, M. Zama, K. Kaji and N. Niimura : FEBS Lett. 160 (1983) 21.

Small Angle Neutron Scattering Measurements of Rice Dwarf Virus

Hideo INOUE, Yoh SANO, Mitsuhiro HIRAI*
and Nobuo NIIMURA**

National Institute of Agrobiological Resources
Tsukuba Science City, Yatabe, Ibaraki-ken 305, Japan

*Department of Physics, and **Laboratory of Nuclear Science,
Tohoku University, Sendai, Japan

This paper reports preliminary results of the small angle neutron scattering measurements of rice dwarf virus(RDV). RDV, a member of Phytoreovirus group, is a class of icosahedral viruses, and has a genome consisting of 12 segments of double-stranded RNA all encapsidated within the same particle by seven kinds of structural proteins. Polyacrylamide gel electrophoresis gave the molecular weights of 12 RNAs and 7 proteins.1) Electron microscopic observations of negatively stained, shadowed particles showed the virus to be about 700 A in diameter with 32 capsomers of which there were 12 pentameric structural units and 20 hexameric units.2) Quasi-elastic light scattering experiments performed on RDV gave a hydrodynamic radius of about 370 A and a diffusion coefficient of 0.586×10^{-7} cm^2/s.3)

No information has been published concerning the relative positions of the protein and the RNA. We, therefore, wish to investigate the radial location of protein and RNA in RDV by small angle neutron scattering with the contrast variation method.

For neutron scattering, the virus samples (about 4 mg/ml) were dialyzed extensively against a buffer at pH 7.0 containing 0.1M Histidine-HCl and 0.01M $MgCl_2$ in H_2O/D_2O mixtures :0, 20, 68 and 100% D_2O. The deuterium oxide content was determined by density measurements.

Neutron scattering measurements were made on the instrument SAN where a sample to detector distance is 5 m and a wavelength of the incident neutron ranges between 4 and 10 A . A Q range measured was, therefore, from 0.3 x 10^{-2} to 5 x 10^{-2} A^{-1}. Neutron intensities scattered by the sample, I_{sample}, was calculated by the equation

$$I_{sample} = [\, I_{solu}/T_{solu} - I_{solv}/T_{solv}]/[I_w/T_w] \qquad (1)$$

where T is the transmission, and subscripts solu, solv, and w mean solution, solvent, and pure water, respectively. Logarithms of neutron intensities scattered by the sample were plotted against Q for four buffer systems as shown in Fig. 1. A log I - Q plot for 100% D_2O indicates 4 maxima and 4 minima, and the Q values at 4 maxima correspond to those obtained from a log I - R plot of small-angle X-ray scattering measurements on the same virus as shown in Fig. 2.[4] The same sample was measured on D11 instrument at ILL under the following conditions: a sample to detector distance 10.6 m, a wavelength 12 A, a measuring time 700 sec, RDV conc. 3.5mg/ml, 100% D_2O buffer. The result was shown in Fig. 3 as a log I - Q curve[5] which is very similar to the plot for RDV in 100% D_2O solvent in Fig. 1. The measuring time of the latter experiment was 60 min. The calculation of Patterson function and radial scattering density distribution is now proceeding.

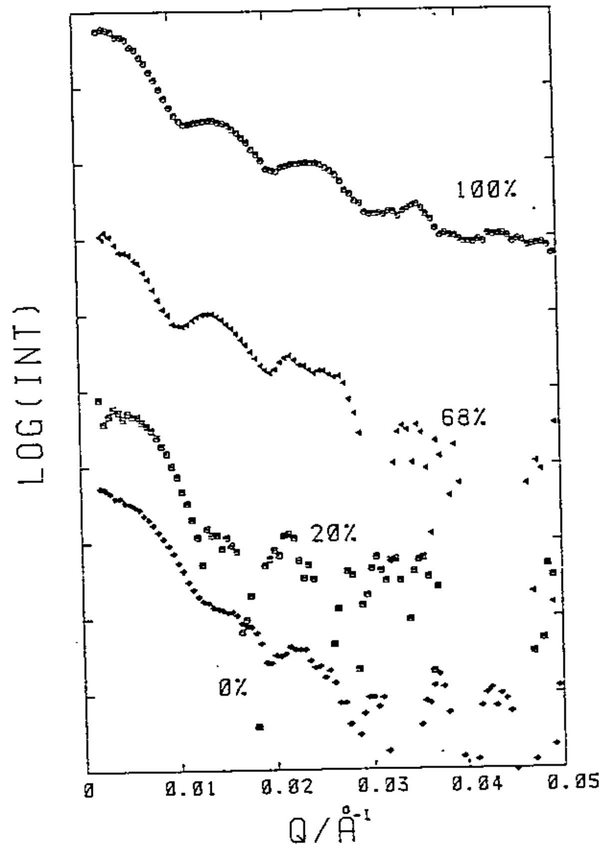

Fig. 1. Neutron scattering profiles for RDV solutions. Percentages in the figure represent D_2O contents in the solutions. The ordinate is log scale in arbitrary unit.

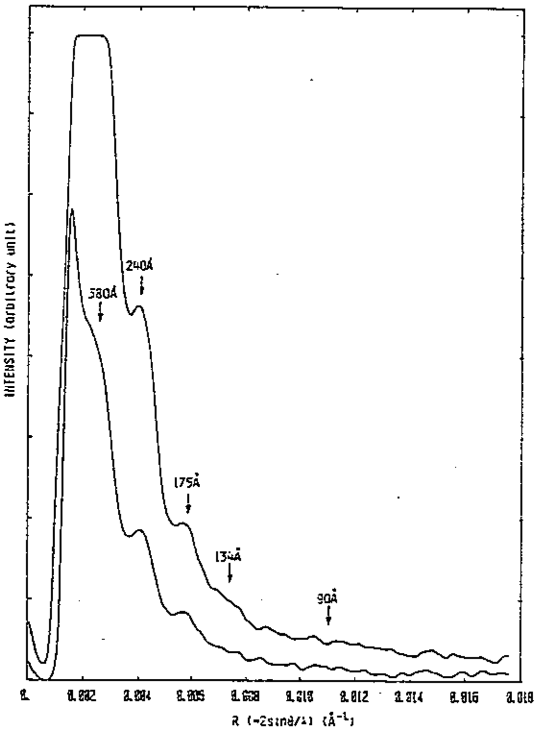

Fig. 2. X-ray small angle scattering profiles for RDV solutions.

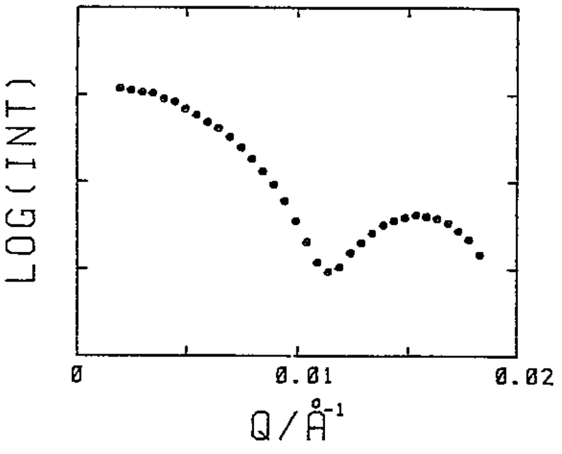

Fig. 3. Neutron scattering profile for RDV solution in 100% D_2O measured at ILL.

References

1) Reddy,D.V.R., Kimura,I. and Black,L.M.(1974) Virology,60,293-296.
2) Kimura,I. and Shikata,E.(1968)Proc. Japan Acad. 44,538-543.
3) Zulauf,M. and Inoue,H.: unpublished data.
4) Wakabayashi,K.,Mitsui,T.and Inoue,H.: unpublished data.
5) Inoue,H. and Timmins,P.A.: unpublished data.

On Integrated Intensity in TOF

H.Watanabe, K.Ohsumi, I.Kawada*, M.Isobe*, F.P.Okamura* and H.Horiuchi**

Mineralogical Institute, Faculty of Science, University of Tokyo,
Hongo, Tokyo 113
*National Institute for Research in Inorganic Materials,
Sakura-mura, Niihari-gun, Ibaraki 305
**Institute of scientific and Industrial Research, Yamadakami,
Suita, Osaka 565

The integrated intensity of a Bragg peak in TOF is given by the summation of the numbers of neutrons over the peak range devided by those of incident neutrons concerning to the reflexion. Considering exact Bragg case, we can write it as

$$I_{int} = \frac{\Sigma\ I_{obs}}{I(\lambda)}\ , \tag{1}$$

where Σ means summation over the peak range and $I(\lambda)$ is the number of neutrons with wavelength λ.

The $I(\lambda)$ is not observed directly. We know only the number of incident neutrons observed between time elapsed t and $t+dt$, denoting $C(t)\ dt$. But we can deduce $I(\lambda)$ by $C(t)\ dt$, as follows.

In general, $C(t)$ can be expressed as the convolution of the burst function $f(\lambda,t)$ and some function $g(t)$, i.e.

$$C(t) = \int_0^t f(\lambda,t-r)\ g(r)\ dr \equiv \int_0^t K(t,r)\ g(r)\ dr\ . \tag{2}$$

And then $I(\lambda)$ is given by

$$I(\lambda) = g(t_\lambda) \int_0^\infty f(\lambda,t')\ dt'\ , \tag{3}$$

where t_λ is the time elapsed when the λ-neutrons should be observed and t' means the time elapsed from the time when the first λ-neutron is observed.

Eq. (2) is Volterra's 1-st integral equation with the kernel $K(t,r)$. If $K(t,t) \neq 0$, differentiating each side of eq. (2), we get Volterra's 2-nd integral equation,

$$g(t) = \frac{1}{K(t,t)}\ \frac{dC(t)}{dt} - \int_0^t \frac{1}{K(t,t)}\ \frac{\partial K(t,r)}{\partial t}\ g(r)\ dr\ . \tag{4}$$

The solution of eq. (4) is given by

$$g(t) = \frac{1}{K(t,t)}\ \frac{dC(t)}{dt} + \sum_{n=1}^{\infty}(-1)^n \int_0^t K_n(t,r)\ \frac{dC(t)}{dt}\ dr\ , \tag{5}$$

with

$$K_1 \equiv \frac{1}{K(t,t)} \frac{\partial K(t,r)}{\partial t} ,$$

$$K_2 \equiv \int_r^t K_1(t,s)\ K_1(s,r)\ ds ,$$

$$K_3 \equiv \int_r^t K_1(t,s)\ K_2(s,r)\ ds ,$$

$$\vdots$$

$$K_n \equiv \int_r^t K_1(t,s)\ K_{n-1}(s,r)\ ds .$$

By eq. (1) with eq. (5) and (3), we can get proper integrated intensity.

For the simplest example, we carry out the calculation to obtain I(λ) when the burst function is given as $f(\lambda,t) = e^{-\alpha t'}$.

Then eq. (2) is rewritten as

$$C(t) = \int_0^t e^{-\alpha(t-r)}\ g(r)\ dr,$$

and then

$$\frac{dC(t)}{dt} = \int_0^t \frac{\partial e^{-\alpha(t-r)}}{\partial t}\ g(r)\ dr + g(t) = -\alpha C(t) + g(t) .$$

Therefore

$$g(t) = \alpha C(t) + \frac{dC(t)}{dt} .$$

Actually, we know that $\alpha C(t) >> \frac{dC(t)}{dt}$, thus

$$g(t) \simeq \alpha C(t) . \tag{6}$$

Therefore we get I(λ), by eq. (3) with (6), as

$$I(\lambda) = \int_0^\infty g(t_\lambda)\ e^{-\alpha t'} dt' = \alpha C(t_\lambda) \int_0^\infty e^{-\alpha t'} dt' = C(t_\lambda) .$$

and eq. (1) should be rewritten as

$$I_{int} = \frac{\Sigma\ I_{obs}}{C(t_\lambda)} .$$

This can be so read that the integrated intensity is given by the summation over the peak range devided by the number of counts of incident neutrons corresponding to the Bragg peak, t_λ. This t_λ should be employed for other corrections, Lorentz factor for example.

In this work, only the simplest burst function was employed. But actual one is more complicated. Further calculation of eq. (5) is required to obtain more precise integrated intensity.

We thank Prof. Tokonami for his stimulating discussion and Dr. Niimura for his cordial advice.

Structure Refinements of Nd-Ga-Garnet, Spinel and Li_3N (400°C) by Neutron TOF Method

I. Kawada, M. Isobe, F. P. Okamura, F. Izumi, H. Watanabe*, K. Ohsumi*,
H. Miyatake** and H. Horiuchi***

National Institute for Research in Inorganic Materials,
1-1 Namiki, Sakura-mura, Niihari-gun, Ibaraki 305, Japan
* Mineralogical Institute, Faculty of Science, University of Tokyo,
Hongo, Tokyo 113, Japan
** Department of Applied Physics, Faculty of Engineering,
Nagoya University, Chikusa-ku, Nagoya 464, Japan
*** Institute of Scientific and Industrial Research, Osaka University,
Mihogaoka, Ibaraki, Osaka 567, Japan

For the attempt to the structure analysis using diffraction intensities through the TOF method at the pulsed neutron source (KENS), a number of experiments were undertaken on the four-circle single crystal diffractometer (FOX). In the present paper three of these are reported.

Scattering angle was set at $2\theta = 90°$ and the intensity data in the wave length range of 0.4 – 6.2 Å were collected with a ^{3}He counter.

At one exposure, one dimensional data of a zone of reciprocal lattice points can be measured. After sufficient measurements of different zones, the data from each zone were combined and scaled so as to build a set of three dimensional data.

From the intensity data of each hkl reflection (I(hkl)), structure factor (|Fo(hkl)|) is obtained from the equation (1).

$$I(hkl) = k \cdot i(\lambda) \cdot \lambda^4/(2\sin^2\theta) \cdot |Fo(hkl)|^2 \cdot A(\lambda,\theta) \cdot Y(\lambda,\theta) \qquad (1)$$

where k: scale factor, $i(\lambda)$: intensity distribution of incident neutron beam, $\lambda^4/(2\sin^2\theta)$: Lorentz factor, $A(\lambda,\theta)$: absorption factor and $Y(\lambda,\theta)$: extinction factor.

In the structure refinements, least squares method was applied by refining scale factor, positional parameters which are not constrained by the symmetry, and thermal parameters. The results are shown in Table 1.

1. Nd-Ga-Garnet ($Nd_3Ga_5O_{12}$)

In order to refine positional parameters of oxygen atom, the experiment was undertaken. $Nd_3Ga_5O_{12}$ is cubic, a = 12.506 Å, space group is Ia3d. The sample was shaped to a sphere of diameter of 0.38 cm.

Thermal parameters of Nd and Ga were refined as isotropic (assuming $U_{ii}(Ga(1))=U_{ii}(Ga(2))$), whereas those of oxygen are anisotropic. After several cycles of least squares refinements, reliability factor (R) was reduced to R = 0.029 with 44 independent reflection data.

2. Spinel ($MgAl_2O_4$)

In order to know the distribution of cations, the experiment was undertaken. $MgAl_2O_4$ is cubic, a = 8.083 Å, space group is Fd3m. The sample was shaped to a sphere of diameter of 0.51 cm.

All thermal parameters were refined as anisotropic. R was reduced to 0.037 with 42 independent reflection data.

3. Li_3N (400°C)

In order to investigate the thermal behavior of Li atoms, the experiment was undertaken. Li_3N is hexagonal, a = 3.698 Å, c = 3.888 Å, space group is P6/mmm. The sample was shaped to a sphere of diameter of 0.40 cm.

All thermal parameters were refined as anisotropic. R was reduced to 0.075 with 21 independent reflection data.

Table 1. Atomic coordinates and thermal parameters (x 10^4)

Thermal parameters are expressed as

$$\exp[-2\pi^2(h^2a^{*2}U_{11}+ k^2b^{*2}U_{22}+ l^2c^{*2}U_{33}+ hka^*b^*U_{12}+ hla^*c^*U_{13}+ klb^*c^*U_{23})]$$

(a) Nd-Ga-Garnet ($Nd_3Ga_5O_{12}$)

	x	y	z	U_{11}	U_{22}	U_{33}	U_{12}	U_{13}	U_{23}
Nd	1250	0	2500	26(10)	26(10)	26(10)	0	0	0
Ga(1)	0	0	0	39(6)	39(6)	39(6)	0	0	0
Ga(2)	3750	0	2500	39(6)	39(6)	39(6)	0	0	0
O	-305(3)	529(3)	1483(5)	113(27)	68(10)	47(14)	-11(10)	42(14)	-31(10)

(b) Spinel ($MgAl_2O_4$)

	x	y	z	U_{11}	U_{22}	U_{33}	U_{12}	U_{13}	U_{23}
Mg	0	0	0	46(5)	46(5)	46(5)	0	0	0
Al	6250	6250	6250	33(4)	33(4)	33(4)	-1(3)	-1(3)	-1(3)
O	3874(2)	3874(2)	3874(2)	66(4)	66(4)	66(4)	-2(3)	-2(3)	-2(3)

(c) Li_3N (400°C)

	x	y	z	U_{11}	U_{22}	U_{33}	U_{12}	U_{13}	U_{23}
Li(1)	0	0	5000	131(162)	131(162)	434(167)	66(81)	0	0
Li(2)	3333	6666	0	367(92)	367(92)	486(159)	184(46)	0	0
N	0	0	0	223(60)	223(60)	372(66)	112(30)	0	0

A Study of Thermal Vibrations in $KMnF_3$ by TOF Neutron Diffraction

H. Miyatake, M. Sakata, J. Harada, M. Isobe*, I. Kawada* and N. Niimura**

Department of Applied Physics, Faculty of Engineering,
Nagoya University, Chikusa-ku, Nagoya 464, Japan
* National Institute for Research in Inorganic Materials,
1-1 Namiki, Sakura-mura, Niihari-gun, Ibaraki 305, Japan
** Laboratory of Nuclear Science, Faculty of Science, Tohoku University,
Mikamine, Sendai 982, Japan

The thermal vibrations in $KMnF_3$ were investigated by the single crystal TOF neutron diffraction technique. The measurements were performed on the [100], [110] and [111] directions in the reciprocal space at room temperature, and 62 integrated Bragg intensities were obtained at the scattering angles of $2\theta = 60°, 75°, 90°, 120°$ and $162.8°$ on the four-circle single crystal diffractometer (FOX) installed at KENS. The maximum scattering vector observed was 13.5 $Å^{-1}$.

In this experiment, one dimensional data through the origin in the reciprocal space were measured simultaneously. In such a case, it is likely that observed peaks overlap each other. For this reason, the profile analysis method, which was usually used for the powder diffraction pattern, was applied to this study to estimate integrated Bragg intensities of overlapped peaks. The observed and calculated values in the profile analysis of (500), (600) and (700) reflections at $2\theta = 162.8°$ are shown in Fig. 1 as an example. The observed and calculated intensities of each channel show an excellent agreement and the estimated integrated intensity by this method also agrees with the simple sum of each channel intensity over the peak within a statistical error. In the further analysis, therefore, the latter was used as the observed integrated Bragg intensities.

The measured intensities were corrected for absorption and thermal diffuse scattering (TDS), and analyzed by least squares to refine a scale factor, thermal parameters and an extinction parameter. For the extinction correction both of the newly developed Kawamura & Kato$^{1)}$ (K & K) and the widely used Becker & Coppens$^{2)}$ (B & C) theories were examined. 6 reflections for which the K & K theory was not appropriate were eliminated in the analysis.

The results obtained by both theories are listed in Table 1. In this analysis, we assumed that the thermal vibrations of all atoms were harmonic. Hence the temperature factors of K and Mn atoms are isotropic, and those of F atoms are anisotropic. Table 1 shows that both theories are not strictly identical and that the significant difference is seen on the value of B_{33}(F). The K & K theory is based on a rigorous treatment of the fundamental equation, while the B & C theory contains some assumptions of which validity is not known.

These facts suggest that it would not be appropriate to use the B & C theory for extinction corrections in the analysis of TOF neutron diffraction data. It is understood from the Table 1 that thermal vibrations of F atoms are extremely anisotropic and that B_{11}(F) and B(K) are anomalously large, while B_{33}(F) and B(Mn) are quite normal. These characteristics resemble to those of $CsPbCl_3$ 3), of which thermal vibrations are interpreted in connection with its structural phase transition.

References

1) Kawamura, T. & Kato, N., Acta Cryst. A39 (1983) 305
2) Becker, P. J. & Coppens, P., Acta Cryst. A30 (1974) 129
3) Sakata, M., Harada, J., Cooper, M. J. & Rouse, K. D., Acta Cryst. A36 (1980) 7

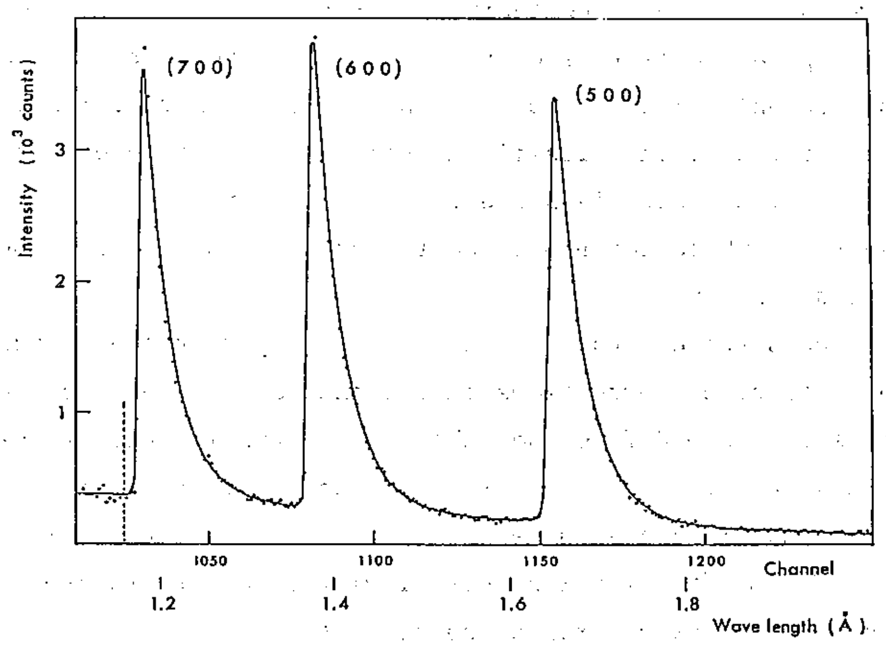

Fig. 1. TOF spectrum of $KMnF_3$ at scattering angle of 162.8°. The points represent observed intensities, and calculated values are shown by a solid curve. The channel width is changed at the broken line.

	K & K	B & C
B(K) (A^2)	1.52±0.06	1.52±0.06
B(Mn)	0.49±0.03	0.50±0.03
B_{11}(F)	2.66±0.03	2.70±0.04
B_{33}(F)	0.68±0.04	0.80±0.05
Scale($\times10^{-1}$)	6.52±0.10	7.24±0.19
C_E ($\times10^{-4}$)	7.45±0.14	16.7±0.9
R (%)	3.47	3.39
wR	4.93	5.07

C_E : Extinction parameter

Table 1. Thermal parameters obtained by using the Kawamura & Kato (K & K), and the Becker & Coppens (B & C) theory for extinction corrections.

Construction of High Resolution Powder Diffractometer (HRP)

N. Watanabe, H. Asano[*], H. Iwasa[**], S. Sato, H. Murata[*],
T. Fukiura[*], S. Tomiyoshi[***], F. Izumi[****] and K. Inoue[**]

National Laboratory for High Energy Physics
Oho-machi, Tsukuba-gun, Ibaraki-ken 305, Japan

[*]Institute of Materials Science, University of Tsukuba
Sakura-mura, Niihari-gun, Ibaraki-ken 305, Japan

[**]Department of Nuclear Engineering, Hokkaido University
Sapporo 060, Japan

[***]The Research Institute for Iron, Steel and Other Metals
Tohoku University, Sendai 980, Japan

[****]National Institute for Research in Inorganic Materials
Sakura-mura, Niihari-gun, Ibaraki-ken 305, Japan

It has been well known for years that high resolution powder diffraction is one of the most promising field of research using pulsed spallation neutron sources. In this application we can take full advantages of the KENS source; low repetition rate of 20 Hz, and narrow pulses of thermal and epithermal neutrons from a solid methane moderator at 20 K. The former characteristic enlarges an accessible range of d-space, and the latter makes a high resolution work possible without sacrificing the neutron intensity in contrast with the case of poisoned moderators.

The experimental halls of the KENS facility are originally designed such that the extension of the C4 beam line, which views the solid methane moderator, is possible for a high resolution powder diffractometer. At the C4 beam hole, however, there exists a quasielastic spectrometer LAM-40 which is already working. Therefore we planned to use the transmitted beam through the LAM-40. We constructed a long flight path penetrating the wall of the main experimental hall and installed a high resolution powder diffractometer, HRP, as shown in Fig. 1. The flight path length between source and sample is about 19 m. A beam stop is located out of the cold neutron experimental hall.

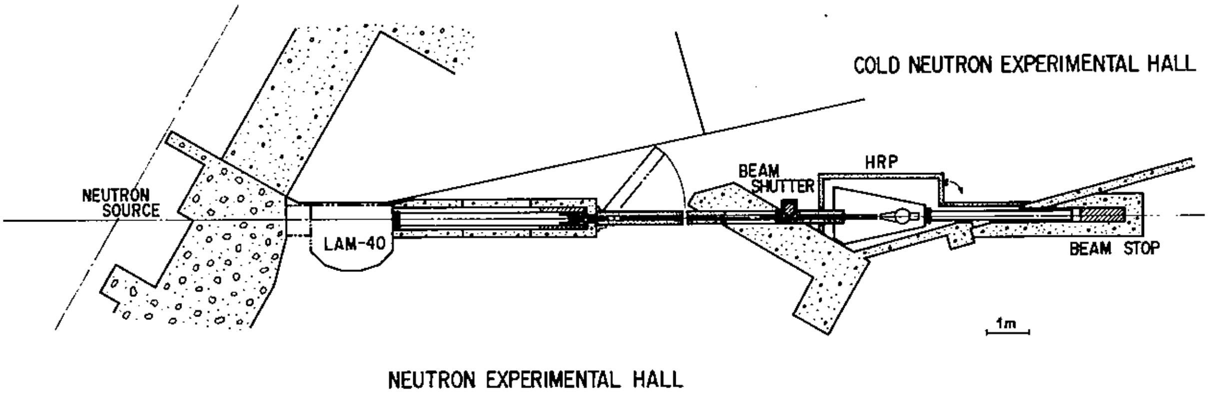

Fig. 1. Location of HRP.

The resolution of a TOF powder diffractometer is, as well known, simply expressed as

$$\Delta d/d = [(\Delta t/t)^2 + (\cot\Theta \cdot \Delta\Theta)^2 + (\Delta L/L)^2]^{1/2}.$$

Here, Δt is uncertainty in time-of-flight t mainly due to the finite pulse width of neutrons from the moderator Δt_z. KENS solid methane "grooved" moderator gives Δt_z as shown in Fig. 2. Below $\lambda \sim 2$ A (dashed line part) it becomes $\Delta t_z \sim 7\lambda(A)$ μs. Then the first term of the bracket is written as

$$\Delta t/t \sim \Delta t_z/t \sim 7\lambda \,/[250\ L(m)\ \lambda] = 2.8 \times 10^{-2} \,/\, L(m).$$

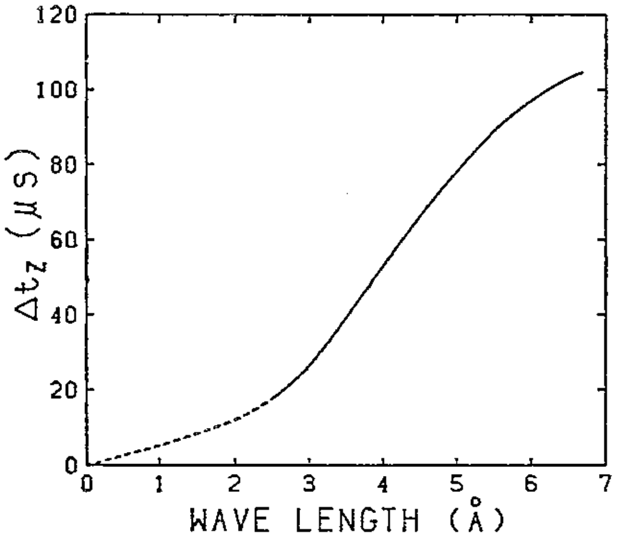

Fig. 2.
Wavelength dependence of the neutron pulse width from the grooved solid methane moderator at 20 k.

For $L = 19$ m, we have $\Delta t/t \sim 1.5 \times 10^{-3}$. $\Delta\Theta$ is uncertainty of Bragg angle Θ, which is approximately one half of the collimation α between sample and detector. If we adopt a cylindrical sample and a detector of 1" in diameter and a scattered flight path length $L_2 = 1$ m, and a semi-backward scattering at $2\Theta \sim 170^{\circ}$, then we have

$$\Delta\Theta \sim \alpha/2 = 2.54/100/2 = 1.27 \times 10^{-2},$$
$$\cot\Theta \cdot \Delta\Theta = 1.1 \times 10^{-3}.$$

Second term in the bracket is much smaller than the first term. ΔL is ambiguity in flight path length L mainly due to finite thickness of sample and detector. A good guess for this quantity will be $\sqrt{2}$ (diameter of sample or detector), and then we have $\Delta L/L \sim \sqrt{2}\,(2.54)/2000 = 1.8 \times 10^{-3}$. In total, we can expect an overall resolution $\Delta d/d \sim 2.6 \times 10^{-3}$.

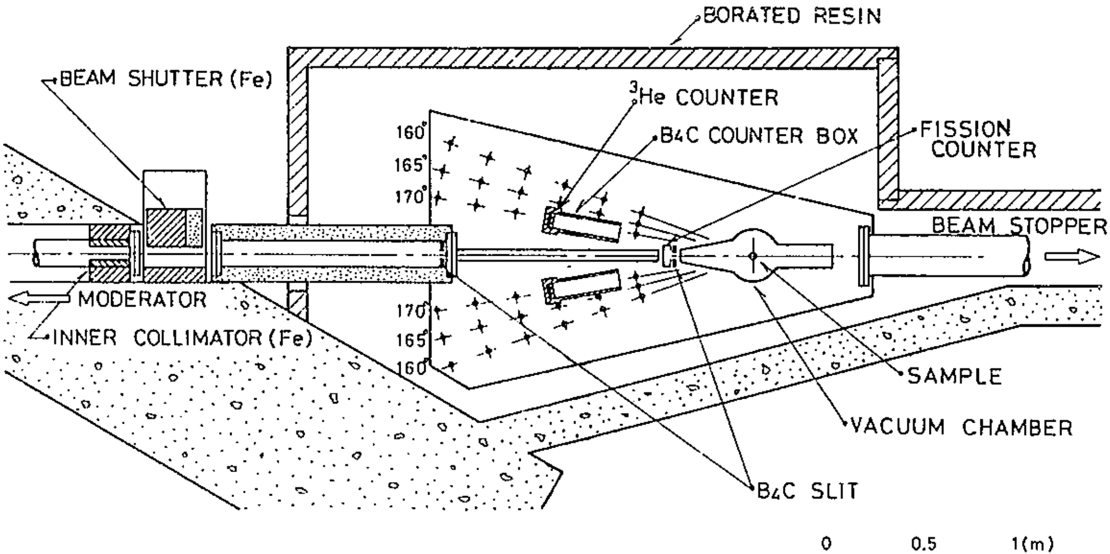

Fig. 3. Layout of HRP.

Figure 3 shows a layout of the HRP. For a moment the diffractometer has two counter banks in both wings, each of which contains three He-3 proportional counters, 1" in diam., filled to 7600 mm Hg. The shielding box for the counter bank consists of B_4C resin (B_4C content about 90 %), of which inner surface is lined by Cd sheets. It is possible to chose any L and 2Θ in stepwise as depicted in the figure. Typical set is $L_2 = 0.8$ or 1 m, with $2\Theta \sim 170^{\circ}$. Neutron wavelength up to 10 A is avairable, because the repetition rate is 20 Hz and the total flight path length is about 20 m. No soller slit is used between sample and detector. The instrument is equipped with a vacuum scattering chamber, made of alminum, which has thin alminum windows for direct and scattered beams. The vacuum is good enough for cryogenic use. Neutron signal from each counter is stored in a 16 k x 4 channel time analyzer of CAMAC module, and the data are handled by a micro computer and finally analyzed by a central computer at KEK via terminals at the data taking room. As a beam monitor a fission counter is used which is located just in front of the final incident collimator. Not only the beam intensity but also the spectrum of the incident beam are very important in this diffractometer, because the spectrum is sensitive to the temperature change in the solid methane moderator and to a sample at the LAM-40. The fission counter does not give a correct spectrum, but it is sufficient for data analysis to know the relative changes of the stored spectra for sample run and cell run to that for the vanadium stantard run.

Operation of HRP began at the end of 1983 and performance of the spectrometer was tested by using standard samples of Al_2O_3 and Si. Crystallographic studies of Ta_2D, Bi_2O_3 and $CrTi_2Se_4$ have also been made in conjunction with the establishment of Rietveld profile analysis. The details are described in subsequent papers.

Performance of High Resolution Powder Diffractometer (HRP)

N. Watanabe, H. Asano[*], H. Iwasa[**], S. Sato, H. Murata[*],
T. Fukiura[*], S. Tomiyoshi[***], F. Izumi[****] and K. Inoue[**]

National Laboratory for High Energy Physics
Oho-machi, Tsukuba-gun, Ibaraki-ken 305, Japan

[*]Institute of Materials Science, University of Tsukuba
Sakura-mura, Niihari-gun, Ibaraki-ken 305, Japan

[**]Department of Nuclear Engineering, Hokkaido University
Sapporo 060, Japan

[***]The Research Institute for Iron, Steel and Other Metals
Tohoku University, Sendai 980, Japan

[****]National Institute for Research in Inorganic Materials
Sakura-mura, Niihari-gun, Ibaraki-ken 305, Japan

Present paper reports a preliminary performance of high resolution powder diffractometer HRP.

Figure 1 shows a TOF diffraction pattern obtained from Al_2O_3 powder sample at room temperature. This is raw data including background, obtained only by two counters at $2\Theta = 170.0^{\circ}$. Measuring time was about 40 hours for the sample volume 3 cm^W x 5 cm^H x 1 cm^T. The sample was contained in a aluminum cell with thin windows made of single crystal Si wafer to avoid unwanted reflections from the cell. Background level is surprisingly low and the diffraction pattern is almost flat over a wide range of λ in contrast with the case of a room temperature moderator. The feature is easily understood as following. Thermal Maxwellian region in a room temperature moderator corresponds to the 1/E region in the solid methane moderator and this region is just important for powder diffractometry. At the Maxwellian region of the solid methane moderator, the overlap of successive diffraction peaks is scarce due to a sufficient separation of d spacings.

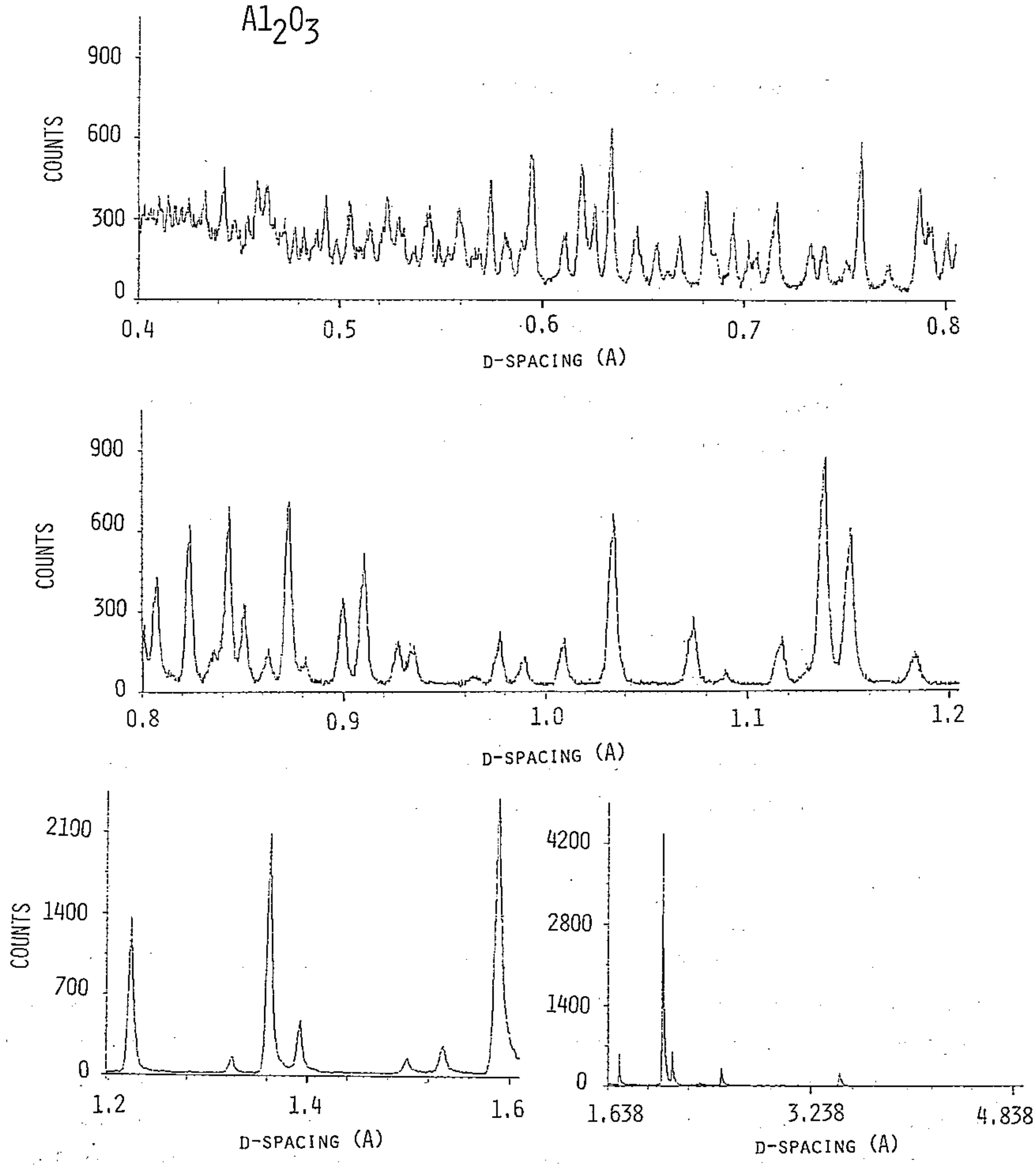

Fig. 1. Raw diffraction pattern of Al_2O_3 obtained by HRP.

Preliminary Rietveld refinement was performed and the result in the range d = 50 ∿ 100 pm is shown in Fig. 2, where the background is subtracted. In order to demonstrate the performance of the HRP, the result is compared in the same d-range with that (Fig.3) obtained by the General Purpose Powder Diffractometer (GPPD), one of the world highest resolution diffractometer, at the pulsed spallation neutron source IPNS, Argonne National Laboratory.

Resolution of the HRP seems to be comparable to that of the GPPD. Nominal resolution of the GPPD is about 0.3 %, and therefore the effective resolution of the HRP would also be about 0.3 %. However, a direct comparison is not easy; typical peak shape of the HRP is rather symmetric in the thermal neutron region (1/E region), while that of the GPPD is asymmetric with the exponentially decaying tail, due to the difference in moderator characteristics. A grooved surface moderator gives the neutron pulse with faster falling time, but with broader FWHM (full width at half maximum) than a flat moderator. Therefore, the separation of the successive peaks becomes better in the former case, if the FWHM value is the same. In the range above 2.5 A, the neutron pulse width from the moderator becomes gradually broader than the value given by $7\lambda(A)$ μs, and approaches to the value in the Maxwellian equilibrium, as shown in Fig. 2 of the preceding paper. Consequently, the resolution approaches to about 0.5 % at large λ range.

Counting rate per counter at the HRP is about one half of the corresponding value at the GPPD. Note that the proton beam current at present KENS is about 1.5 μA, while that of IPNS is about 10 μA.

An off-line computer focussing has been tried to obtain better statistics. Three independent data from three counters at slightly different angles around $2\Theta = 170^{\circ}$ were combined according to the similar equation given by Jorgensen and Faber.1) The result shows that no significant peak broadening or change in peak shape is introduced by the focussing process, if the channel width of the original data is reasonably narrow. Details will be discussed elswhere.

The Rietveld refinement method has been applied. We encountered two difficulties. The first problem is that the diffraction data cover a wide range of λ-space from about 0.5 A up to 10 A, extending from 1/E region ($\lambda \lesssim$ 2.5 A) to cold Maxwellian region ($\lambda \gtrsim$ 4 A) via transition region ($2.5 \lesssim \lambda \lesssim$ 4 A). Accordingly, characteristic parameters of the burst shape of neutrons vary drastically depending on the regions and no unique set of parameters can cover the entire λ-range. A preliminary Rietveld refinement is, therefore, performed dividing the total region into three, with reasonable overlap with each other. The second problem is the special shape of the neutron pulse from the grooved surface moderator. A small front porch necessitates additional parameters to describe the burst function. At a moment, the additional component is ignored in the present data analysis because it is not so significant. Some improvements in the refinement method are in progress to overcome these difficulties.

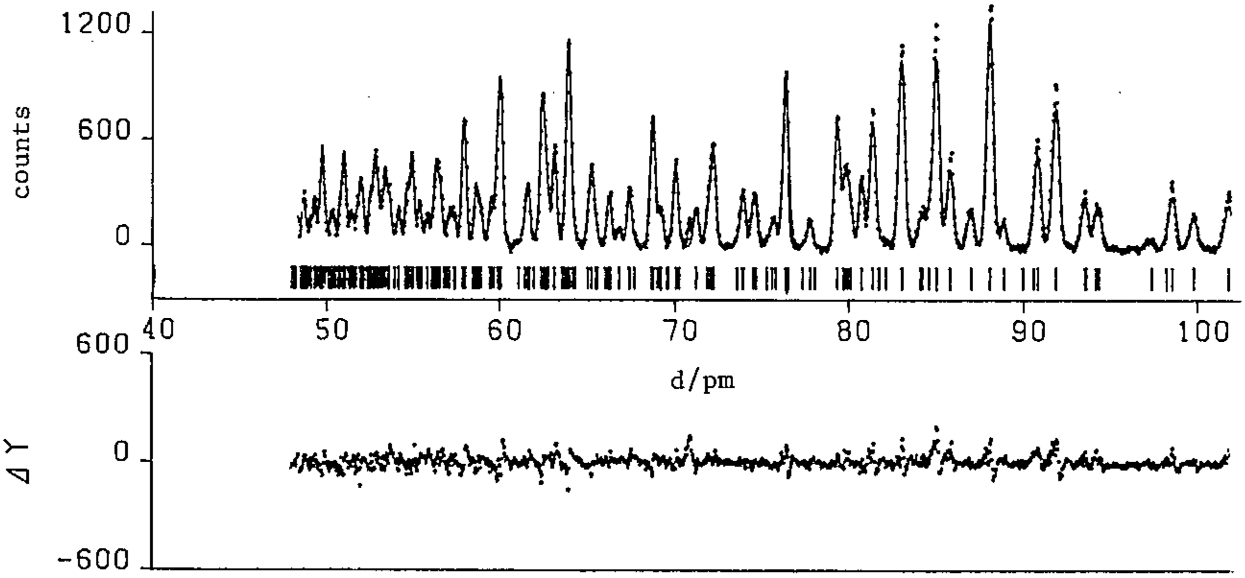

Fig. 2. A part of diffraction pattern of Al_2O_3 taken by HRP. The solid line is the Rietveld profile.

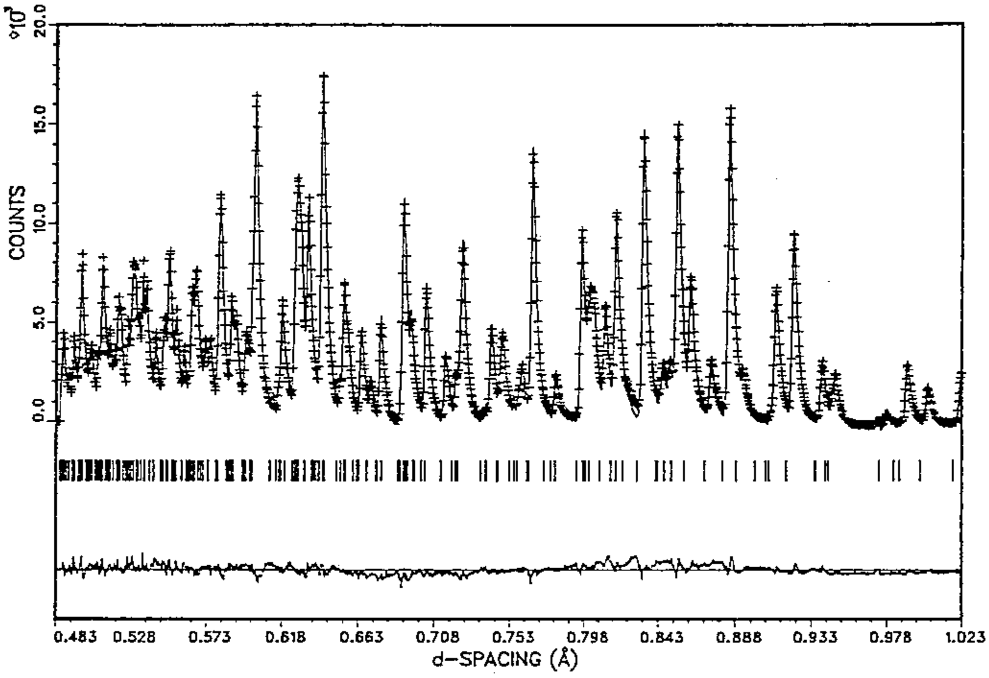

Fig. 3. A part of diffraction pattern of Al_2O_3 taken by GPPD. The solid line is the Rietveld profile.

References

1) J. D. Jorgensen and J. Faber, Electronically Focused Powder Diffractometer at IPNS-I, Proc. 6th Meeting of the International Collaboration on Advanced Neutron Sources (Argonne, June 28-July 2, 1982), ANL-82-80 (1982) 105.

Medium-Resolution Powder Diffractometer (MRP)

Hajime ASANO, Takeshi FUKIURA, Hideaki MURATA, Hirokatsu IWASA*,
Shoichi TOMIYOSHI**, Fujio IZUMI$^+$, Setsuo SATO^{++} and Noboru WATANABE^{++}

Institute of Materials Science, University of Tsukuba
Sakura-mura, Niihari-gun, Ibaraki 305, Japan

* Department of Nuclear Engineering, Hokkaido University
Sapporo 060, Japan

**The Research Institute for Iron, Steel and Other Metals
Tohoku University, Sendai 980, Japan

$^+$ National Institute for Research in Inorganic Materials
Sakura-mura, Niihari-gun, Ibaraki 305, Japan

$^{++}$National Laboratory for High Energy Physics, Oho-machi
Tsukuba-gun, Ibaraki 305, Japan

A spectrometer for powder neutron diffraction with a resolution $\Delta d/d \sim 2$ % was constructed at the H4 beam port viewing a room-temperature polyethylene moderator. A layout of the spectrometer is displayed in Fig. 1. Pulsed white neutrons generated at the moderator run through a flight tube of 6.35 m and hit the sample. Scattered neutrons from the sample are detected by a ^{3}He counter located at a fixed scattering angle of $2\theta = 150°$, 90°, 45°, 30° or 15°. Wavelength of scattered neutrons is analyzed by the time of flight from the moderator to the detecter, and thus the lattice spacing d is determined from the Bragg relation $2d\sin\theta = \lambda$. Incident and transmitted neutron paths as well as a sample chamber are evacuated to avoid unwanted air scattering. The incident neutron flux is monitored by a fission counter just outside the biological shield. A beam size on the sample position is restricted to $15^W \times 50^H$ mm^2 by two B_4C slits near the fission counter and in front of the sample chamber. A sample holder[#] (10 mm $\phi \times 60$ mm long) is made of a vanadium foil of 25 μm thick. The sample

---

[#] Sample holders were kindly provided by Dr. T. Fukunaga.

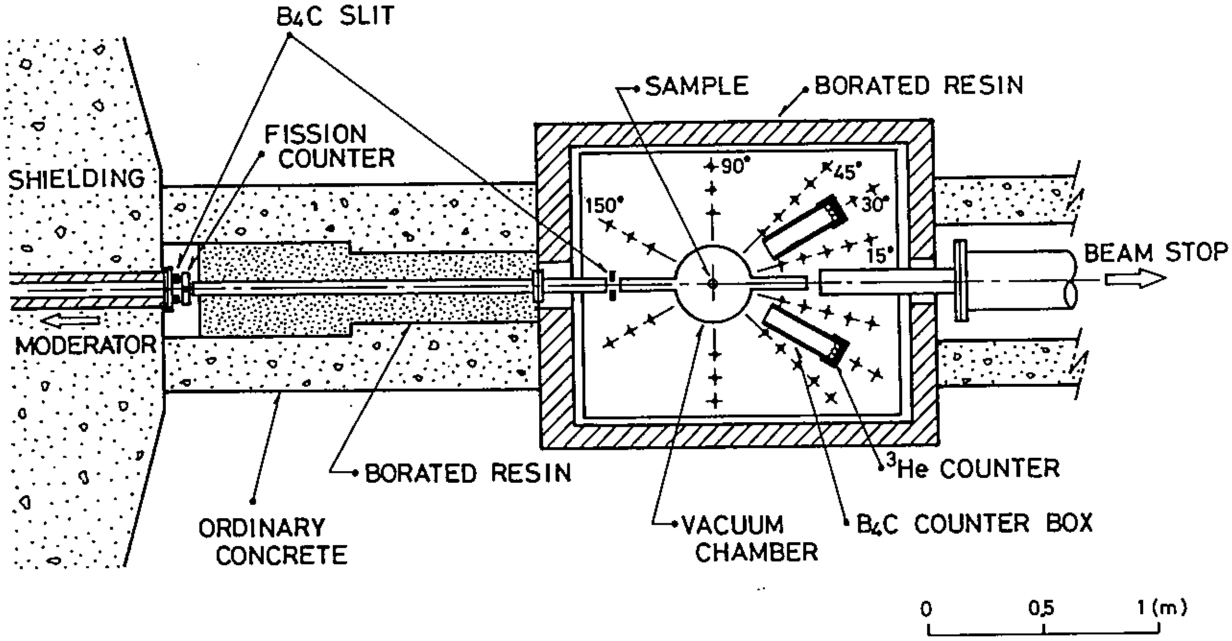

Fig. 1 Layout of MRP

can be cooled down to 30 K using a Cryo-Mini or heated by a heating element connected to the sample holder. A B_4C counter box lined with thin cadmium sheet can contain three ^{3}He gas counters of 1" in diameter and 12" in length, which is placed at desired scattering angles and flight paths of L_2 = 50, 60 and 70 cm. Signals from the counter are passed through a pre-amprifier and a main amprifier, fed to a time analyser unit and stored in a micro-computer NEC PC 9801. Time focussing of data from three counters in a counter box is carried out in a computer by adjusting apropriately the TOF scales.

Figure 2 shows a diffraction pattern of Si at room temperature. The scattering angle 2θ = 150° and L_2 = 50 cm, and the time of measurements is 20 hours. We see a number of reflections 111, 220, 311 and so on from the right to the left (Bragg positions are marked by bars in the abscissa). The present result represents raw data minus background of the Maxwellian flux distribution. The solid line in the figure is a result of Rietveld analysis which is described in detail elsewhere$^{1)}$. The agreement between the experiment and the fitting curve is excellent. In Fig. 3 is shown a normalized diffraction pattern, where the raw data are devided by the incident neutron spectrum $i(\lambda)$. It is natural that the lower index reflections become intense by the normalization.

Resolution of the total scattering spectrometer is given as

$$\Delta d/d = \{(\Delta t/t)^2 + (\Delta L/L)^2 + (\cot\theta\Delta\theta)^2\}^{1/2},$$

where Δt, ΔL and $\Delta\theta$ represent time, distance and angular uncertainties, respectively. The second and third terms are independent of λ and are estimated as $\Delta L/L$ = 0.3 % and $\cot\theta\Delta\theta$ = 0.5 % at 2θ = 150°, which are small compared to the first term. The main component of the first term comes from the finite pulse width of the neutron burst at the moderator. $\Delta t/t$ is as large as 1.3 % in the range of λ = 1.2 ∼ 2 Å (d = 0.6 ∼ 1 Å) and gradually decreases in both sides of λ. Accordingly, the time resolution is limiting overall resolution of the diffractometer in the case of 2θ = 150°.

Figures 2 and 3 demonstrate that performance of the spectrometer is satisfactory in the conventional use. As is noticed in Fig. 2, however, counting rate of the low-index peak is insufficient because of the poor flux at long wavelength ranges from the room temperature moderator. Crystallographic studies of chemical or magnetic superstructures need accurate intensity measurements on the reflections with long d spacing. Low angle counters are used for this purpose. Figure 4 shows a result on Si using a 30° counter. In comparison with Fig. 2 low-index

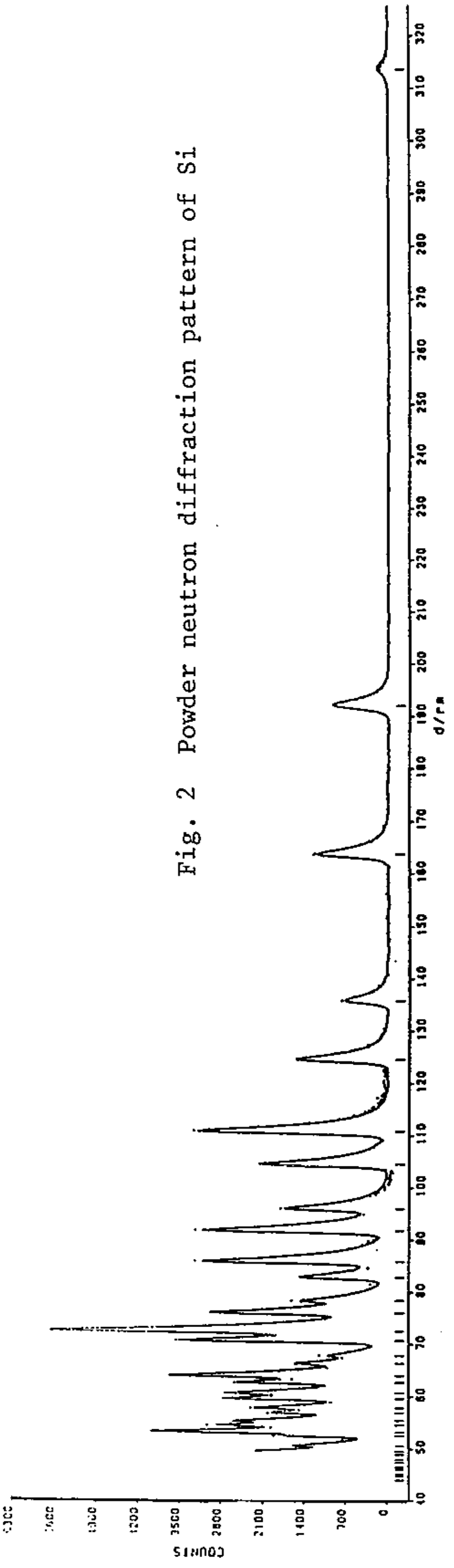

Fig. 2 Powder neutron diffraction pattern of Si

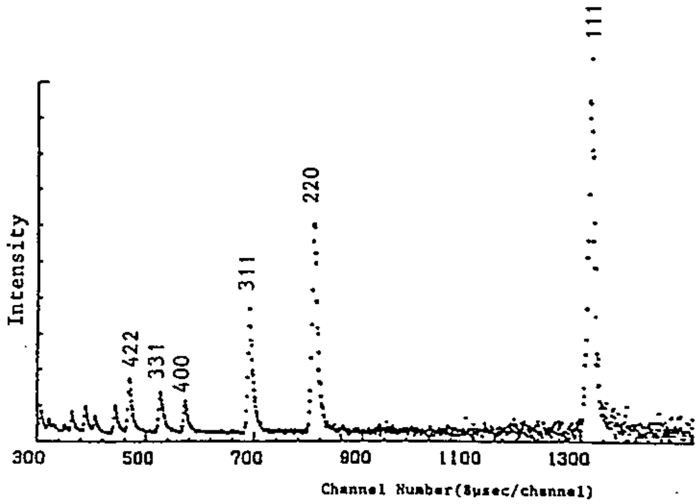

Fig. 3 Normalized diffraction pattern of Si

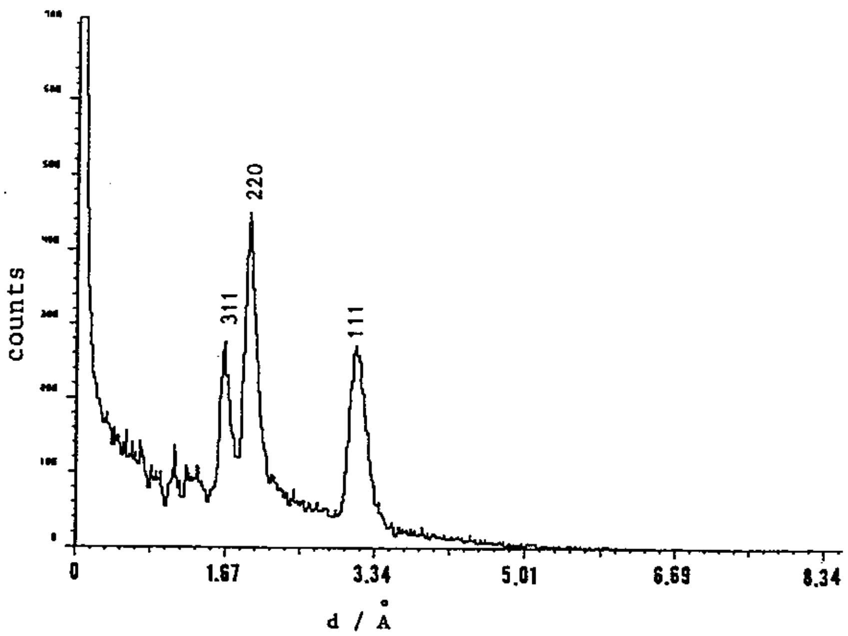

Fig. 4 Raw diffraction data of Si, 2θ = 30° and L_2 = 70 cm

reflections 111, 220 and 311 are enhanced, while reflections with higher indices are not well identified due to the poor resolution. In the geometry of 2θ = 30°, contribution of the angular resolution is dominant and $\cot\theta\Delta\theta$ reaches to 4.7 % owing to the factor $\cot\theta$. It is under examination to overcome this problem, for instance by using a Soller collimator.

References

1) F. Izumi, H. Asano, H. Murata, T. Fukiura, H. Iwasa, S. Tomiyoshi, S. Sato and N. Watanabe, Rietveld Analysis with TOF Neutron Powder Diffraction Data Taken on the MRP and HRP, in this volume.

Rietveld Analysis with TOF Neutron Powder Diffraction Data Taken on the MRP and HRP

Fujio IZUMI, Hajime ASANO*, Hideaki MURATA*, Takeshi FUKIURA*,
Hirokatsu IWASA**, Shoichi TOMIYOSHI+, Setsuo SATO++, and Noboru WATANABE++

National Institute for Research in Inorganic Materials
Sakura-mura, Niihari-gun, Ibaraki 305, Japan

* Institute of Materials Science, University of Tsukuba
Sakura-mura, Niihari-gun, Ibaraki 305, Japan

** Department of Nuclear Engineering, Hokkaido University
Sapporo 060, Japan

\+ The Research Institute for Iron, Steel and Other Metals
Tohoku University, Sendai 980, Japan

++ National Laboratory for High Energy Physics
Oho-machi, Tsukuba-gun, Ibaraki 305, Japan

The Rietveld method has been applied very successfully to time-of-flight (TOF) neutron powder diffraction data1),2). The object of this work is to obtain profile and structure parameters from diffraction patterns taken on the Medium-Resolution Powder diffractometer (MRP) and High-Resolution Powder diffractometer (HRP) at KENS. The XPD system, which one of the authors3),4) developed for Rietveld analysis and simulation of X-ray powder diffraction patterns, has now been modified to implement the mathematical functions described by Von Dreele et al.2)

The calculated intensity, $I_c(t)$, at a particular TOF, t, is determined from summation of the contributions from neighboring Bragg reflections multiplied by a scale factor, k, the effiective incident intensity for that TOF, $I_s(t)$, and the absorption factor, $A(t)$, plus the background, $y_b(t)$:

$$I_c(t) = kI_s(t)A(t)\sum|F_i|^2 m_i d_i^4 E_i P_i f(\Delta_i) + y_b(t). \qquad (1)$$

In the above equation, i = reflection number, F_i = structure factor, m_i = multiplicity, d_i = d spacing, E_i = correction factor for extinction, P_i = correction factor for preferred orientation, $f(\Delta_i)$ = profile shape function, and Δ_i is the difference in TOF from the Bragg position of the i-th reflection.

$I_s(t)$ for the MRP in the TOF range above 840 μs was modeled by the exponetial series

$$I_s(t) = a_0 + a_1\exp(-a_2t) + a_3\exp(-a_4t^2) + a_5\exp(-a_6t^3) + a_7\exp(-a_8t^4). \qquad (2)$$

$I_s(t)$ multiplied by the absorption factor of vanadium, $A_V(t)$, was fitted by least-squares to the intensity spectrum measured from a sample of vanadium, $I_V(t)$.

$I_s(t)$ for the HRP was not a smooth function of TOF owing to the presence of thick aluminum windows; an analytical expression such as eq. (2) cannot be formulated over a wide range of TOF. In addition, the incident intensity spectrum was appreciably influenced by experimental conditions in the LAM placed upstream from the HRP. Therefore, $I_V(t)$, was normalized by the monitor count, $n_V(t)$, corrected for absorption, smoothed by a 9-point quadratic algorithm, and multiplied by the monitor count for the sample run, $n_s(t)$. The resulting value, $I_V(t)n_s(t)/[n_V(t)A_V(t)]$, was used as $I_s(t)$ for the subsequent calculations.

$f(\Delta_i)$ was approximated by the convolution of exponential moderator pulse functions and a Gaussian instrumental function:

$$f(\Delta_i) = \frac{\alpha\beta}{2(\alpha + \beta)}[\exp(u)\mathrm{erfc}(y) + \exp(v)\mathrm{erfc}(z)], \qquad (3)$$

where $u = \alpha(\alpha\sigma^2 + 2\Delta_i)/2$, $y = (\alpha\sigma^2 + \Delta_i)/(2^{1/2}\sigma)$, $v = \beta(\beta\sigma^2 - 2\Delta_i)/2$, and $z = (\beta\sigma^2 - \Delta_i)/(2^{1/2}\sigma)$. Profile shape function (3) has three profile shape coefficients, α, β, and σ, each of which shows its own TOF dependence; the variation of these coefficients with d values in the MRP was represented by

$$\alpha = \alpha_0 + \alpha_1/d \qquad (4)$$

$$\beta = \beta_0 + \beta_1/d^4 \qquad (5)$$

$$\sigma = \sigma_0 + \sigma_1 d. \qquad (6)$$

In the case of the HRP, eqs. (4) and (5) were replaced by equations containing more refinable parameters because of the rapid change of α and β with d.

The data taken from the MRP[5)], which uses neutrons in the wavelength range of the ambient Maxwellian distribution, could be refined very successfully with the above model function. On the other hand, Rietveld analysis of HRP data gave much higher R factors[6)] than MRP data. Figure 1 shows the Rietveld refinement patterns for α-Bi_2O_3 with the HRP (R_{wp} = 0.078; R_p = 0.060; R_B = 0.043). The trailing edges of calculated peaks fell off much more rapidly than those of observed peaks in the d range from 140 to 250 pm; in addition, calculated peak heights were often lower than observed ones above 160 pm. This poor fit is ascribable to the simultaneous use of epithermal, thermal, and cold neutrons from the grooved cold moderator at 20 K. That is, cold neutrons give rise to a long trailing tail to the peak which is removed in the case of thermal or epithermal neutrons, with a result that profile shape function (3) does not give an entirely satisfactory description of the profiles over wide wavelength ranges. However, it should be pointed out that the above R factors were considerably lower than those obtained by Rietveld analysis of Guinier-Hägg X-ray powder film data for α-Bi_2O_3[6)]: R_{wp} = 0.237; R_p = 0.195; R_B = 0.108. Work is now under way to find a better profile shape function for the HRP.

Application of the correction factor for extinction gave a small and negative extinction parameter suggesting that it was physically meaningless. This finding does not agree with the previous observation[2)] that the reflections with the largest d spacings displayed considerable extinction (30-50%). The apparent discrepancy needs to be investigated further.

References

1) J. D. Jorgensen and F. J. Rotella, J. Appl. Crystallogr., 15, 27 (1982).
2) R. B. Von Dreele, J. D. Jorgensen, and C. G. Windsor, J. Appl. Crystallogr., 15, 581 (1982).
3) F. Izumi, "Advances in X-Ray Chemical Alnalysis, Japan," No. 14, Agne, Tokyo (1983), p. 43.
4) F. Izumi, "Advances in X-Ray Chemical Analysis, Japan," No. 15, Agne, Tokyo (1984), p.155.
5) H. Asano, T. Fukiura, H. Murata, H. Iwasa, S. Tomiyoshi, F. Izumi, S. Sato, and N. Watanabe, "Medium-Resolution Powder Diffractometer (MRP)," in this volume.
6) G. Malmros and J. O. Thomas, J. Appl. Crystallogr., 10, 7 (1977).

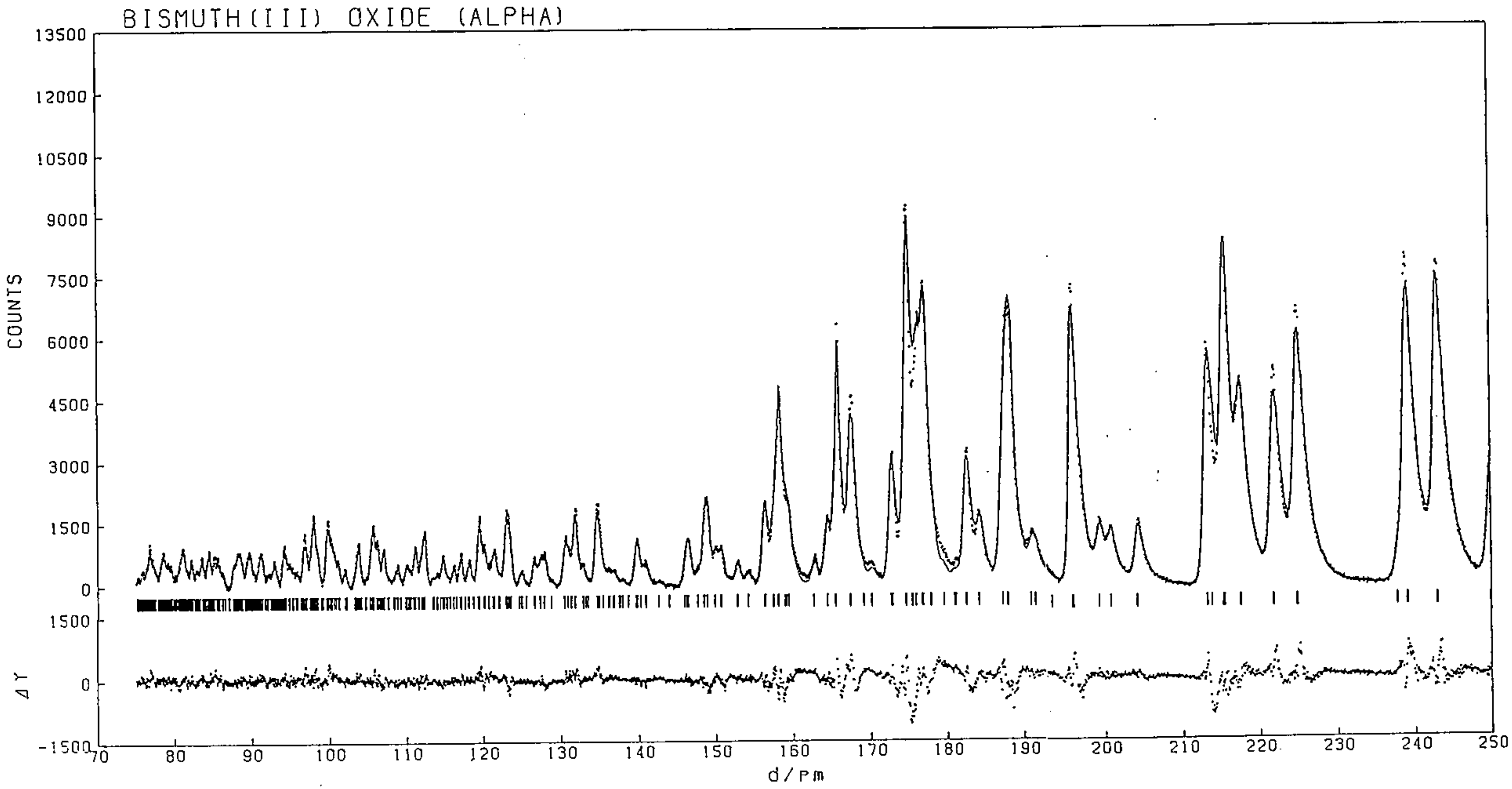

Figure 1. Rietveld refinement patterns for α-Bi_2O_3 in the d range 70 to 250 pm. In the upper portion, the observed data are indicated by the dots; the calculated pattern is shown as the solid line overlying them. The vertical markers in the central portion show positions of Bragg peaks. The lower portion is a plot of the differences between the observed and calculated intensities.

Neutron Diffraction of Ta_2D

Hajime ASANO, Hideaki MURATA, Takeshi FUKIURA, Fujio IZUMI*
Shoichi TOMIYOSHI**, Hirokatsu IWASA[+], Setsuo SATO[++] and Noboru WATANABE[++]

Institute of Materials Science, University of Tsukuba
Sakura-mura, Niihari-gun, Ibaraki 305, Japan

* National Institute for Research in Inorganic Materials
Sakura-mura, Niihari-gun, Ibaraki 305, Japan

**The Research Institute for Iron, Steel and Other Metals
Tohoku University, Sendai 980, Japan

[+] Department of Nuclear Engineering, Hokkaido University
Sapporo 060, Japan

[++]National Laboratory for High Energy Physics, Oho-machi
Tsukuba-gun, Ibaraki 305, Japan

Crystallography of metal hydrides is one of the most suitable research subjects of neutron diffraction, because X-rays cannot see hydrogen. In the present work, a crystal structure of Ta_2D has been investigated by means of MRP1) and HRP2).

V-group transition metals (V, Nb and Ta) dissolve a large amount of hydrogen in the bcc metal matrix and form an interstitial metal-hydrogen alloy over a wide composition range. Hydrogen atoms randomly distributed in the interstitial sites become ordered at low temperatures near the compositions of M_2H, M_3H_2, M_4H_3 and MH. A crystal structure of Ta_2H has already been studied by neutron3) and X-ray diffraction4),5), and the ordered structure is determined as shown in Fig. 1. Hydrogen atoms are arranged in an ordered manner among tetrahedral sites of the tantalum lattice. In addition, the original metal lattice shown by dotted lines is slightly deformed to monoclinic ($c/a \sim 1.01$ and $\gamma \sim 90.3°$) due to the hydrogen ordering. The superstructure is described by orthorhombic space group C222 with lattice parameters $A = a\{2(1 + \cos\gamma)\}^{1/2}$, $B = c$ and $C = a\{2(1 - \cos\gamma)\}^{1/2}$, where a and c are the lattice parameters of the tantalum

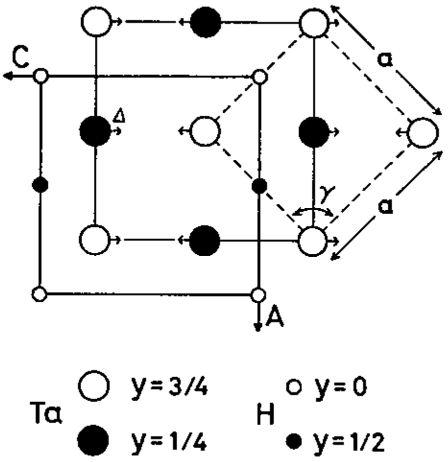

Fig. 1 Ordered structure of Ta$_2$H

lattice and γ the axial angle. The atomic coordinates are

(0 0 0; 1/2 1/2 0) +

2H in 2(a): 0 0 0

4Ta in 4(k): 1/4 1/4 z; 1/4 3/4 $\bar{z}$

with z = 3/4 - Δ.

It should be noted that tantalum atoms are shifted from the normal positions by an amount Δ upon hydrogen ordering. The value of Δ has been reported as 0.012 and 0.0127 from neutron[3)] and X-ray diffraction[5)], respectively.

Figure 2 shows a raw neutron diffraction pattern by MRP on Ta$_2$D. The scattering angle 2θ is 150°. Bragg positions are marked by bars in the abscissa. The solid line is a result of Rietveld analysis[6)] based on the structure model of Fig. 1, where the displacement Δ is taken into acount as an adjustable parameter. The best fit is obtained when Δ = 0.009 and R-factor = $\sum_i|\Delta Y_i|/\sum_i Y_i(\mathrm{obs})$ = 2 %, where ΔY_i and $Y_i(\mathrm{obs})$ are respectively the deviation and the observed count for the i-th data point. The result also shows that as much as 249 reflections are used for

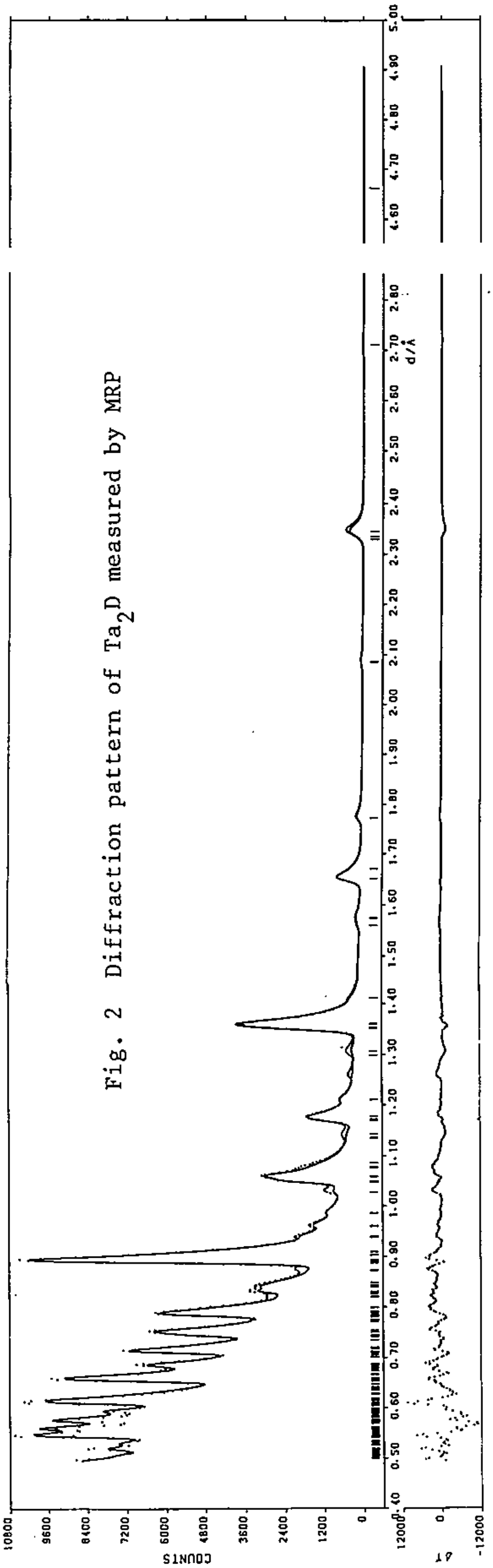

Fig. 2 Diffraction pattern of Ta$_2$D measured by MRP

refinement. The reason for discrepancy between the present value of displacement and the previously reported ones3),5) is not clear at this moment. It is to be mentioned that intensities of low-index reflections which are well separated to each other are relatively poor due to the low neutron flux at long wavelengths from the room-temperature moderator. This might cause an inaccurate estimation of parameters to be refined.

A neutron diffraction experiment of Ta_2D was also made by using HRP. HRP is a high-resolution powder diffractometer2) installed at the C4 beam hole viewing a cold moderator. In order to achieve high resolution a 20 m flight path and the back scattering geometry ($2\theta = 170°$) are adopted. Figure 3 shows a raw diffraction data of Ta_2D. It is marked that background is low and monotonic over a wide d range, which differs from the raw diffraction data of MRP shown in Fig. 2. Reflections with long d spacings have sufficient count-rates owing to the high neutron flux of the cold moderator at long wavelengths. The resolution is high enough and we can observe reflections separately as far as d = 40 pm. The Rietveld method on the data taken by HRP is partly established6) and the complete analysis of Fig. 3 as well as accurate evaluation of the displacement will appear in near future.

References

1) H. Asano, T. Fukiura, H. Murata, H. Iwasa, S. Tomiyoshi, F. Izumi, S. Sato and N. Watanabe, Medium-Resolution Powder Diffractometer (MRP), in this volume.

2) N. Watanabe et al., in this volume.

3) V. F. Petrunin, V. A. Somenkov, S. Sh. Shil'shtein and A. A. Chertkov, Soviet Phys. Cryst. 15, 137 (1970).

4) H. Asano, Y. Ishikawa and M. Hirabayashi, J. Appl. Cryst. 11, 681 (1978).

5) H. Asano, S. Uematsu and T. Fukiura, Trans. JIM 24, 661 (1983).

6) F. Izumi, H. Asano, H. Murata, T. Fukiura, H. Iwasa, S. Tomiyoshi, S. Sato and N. Watanabe, Rietveld Analysis with TOF Neutron Powder Diffraction Data Taken on the MRP and HRP, in this volume.

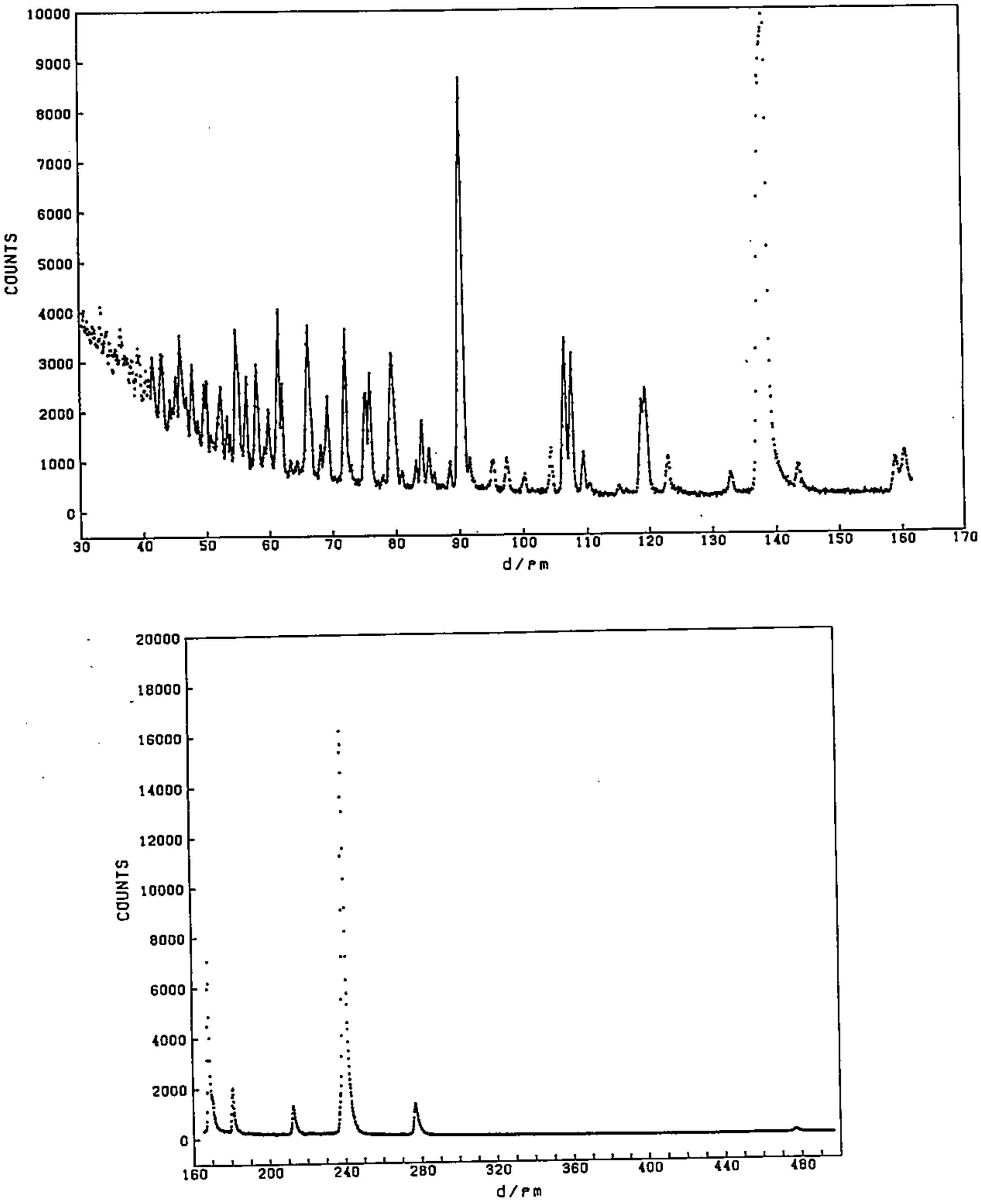

Fig. 3 High-resolution powder diffraction pattern of Ta_2D

Neutron Diffraction Study of the Cold Working Effects on Pd_2MnSn

S. Tomiyoshi, T. Kamiyama, T. Shinohara, H. Asano*,
N. Watanabe** and H. Iwasa***

The Research Institute for Iron, Steel and Other Metals,
Tohoku University, Sendai 980

*Institute of Materials Science,
University of Tsukuba, Ibaraki 305

**National Laboratory for High Energy Physics,
Oho-machi, Tsukuba-gun, Ibaraki 305

***Department of Nuclear Engineering,
Hokkaido University, Sapporo 060

One of the most promising application of high resolution powder neutron diffraction will be the study of cold working effects on metals. Up to now works on such a problem have been done mainly by X-ray diffraction and the studies by neutron diffraction have been limited, since the resolution of the latter is not enough to detect line broadening and peak shift in the diffraction patterns of cold worked samples. The neutron powder diffractometers HRP and MRP installed recently in KENS have fairly good resolution, so we tested their applicability for cold worked samples.

As the first example we take up Heusler alloy Pd_2MnSn. It is a simple ferromagnet with the Curie temperatutc of 200 K, but by cold working it shows remarkable reduction of the magnetization.1) From the studies of NMR and Mössbauer effect it was suggested that the reduction of the magnetization has some connection with atomic disordering.2) The aim of our neutron diffraction is to make atomic and magnetic disordering clear and also to obtain some information about faults or slips which make such disordering.

The cold worked sample was prepared by crushing the arc melted ingots into powders with a diameter less than 50 μm, whose saturation magnetization was determined to be about 39 % to that of the ordered sample. TOF neutron diffraction measurements were carried out at room temperature and 30K by MRP, and at room temperature by HRP. Fig. 1 shows diffraction patterns of the cold worked sample at room temperature and 30K measured by MRP at the scattering angle of 150°. Fig. 2 shows data of the sample annealed at 310°C for 16 hours (cold working effects are partly removed) and Fig. 3 shows data of the sample annealed at 820°C for 28 hours (cold working effects are completely removed). As can be seen in the figures, main effects of cold working on the diffraction patterns are line broadening and reduction of the peak height. They depend largely on line indices; the line broadening are more pronounced for the 200 and 400 lines and less for the 111 and 222 lines, and the peak height reduction at paramagnetic state is remarkable for the 111 and 311 lines. The annealing at 310°C makes considerable recovery of the line broadening and peak height as easily seen from Fig. 2. By this heat treatment saturation magnetization increases from 39 % to 66 % of the completely ordered sample, but the diffuse peak observable around the 111 line in Figs. 1 and 2 does not recover by this heat treatment. These facts suggest that the peak intensity and the peak width are closely related with the reduction of the magnetization. In this paper, we consider only the peak intensity.

The integrated intensity of the nuclear peaks for the Pd_2MnSn type structure is given as follows:

$$I(hkl) = C(b_{Sn} - b_{Mn})^2 \qquad \text{for } h,k,l \text{ all odd,}$$

$$I(hkl) = C(b_{Sn} + b_{Mn} - 2b_{Pd})^2 \qquad \text{for } h,k,l \text{ all even and } h+k+l=4n+2,$$

$$I(hkl) = C(b_{Sn} + b_{Mn} + 2b_{Pd})^2 \qquad \text{for } h,k,l \text{ all even and } h+k+l=4n,$$

where C is a constant, b_{Sn}, b_{Mn} and b_{Pd} are the nuclear scattering lengths for the respective atoms indicated, and n is an integer. When the interchange of atoms between the Mn and Sn sites takes place, the intensities of all odd lines decrease proportional to $(1-2\alpha)^2$, but the intensities of all even lines do not change, here we defined α as a fraction of Mn atoms which are replaced by Sn atoms. The observed line intensities almost agree with the intensities calculated assuming the interchange of Mn and Sn atoms, and the fraction α is found to be 0.2 for the crushed sample and about 0.1 for the sample annealed at 310°C.

The magnetic part of the diffraction lines shows quite different trend compared with that of the nuclear part; all odd lines have large magnetic intensity and all even lines have small one. These show that the Mn moment

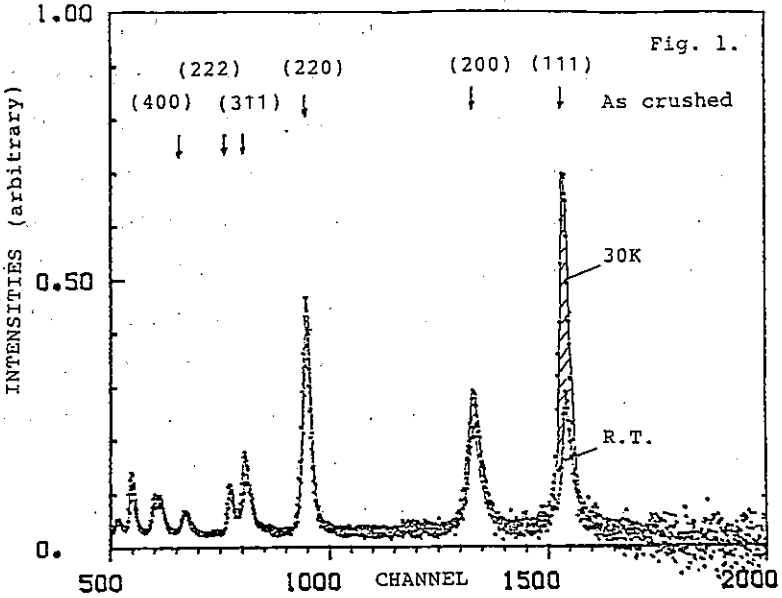
Fig. 1.

As crushed

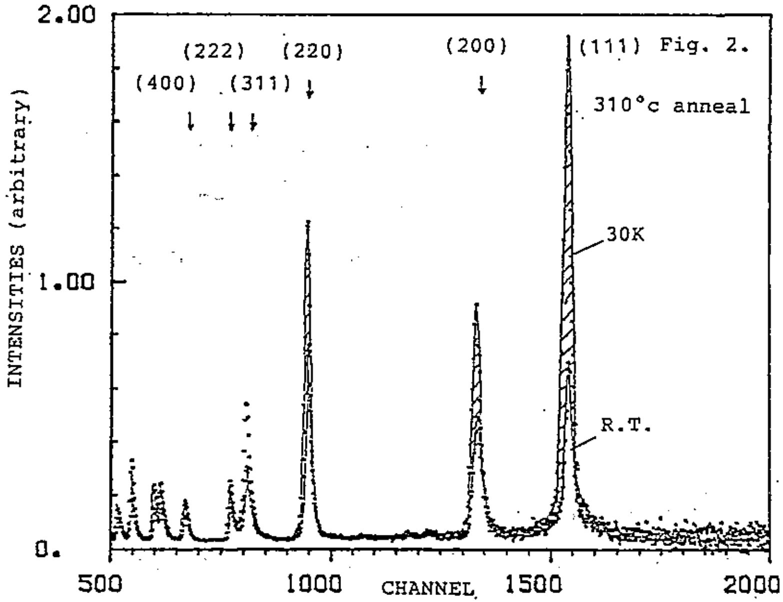
Fig. 2.

310°c anneal

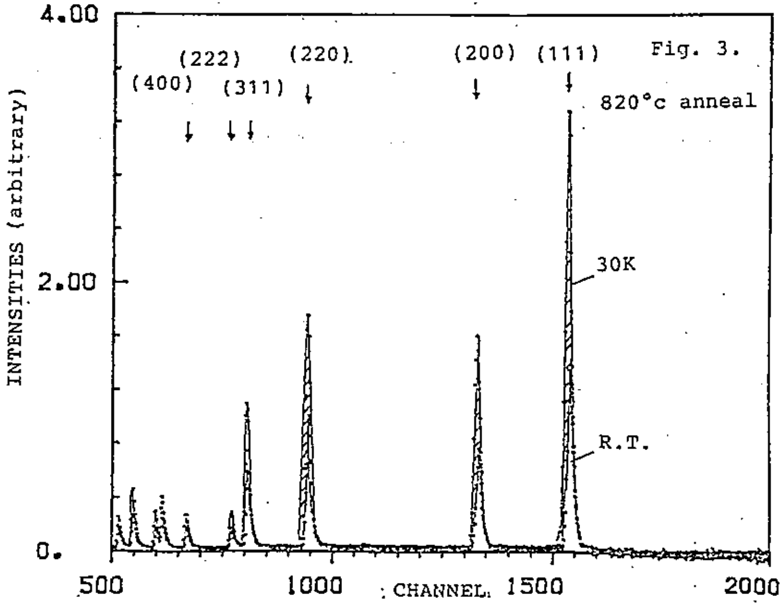
Fig. 3.

820°c anneal

which occupy Sn site couples antiparallel to the Mn moment in the regular site. From the hatched area of the three lower indes lines in the figures, it is concluded that the Mn moment in the wrong site have approximately the same value as the moment in the right site. The magnetization is easily calculated for this antiparallel coupling model. For the crushed sample 20 % Mn moments are antiparallel, so the magnetization is 60 % to that of the ordered sample, and for the sample annealed at 310°C 10% Mn moments are antiparallel, so the magnetization is 80 %. The magnetization determined from the magnetization measurements is 39 % for the former case and 66 % for the latter case, so by this model major part of the magnetization reduction is explained, but the agreement is not satisfactory. To obtain better agreement, an analysis including the line broadening effect will be required and now in progress.

References

1) T. Shinohara, K. Sasaki, H. Yamauchi, H. Watanabe, H. Sekizawa and T. Okada : J. Phys. Soc. Japan 50 (1981) 2904.

2) J. Schaf, K. L. Dang, P. Veillet and I. A. Campbell : J. Phys. F Metal Phys. 13 (1983) 1311.

Figure Captions

Fig. 1 Time-of-flight spectra of MRP at the scattering angle of 150° from the as-crushed Pd_2MnSn Heusler alloy at room temperature and 30 K.

Fig. 2 Time-of-flight spectra of MRP from the alloy annealed at 310°C.

Fig. 3 Time-of-flight spectra of MRP from the alloy annealed at 820°C.

Neutron Diffraction Study on the Cation Distribution in $CrTi_2Se_4$

Hajime ASANO, Hideaki MURATA, Fujio IZUMI*, Noboru WATANABE**
Akihiko HAYASHI+, Yutaka UEDA+, Koji KOSUGE+ and Sukeji KACHI+

Institute of Materials Science, University of Tsukuba, Sakura-mura
Niihari-gun, Ibaraki 305, Japan

* National Institute for Research in Inorganic Materials, Sakura-mura
Niihari-gun, Ibaraki 305, Japan

**National Laboratory for High Energy Physics, Oho-machi, Tsukuba-gun
Ibaraki 305, Japan

+ Department of Chemistry, Faculty of Science, Kyoto University, Kyoto 606
Japan

It is well known that many of the transition metal chalcogenides crystallize in a berthollide compound between NiAs and CdI_2 structures. Chalcogen atoms form a close-packed hexagonal structure, and metal atoms are intercalated between the chalcogen layers parallel to the hexagonal basal plane. The NiAs structure is composed of alternating layers of metal and chalcogen atoms, while an every second layer of the metal atoms is missing in the CdI_2 structure. At the composition of M_3X_4, half of the metal planes are deficient in an ordered manner as shown in the left of Fig. 1. In the

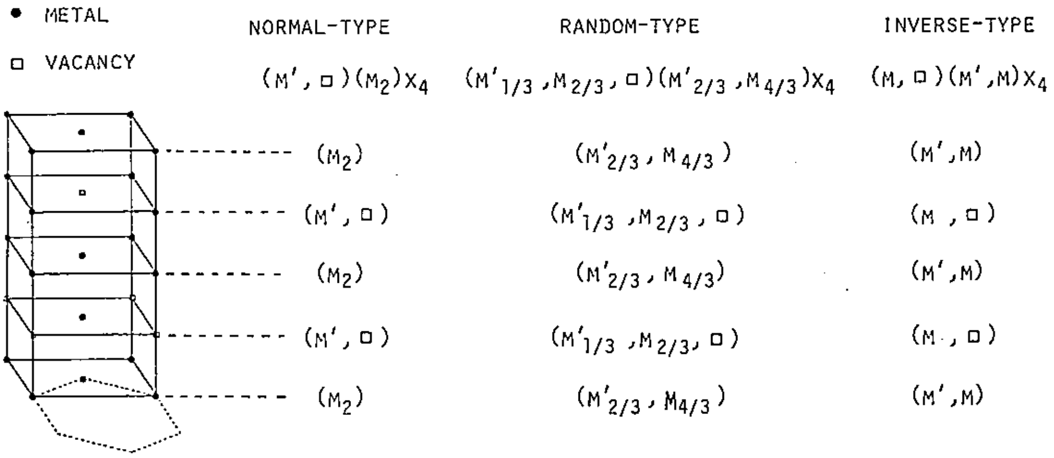

Fig. 1 Probable structure models of $M'M_2X_4$

figure, the basal plane of the hexagonal lattice is drawn by dotted lines, but chalcogen atoms are omitted for simplicity. In the present substance $CrTi_2Se_4$, three models indicated in Fig. 1 are considered for the metal atom distribution. Vacancy sites are settled in the 1st and 3rd layers in all three models. In a normal-type model, M atoms occupy the 0th and 2nd layers and M' atoms occupy the 1st and 3rd layers. In an inverse-type model, M' atoms are located in even layers. A random model has a statistical distribution of M and M' among the metal positions of M_3X_4. Discrimination of the three models is important not only from the crystallographic view point but also to understand the origin of magnetic ordering at lower temperatures. Ti and Cr are hardly distinguishable by X-rays and the compound needs to be examined by neutrons.

A result of preliminary intensity calculations for the above three models is listed in Table 1. Although the calculations are made for the data taken by a two-axis diffractometer at the reactor, we can roughly compare them with the present TOF data. Keys to distinguish the models are (1) the intensity distribution of a series of reflections from 004 to 112 and (2) whether a 002 reflection is intense or not.

Table 1 Comparison of the calculated reflection intensities for the normal-, random- and inverse-type models

hkl	d-spacing	I_{normal}	I_{random}	$I_{inverse}$
002	5.994	18	0	3
$10\bar{1}$	5.623	2	0	3
101	5.527	2	0	2
011	3.426	1	0	2
$10\bar{3}$	3.406	1	0	1
103	3.342	1	0	1
200	3.148	17	30	25
110	3.109	33	58	48
004	2.997	52	90	75
$20\bar{2}$	2.812	52	52	31
$11\bar{2}$	2.771	21	87	100
202	2.763	11	43	50
112	2.748	100	100	59

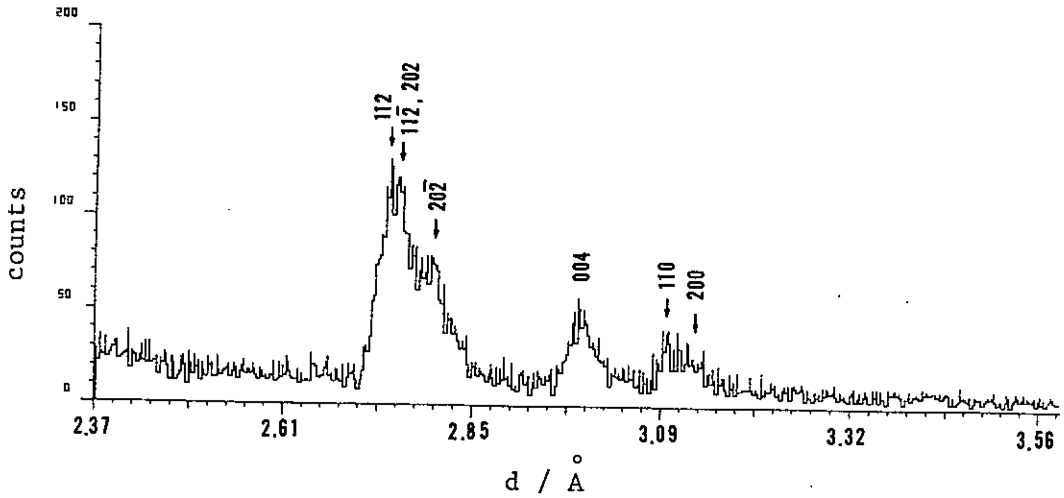

Fig. 2 A part of the diffraction pattern on $CrTi_2Se_4$ by MRP (2θ = 150°)

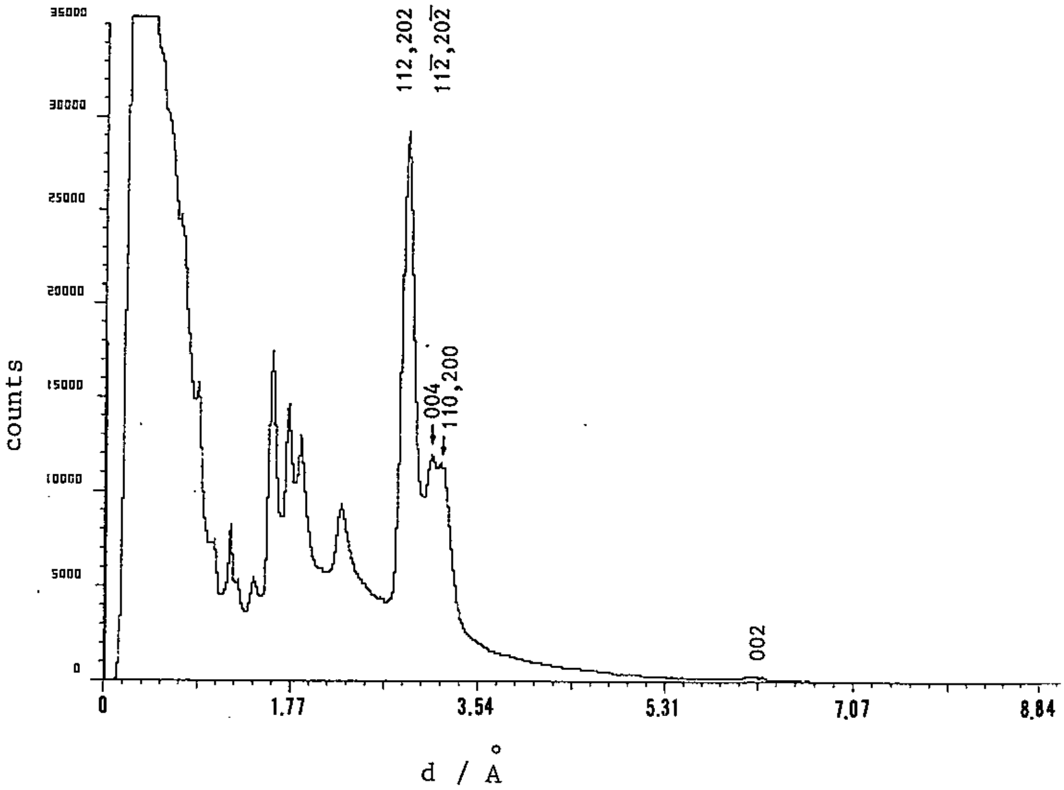

Fig. 3 Diffraction pattern of $CrTi_2Se_4$ by MRP (2θ = 30°)

Figures 2 and 3 show raw diffraction data of $CrTi_2Se_4$ taken by MRP[1)] at 2θ = 150° and 30°, respectively. The 150° counter possesses a relatively good resolution (Δd/d ~ 1.5 %), and we can identify reflections 200, 110, 004, $20\bar{2}$, $11\bar{2}$ + 202 and 112 separately as seen in Fig. 2. The intensity distribution suggests that the normal or random model is probable. In the data of Fig. 3 taken by the 30° counter, a series of reflections from 200 to 112 is not well resolved, but we can notice a 002 reflection. It is

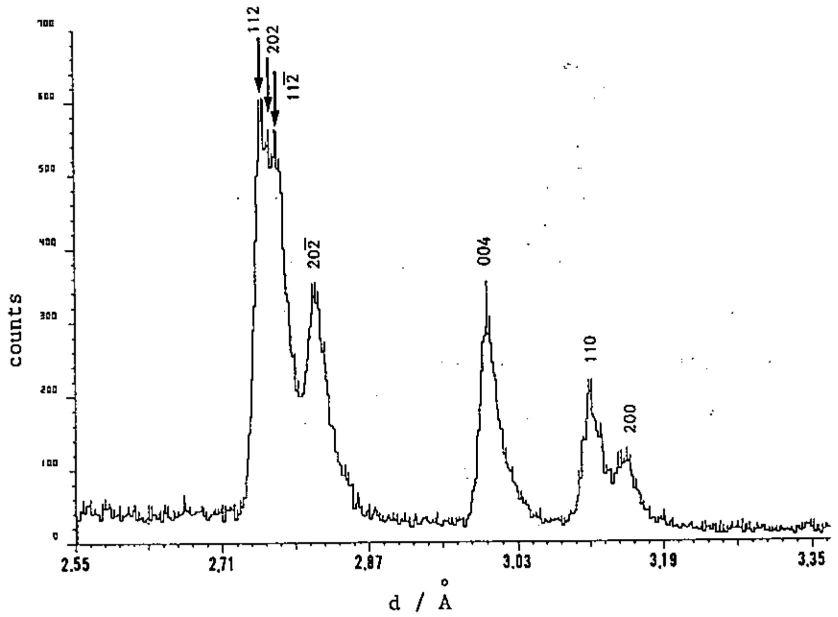

Fig. 4 A part of the diffraction pattern on $CrTi_2Se_4$ by HRP

uncertain whether the 002 reflection is intense or not, because the intensity depends on the incident neutron spectrum i(λ) and the Lorentz factor λ^4. Figure 4 shows a diffraction pattern of $CrTi_2Se_4$ by HRP$^{2)}$ in the same d range as in Fig. 2. The higher resolution of HRP gives well separated peaks, the intensity distribution of which supports the normal or random model. The 002 reflection (d = 5.994 Å) has not been measured by HRP because the frame overlap occurs in the d-range longer than 5.0 Å.

A definite conclusion on the cation distribution is not obtained at the present stage, and we must await the result of Rietveld refinement$^{3)}$ which is in progress. Measurements on analogous systems $TiCr_2Se_4$ and $CrTi_2Te_4$ have also been made by MRP and HRP, the analysis of which will appear in near future.

References

1) H. Asano, T. Fukiura, H. Murata, H. Iwasa, S. Tomiyoshi, F. Izumi, S. Sato and N. Watanabe, Medium-Resolution Powder Diffractometer (MRP), in this volume.
2) N. Watanabe et al., in this volume.
3) F. Izumi et al., in this volume.

Quasielastic Spectrometers Using the Pulsed Cold Neutron Source at KENS

K. INOUE*, Y. ISHIKAWA**, N. WATANABE+, Y. ENDOH**,
Y. KIYANAGI*, H. IWASA*, M. KOHGI** and S. IKEDA+

* Department of Nuclear Engineering, Hokkaido University,
Sapporo, 060 Hokkaido, Japan
** Physics Department, Tohoku University,
Sendai, 980 Miyagi-ken, Japan
\+ National Laboratory for High Energy Physics,
Oho-machi, 305 Ibaraki-ken, Japan

1. Introduction

We have installed two quasielastic spectrometers, the LAM-40 and the LAM-80, at the KENS cold source. The former is an improved version of the prototype spectrometer installed within the electron linear accelerator-based cold source at Hokkaido University$^{1)}$. These spectrometers use LAM-type analyser mirrors(Latticed crystal Analyser Mirror), in which about 70 pieces of pyrolitic graphite are arranged on an optimally curved array in order to achieve energy focussing.

The spectrometers were designed according to a design philosophy which utilizes to the utmost the significant features of the 20 K methane pulsed cold source. The LAM-40 is a 100 μeV resolution device with high efficiency, and the LAM-80 provides 10 μeV resolution and has the special feature of a wide energy window. In this report we will briefly introduce some of our findings concerning the pulsed cold source, the benefits of the analyser mirrors and the overall performance of the spectrometers.

2. Time structure of Pulses Emitted from 20 K Methane

The time structure of the pulses was measured by a thermica monochrometer for the 20 K methane cold moderator, and the pulse data were corrected for the monochrometer resolution using the QUESA-40 code$^{2)}$. Fig.1 illustrates the FWHM of the pulses, Δt_z, as a function of wave length. Utilizing these data, we can assess the energy resolution of incident neutrons impinging on the sample, ΔE_1, as shown in Fig.2.

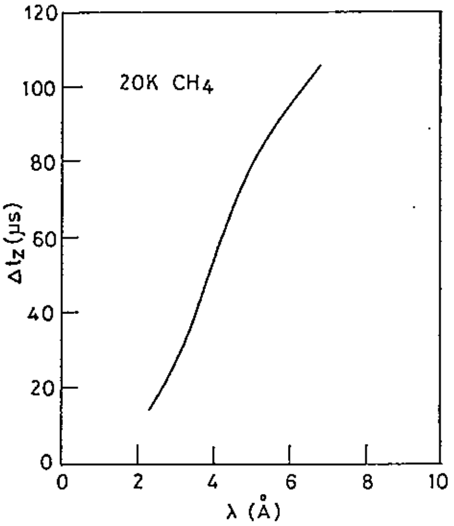

Fig.1 Pulse width of 20 K methane moderator.

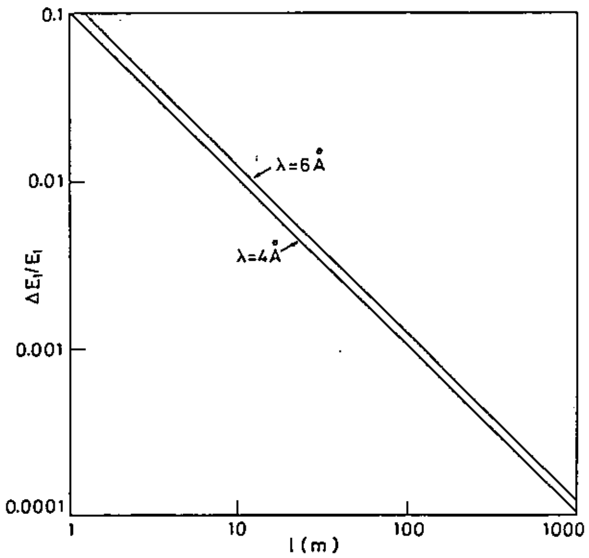

Fig.2 Energy resolution of time-of-flight measurement.

3. Resolution function of the LAM-type Mirror

The resolution function of the mirrors, $M(\theta)$, is calculated by the following equation[3],

$$M(\theta) = \mathrm{const.}\iiint p(\mathbf{r},\Sigma,S)\,\delta[\theta - \hat{\theta}(\mathbf{r},\Sigma,S)]\,d\mathbf{r}\,d\Sigma\,dS. \qquad (1)$$

Calculated results for the case of 40° and 80° Bragg angles and a 14 mm diameter and 80 mm height cylindrical sample are depicted in Fig.3. The variance of the Bragg angle, $\Delta\theta$, is about 0.8° for both cases.

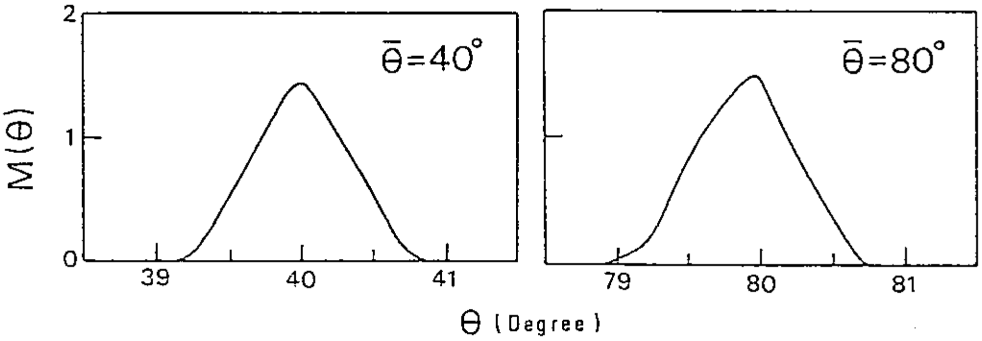

Fig.3 Resolution function of analyser mirrors.

4. Energy Resolution of Spectrometers

The energy resolution is assessed by:

$$\Delta\varepsilon/2E = [(\Delta t_z/t)^2 + (\cot\theta\,\Delta\theta)^2 + (\Delta\tau/\tau)^2]^{1/2}. \qquad (2)$$

Here, t is the flight time, $\Delta\tau$ is a variance of the reciprocal lattice vector due to the limitation of the number of lattice planes contributing to the reflection. For three cases of flight path length, 6 m, 30 m and 150 m, the overall energy resolution of the spectrometers is shown in Fig. 4. as a function of the Bragg angle of the mirrors.

Fig.4 Overall energy resolution of the spectrometers which utilize 20 K methane pulsed source and the LAM - type analyser mirrors. ℓ means flight path length.

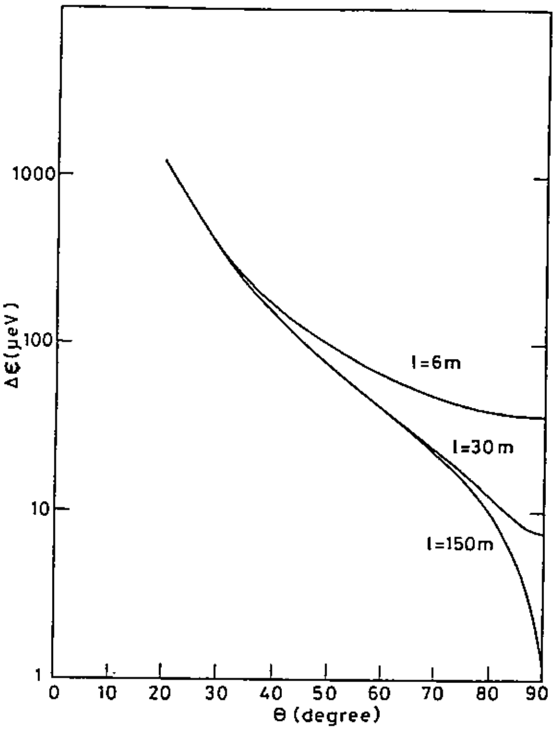

5. Spectrometers

The LAM-40 consists of eight equivalent analysers, of which the Bragg angle is about 40°. All of the analysers are mounted on a turntable which enables measurements at different scattering angles and is housed in an evacuated container (Fig.5).

The LAM-80 consists of four equivalent analysers, of which the Bragg angle is 80°. The evacuated container for the LAM-80 is able to rotate on a turntable to change the scattering angle (Fig.6).

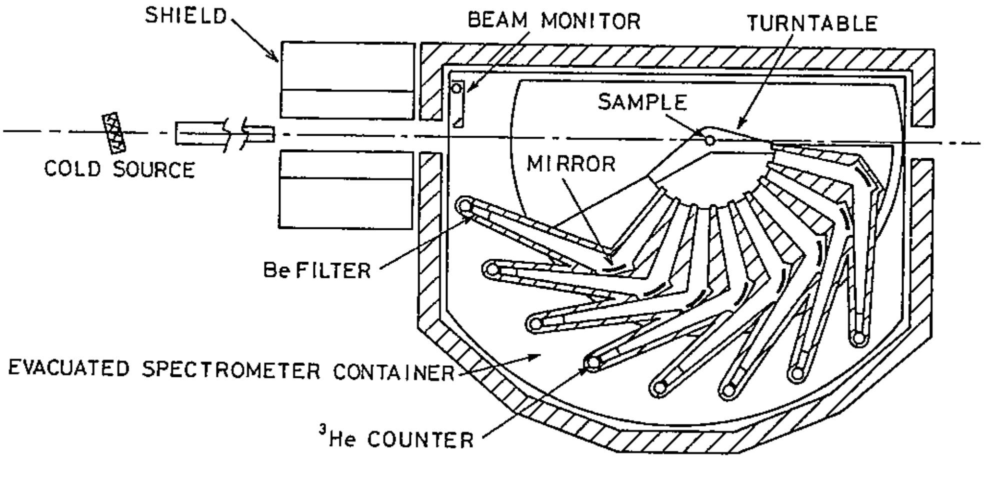

Fig.5 The LAM-40 spectrometer.

The neutron flight path lenghts are about 6 m for the LAM-40, and about 30 m, including the neutron guide tube, for the LAM-80, respectively. Fig.7 shows the scattered spectra from vanadium measured by two spectrometers.

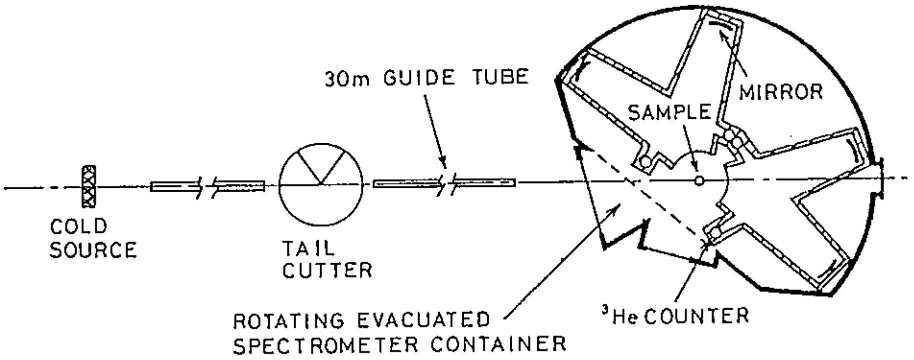

Fig.6 The LAM-80 spectrometer.

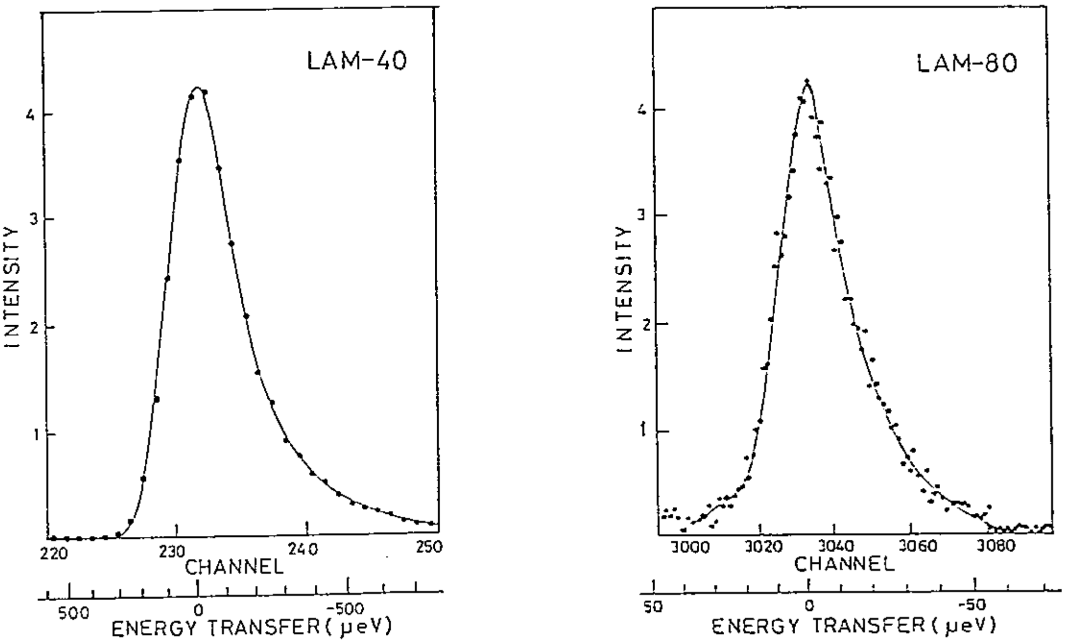

Fig.7 Scattered spectra from vanadium.

6. Conclusions

To utilize both spectrometers effectively, appropriate data analysis code system are needed. Such a code system has just been completed for the LAM-40. At present we are devising one for the LAM-80.

References

1) K. Inoue et al.: Nucle. Instr. Meth., 178(1980)459.
2) K. Inoue: Bull. of Faculty of Engrg. Hokkaido University, 112(1983)83.
3) K. Inoue: Bull. of Faculty of Engrg. Hokkaido Univeristy, 94(1979)85.

Statistical Data Analysis of Quasielastic Neutron Spectra for the LAM-40 Spectrometer

Kazuhiko INOUE

Department of Nuclear Engineering, Hokkaido University
Sapporo 060, Japan

1. Introduction

The experimental results obtained by the LAM-40 spectrometer demonstrated several features of the facility in quasielastic scattering studies using the pulsed cold source$^{1)}$: an extraordinary low level of background of the measurement; absence of the cumbersome distortion in spectral shape due to the t^{-3} weighting factor in the time-of-flight, which inevitably appears in ordinary direct geometry facilities; and simplicity and stability of the mechanical structure of the device without the need of moving gears. However, the measured neutron spectra are not simply related to the neutron cross section of the sample, as in the case of ordinary direct geometry facilities. Instead, they are expressed as the results of complex double convolution integrals concerning the scattering function, the time structure of incident neutron pulse and the resolution of the analyser mirror.

We developed a statistical data analysis technique for the extraction of the scattering functions from measured spectra. The data analysis technique consists of procedures for curve fitting of the spectra and hypothesis testing of the scattering model.

2. Scattered Spectra and Effective Resolution

The measured time spectrum on the time analyser at time t at scattering angle θ is as follows$^{1)}$,

$$\eta(t;\theta) = \text{const.}\iint\phi(E_1, t - \ell_2/\sqrt{2E_2/m})\sigma(E_1 \to E_2, \theta)R(E_2)dE_1dE_2, \qquad (1)$$

where $\phi(E_1, t_1)$ is the incident neutron beam of energy E_1 at time t_1 on the sample, of which the scattering cross section $\sigma(E_1 \to E_2, \theta)$, $R(E_2)$ is the resolution function of the analyser mirrors, and ℓ_2 is the path length from the sample to the counters.

We introduce an effective resolution function for the inverted geometry type spectrometer as follows[2,3],

$$Y(t,\varepsilon) = \int\phi(E+\varepsilon, t-\ell_2/\sqrt{2E/m})\sqrt{E/(E+\varepsilon)}R(E)dE. \tag{2}$$

Utilizing the effective resolution function, we can calculate $\eta(t;\theta)$ rapidly with sufficiently high accuracy in iterative numerical calculations, and Eq.(1) becomes as follows,

$$\eta(t;\theta) = \text{const.}\int Y(t,\varepsilon)S_{inc}(Q^*,\varepsilon)d\varepsilon, \tag{3}$$

where

$$\varepsilon = E_1 - \bar{E}_2, \tag{4}$$

$$Q^* = k_1 - k^*_2, \tag{5}$$

$$(Q^*)^2 = (2m/\hbar^2)[2\bar{E}_2 + \varepsilon - 2\sqrt{(2\bar{E}_2+\varepsilon)E_2}\cos\theta], \tag{6}$$

$$\bar{E}_2 = \int ER(E)dE/\int R(E)dE. \tag{7}$$

In the case of elastic scattering, the exact scattered spectrum is expressed as

$$\eta(t,\theta)\big|_{\varepsilon=0} = \text{const.}Y(t,0). \tag{8}$$

This expression is very useful for the data analysis, since the validity of instrument functions is directrly checked by comparing Eq.(8) with the measured elastic spectrum.

Figs.1 and 2 illustrate the measured and calculated instrument functions, the time structure of emitted neutron pulses from the 20 K methane cold source and the resolution function of the analyser mirrors. A scaling technique of the instrument functions needed for accurate interpolation has also been devised[3].

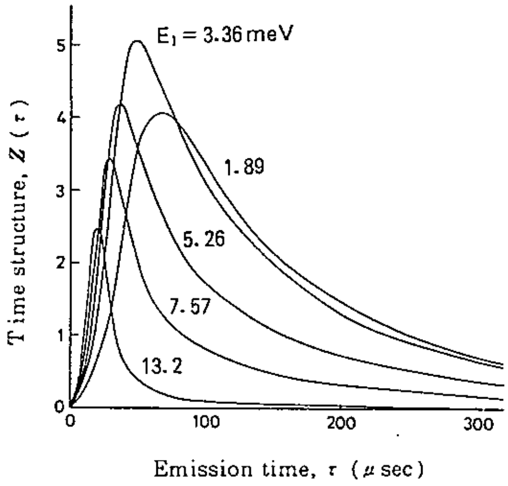

Fig.1 Measured time structure of emitted neutron pulses from 20 K methane cold source.

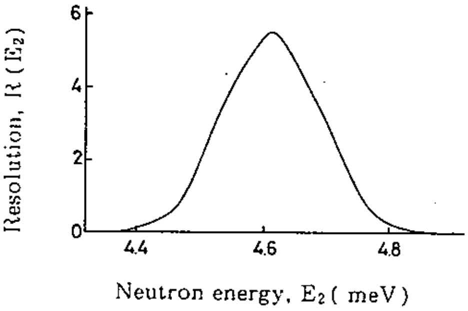

Fig.2 The resolution function of the analyser mirrors calculated by using the AMF code.

3. Minimum Function

Our curve fitting method is based on the following procedures$^{4)}$: If we use the correct scattering function to calculate Eq.(1), the measured spectra $y(t_n;\theta)$ may be regarded as the sum of $\eta(t_n;\theta)$ and measurement errors Δy_n,

$$y(t_n;\theta) = \eta(t_n;\theta) + \Delta y_n, \tag{9}$$

where t_n is n-th channel time of the time analyser. Δy_n should be determined in such a way that the sum of weighted squares of Δy_n, M, takes its minimum.

$$M = \sum_{n=1}^{N} (w_n \Delta y_n)^2 = \min. \tag{10}$$

If we succeed in removing completely any systematic errors in the measurements, we can assume the measurement errors to be distributed normally at about zero. To execute this curve fitting method, we devised a computer code named QUESA-40.

4. Example of Curve Fitting

As a numerical example, we applied the procedure to the data obtained in an experiment using the LAM-40 for a typical molecular liquid sample.

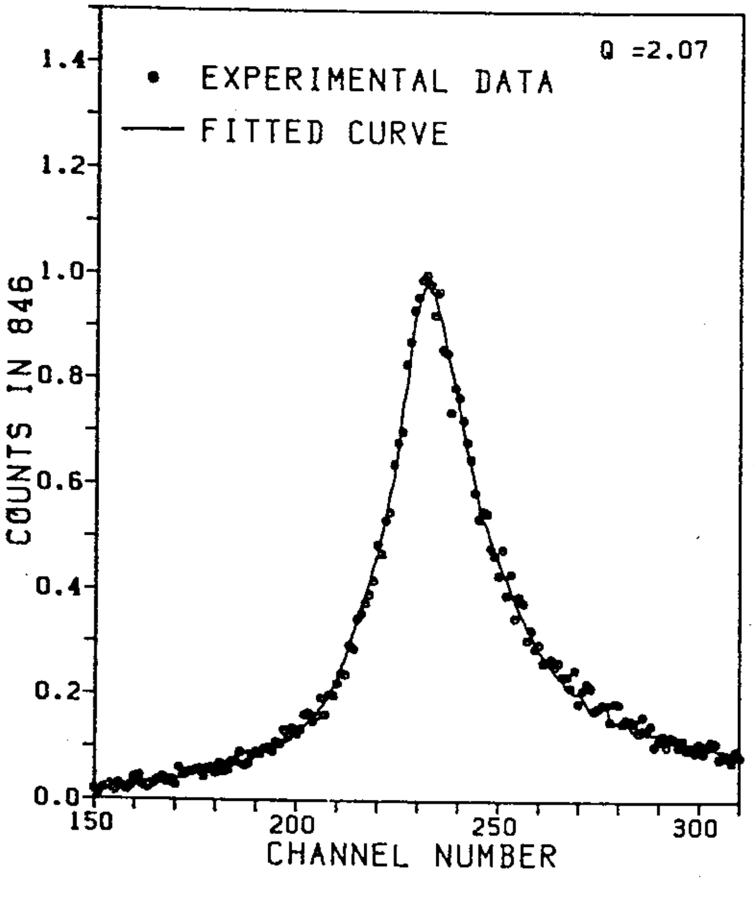

Fig.3 Result of curve fitting, obtained after seven iterations. Four unknown parameters are used. The fine structure in the fitted curve is due mainly to the structure of the aluminum cross section of the moderator chamber.

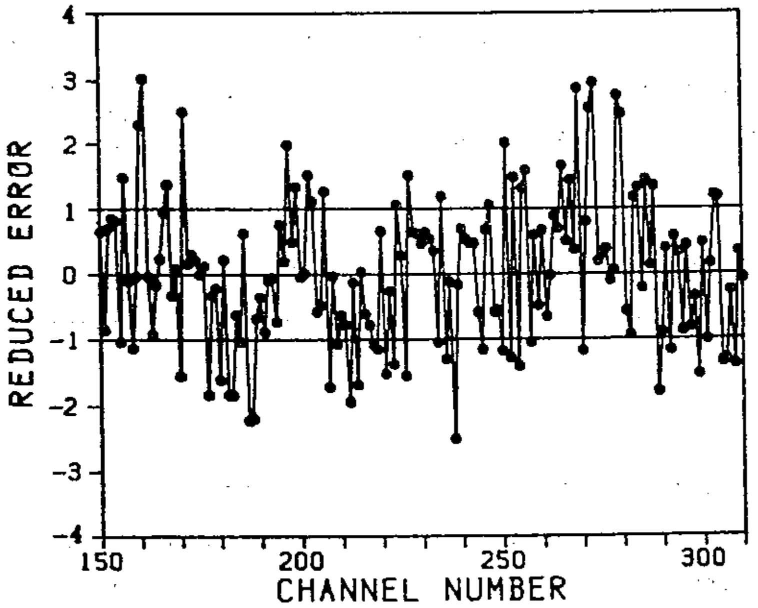

Fig.4 The ratio of errors Δy_n to statistical error of counts as a function of channel number. If the guess cross section curve is correct, about 68 % points are distributed within the interval of ± 1.

We assumed an analytical function including 4 to 5 non-linear unknowns for the scattering function. One example using the QUESA-40 is illustrated in Fig.3 and 4. As shown, there is good agreement in Fig.3. An inspection of Fig.4 also reveals satisfactory agreement throughout all the channels adopted in the analysis.

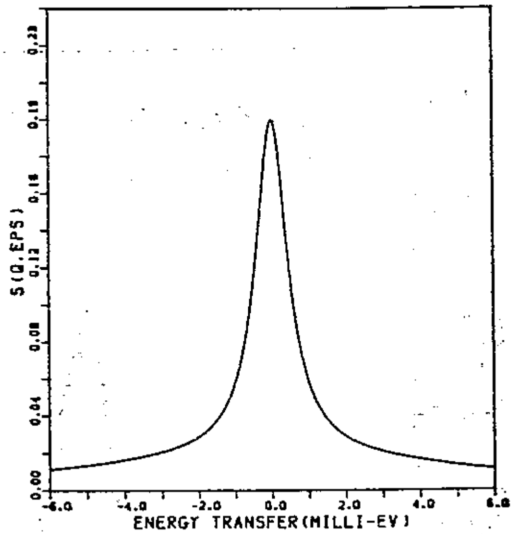

Fig.5 Scattering function obtained from Fig.3 data

5. Conclusions

The statistical data analysis technique adopted for the QUESA-40 code has been proved to be very useful. This technique enables us to extract the curves of scattering functions from the time-of-flight spectra without any ambiguities, as shown in Fig.5, in the case of using inverted geometry type spectrometers.

References

1) K. Inoue et al.: Physica, 120B(1983)422.
2) K. Inoue: Bull. of Faculty of Engrg., Hokkaido University, 98(1980)77.
3) K. Inoue: Bull. of Faculty of Engrg., Hokkaido University, 112(1983)83.
4) S. Brandt: "Statistical and Computational Methods in Data Analysis", (1970), North-Holland.

Multiple Scattering Corrections for the Quasielastic Scattering Measurements

Kazuhiko INOUE

Department of Nuclear Engineering, Hokkaido University,
Sapporo, 060 Hokkaido, Japan

Multiple scattering correction is one of the most important corrections for the neutron scattering studies and has been investigated by many authors$^{1\sim6)}$. Especially, for data analysis of quasileastic scattering, it is essential that multiple scattering corrections, which include energy transfer and angulare dependent information, are as accurate as possible. A new method of computing the multiple scattering corrections has been developed, which is useful in analysing the time-of-flight spectral data for quasielastic neutron scattering measurements. We devised an instantaneous scattering approximation, which let us to treat the sequential time-dependent process as a simple time-independent process and to calculate readily the formal set of integral type solutions of neutron transport equation. According to this approximation, a computer code has been written for a cylindrical geometry, and it is readily adapted to other geometrical configulations.

We expand the total scattered spectra, η^+, in terms of the numbers of scattering events:

$$\eta^+ = \Sigma\, \eta^{(\nu)}.$$

Here, ν is the number of scatterings and $\eta^{(1)}$ is given by following equation,

$$\eta^{(1)}(t;\theta) = \text{const.}\int\int \phi(E_i, t - l_2/\sqrt{2E_f/m})\,\Sigma(E_i \rightarrow E_f, \theta) R(E_f) dE_i dE_f. \qquad (1)$$

Practically, $\eta^{(2)}$ is the leading correction term for the 10 to 20 % scattering sample. Let us consider: a neutron of energy E_i with direction $\boldsymbol{\Omega}_i$ is impinging on the sample, and at first it is scattered at $\mathbf{r}_1$, and then subsequently scattered at $\mathbf{r}_2$, finally leaving the sample with energy E_f and direction $\boldsymbol{\Omega}_f$. In this case $\eta^{(2)}$ is given by

$$\eta^{(2)}(t;\theta) = \text{const.}\int\int \phi(E_i, t - l_2/\sqrt{2E_f/m})\; K_2(E_i, E_f;\theta) R(E_f) dE_i dE_f, \qquad (2)$$

where

$$\begin{aligned} K_2(E_i, E_f;\theta) &= \int\int\int \Sigma(E_i \rightarrow E, \theta_1) W(\theta_1, \theta_2;\theta)\; \Sigma(E \rightarrow E_f, \theta_2) d\theta_1 d\theta_2 dE \\ &= (E_f/E_i)^{1/2} S_2(E_i, E_f;\theta), \end{aligned} \qquad (3)$$

and

$$\begin{aligned} W(\theta_1, \theta_2;\theta) = \int\int q_i(\boldsymbol{\Omega}_i, \mathbf{r}_1)\; \delta[\theta_1 - \tilde{\theta}(\boldsymbol{\Omega}_i, \mathbf{r}_1, \mathbf{r}_2)]\; \exp(-\Sigma_s \|\mathbf{r}_2 - \mathbf{r}_1\|) \times \\ \times (4\pi |\mathbf{r}_2 - \mathbf{r}_1|^2)^{-1} \delta[\theta_2 - \tilde{\theta}(\mathbf{r}_1, \mathbf{r}_2, \boldsymbol{\Omega}_f)]\; q_f(\mathbf{r}_2, \boldsymbol{\Omega}_f) d\mathbf{r}_1 d\mathbf{r}_2. \end{aligned} \qquad (4)$$

Here $\|\mathbf{r}_2 - \mathbf{r}_1\|$ means the total flight length within the sample medium, Σ_s and $\Sigma(E \rightarrow E', \theta)$ are macroscopic total and differential scattering cross sections, q_i and q_f are self-shielding factors and $\tilde{\theta}(\boldsymbol{\Omega}_i, \mathbf{r}_1, \mathbf{r}_2)$ is the scattering angle determined by $\boldsymbol{\Omega}_i$, $\mathbf{r}_1$ and $\mathbf{r}_2$ at $\mathbf{r}_1$.

We applied our method to the data shown in Fig. 1, which is the time-of-flight spectra from water at 5°C measured by the LAM-40. Some of the results are illustrated in Figs. 2 and 3. Fig. 2 depicts the results for $W(\theta_1, \theta_2;\theta)$, and Fig. 3 shows the effective scattering function of multiple scatterings in which the neutrons were scattered twice inside a water sample of cylindrical shape with the dimensions quoted in Fig. 1. Fractional intensity of $\eta^{(2)}$ to $\eta^{(1)}$ is about 13 % in this example.

References

1) G. H. Vineyard: Phys. Rev., 96, 93(1954).
2) I. A. Blech and B. L. Averbach: Phys. Rev., 137, A1113(1965).
3) V. F. Sears: Advances in Physics, 24, 1(1975).
4) F. G. Bischoff, M, L. Yeater and W. E. Moore: Nucl. Sci. Eng., 48, 266(1972).
5) J. R. D. Copley, D. L. Price and J. M. Rowe: Nucl. Instr. and Meth., 107, 501(1973).
6) J. R. D. Copley: Comput. Phys. Commun., 7, 289(1974).

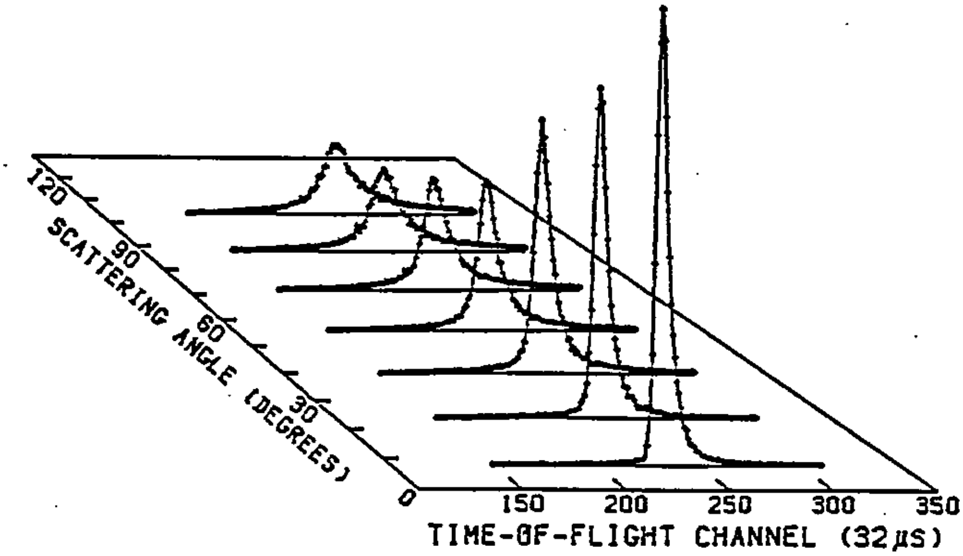

[Fig. 1] Time of flight spectra from water at 5°C measured by the LAM-40. The water sample is a 14 mm diameter cylinder of 80 mm height 0.1 mm thickness.

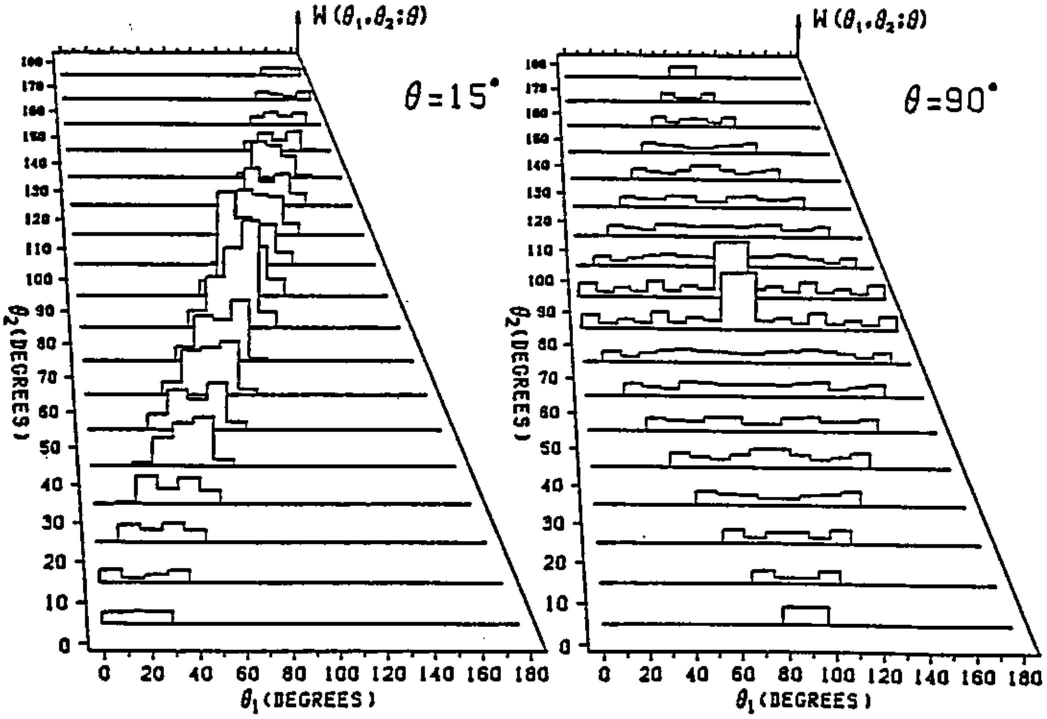

[Fig. 2] Calcualted results for W(θ_1,θ_2;θ).

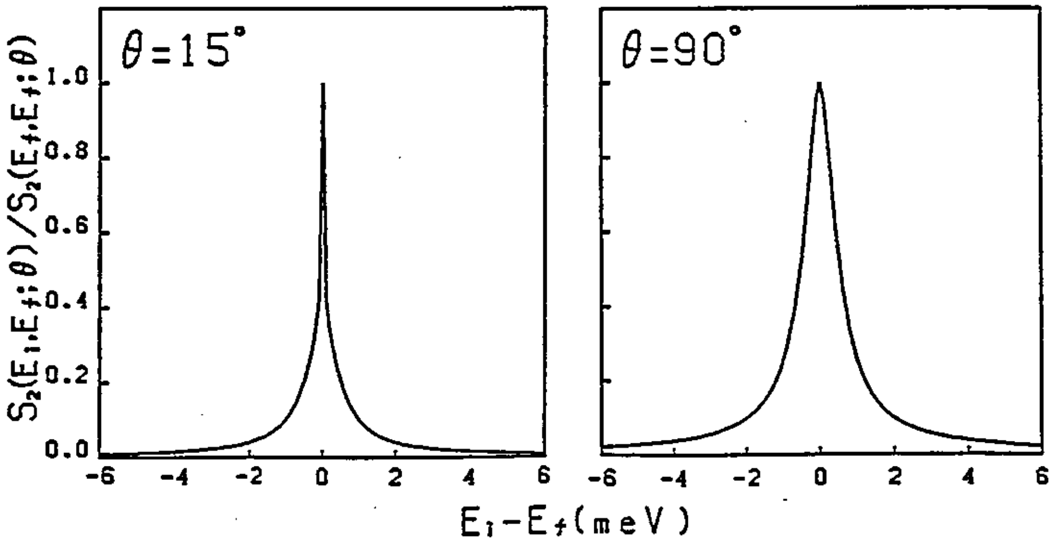

[Fig. 3] The effective scattering function of multiple scatterings, $S_2(E_i,E_f;\theta)$, in which the neutrons were scattered twice inside a water sample quoted in Fig. 1.

Quasielastic Neutron Scattering of Rare Earth Chloride Aqueous Solutions

Takashi Sakuma, Kaoru Shibata*, Hideshi Fujishita*,
Sadao Hoshino* and Kazuhiko Inoue**

Department of Physics, Ibaraki University
Mito 310, Japan

*Institute for Solid State Physics, The University of Tokyo
Roppongi, Minato-ku, Tokyo 106, Japan

**Department of Nuclear Engineering, Faculty of Engineer
Hokkaido University, Sapporo 060, Japan

Rare earth chloride aqueous solutions behave as typical strong electrolytes containing ions of high charge1), 2). From an analysis of radial distribution functions obtained by X-ray diffraction measurements, it was found that the water coordination number of the rare earth ions in aqueous solutions decreases from nine to eight due to the decreasing rare earth ionic radii. From this result it was inferred that the octaaquo complex $[RE(H_2O)_8]^{3+}$ and the nonaaquo complex $[RE(H_2O)_9]^{3+}$ are the predominant hydration species for the ions Tb^{3+} through Lu^{3+} and for the ions La^{3+}, Pr^{3+} and Nd^{3+}, respectively. The water coordination of rare earth ions is larger than that of Al^{3+} ion ($Al(H_2O)_6{}^{3+}$) and Ni^{2+} ion ($Ni(H_2O)_6{}^{2+}$) which exibit strong hydration. To confirm the complexity of rare earth ions from the measurement of dynamical properties of water molecules, we performed quasielastic measurements of 1.75M $LaCl_3$, $HoCl_3$ and $YbCl_3$ aqueous solutions using the LAM spectrometer.

Scattering specimens were prepared in a sample container of 14mm diameter cylinder, 2mm in thickness and 80mm in length. The thin wall of the container, made of Al, was gold plated. The quasielastic scattering at room temperature was measured at seven different values of scattering angles satisfying $2\theta=8^\circ+(n-1)\times16^\circ$ (n=1, 2, ... , 7). The elastic scattering energy corresponded to 4.6meV. The observed spectra of 1.75M $LaCl_3$ aqueous solution are shown in Fig. 1.

Analyzing the whole shape of energy spectrum of scattered neutron, the hydration of rare earth ions is studied. Using H_2O as the solvent, most part of the scattering intensity from solution can be regarded as due to the proton incoherent scattering. The scattering law is written using two Lorentzians;

$$S_{inc}(Q,\omega) \propto \frac{1}{\pi}\{ \delta_b \frac{\Gamma(Q)}{\omega^2+\Gamma(Q)^2} + \delta_f \frac{\Gamma(Q)}{\omega^2+\Gamma(Q)^2} \}$$

where $\Gamma_b(Q)$ and $\Gamma_f(Q)$ are the half of the full width at half maximum (FWHM) of the Lorentzians for water bound to rare earth ion and for free water, respectively. The intensity of the scattered spectrum around $\omega=0$ corresponds to the scattering mainly from water bound to rare earth ion. Comparing to the scattered spectra for $AlCl_3$ aqueous solution$^{1)}$, the scattered spectrum around $\omega=0$ of $LaCl_3$ aqueous solution in Fig. 1 is not so remarkable. This might suggest that the number of water molecules bound to rare earth ion is less than 8, and the octaaquo and nonaaquo complex do not exist. The detailed analysis of the data of rare earth chrolide aqueous solution using above scattering law is now in progress.

References

1) Y. Waseda and T. Sakuma: Metal Physics Seminar 5(1982)201.
2) A. Havenshuss and F. H. Spedding: J. chem. Phys. 73(1980)442.
3) T. Sakuma, S. Hoshino and Y. Fujii: J. Phys. Soc. Jpn. 46(1979)617.

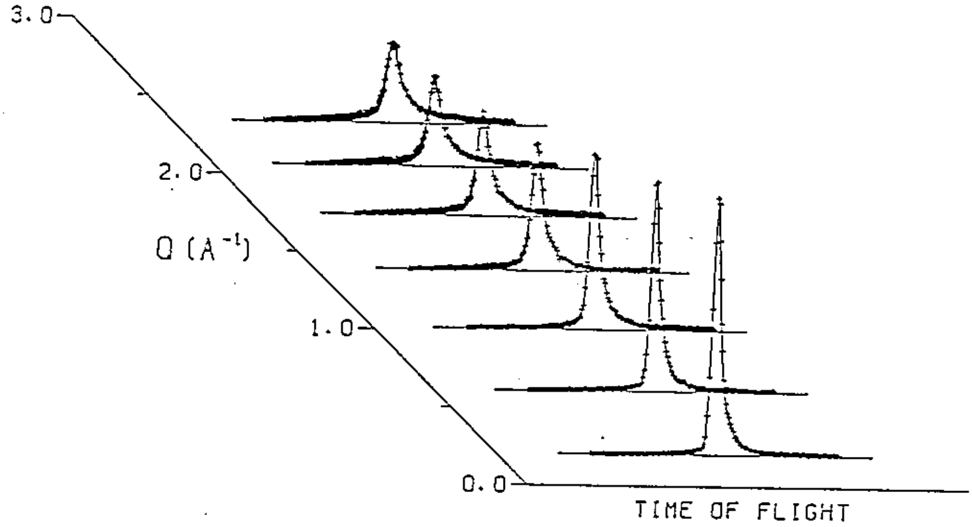

Fig. 1 Quasielastic scattering spectra of 1.75M $LaCl_3$ aqueous solution

Thermoreversible Gelation of the Polystyrene—Carbon Disulfide System

Yoshinobu IZUMI, Yasuhiro MIYAKE and Kazuhiko INOUE*

Department of Polymer Science, Faculty of Science,
*Department of Nuclear Engineering , Faculty of Engineering,
Hokkaido University, Sapporo 060, Japan

Recently, it has been found that atactic polystyrene (aPS) exhibits thermoreversible gelation in a large number of solvents$^{1)}$. Although the characterization of thermoreversible gelation in aPS solutions has been examined, no clear explanation has been given for the gel formation. Furthermore, the aPS—carbon disulfide (CS_2) system among these solutions shows a multicritical phenomenon, where one end of gelation curve ends in the ordinal critical point$^{2)}$. Such a multicritical point is indicated by c_{MC} and T_{MC} in Fig. 1, where the curved solid line indicates the gelation curve and the broken curve indicates the phase boundary line. The inverse triangles shown in the figure indicate the data points measured in the present work. As the system approaches the multicritical point, the correlation range ascribed to concentration fluctuations and the connectivity ascribed to the gel formation diverge simultaneously. It is therefore very interesting to study how observables behave at the multicritical point.

The present work is concerned with the first observation of the dynamic behavior of multicritical phenomena of the aPS—CS_2 system by neutron quasielastic scattering(NQES) measurements. This system is also very suitable for neutron experiments, because CS_2 is almost transparent to neutrons, a condition of which permits us to study the incoherent scattering of only polystyrene. Polystyrene (Pressure Chemical Company) characterized by MW=9000 and M_w/M_n<1.06 was used.

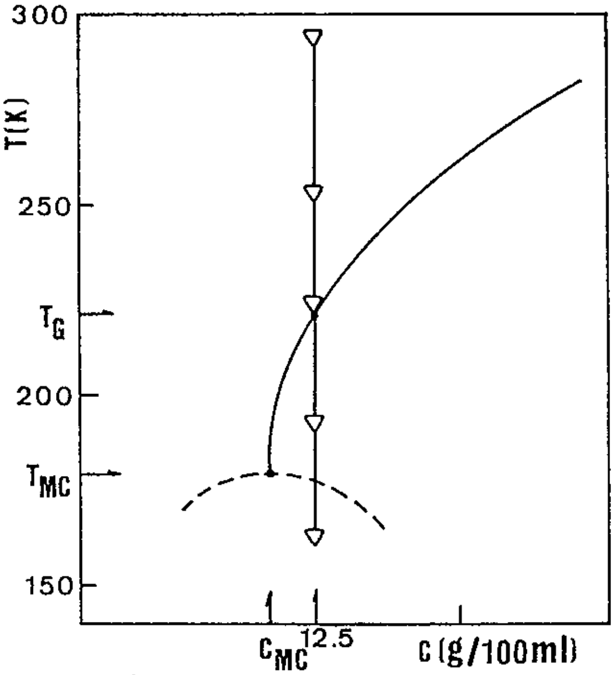

Fig. 1. Phase diagram of the aPS (MW=9000,M_w/M_n<1.06)—CS_2.

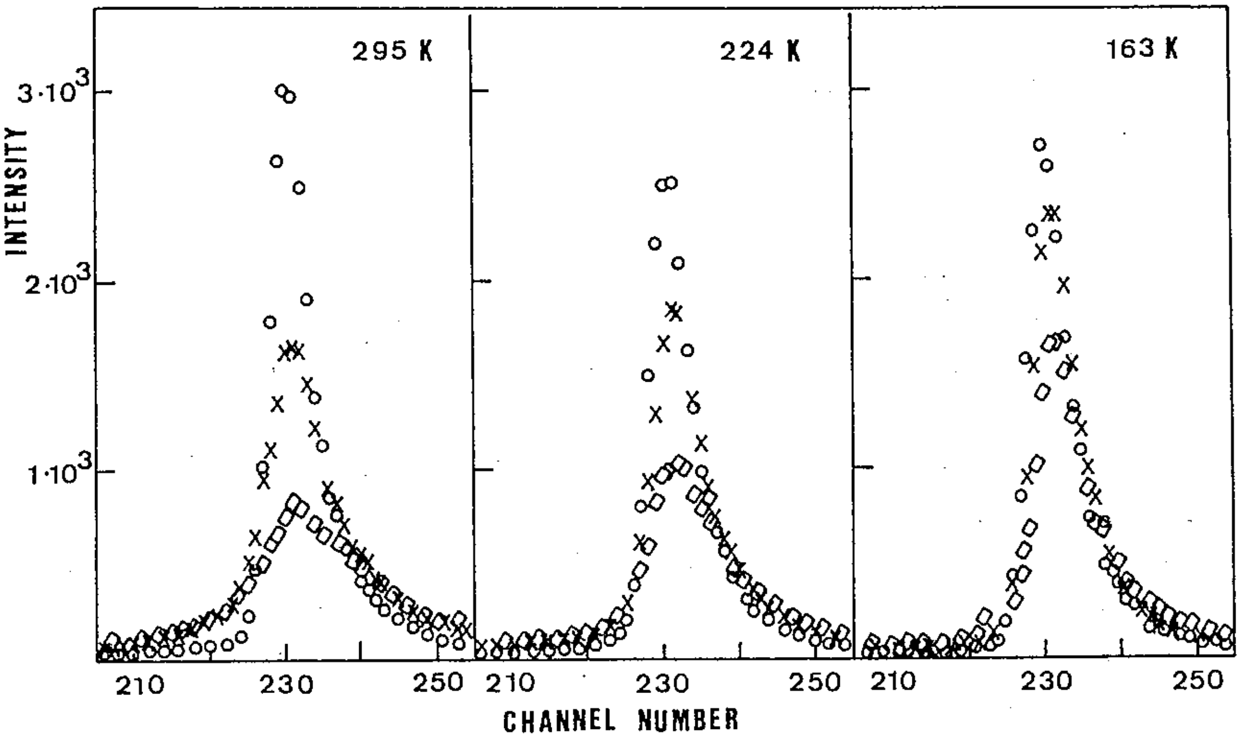

Fig. 2. Time–of–flight spectra of the aPS–CS$_2$ system at 295, 224 and 163 K; (o) 8°; (x) 56°; (◇) 104°.

Reagent grade CS$_2$ after fractionally distilled was used as the solvent.

Fig. 2 shows the time–of–flight spectra at 295, 224 and 163 K. Fig. 3 shows the Q^2 dependence of the full width at half maximum (FWHM) estimated from the NQES spectra in Fig. 2. It is seen that the FWHM at each temperature is proportional to Q^2, which is in accordance with the theoretical prediction by Akcasu et al[3]. From the slopes, we can estimate the apparent diffusion coefficient Γ/Q^2 of the size corresponding to the monomer unit (or benzene ring)[3]. The gelation temperature t_G is then defined as the temperature at which the value of Γ/Q^2 disappears (t_G= 139 K). The value of t_G is clearly different from the T_G shown in Fig. 1. This means that the T_G determined from the macroscopic method, like the ball–drop method, does not equal the t_G obtained from the microscopic method, as in the NQES method.

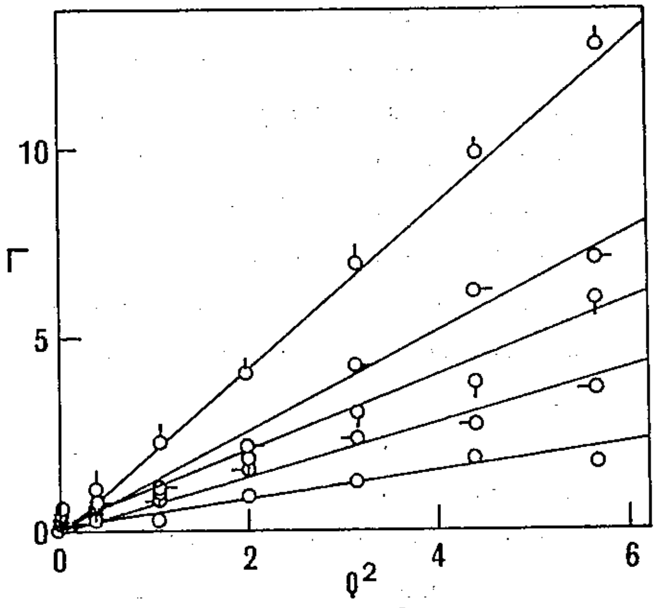

Fig. 3. Plot of FWHM vs Q^2: (ȯ)295 K; (o-)253 K; (ọ)224 K; (-o)193 K; (o)163 K.

Fig. 4 shows the plot of Γ/Q^2 vs $T-t_G$. The straight line in the figure has a slope of 0.90±0.10. Further study on the dynamic property of the present system is being planned using the deuterated polystyrene, which permits us to study the coherent scattering of the present system.

This work was partly supported by the Grant-in-Aid from the Ministry of Education, Science and Culture.

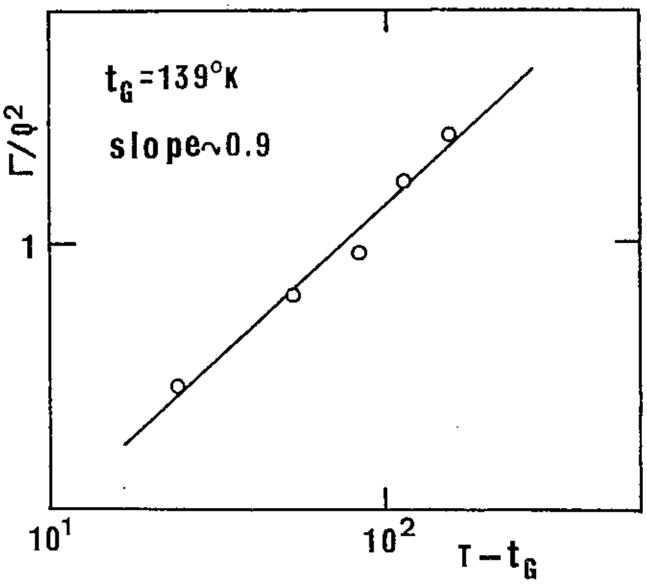

Fig. 4. Plot of the apparent diffusion coefficient Γ/Q^2 vs $T-t_G$.

References

1) Hui-Min Tan, A.Moet, A.Hiltner and E.Baer, Macromolecules, 16,28(1983).
2) In connection with critical phenomena in a polymer solution, for example, Y.Izumi, H.Sawano and Y. Miyake, Phys.Rev.A29, 826(1984).
3) Z.Akcasu and H.Gurol, J.Polym.Sci., Polym.Phys.Ed., 14, 1(1976).
Z.Akcasu, H.Benmouna and C.C.Han, Polymer, 21, 866(1980).

Quasielastic Neutron Scattering from Polyelectrolytes in Solution

Ichiro NODA, Yoshio MUROGA, Yuji HIGO and Kazuhiko INOUE*

Department of Synthetic Chemistry, Faculty of Engineering
Nagoya University, Furo-cho, Chikusa-ku, Nagoya 464, Japan

*Department of Nuclear Engineering, Faculty of Engineering
Hokkaido University, Sapporo 060, Japan

Studies on hydrodynamic properties of polyelectrolyte solutions have revealed that the translational motion of a polyelectrolyte as a whole is directly affected by the electrostatic interaction. However, little is known about local motions of polyelectrolytes. In the present work, therefore, we measured quasielastic neutron scattering from polyelectrolyte solutions to clarify the effect of electrostatic interaction on the local motions of polymer chains.

Poly(sodium acrylate)s with two different degrees of ionization α = 0.1 and 1.0 were used as the sample to examine the effect of charge density, and pure D_2O and D_2O solution of 0.5 M NaBr were used as the solvent to examine the effect of ionic strength. The concentrations of poly(sodium acrylate)s with $\alpha = 0.1$ in D_2O, $\alpha = 1.0$ in D_2O and NaBr solution were 0.163, 0.140 and 0.137 g/cm^3, respectively.

The measurements of quasielastic neutron scattering were carried out at room temperatures by using the LAM-40 spectrometer at KEK. A gold plated aluminum cell of coaxial cylinder was used to avoid ionic contamination in the sample solutions.

Figure 1 shows the data of quasielastic neutron scattering spectra from poly(sodium acrylate)s with $\alpha = 0.1$ in D_2O, $\alpha = 1.0$ in D_2O and NaBr solution. It is observed in Figure 1 that there is a difference between the spectra of poly(sodium acrylate)s with α = 0.1 and 1.0 in D_2O, while there is no significant difference between the spectra of poly(sodium acrylate)s with $\alpha = 1.0$ in D_2O and NaBr solution. The results imply that the local motions of polyelectrolytes are almost independent of ionic strength, but may be affected by the charge density.

We are now conducting detailed analysis of the scattering data by taking into account the resolution function of the spectrometer, and fitting the spectra to scattering functions for diffusion models. An example of the analysis is shown in Figure 2. The detailed results will be reported elswhere.

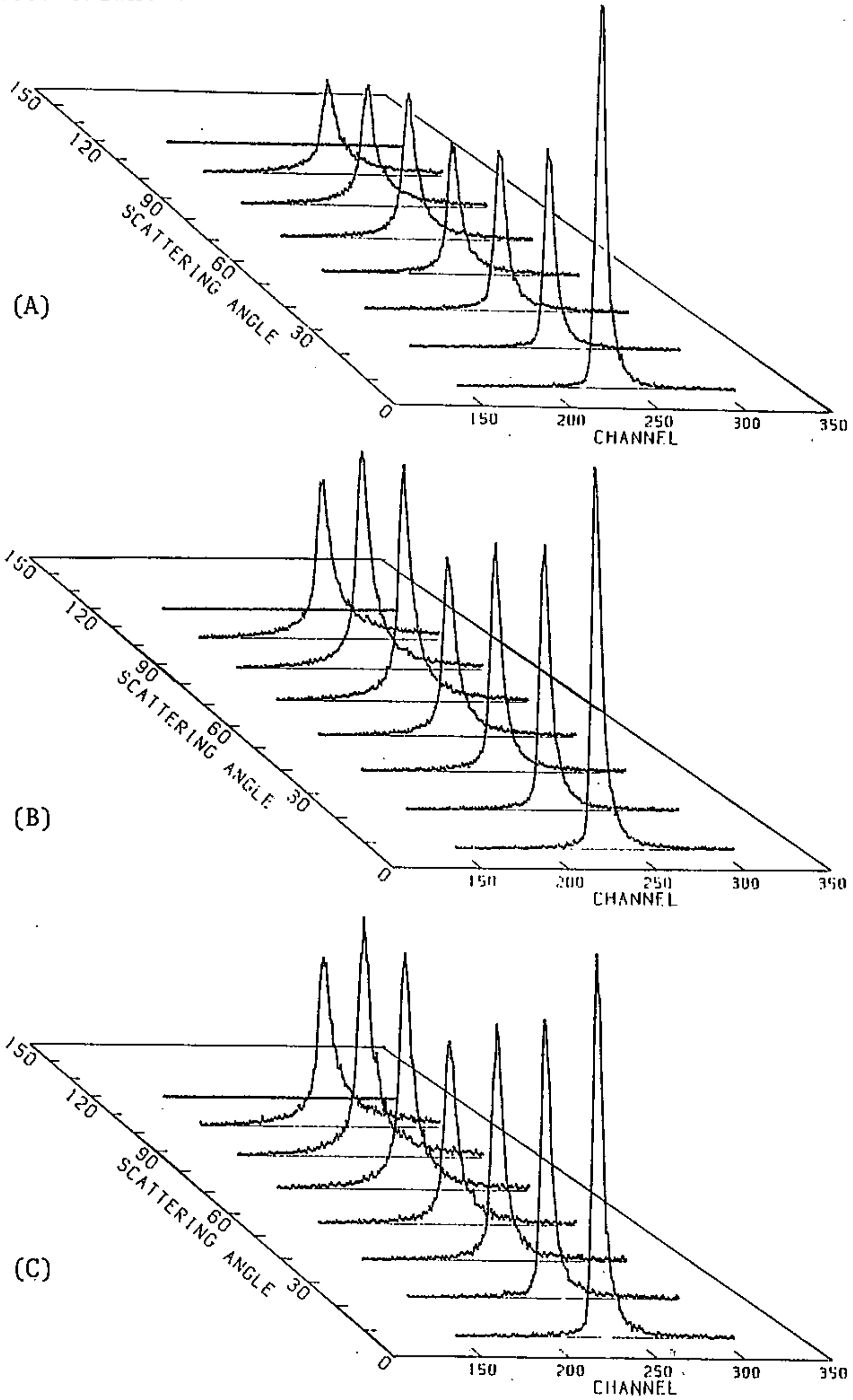

Fig.1. Quasielastic neutron scattering data of poly(sodium acrylate)s with α = 0.1 in D_2O(A), α = 1.0 in D_2O(B) and in NaBr solution(C).

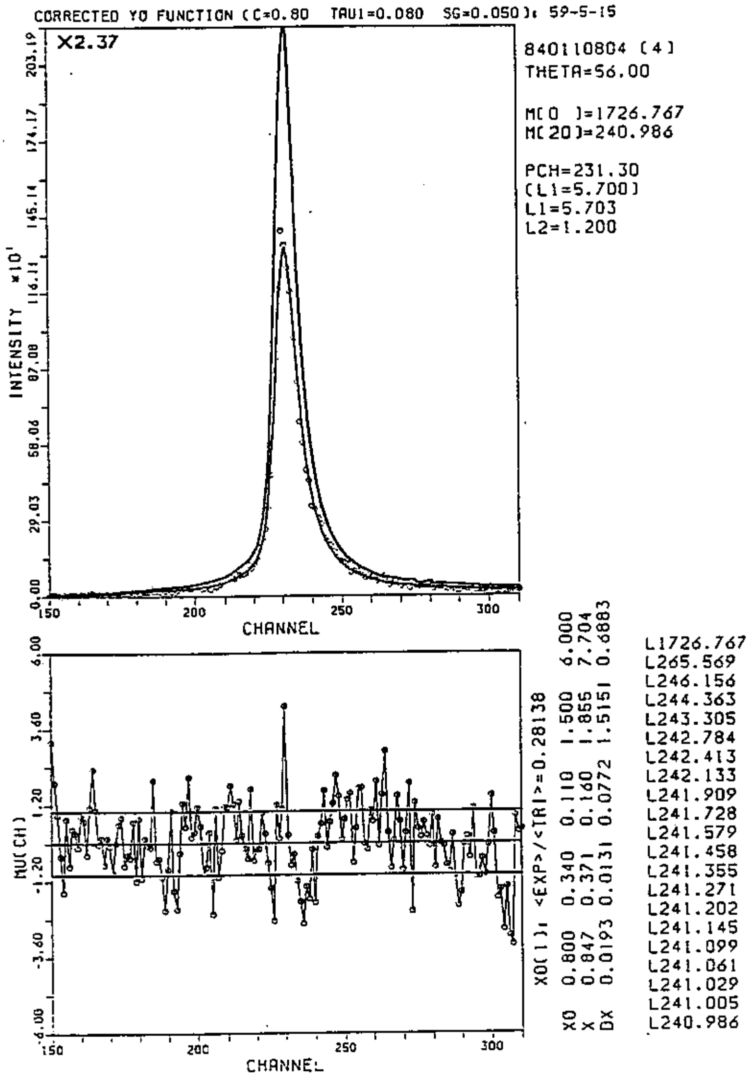

Fig. 2. An example of analysis of quasielastic neutron scattering data. Sample : poly(sodium acrylate) with α = 1.0 in D_2O.

Dynamic Scattering Function of Liquid Bismuth

Kaoru SHIBATA, Sadao HOSHINO, Hideshi FUJISHITA,
Takashi SAKUMA* and Kazuhiko INOUE**

Institute for Solid State Physics, The University of Tokyo
Roppongi, Minato-ku, Tokyo 106, Japan

*Department of Physics, Ibaraki University
Mito 310, Japan

**Department of Nuclear Engineering, Hokkaido University
Sapporo 060, Japan

Liquid Bi may be regarded as one of the most appropriate substances to study the dynamic properties of monoatomic liquids by neutron scattering. The reasons are that Bi scatters neutron almost coherently with little absorption and exhibits relatively low melting temperature. Recently we found propagating collective excitations in liquid Bi in the momentum range of $Q \leq 1.2$ A^{-1} 1). Liquid Bi is considered to exhibit a 'ledge' type attractive potential 2). This potential is fairly different from the one expected for normal metals like Rb, which is regarded as a cause of the appearance of a shoulder on the high Q side of the principal peak in S(Q). Then it is expected that the dynamic scattering function $S(Q,\omega)$ of liquid Bi near the principal peak of S(Q) is distorted by this potential. The dynamic scattering function $S(Q,\omega)$ of liquid Bi was reported by U.Dahlborg and L.G.Olsson in a relatively large Q region 3). Their measurements were performed in a relatively wide Q-ω space, but with poor energy resolution. Though our measurements were restricted in the range near the principal peak of S(Q), they were carried out with high energy resolution.

In this report, preliminary results of time spectra measured for liquid Bi at 673 K are presented. Measurements were carried out with LAM-40 in the range of Q from 0.2 to 2.5 A^{-1} for the elastic time channel. A sample container with 14 mm inner diameter and about 100 mm length was made of aluminum and its inner surface was anodized.

Figure 1 shows the time spectra corrected for the background. In

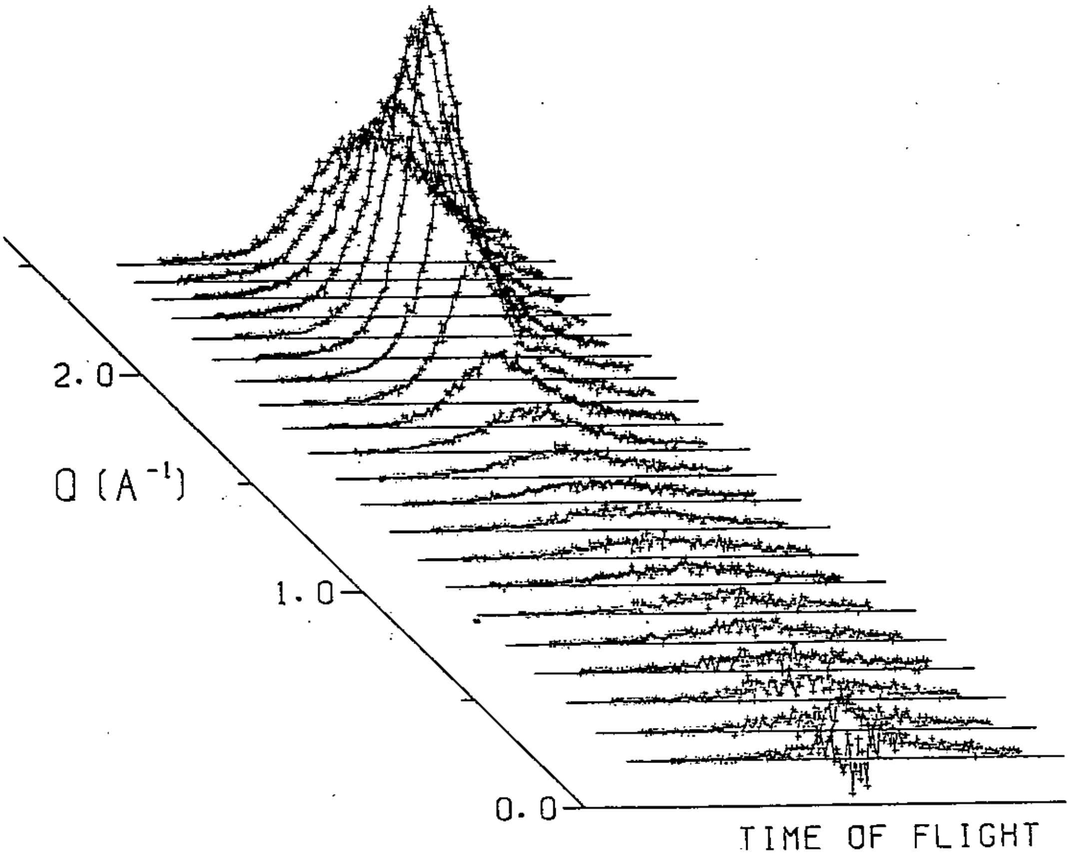

Fig. 1. Time spectra corrected for the background for liquid Bi at 673 K. Momentum values indicated in this figure correspond to the elastic time channels.

order to obtain constant-Q spectra of dynamic scattering function, and to compare with theories, detailed analysis is now in progress.

The authers thank Mr. Y.Kiyanagi for his kind help throughout the present experiment.

References

1) K.Shibata, S.Hoshino and H.Fujishita; J.Phys.Soc.Jpn.53(1984)899.
2) L.G.Olsson and U.Dahlborg; Phys.Chem.Liq.11(1982)225.
3) U.Dahlborg and L.G.Olsson; Phys.Rev.A25(1982)2712.

Cation Dynamics of Superionic Conductor Ag_3SI

Kaoru SHIBATA, Sadao HOSHINO, Hideshi FUJISHITA,
Takashi SAKUMA* and Kazuhiko INOUE**

Institute for Solid State Physics, The University of Tokyo
Roppongi, Minato-ku, Tokyo 106, Japan

*Department of Physics, Ibaraki University
Mito 310, Japan

**Department of Nuclear Engineering, Hokkaido University
Sapporo 060, Japan

A microscopic mechanism related to the high ionic conductivity in so-called superionic conductors is an interest subject to study. A superionic conductor Ag_3SI exhibits two phase transitions as shown in Fig. 1$^{1)}$. At its β-α phase transition at 246°C, an order-disorder arrangement of the two kinds of anions, S and I, takes place. The structure of α-Ag_3SI is of the α-AgI type, and it was found to be retained at low temperature by quenching. Then we can study an equilibrium as well as a non-equilibrium state of α-Ag_3SI in a wide temperature range.

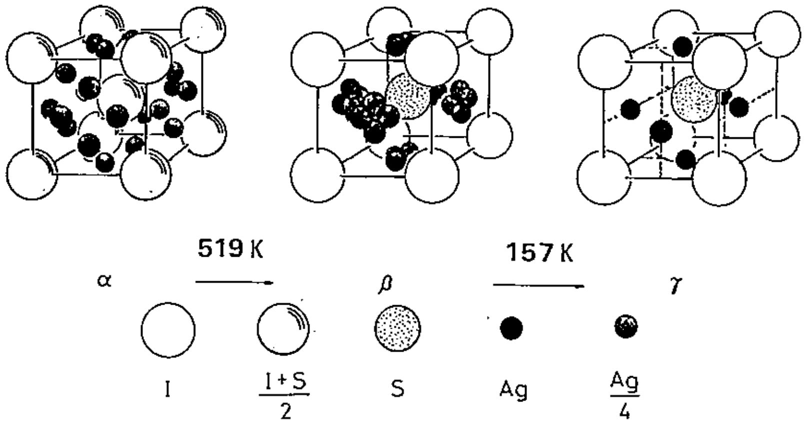

Fig. 1. Structure change of Ag_3SI by means of successive phase transitions.

In this note results of a quasielastic and an inelastic neutron scattering of α- and β-Ag_3SI at the equilibrium and the non-equilibrium states are reported. Measurements were carried out with LAM-40 and LAM-D spectrometers using powder samples which were contained in an aluminum cylindrical tube with 14 mm inner diameter and about 100 mm length. In the measurements at high temperature, heater blocks were attached on a top and a bottom of the sample container.

Figure 2 shows quasielastic scattering spectra measured by LAM-40 spectrometer. The spectra of α- and β-Ag_3SI at high temperature consist of a broad and a narrow quasielastic component. The two components are usually explained as follows; the narrow quasielastic component is caused by a translational motion of cations and the broad one by a local motion of cations. However details are still unknown.

The spectra of β- and quenched α-Ag_3SI at room temperature, on the other hand, consist of the elastic and the inelastic component. The measurement with LAM-D spectrometer shows an existence of the inelastic peak with a low energy transfer as indicated in Fig. 3. Though such

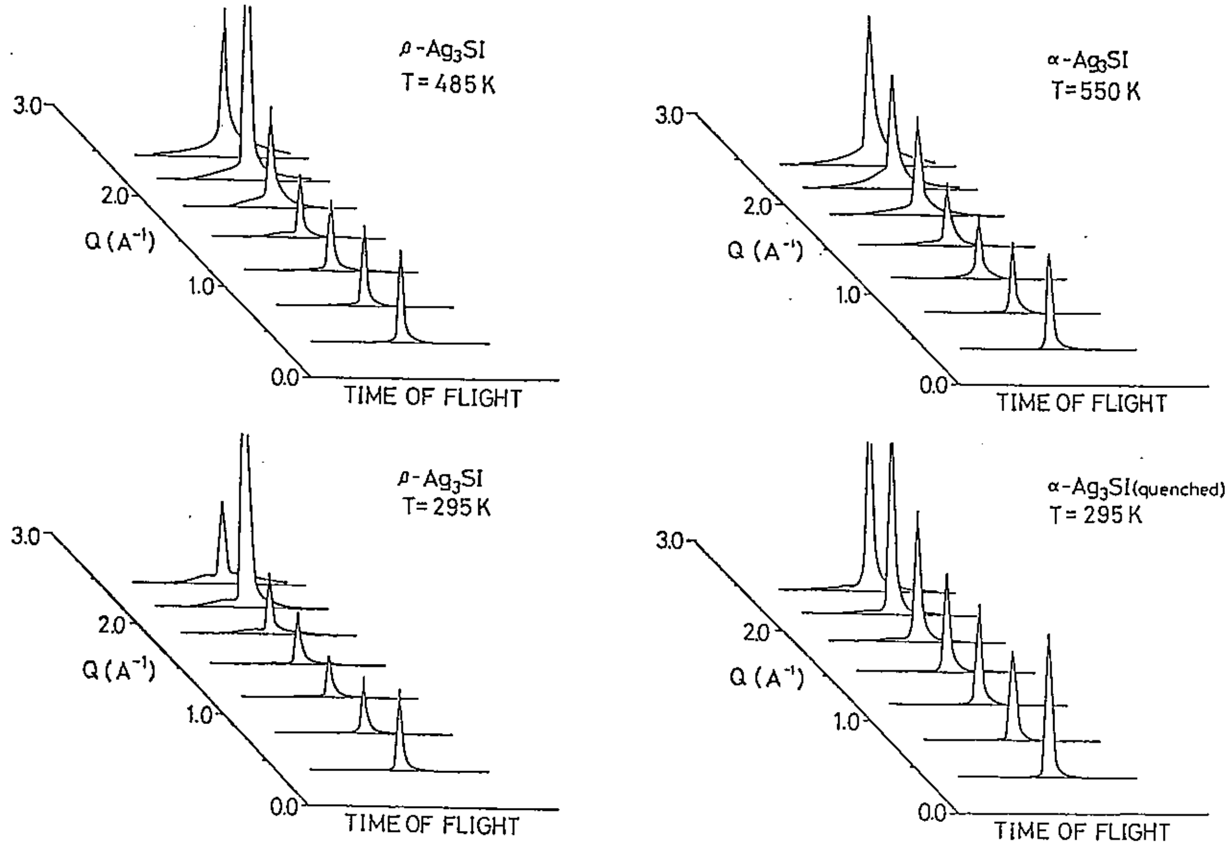

Fig. 2. Quasielastic scattering spectra of Ag_3SI by LAM-40

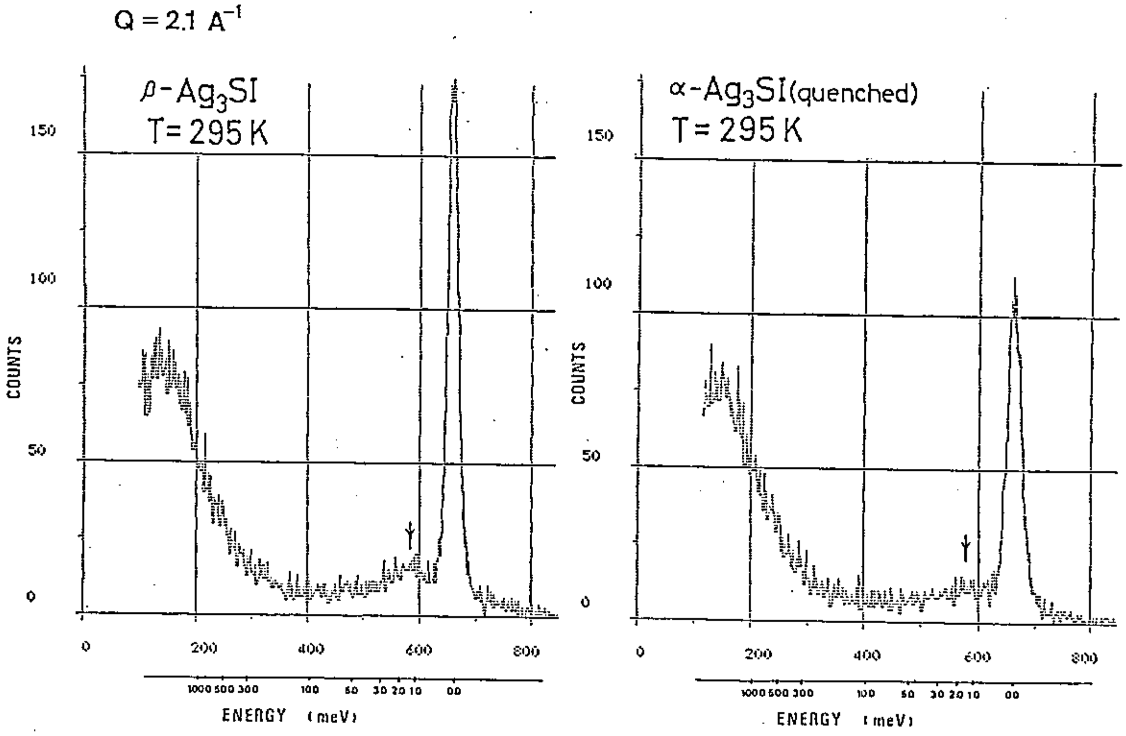

Fig. 3. Local mode excitations of Ag ions in Ag$_3$SI by LAM-D

a low energy excitation has already been found in other superionic conductors (AgI,RbAg$_4$I$_5$,etc.), this is the first observation in β- and quenched α-Ag$_3$SI. The low energy excitation is explained by a local Einstein-type vibration of cations.

Detailed analysis of the above results are now in progress.

The authors thank Mr. Y.Kiyanagi for his kind help throughout the present experiment.

Reference

1) S.Hoshino, T.Sakuma and Y.Fujii : J.Phys.Soc.Jpn.47(1979)1252.

Quasielastic Scattering Studies of Rubber Polymers

K. INOUE*, K. KAJI**, T. KANAYA** and R. KITAMARU**

* Department of Nuclear Engineering, Hokkaido University,
Sapporo, 060 Hokkaido, Japan
** Institute for Chemical Research, Kyoto University,
Uji, 611 Kyoto-hu, Japan

Neutron quasielastic scattering spectra of rubber state polymers can provide information on the segmental diffusive motions of polymers. We measured the quasielastic spectra from cis-poly(butadiene) and cis-poly (isoprene) above and below the melting temperatures. In this short report we will describe some preliminary results.

Figs.1 and 2 show the measured spectra using the LAM-40 spectrometer at ambient temperature; the temperature is above the melting point for poly(butadiene), and is between the melting and glass transition points for poly(isoprene), respectively. The width of the central narrow peaks as a function of Q reflects these conditions. In the former case, as also described below, the central peak width becomes wider for larger scattering angles. On the

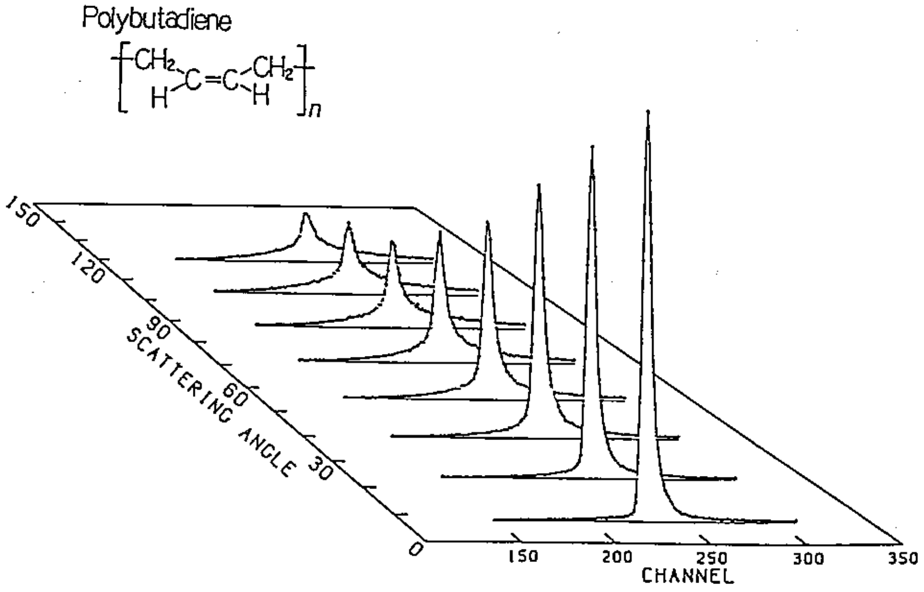

Fig.1 Scattered spectra from poly(butadiene) measured by the LAM-40 at ambient temperature.

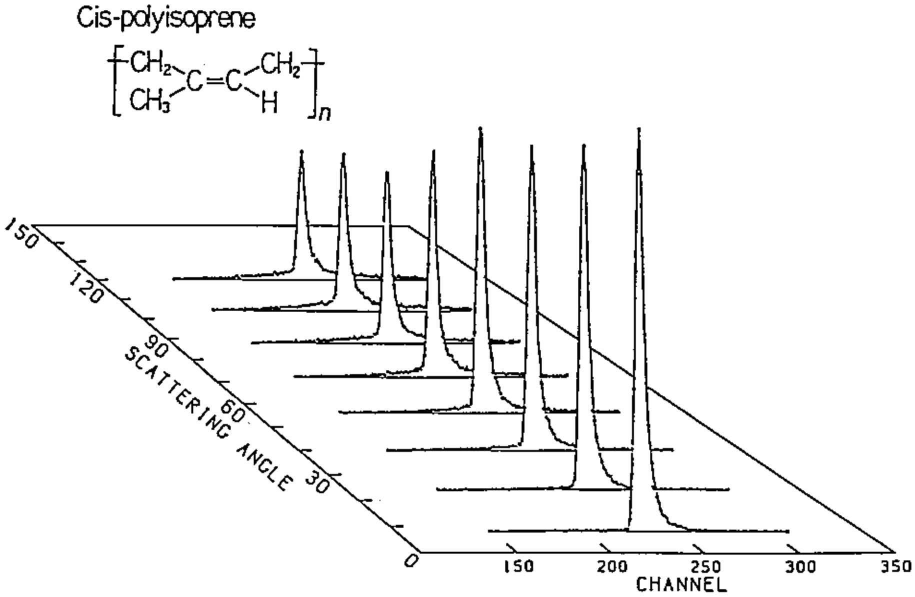

Fig.2 Scattered spectra from poly(isoprene) measured by the LAM-40 at ambient temperature.

other hand, in the latter case, the central peak width does not change, and is the same as the one for the elastic scattering.

Fig.3 depicts the spectra from poly(butadiene) measured by the LAM-80 at two temperatures, above the melting point and between the melting and glass transition points. Fig.4 shows the FWHM of the central sharp peaks as a function of Q^2. Above the melting point, the main chaine of poly(butadiene) executes translational diffusive motion, but its

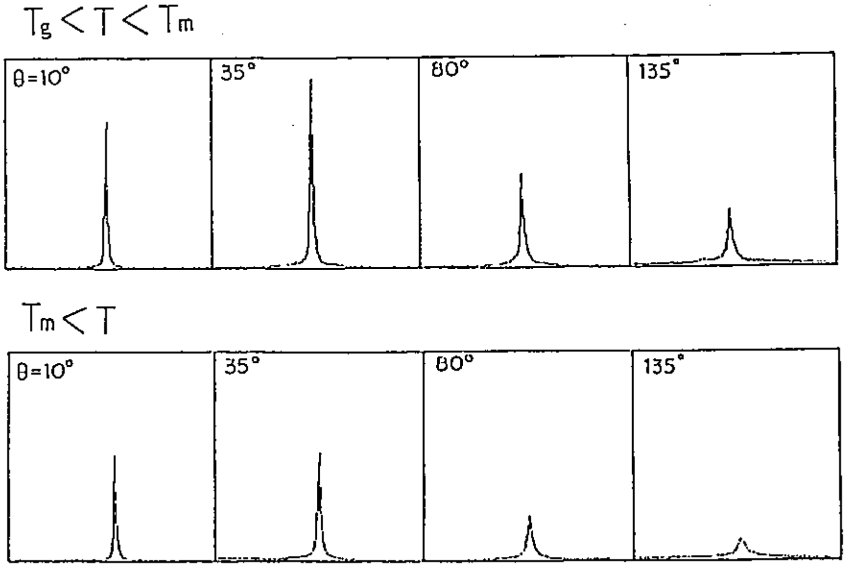

Fig.3 Scattered spectra from poly(butadiene), between the melting and glass transition temperatures and above the melting temperature, measured by the LAM-80.

characteristic pattern is still not clear. We are now conducting data analysis of the spectra using a statistical data analysis code1), and will report the results elsewhere.

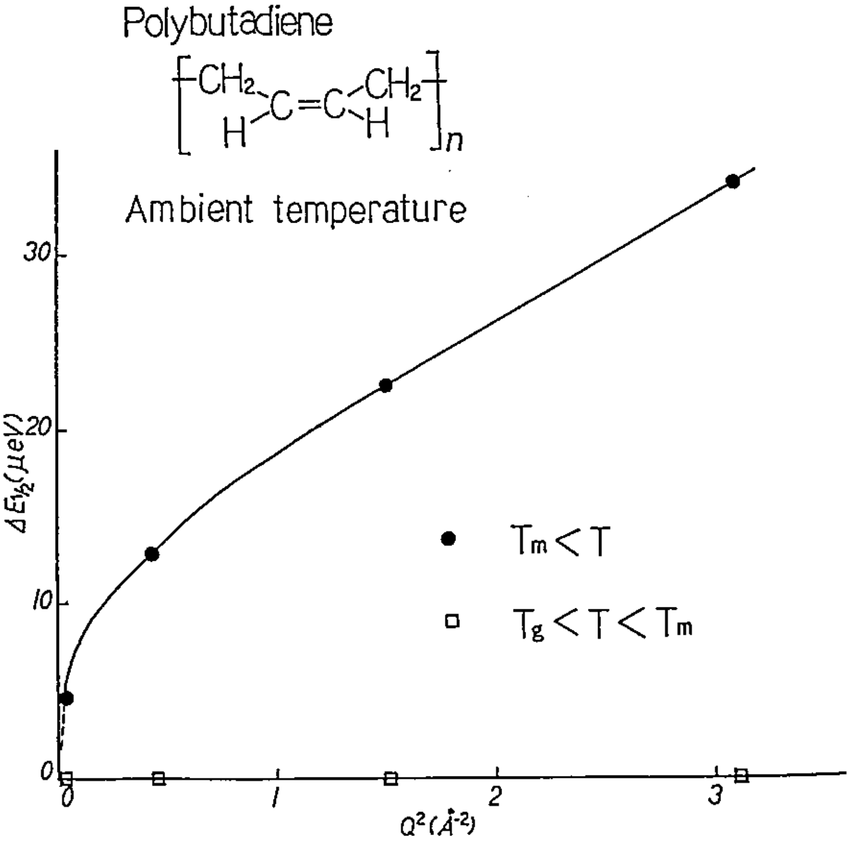

Fig.4 The FWHM of the central sharp peak of the scattered spectra from poly(butadiene) at two temperatures.

References

1) K. Inoue: Bull. of Faculty of Engrg. Hokkadio University, 112(1983)83.

Observation of the Phase Transition in the Bilayer Membrane of Dialkyl Amphiphile by Neutron Inelastic Scattering

Yuji MATSUDA, Yuji ITO and Kazuhiko INOUE*

Institute for Solid State Physics, the University of Tokyo
Roppongi, Minato-ku, Tokyo 106, Japan

*Department of Nuclear Engineering, Hokkaido University
Sapporo 060, Japan

Dialkyl ammonium amphiphiles are known to form the multilamellar liposome composed of the bimolecular layers when dispersed in aqueous solution. It is also well known that such artificial bilayer membranes exhibit the phase transition near room temperature which is attributed to the melting of the alkyl carbon chains$^{1)}$.

Understanding the nature of the transition is important, since many physiological functions taking place in biomembranes are related to the characteristics of the mesomorphic phase of the bilayer system. From this point of view, the dialkyl amphiphiles are considered to be the simplest model substance of the bio-lipidmembrane.

Many structural and dynamical studies on artificial lipid membrane systems have thus been carried out to elucidate the nature of the phase transition. By these investigations the following general picture of the melting transition emerges.

As the transition point T_m is approached from below T_m, the trans-guache kink clusters are formed in the hitherto all trans crystalline state of the alkyl chains. Associated with the kink formation, the local molar volume is diminished, and such a process is regarded as the origin of the fast nano-second relaxation observed by various probes as ultrasonic attenuation$^{2)}$, fluorescence polarized light spectroscopy$^{3)}$ and laser turbidity measurement$^{4)}$. The subsequent slow milli-second relaxation process observed by the various temperature jump methods$^{5,6)}$ in turn arises from the interaction of the propagating kinks with other degrees of freedom including the head groups and aqueous bath. The melting of the chains then increases the volume of the bimolecular layers.

Detailed investigation of the elementary process of the chain melting would best be done by means of the neutron scattering technique, since it can probe the spatial extent and the life time of the kink formation simultaneously, provided the time scale involved is within the resolution of the neutron spectroscopy.

In this regard, we undertake to study the melting process of didodecyldimethyl ammonium bromide $[CH_3(CH_2)_{11}]_2N(Br)(CH_3)_2$ (DDAB) by following the change of the proton motion of the alkyl chain through the transition temperature by means of neutron incoherent inelastic scattering.

DDAB is chosen, since it is commercially available and has the shortest carbon chain length which exhibits the phase transition (actually the phase transition can be observed only when the temperature is increased after the DDAB solution is once frozen below 0°C), and because of this there is reason to believe that the characteristic time for the kink diffusion may be relatively short in this system.

Measurements were taken using a 5% DDAB/D_2O solution in the specially fabricated thin wall Al container both at LAM-40and at LAM-80spectrometers of KENS situated at KEK, Tsukuba. As the temperature dependence was taken only at LAM-80, we report here the data taken at LAM-80, which compared to LAM-40 has better energy resolution by an order of magnitude.

Figures 1–4 summarize the observation. In each figure, the numbers (1 to 4) correspond to the detector number. The scattering angle for each detector is fixed at 10° for No.2, 35° for No.1, 80° for No.3, 135° for No.4. In Fig.1, the sample was once cooled down to about -10° C, and then the temperature was slowly raised and held at about -5° C; data were collected for a period of one hour. In Fig.2, T=5°C and the data collecting time was 0.5 hrs. In Fig.3, T=10°C with 1.5 hrs, and in Fig.4, T=20° C with 1.5 hrs data collection time. Notice the change of the time channel scale of Fig.4 compared to others.

These data reveal that some drastic change took place in the temperature range between 10 and 20°C in accordance with the known transition temperature of 16°C for DDAB$^{1)}$. The change is seen most clearly in the data taken by detectors No.2 and No.4. With the mean wavelength of 6.60Å used in the present measurements, the observed strong elastic peak of No.2 detector at T=20°C indicates the bimolecular distance of the liposome being about 38Å. However, $T \lesssim 10°C$, the distance should be larger than this, since no such peaks are observed at $2\theta = 10°$ by No.2 detector. Therefore, the bilayer distance decreases upon melting in the 5% DDAB/D_2O system.

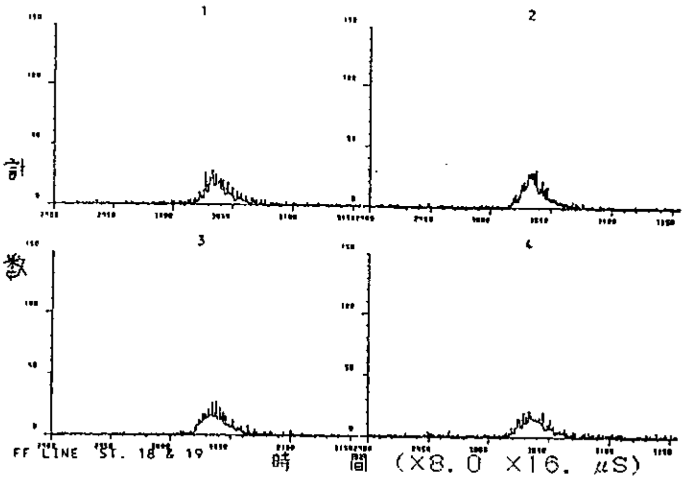

Fig.1

DDAB at -5°C for 1 hour

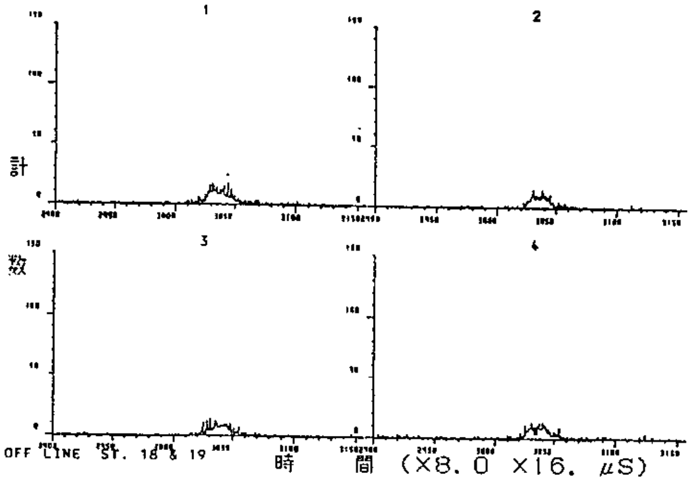

Fig.2

DDAB at 5°C for 0.5 hrs

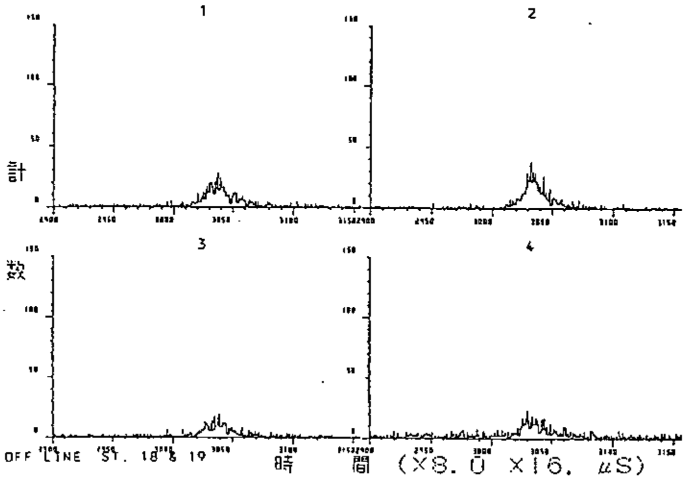

Fig.3

DDAB at 10°C for 1.5 hrs

Fig.4

DDAB at 20°C for 1.5 hrs

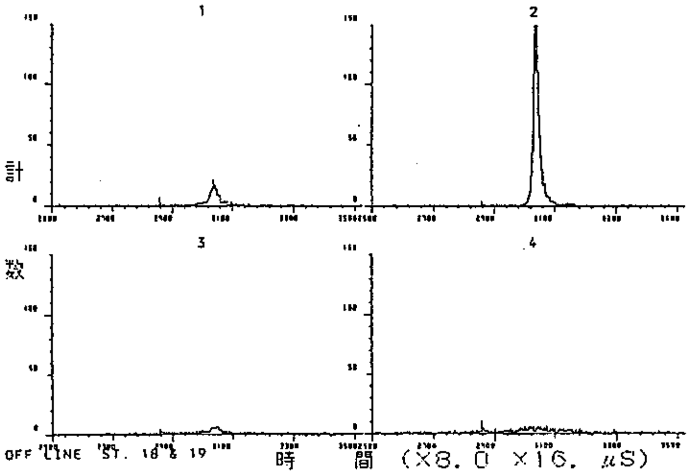

It is evident from the large increase of the inelasticity observed at the high momentum transfer region at T=20°C, that change of the proton dynamics upon the chain melting could be observed in the present system. Valuable information concerning the elementary melt-process can indeed be obtained by the high resolution inelastic neutron spectroscopy. These data are now being analyzed using a model of the proton rotational diffusion in the liquid crystalline phase.

1) Y.Okahata, R.Ando and T.Kunitake, Ber. Bunsenges. Phys. Chem., 85, 789 (1981).
2) R.C.Gamble and P.R.Schimmel, Proc. Natl. Acad. Sci. USA, 75, 3011 (1978).
3) K.Kinoshita, S.Kawato and A.Ikegami, Biophys. J. 20, 289 (1977).
4) J.F.Holzwarth, W.Frisch and B.Gruenwald, Microemulsion p.185, Plenum Publishing Corp. (1982).
5) T.Y.Tsong and M.I.Kanehisa, Biochemistry 16, 2674 (1977).
6) S.Inoue, M.Nishimura, T.Yasunaga, H.Takemoto and Y.Toyoshima, J.Phys. Chem., 85, 1401 (1981).

Neutron Quasielastic Scattering from Solid Benzene

Yoshiaki KIYANAGI and Kazuhiko INOUE

Department of Nuclear Engineering, Hokkaido University,
Sapporo, 060 Hokkaido, Japan

Rotational diffusion modes in solid phase of the globular molecules have been studied by the neutron quasielastic scattering$^{1)}$. However, the presence of the rotational diffusion mode in solid benzene, which is a plane molecule, has not been confirmed although NMR study suggested that the benzene molecule ratated at a temperature jsut below the melting point$^{2)}$. The time constant of the rotational mode in solid benzene will be larger than that of the globular molecules, so that the high resolution neutron quasielastic spectrometers is required in order to study the rotation in solid benzene. We measured the neutron quaseilastic scattering spectra by using LAM-40 and LAM-80 spectrometers at KENS in order to comfirm the presence of the rotational diffusion mode and studied the rotational mode of solid benzene. The resolutions of the two spectrometers are about 200 μeV and 20 μeV, respectively.

The TOF spectra measured by LAM-40 are shown in Fig.1. The sample temperature was 253°K. The spectra at seven different scattering angles show no remarkable change in peak width and are similar to pure elastic ones. However, the expanded spectra of 253 K and 200 K data show that the

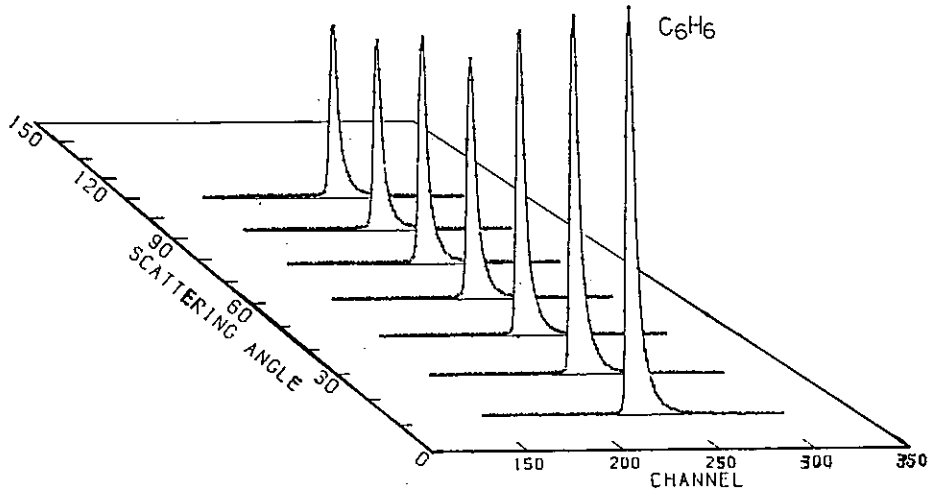

Fig.1 TOF spectra measured by LAM-40.

peak width of 253 K spectrum is slightly wider than that of 200 K ones as shown in Fig.2. As the broadening of quasielastic peak of benzene is less than the LAM-40 resolution by about one order, it is necessary to measure the quasielastic spectra by using a higher resolution spectrometer. We

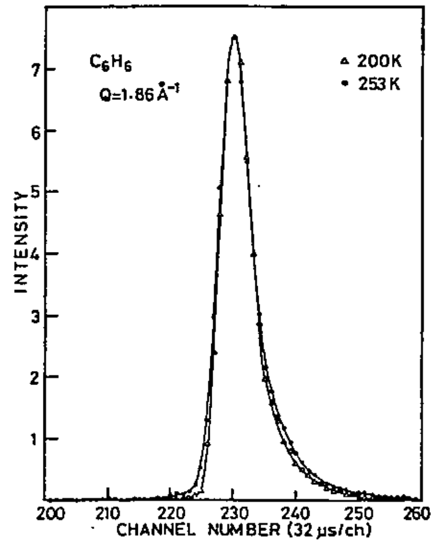

Fig.2 Expanded spectra at 1.86 Å^{-1}.

used the LAM-80 spectrometer to carry out these measurements. Figure 3 shows the spectra measured at scattering angles of 10, 35, 80 and 135°. The peak shapes of the spectra become broad with increase of scattering angles. The FWHM of the quasielastic parts is shown in Fig.4, which does not depend strongly on momentum transfer Q at large Q values. This is typical for rotational diffusion mode. It is clearly confirmed that there is the rotational diffusion mode in solid benzene. The crystal structure of solid benzene belongs to the space group P_{bca} (D^{15}_{2h}). The arrangement of benzene molecules is illustrated in Fig.5 3). Two types of the rotations

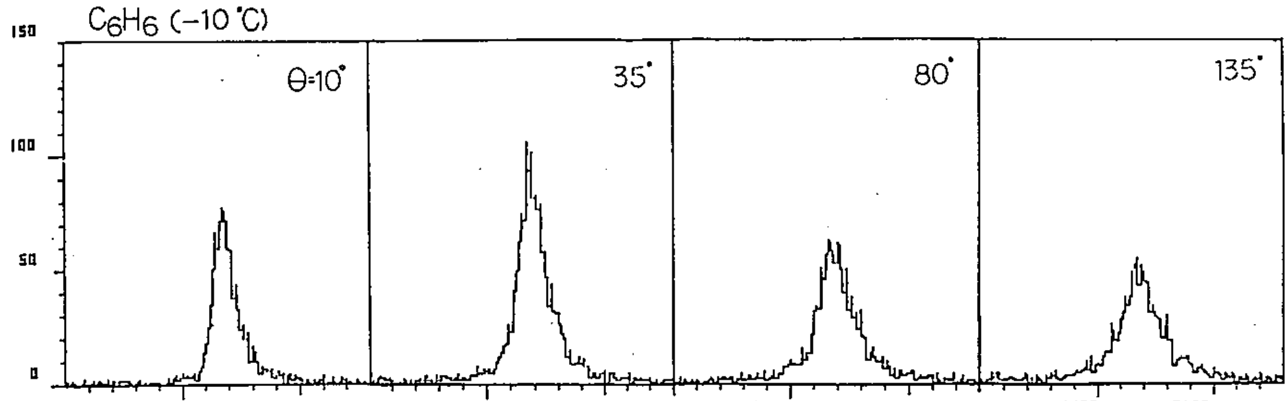

Fig.3 TOF spectra measured by LAM-80.

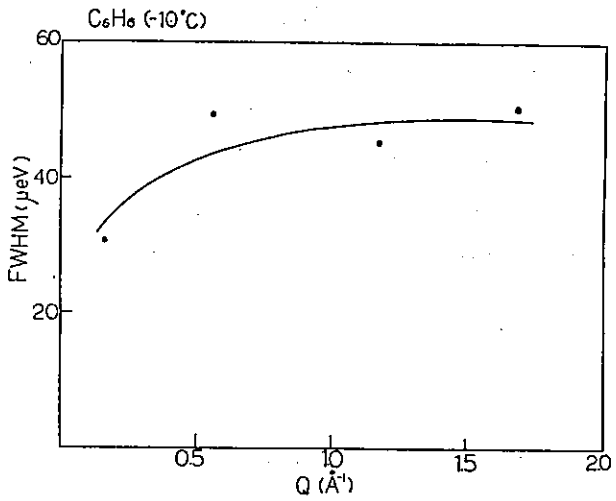

Fig.4 Full width at half maximum of quasielastic parts.

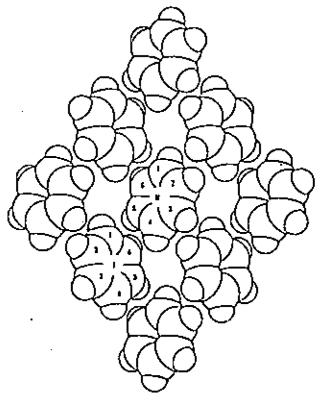

Fig.5 Crystal structure of benzene 3).

are considered in solid benzene, namely, the rotation about a hexad axis and a diad axis. It was suggested that the former was easier to take place than the latter$^{4)}$, so that we performed the prelimary analysis of quasielastic spectra measured by LAM-80 with the aide of uniaxial rotational diffusion model$^{4)}$. Here the rotational axis was the hexad one, which was perpendicular to the molecular plane. The EISF of this model is expressed as follows:

$$\mathrm{EISF} = \frac{1}{N}\sum_{p=1}^{N} j_0\left(2Qa \sin\frac{\pi p}{N}\right)$$

where N is the number of the site of the rotational jump and a is the radius of the rotation. a is 2.4 Å for benzene. Figure 6 shows the EISF obtained

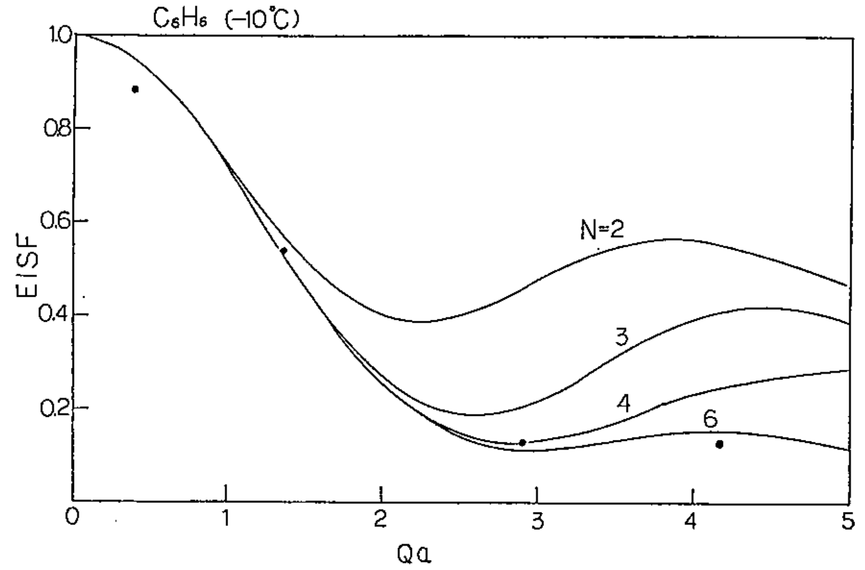

Fig.6 E I S F.

by the experimental and the numerical analyses. The values of EISF obtained by the calculation are almost the same for the N larger than 6. The experimental data are best fited by the model of N = 6, so that it is supposed that the number of jump sites is not less than 6. Series measurements scanning the wide Q range at various sample temperatures are required in order to study the rotational diffusion mode and its activation energy.

References

1) J. N. Sherwood: "The Plastic Crystalline State", John Wiley & Sons, Chichester, (1979).
2) E. R. Andrew and R. G. Eades: Proc. Roy. Soc., A218, 537(1953).
3) E. G. Cox, et al.: Proc. Roy. Soc., A247, 1(1958).
4) A. J. Dianoux, et al.: Mol. Phys., 30, 1181(1975).

Molecular Spectroscopy of Native and Regenerated Celluloses by Neutron Inelastic Scattering

K. KAJI, T. KANAYA, R. KITAMARU, and K. INOUE*

Institute for Chemical Research, Kyoto University,
Uji, Kyoto-Fu 611, and *Faculty of Engineering,
Hokkaido University, Sapporo 060

Spectroscopic studies of native and regenerated celluloses(cellulose I and II, respectively) were extensively carried out by IR and Raman scattering methods. However, no neutron scattering spectroscopy for celluloses has been reported thus far. The intensities of vibration modes in the former two spectroscopies depend on the transition dipole moment and the induced dipole moment(or the polarizability), respectively, which gives selection rules based on the symmetries of vibration. In the case of the neutron scattering spectroscopy, no such selection rules exist since neutrons are scattered with nuclei. It is therefore expected that this spectroscopy will give new information on the molecular vibrations of celluloses. Therefore, we have carried out neutron incoherent inelastic scattering(NIIS) measurements of ramie(cell. I) and rayon(cell. II) fibers, both with a moisture regain of 2.7%, by using the down-scattering spectrometer LAM-D with an inverted geometry at KENS.

Fig. 1 and 2 show, respectively, the observed time-of-flight(TOF) spectra of ramie and rayon fibers; the scattering vecter $\underset{\sim}{Q}$ is parallel (a) and perpendicular (b) to the fiber axis. These spectra cover a very wide range of frequency from the far-infrared to the near-infrared or 130 to 600 cm^{-1} though the energy resolution decreases with increasing frequency. The peaks above 500 cm^{-1} in the near-infrared range are assigned to overtones and combinations of fundamental frequencies.[1] Below 4000 cm^{-1} three main peaks around 3000, 1400, and 600 cm^{-1} are seen; from the literature[2-4] the first is assigned to the superposition of OH, CH, CH_2

stretching modes, the second to OH and CH deformation, and the last to OH out-of-plane bending. The peak consisting of CO stretching and ring modes around 1100 cm^{-1}, observed strongly both in the IR and Raman spectra, is weak in the NIIS spectra. This indicates that most of these modes do not involve vibrations of hydrogens. The comparison between the spectra of cell. I and II shows that the difference is remarkable in the range 300 to 500 cm^{-1}, as in the case of the Raman spectra. Most of the peaks in this range are parallel bands, a point which was not measured in the Raman studies.

References

1. K.H. Bassett, C.Y. Liang, and R.H. Marchessault, J. Polym. Sci., A. 1, 1687(1963).
2. J. Blackwell, P.D. Vasko, and J.L. Koenig, J. Appl. Phys., 41, 4375(1970).
3. R.H. Atalla, Appl. Polym. Symp., 28, 659(1976).
4. R.H. Atalla, R.E. Whitmore, and C.J. Heimbach, Macromolecules, 13, 1717(1980).

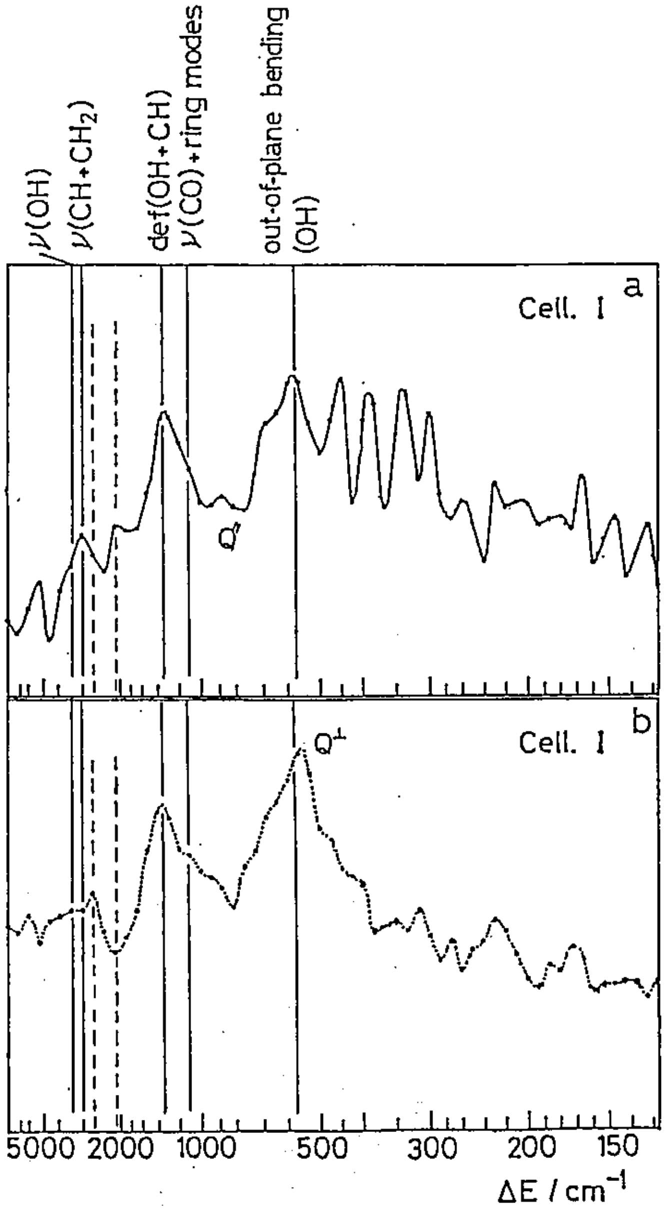

Fig. 1. NIIS TOF spectrum of ramie fibers. Scattering vector Q is parallel (a) and perpendicular (b) to the fiber axis.

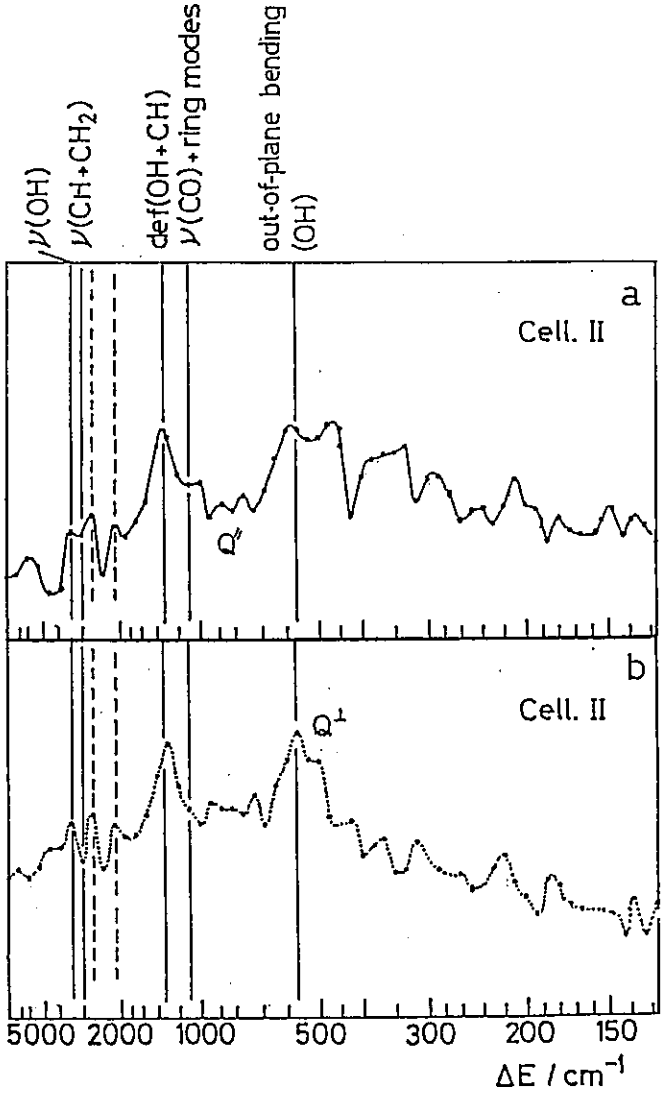

Fig. 2. NIIS TOF spectrum of rayon fibers. Scattering vector Q is parallel (a) and perpendicular (b) to the fiber axis.

Tortional Frequencies of Methyl Groups in Hydrogenated and Deuterated Poly(methly methacrylate)

Toshiji KANAYA, Koji NISHIDA, Keisuke KAJI, Ryozo KITAMARU
and Kazuhiko INOUE*

Institute for Chemical Research, Kyoto University, Kyoto 611
* Department of Nuclear Engineering, Faculty of Engineering,
Hokkaido University, Sapporo 060

Deuterium labeling is very powerful for assignment of vibrational modes in the neutron incoherent inelastic scattering spectrum because of its very low incoherent scattering cross-section compared with that of hydrogen. In this work, torsional frequencies of two methyl groups in poly(methyl methacrylate) have been distinguishably observed by using hydrogenated polymer (PMMA) and deuterated one (PMMA-d_5) (see Fig. 1). Measurements of neutron inelastic scattering were carried out on the polymer films 0.25 mm thick by using the spectrometer LAM-D at KENS. The observed time-of-flight (TOF) spectra of PMMA and PMMA-d_5 are shown in Fig. 1(a) and (b). The TOF spectra were converted to the hydrogen amplitude-weighted density of phonon states, $Z(\omega)$, which is essential for discussion of vibrational frequency distribution because it corresponds to the number of energy levels per unit volume of a sample. The results are shown in Fig. 2. In the spectrum of PMMA a large peak is observed at 340 cm^{-1}, whereas it disappears in the spectrum of PMMA-d_5 resulting in a very broad peak at about 200 cm^{-1}. Taking into account that all hydrogen atoms except for those of ester-methyl groups are deuterated in PMMA-d_5, we can immediately assign the peaks at 340 cm^{-1} and at 200 cm^{-1} to α-methyl torsion and ester-methyl one, respectively.

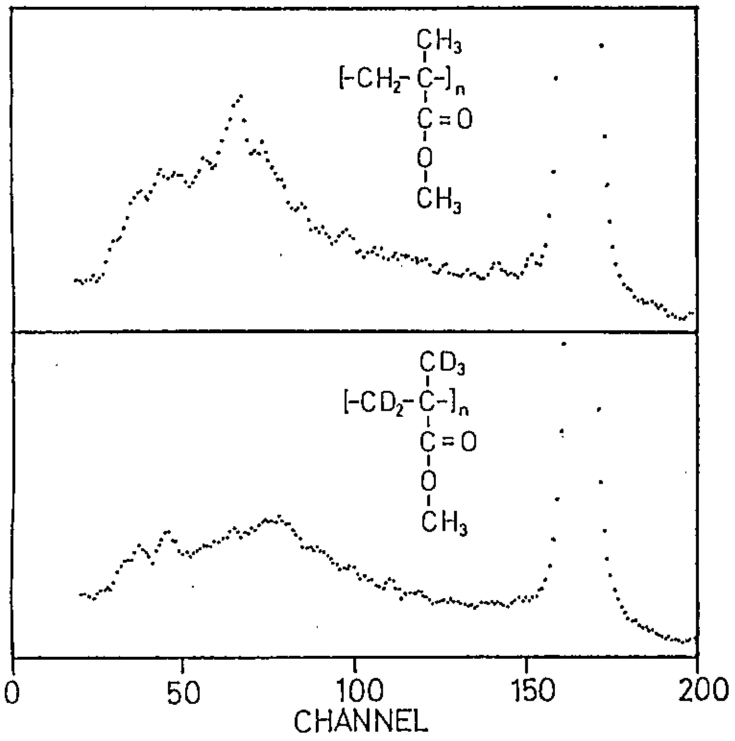

Fig. 1. TOF spectra of PMMA (a) and PMMA-d_5 (b).

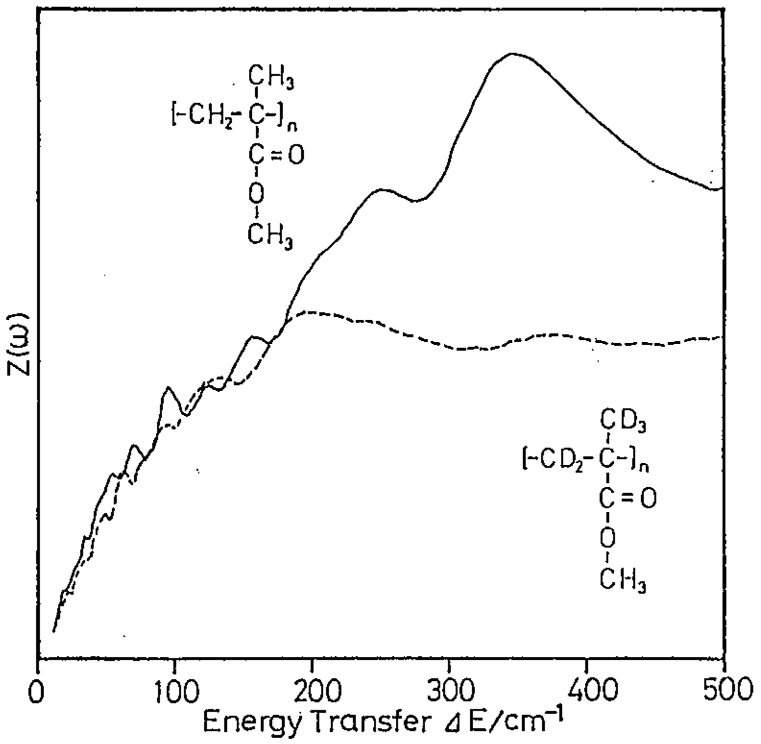

Fig. 2. Hydrogen amplitude-weighted density of phonon states, Z(ω), of PMMA (a) and PMMA-$_5$ (b).

Effects of Cross-linking on the Phonon Density in Rubbers

Kazuhiko INOUE*
Toshiji KANAYA, Keisuke KAJI and Ryozo KITAMARU
* Department of Nuclear Engineering, Faculty of Engineering,
Hokkaido University, Sapporo 060
Institute for Chemical Research, Kyoto University, Kyoto 611

Some properties of rubber polymers are extremely affected by cross-linking (e.g. elasticity) and it is very important from veiwpoint of practical use. In this work, we have investigated the effect of cross-linking on the phonon density in rubbers by neutron incoherent inelastic scattering and found a new band attributable to the cross-linking. Commercial vulcanized polyisoprene (PIP) and C_o^{60} γ-ray irradiated polybutadiene (PB) (16.6 Mrad) were used as samples. Neutron inelastic scattering measurements were carried out with the down-scattering spectrometer LAM-D at KENS.

The observed time-of-flight (TOF) spectra are shown in Fig. 1, where (a) corresponds to unvulcanized PIP, and (b) and (c) to vulcanized PIP, respectively. The degree of vulcanization of the sample of (b) is lower than that of (c). A new band is observed at about $\Delta E = 350$ cm^{-1} in PIP cross-linked by vulcanization and the intensity increases with degree of vulcanization. This suggests that the new band is attributable to the cross-linking. To confirm this, the TOF spectra of the γ-ray cross-linked PB were measured. The results are shown In Fig. 2. In this case a new band at about 350 cm^{-1} also appears, though the intensity is not very high because of a low degree of cross-linking.

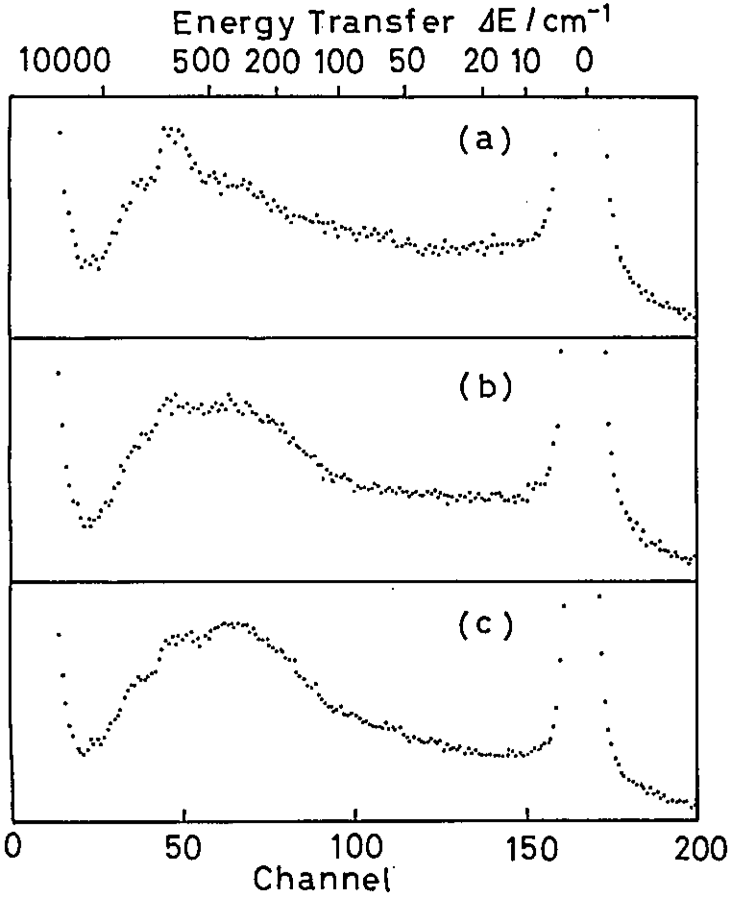

Fig. 1. TOF spectra of unvalcanized PIP (a) and valcanized PIP (b) and (c). Degree of valcanization of sample of (b) is lower than that of (c).

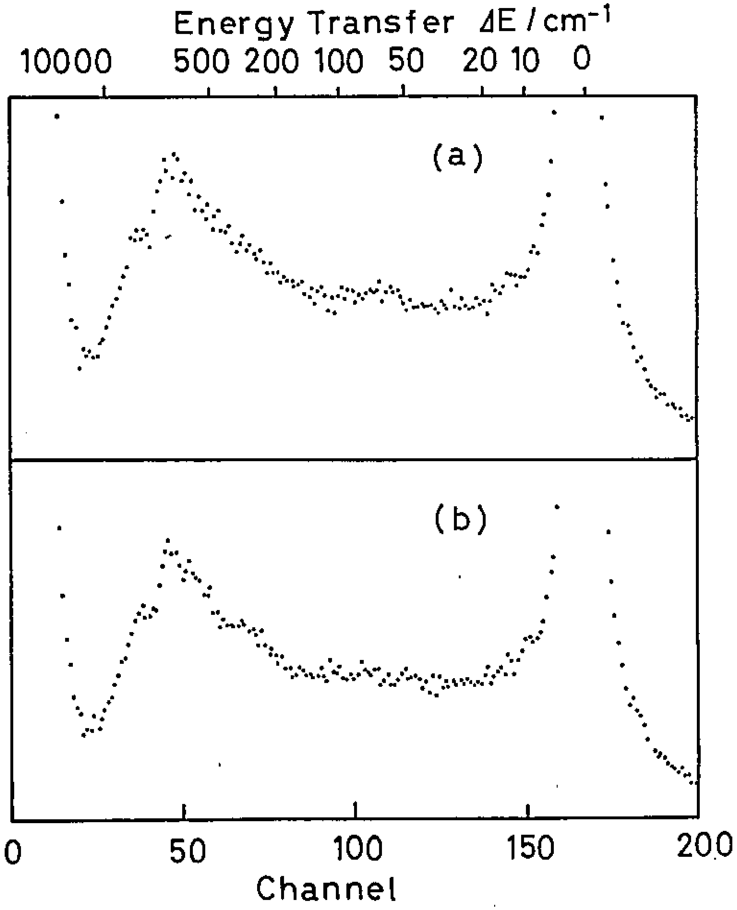

Fig. 2. TOF spectra of starting PB (a) and γ-ray irradiated PB (b).

Neutron Scattering from $CeSi_2$

Masahumi KOHGI, Nobuya SATO and Takeo SATO

Physics Department, Tohoku University
Sendai 980, JAPAN

The α-$ThSi_2$ type compound $CeSi_2$ was found to exibit various anomalies associated with the intermediate valence or the Kondo effect of the Ce ions.[1,2] In order to further characterize the status of this system, the measurement of neutron inelastic scattering is a powerful tool because it gives direct information on the spin fluctuations. We report here the results of the preliminary neutron scattering experiment performed at KENS.

The measurements were carried out on the inverted geometry TOF spectrometers LAM-40 and LAM-D, which utilize cold neutrons and thermal neutrons, respectively, as the incident beams. The final energies were 4.6 and 4.4 meV, respectively. The powdered sample was filled in a cylindrical aluminum cell with diamter of 14mm and 100mm length. The sample temperature was about 300K.

Fig. 1 shows the obtained frequency distribution of the response function of this system. This is expressed as $R(Q,\omega)=d^2\sigma/d\Omega d\omega \cdot k_i/k_f \cdot \{1-\exp(-\hbar\omega/kT)\}/\hbar\omega$. No resolution correction was made in the data analysis. The closed circles represent an average value of 4 detectors of LAM-40, corresponding to the scattering angles of 8°, 23°, 38° and 53°. The open circles represent the data of LAM-D with the scattering angle of 55°. Both data are normalized at $\hbar\omega$=4.6meV. The dashed line is the phonon contribution estimated as the maximum case from the measurement on $LaSi_2$ which is isomorphous to $CeSi_2$ and shows no magnetic anomaly.

Though the data points are scattered because of the low counting statistics, we can see that a diffusive magnetic response exists around $\hbar\omega$=0 and extends up to about 10meV. If the spin fluctuations in this system is a relaxation type, the function $R(Q,\omega)$ must be propotional to a Lorentzian centered at $\hbar\omega$=0. The half width $\Gamma/2$ of this function is estimated to be about 5meV. This value is the same order as those at 300K of $CeAl_2$ and $CeCu_2Si_2$, which are considered to be good examples of dense Kondo systems.[3] It is not clear at this stage that crystal field transitions exist or not.

We are now planning to measure the temperature dependence of the magnetic response of this system as well as to improve the counting statistics.

references

1) H. Yashima, T. Sato, H. Mori, D. Watanabe and T. Ohtuska ; Solid State Commun., 41(1982)1.

2) W. H. Dijkman, A. C. Moleman, E. Kesseler, F. R. de Boer and P. F. de Chatel; *Valence Instabilities* , ed. P. Wachter and H. Boppart (North-Holland, 1982) p.515.

3) S. Horn, F. Steglich, M. Loewenhaupt and E. Holland-Moritz ; Physica, 107B (1981)103.

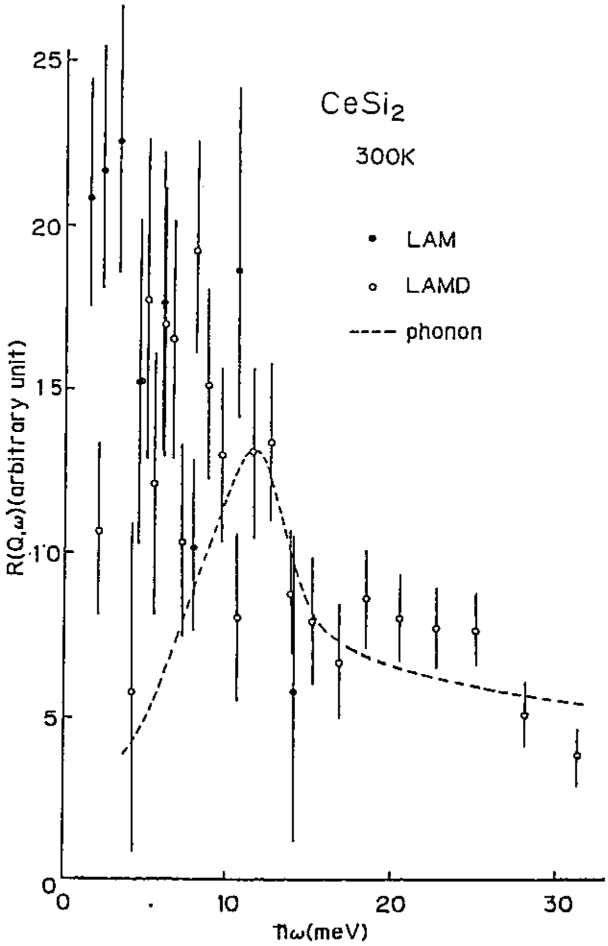

Fig. 1. Frequency distribution of the response function of $CeSi_2$ at 300K.

Improvement of MAX Spectrometer

K. Tajima,[†] Y. Todate,[††] Y. Ishikawa[††] and S. Tomiyoshi[†††]

[†] Department of Physics, Faculty of Science and Technology,
Keio University, Yokohama

[††] Department of Physics, [†††] Institute for Iron, Steel and Other Metals
Tohoku University, Sendai

The MAX spectrometer is a TOF crystal analyser spectrometer which is able to perform inelastic scattering experiments along a desired direction in the reciprocal lattice space of a single crystal sample. The configuration of the spectrometer is shown in Fig. 1(a). Detector arms are moved in the counterclockwise direction to determine the scattered neutron energy. In the case of a sample with a large lattice parameter, however, it is sometimes difficult to align all the detectors so as to scan along a single line in reciprocal lattice space. This is because large analyser angles are required in such a case and the detector arm hits each other in the present geometrical configuration. In order to eliminate this limitation for measurements, all the detector arms have been modified to move in the clockwise direction, as shown in Fig. 1(b).

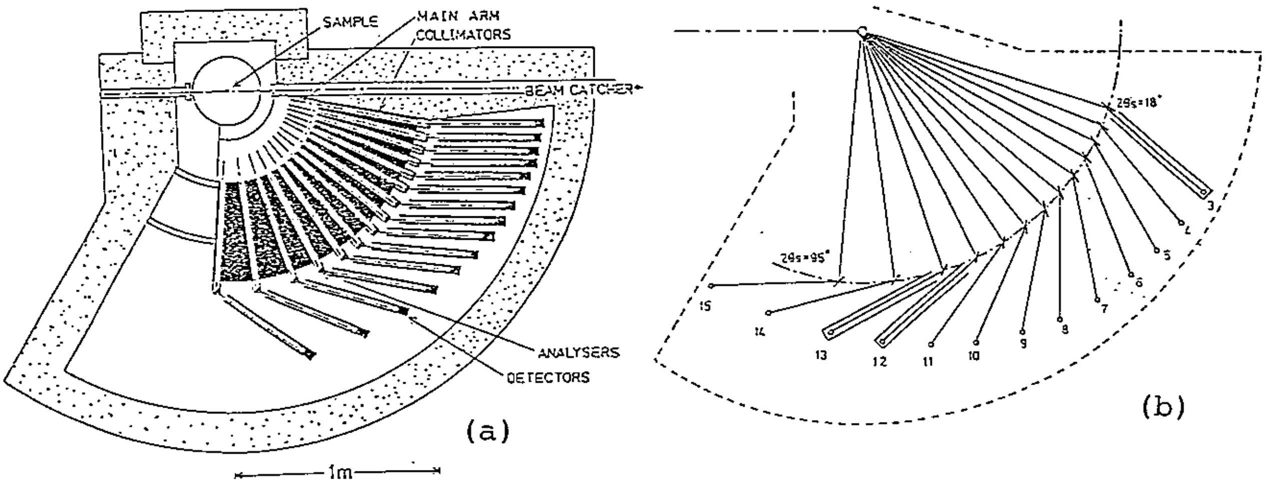

(a)

(b)

Fig.1 The geometrical configuration of (a) old and (b) new MAX.

The test measurement with the improved MAX was made on a b.c.c. iron single crystal. The TOF spectra of phonons and magnons, which were collected by using P.G(002) reflection as the analyser, are shown in Fig. 2(a). These results are compared with the equivalent measurement

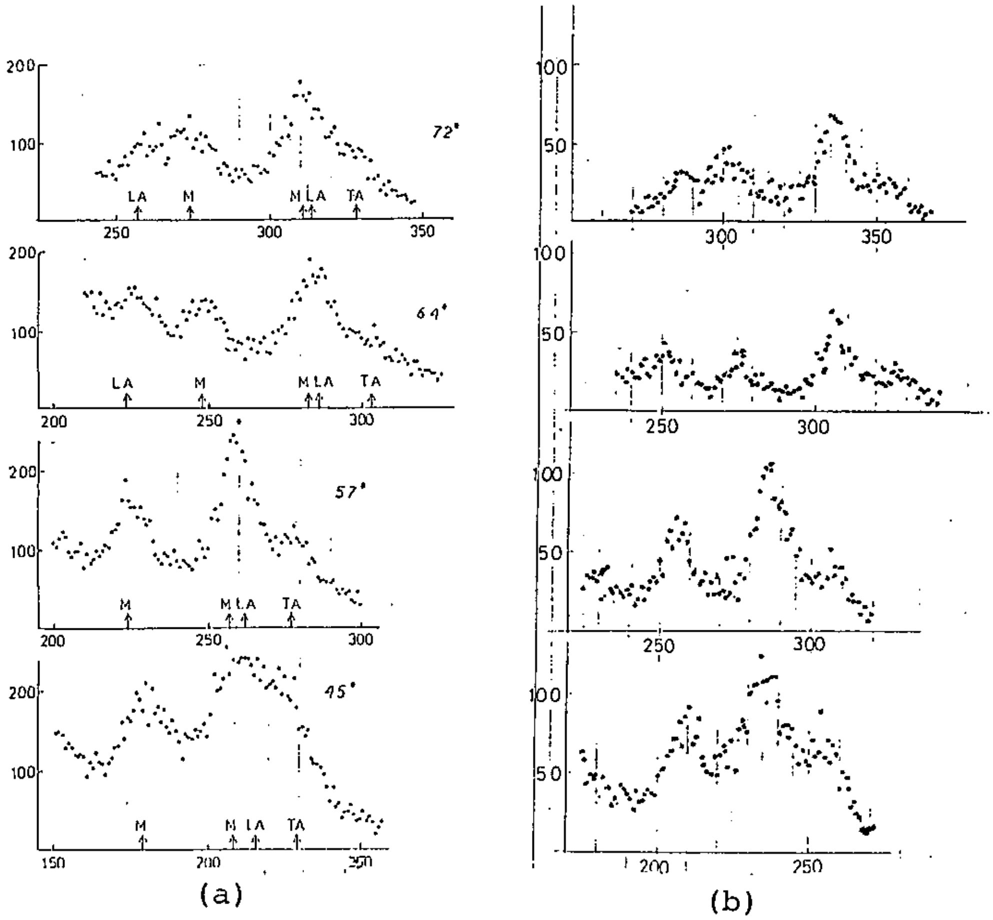

Fig.2 TOF spectra of Iron measured by (a) old and (b) new MAX.

which was made 2.5 years ago.(Fig. 2(b)) The S/N ratio as well as the resolution are greatly improved, which is partly due to the present improvement.

This improvement also makes it possible to utilize the Si(311) reflection as the analyser and hence, measurements with much higher resolution can be performed. Measurements with the new configuration are scheduled as the first experiment at the more intense neutron source of KENS I' or KENS II.

Spin dynamics of a quasi two-dimensional antiferromagnet $MnTiO_3$

Yoshiei TODATE, Yoshikazu ISHIKAWA, Keisuke TAJIMA*,
Shoichi TOMIYOSHI** and Fumihiko TAKEI**

Physics Department, **Institute for Iron, Steel and Other metals,
Tohoku University, Sendai and *Faculty of Science and Technology,
Keio University, Yokohama

A quasi two-dimensional antiferromagnet $MnTiO_3$ has the ilmenite type layered structure. We observed highly anisotropic spin-wave dispersions in this material$^{1)}$. However, we could not determine uniquely exchange interaction parameters and an anisotropy field from the spin-wave dispersion curves along only two directions of high symmtry; [100] and [001]. Therefore we have measured a spin-wave dispersion along another direction of [104] through (006) at 17K. Using all data for three [104], [100] and [001] directions, we have fitted the theoretical spin-wave dispersion based on the Heisenberg model to the experimental results and deduced the exchange interaction parameters up to 6th nearest neighbours which are listed in Table 1. Figure 1(b) depicts how the calculated curve fits well to the experimental data.

We have calculated the ratio of the molecular field H^{inter} $(=\sum_{interlayer} 2J_i S_i)$ to H^{intra} in order to elucidate the two-dimensional exchange anisotropy. The ratio is obtained to be 0.045 ± 0.05. Therefore it is now well confirmed that $MnTiO_3$ is regarded as the quasi two-dimensional antiferromagnet.$^{2)}$ Note that this anisotropy arises in a cancelation among the interlayer exchange interactions.

We have studied also paramagnetic scattering of $MnTiO_3$ with MAX spectrometer using the same single crystal at room temperature. The scans were made along [100] direction through (104) point and [001] through (101). Some of the neutron spectra are shown in Fig. 2. As is usually analysed for the Heisenberg system, the observed spectra were fitted to the Gaussian

$$\sqrt{1/2\pi\langle\omega^2\rangle}\ \mathrm{Exp}(-\omega^2/2\langle\omega^2\rangle)$$

in the proper limits of q. ,where

$$\hbar^2\langle\omega^2\rangle = \frac{8}{3}S(S+1)\sum_{R}(J(R))^2(1-\cos(q.R))$$

is the second moment.[3] The solid lines in Fig. 2 are the calculated spectra using the values of the parameters in Table 1. We emphasize here that the exchange interaction parameters derived from the spin-wave dispersion curves well reproduce the observed spectra of paramagnetic scattering in $MnTiO_3$.

References

1) Y. Todate, Y. Ishikawa, K. Tajima, S. Tomiyoshi and H. Takei; KENS Report IV (1983) 150.

2) J. Akimitsu and Y. Ishikawa; J. Phys. Soc. Jpn. 42 (1972) 462.

3) M. F. Collins and W. Marshall; Proc. Phys. Soc. (London) 92 (1967) 390.

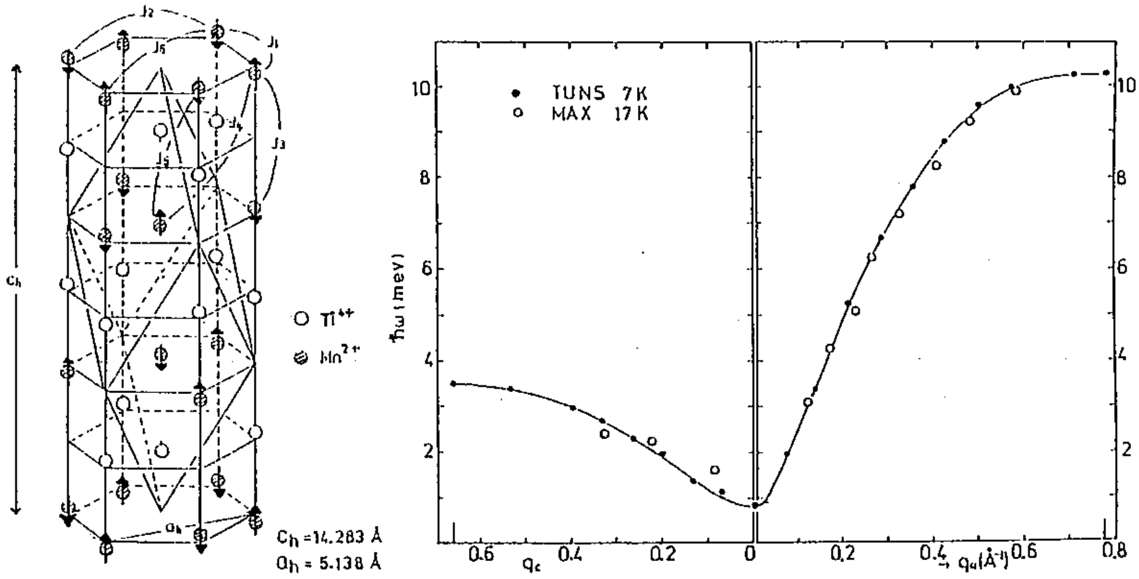

(a) (b)

Fig. 1 (a) Crystal and Magnetic structures of $MnTiO_3$.
(b) Spin-wave dispersions along [100] and [001].

Table 1 Exchange and anisotropy parameters determined from spin-wave dispersions.

		K
J_1	-7.55	±0.60
J_2	-0.04	±0.30
J_3	-2.70	±0.40
J_4	-1.32	±0.15
J_5	-2.10	±0.10
J_6	-0.48	±0.10
$g\mu_BH_A$	0.30	±0.05

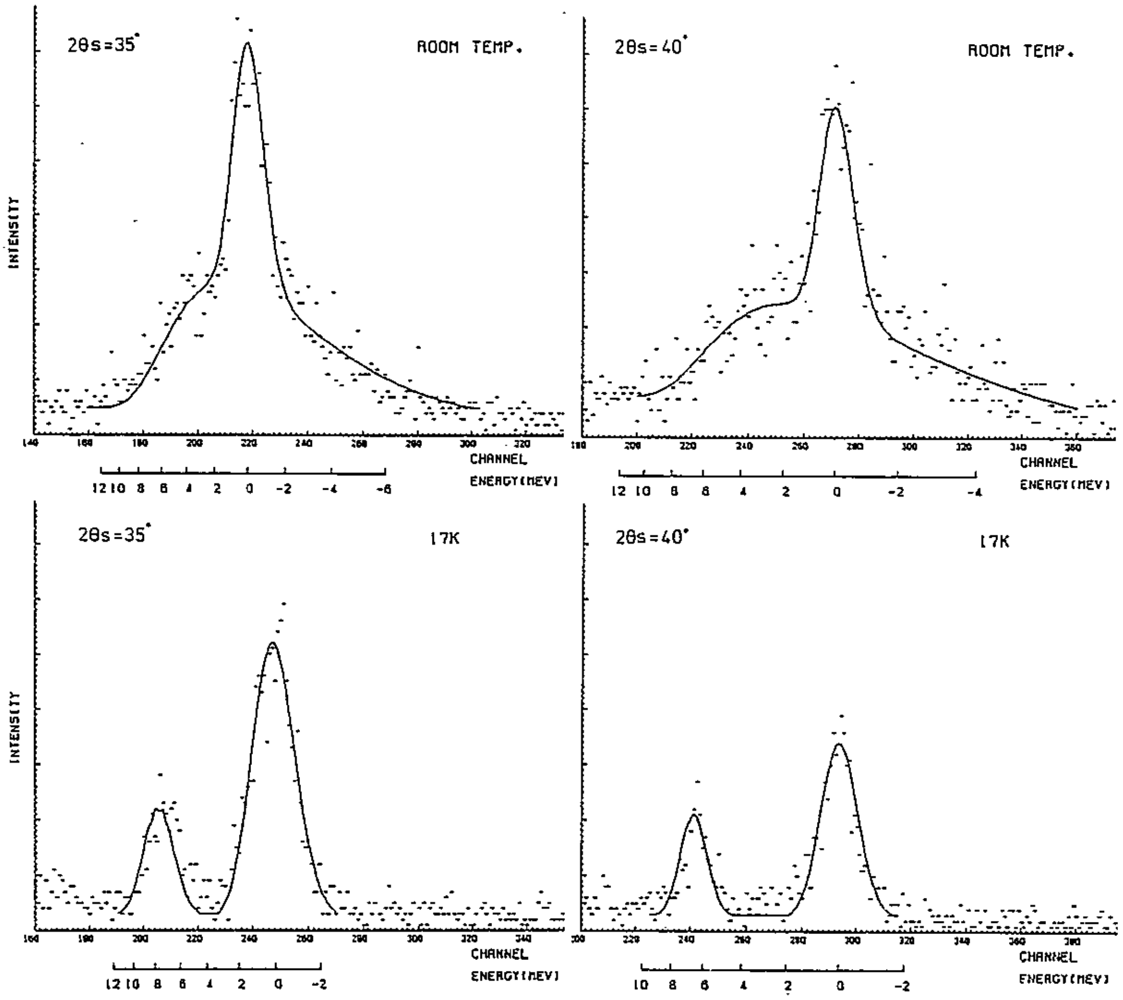

Fig. 2 Observed and calculated spectra at 17 K and at room temperature. Peaks centering around zero energy transfer are incoherent elastic ones.

A Trial for Measuring High Energy Magnetic Excitations in Ferromagnetic Metals by MAX

Yoshikazu Ishikawa, Yoshiei Todate, Shoichi Tomiyoshi* and
Keisuke Tajima**

Physics Department, *Institute for Iron, Steel and Other
Metals, Tohoku University, Sendai

**Faculty of Science and Technology, Keio University,
Yokohama

We have shown in a previous report[1)] that MAX has a good potential for studying the low energy "anisotropic" magnetic excitations as those in a quasi-two dimensional antiferromagnet $MnTiO_3$, which is quite difficult to study with a conventional TOF machine. However for the study of the high energy magnetic excitations along a crystallo-graphic axis, which is one of the most important subject for the spallation neutron source, MAX has a serious demerit that the incident neutron energy inevitably increases more than required because of the restriction of scanning along a special direction in the resprocal lattice, resulting in decreasing substantially the energy resolution. This demerit can be improved, of cource, if the neutron source intensity is sufficient enough to make collimation tight, but for the small neutron source as KENS, it makes difficult the observation of high energy excitations of magnons with MAX. The existence of high order contamination is another demerit of MAX which prevents also the observation of high energy excitations because of overlapping problem. The latter problem can however, be resolved if we use Si or Ge as the analyzer. The development of the Si analyzer with high reflectivity is now successfully in progress by using the stack of Si wafer as reported previously.[2)]

This paper discusses the result of trial for improving the energy resolution problem. In case of magnetic excitations in Fe or Ni, the dispersions can be assumed to be isotropic up to about 100meV. Therefore the data can be accumulated by scanning along any direction which passes through the main Bragg point. We found that the slight change of scanning direction can improve the demerit. We list in Table 1 the magnon energy transfers in Fe detected by five different counters (No.1-5) with scattering angles θ_i as well as E_F and $2\theta_A$ for two different scans. One is the scan along [111](α=54.7°) which passes through (110) and another is along the direction with α=70°(see Fig.1(a)). We can find in the talbe that E_F can be reduced for the same energy transfer, if we choose a large α value. We found also, however, that No.4 and No.5 counters in α=70° scans can not detect magnons with the PG analyzers because of overlapping with the $\lambda/2$ contamination. This difficulty can be removed if the scanning direction is shifted parallel to make QY larger. The situation is also listed in the Table, where the best condition from the stand point of the energy resolution is marked by circles and is also displayed in Fig.1(a). Fig.1(b) is also shown the $\hbar\omega$ - Q diagrams for the scans with α=54.7([111])and α=70°. We find from Table and Fig. 1 that the α=70 scanning configuration is better than the [111] scan for studying the energy transfers of 90meV > $\hbar\omega$ > 50meV in Fe.

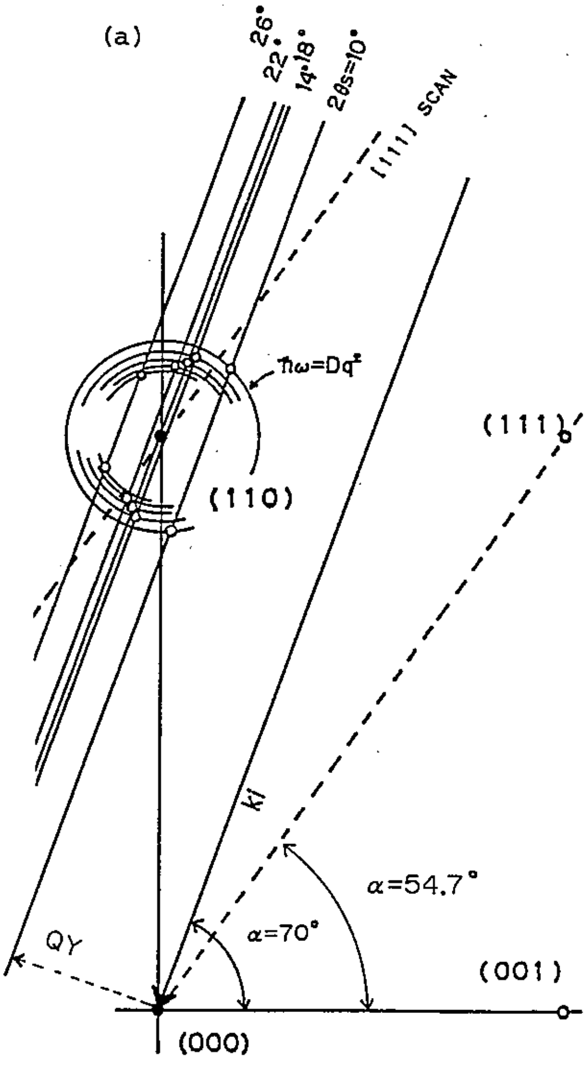

Fig. 1(a) Two different scans,

i) [111] scan with α=54.7°

ii) α=70° scans with different QY.

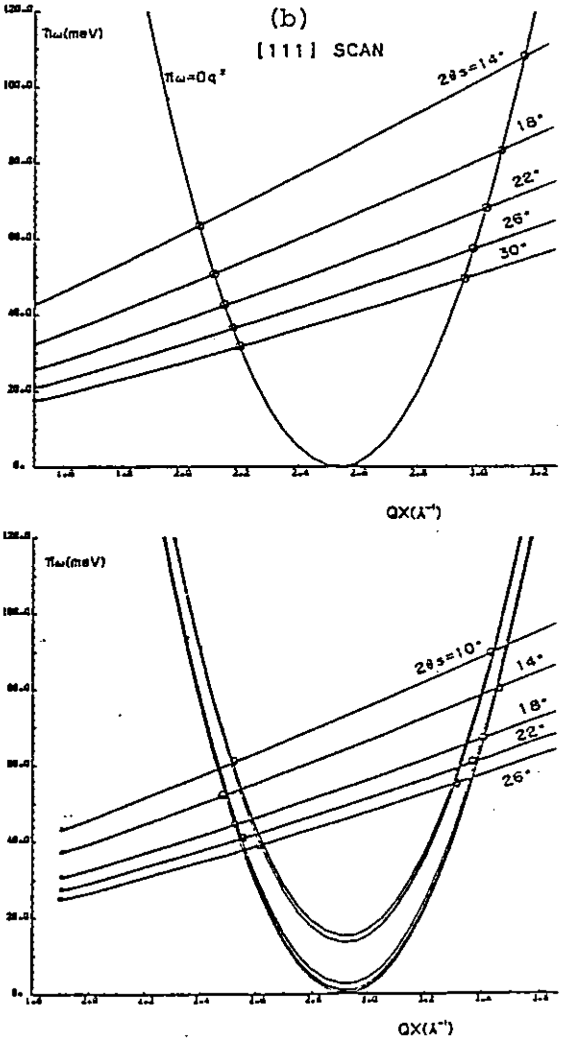

Fig. 1(b)

$\hbar\omega$ - Q diagrams of two scans.

The results of measurements with $\alpha=70°$ scan are displayed in Figs. 2(b) and (d) and are compared with those of the [111] scans (Figs. 2(a) and (c)). These figures show clearly that the energy resolutions ($\Delta\hbar\omega$) are improved by the $\alpha=70°$ scan. The magnon scattering for which no signal could be found for the [111] scan could be detected for the $\alpha=70°$ scans. Note that Fig.2(d) is the result taken by using a Si wafer analyzer. Although the counting satistics is still very poor, the absence of $\lambda/2$ contamination makes the magnon spectrum more definitive.

The trial we made has shown that MAX has the variety in the way of measurements and the selection of the scanning parameter is quite important for the success of observation, just as is the case with the triple axis spectrometer in the reactor.

References

1) Y. Todate, Y. Ishikawa, K. Tajima, S. Tomiyoshi and F. Takei, KENS Report IV (1983) 150, KENS Report IV (1984)

2) S. Tomiyoshi, Y. Ishikawa and K. Tajima, KENS Report IV (1983) 154

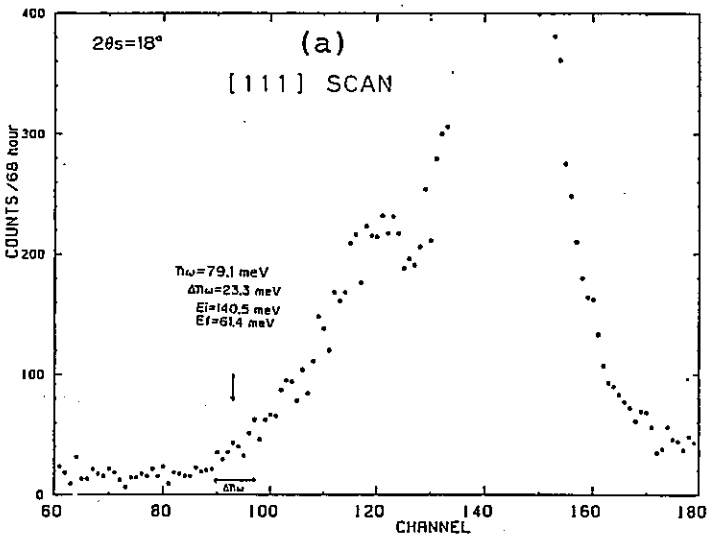

Fig. 2(a)
Neutron scattering spectra for the [111] scan measured by the counter No.3 with $2\theta_s=18°$.

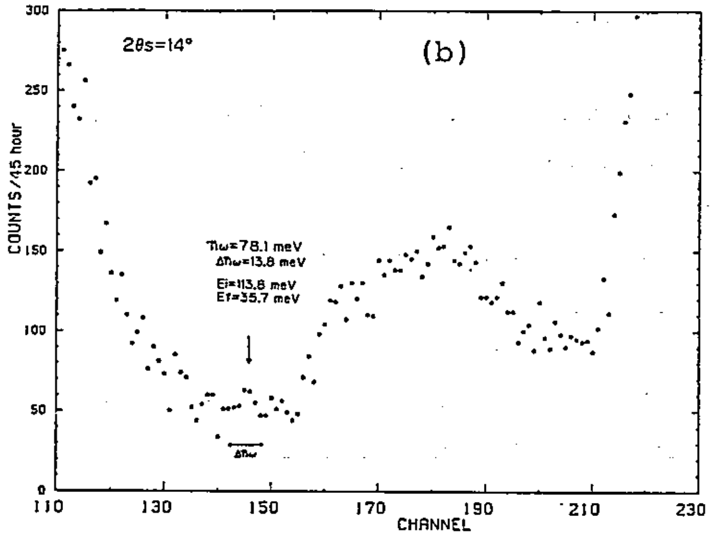

Fig. 2(b)
Neutron scattering spectra for the α=70° scan measured with the counter No.2 with $2\theta_s$=14°.

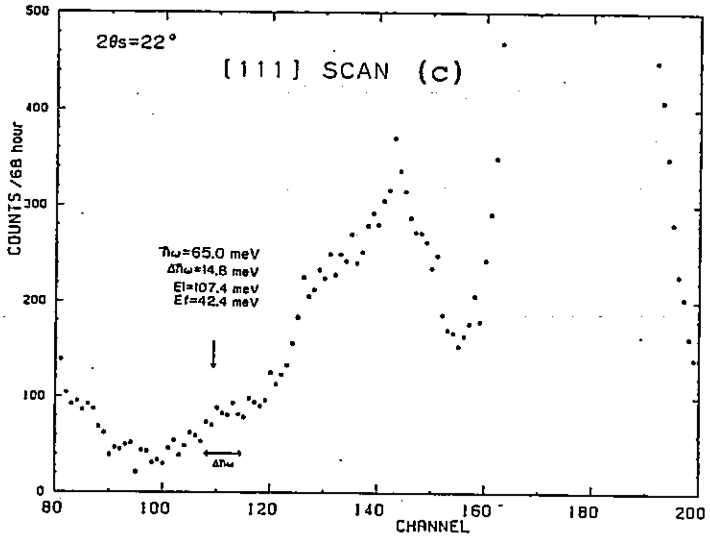

Fig. 2(c)
Neutron scattering spectra for the [111] scan measured by the counter No.4 with $2\theta_s$=22°.

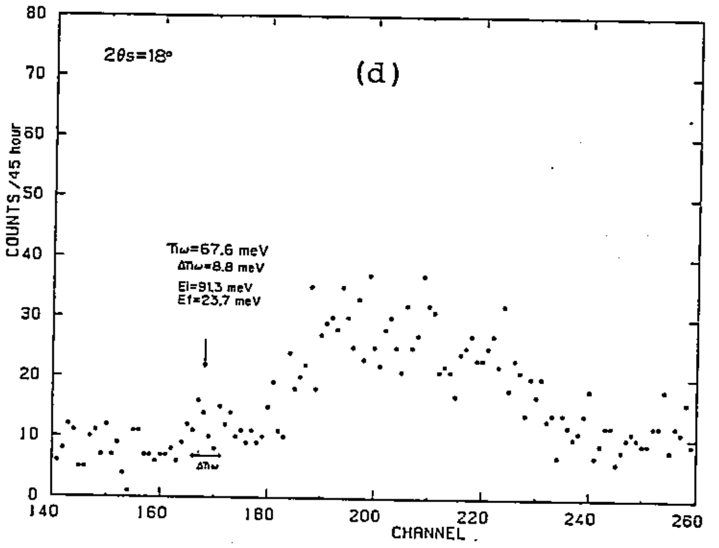

Fig. 2(d)
Neutron scattering spectra for the α=70° scan measured by the counter No.3 with $2\theta_s$=18°.

Table 1. Energy transfers $\hbar\omega$, final energy E_F and alalyzer angles $2\theta_A$ of two different scans with α=54.7°([111]) and α=70° for magnon scattering in Fe measured with five counters of MAX.

	α	54.74°	70°			
Counter No.	QY ($\mathring{A}^{-1}$)	(110) 1.794	1.3	1.2	1.1	(110) 1.063
1	$2\theta_s$ (°)	○ 10°	10	10	10	10
	$h\omega$ (meV)	152	130	123	115	112
	E_f (meV)	221	116	99	83	78
	$2\theta_A$	10.4	14.4	15.6	17	17.6
2	$2\theta_s$	○ 14	14	14	14	○ 14
	$h\omega$	107	95	91	85	83
	E_f	114	60	51	43	40
	$2\theta_A$	14.5	20.1	21.8	23.8	24.6
3	$2\theta_s$	○ 18	18	○ 18	○ 18	△ 18
	$h\omega$	83	76	73	69	67
	E_f	170	37	31	26	25
	$2\theta_A$	18.6	25.7	27.9	30.5	31.6
4	$2\theta_s$	○ 22	○ 22	○ 22	× 22	× 22
	$h\omega$	68	63	62	59	58
	E_f	48	25	21	18	17
	$2\theta_A$	22.6	31.3	34.0	37.2	38.6
5	$2\theta_s$	○ 26	○ 26	△ 26	× 26	× 26
	$h\omega$	57	55	54	52	51
	E_f	35	18	16	13	12
	$2\theta_A$	26.5	36.8	40.0	43.8	45.5

x: overlapping with $\lambda/2$ contamination

Neutron Scattering from Liquid ^{4}He at Very Large Momentum Transfer

S. Ikeda and N. Watanabe
National Laboratory for High Energy Physics

Oho-machi, Tsukuba-gun, Ibaraki-ken 305, Japan

The observation of Bose-Einstein condensation in superfluid helium (^{4}He-II) has been a most attractive problem in the field since London's first proposal1). In the last several years neutron scattering experiments at medium momentum transfer ($Q = 4 \sim 7$ A^{-1}) have confirmed that a finite fraction ρ_0 of the atoms in He-II has zero momentum2). The recent experimental value of ρ_0 is about 13 % at 1 K2), and many theoretical estimates are in the range 8 ∿ 13 % 2).

In neutron scattering at large Q, the scattering function $S(Q,\omega)$ asymptotically approaches S_{IA} in the impulse approximation, which is directly related to the momentum distribution $n(\vec{p})$ of the atoms in the initial state3), 4),

$$S_{IA}\ (Q,\ \omega) \sim \int d^3p\ (\omega - R - \frac{\vec{Q}\bullet\vec{P}}{M})\ n(\vec{p}). \tag{1}$$

Here $R = h^2Q^2/2M$ is the recoil energy of the target particle. The final state effects becomes unimportant if the condition $n\sigma \ll p$ is satisfied, where n is the number density and σ the atomic scattering cross section of the scattering particles. For liquid ^{4}He, however, the value of σ is very large in the momentum transfer range mentioned above ($Q = 4 \sim 7$ A^{-1}), and therefore the condensate peak is observed much broader than the resolution function of the instrument.

On the other hand, at very large momentum transfer, $Q > 100$ A^{-1}, σ becomes small and final state effects becomes no longer important5). Such a high Q experiment with a sufficiently high resolution to resolve the condensate peak is desirable, but has never been achieved for technical reasons.

Martel et al.6) proposed that neutron scattering data at medium momentum transfer region could be analyzed by a "sum rule" of moment relations for the dynamic structure factor $S(Q,\ \omega)$. This sum rule reduces an enormous distortion on the neutron scattering spectrum due to final state effect in medium momentum transfer region. Up to this time measurements of momentum distribution for liquid He were performed at this region ($\lesssim$ 15 A^{-1}) but with a higher resolution, and analyzed based on this rule.

We attempted a neutron inelastic scattering experiment on liquid He at very large momentum transfer range using a pulsed spallation neutron source KENS (KEK, Japan) with an eV spectrometer, a Resonance Detector Spectrometer (RDS)7) ∿ 9), which we developed mainly for this purpose.

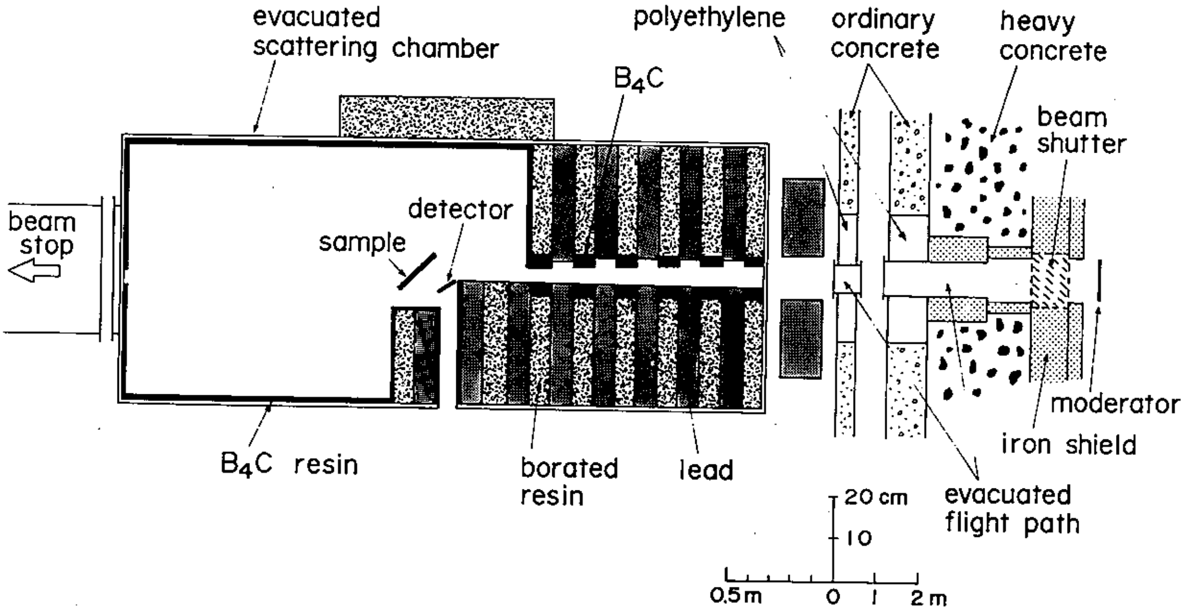

Fig. 1 Layout of the RDS at KENS for liquid ^{4}He experiments

The geometry of the present experiment is shown in Fig. 1. Epithermal neutron beam from the room temperature polyethylene moderator was extracted from H7 beam hole which is perpendicular to the moderator surface. The incident beam is collimated at the sample to a 3 x 6 cm^2 rectangle by a complicated heavy collimator section consists of a large amount of lead, borated resin and $^{10}B_4C$ sintered plate. Flight path length for incident neutrons was 8.37 m. The sample was contained in a thin alminium cell, 5 x 6 cm^2 x 1 cm thick, and cooled down by pumping liquid helium. In order to attain a very high Q measurement with a higher resolution, extensive optimization studies have been performed between counting rate and resolution. Among the various contribution to the resolution, it is known that the geometrical contribution is dominant for a scattering sample made of light atoms such as helium. To minimize this effect, a focussing principle has been proposed10) and confirmed experimentally11). We adopted the principle in our arrangement between sample and detector. Scattered neutrons were detected at the distance 0.15 m by a ^{238}U resonance detector foil, which was at room temperature for convenience. Details will be published elsewhere[12)].

Using a fixed scattering angle $\theta = 167°$ and a final energy $E_f = 6.67$ eV, which is the first resonance level of ^{238}U, we attained very high momentum transfer $Q \sim 150$ A^{-1} which corresponds to the recoil energy R 11 eV and the incident neutron energy $E_i \sim 18$ eV.

The measurements were performed at both 1.2 K and 2.5 K under saturated vapor pressure. The density is almost the same at both temperatures. Figure 2 shows the measured time-of-flight spectra for He-II (1.2 K) and for He-I (2.5 K) after subtracting the cell pattern and the backround spectrum.

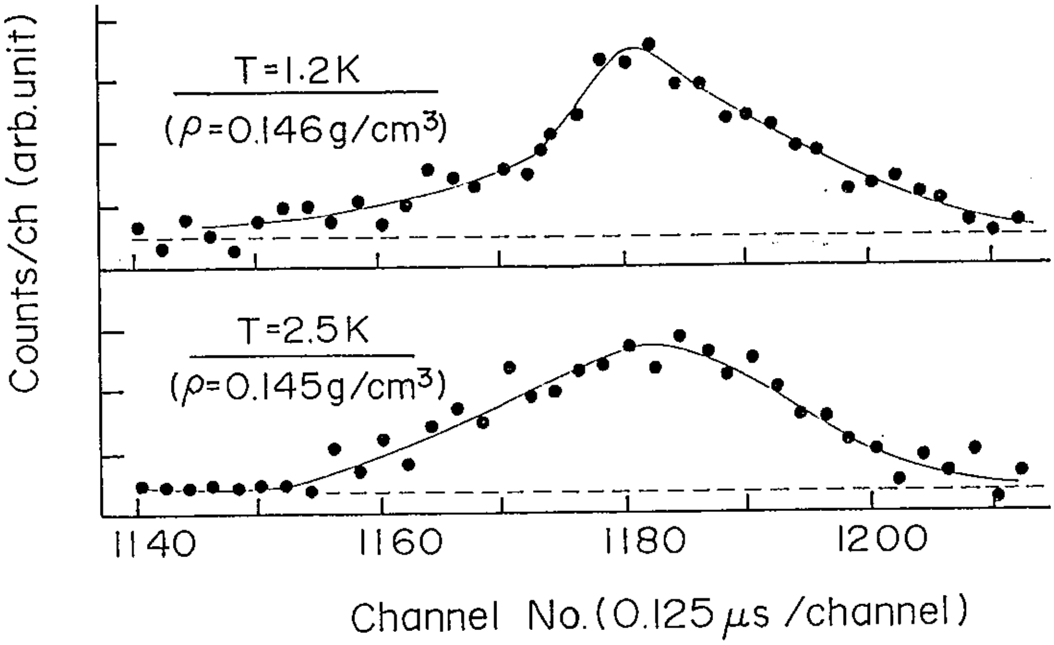

Fig. 2 Measured high-Q scattering spectra for He-II at 1.2 K (upper) and He-I at 2.5 K (lower). Solid lines are only guide for eyes.

The spectra are normalized by the monitor counts. Counting statistics of the present data are not so good compared with the measurements performed at modest Q (< 15 A^{-1}), but we can see a distinct difference between the two spectra. In the spectrum for He-II there exists a distinct condensate peak at the central part of the broad spectrum corresponding to the momentum distribution of normal component in He-II. Note that the cell pattern appears at the channels about 1770, far away from the helium peak. Instrumental resolution is not so good as a consequence of compromise between counting rate and resolution, but good enough to distinguish the condensate peak from the broad spectrum, because the leading edge (lower channel side) of the condensate peak is very sharp due to the special characteristic of the resolution function of this instrument discussed in succeeding paper.

References

1). F. London, Nature 141, 643 (1938), and Phys. Rev. 54 (1938) 947.
2). For example V. F. Sears, E. C. Svensson, P. Martel, and A. D. B. Woods, Phys. Rev. Lett. 49 (1982) 279, and references therein.
3). P. C. Hohenberg and P. M. Platzman, Phy. Rev. 152 (1966) 196
4). V. F. Sears, Phys. Rev. 185 (1969) 200.
5). P. M. Platzman and N. Tzoar, Impulse Corrections to the Impulse Approximation for High Momentum Transfer Neutron Scattering, to be pablished.
6). P. Martel, E. C. Svenson, A. D. B. Woods, V. F. Sears and R. A. Cowly, J. Low Temp. Phys. 23 (1976) 285.
7). J. M. Carpenter, N. Watanabe, S. Ikeda, Y. Masuda, and S. Sato, Physica 120B (1983) 126.
8). H. Rauh and N. Watanabe, Nucl. Instr. Meth. 222 (1984) 507.
9). H. Rauh and N. Watanabe, Phys. Lett. 100A (1984) 244.
10). J. M. Carpenter and N. Watanabe, Nucl. Instr. Meth. 213 (1983) 311.
11). H. Rach, S. Ikeda and N. Watanabe, Nucl. Instr. Meth. 224 (1984) 469.
12). S. Ikeda and N. Watanabe, to be published.

Bose condensate Fraction in He-II and Effective Temperature of He-I

S. Ikeda and N. Watanabe
National Laboratory for High Energy Physics

Oho-machi, Tsukuba-gun, Ibaraki-ken 305, Japan

In the preceding paper we presented scattered neutron spectra from liquid ^{4}He at 1.2 K and 2.5 K measured at very high momentum transfer $Q \sim 150\ \text{Å}^{-1}$. Present paper reports the results of the data analysis.

In order to understand the measured spectra, we must know the special feature of the resolution function in the present experiment. At back scattering, the contribution due to the finite vertical extent of the sample and detector becomes significant, especially in the case of short scattered flight path. Since the vertical size effect is not taken into

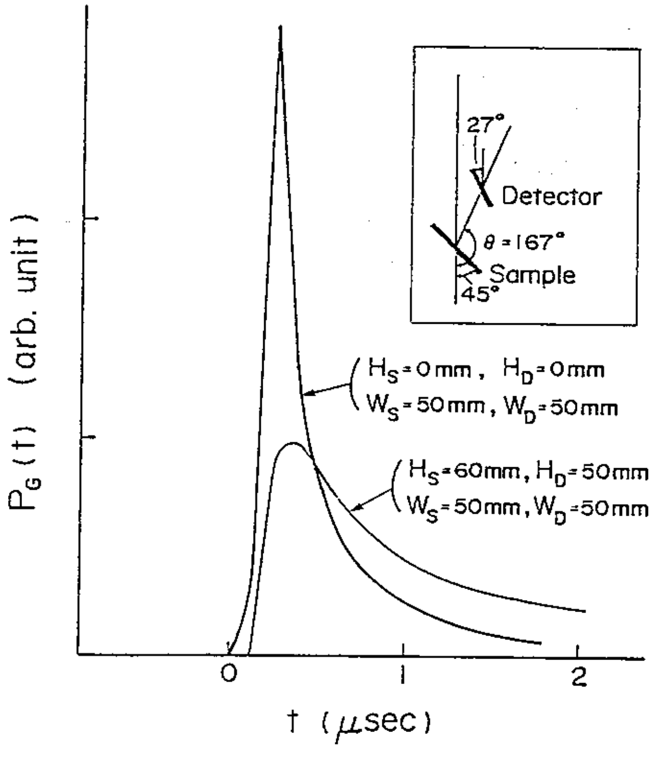

Fig. 1 Calculated time spectra of the detection probability including the effect of sample and detector heights. Inset illustrates the configuration for the helium measurement.

account in the focussing theory[1)], we estimated this with a computer simulation. Figure 1 shows the calculated time spectra of the detection probability for a zero height sample and for a 6 cm high sample with the same detector size. Broadening is asymmetrical. For a finite sample-detector height, the FWHM value becomes broader compared to the zero height case, but the leading edge remains still sharp.

Assuming that the momentum distribution of the normal component in He-II is same as that in He-I, we can extract the condensate peak directly from the two spectra (Fig. 2 in the preceding paper) by subtracting the He-I spectrum from the He-II spectrum, with a coefficient just to eliminate the broad spectrum in the latter. The best value of the coefficient was 0.65 ± 0.05. The result is shown in Fig. 2 where the solid line is a calculated instrumental resolution function including Doppler broadened detector resolution, geometrical contribution mentioned above, as well as the finite burst width of neutrons from the moderator, etc. The line profile of the subtracted peak coincides well with the calculated resolution function within experimental accuracy. The result provides a direct evidence for the existence of the atoms at zero momentum in He-II.

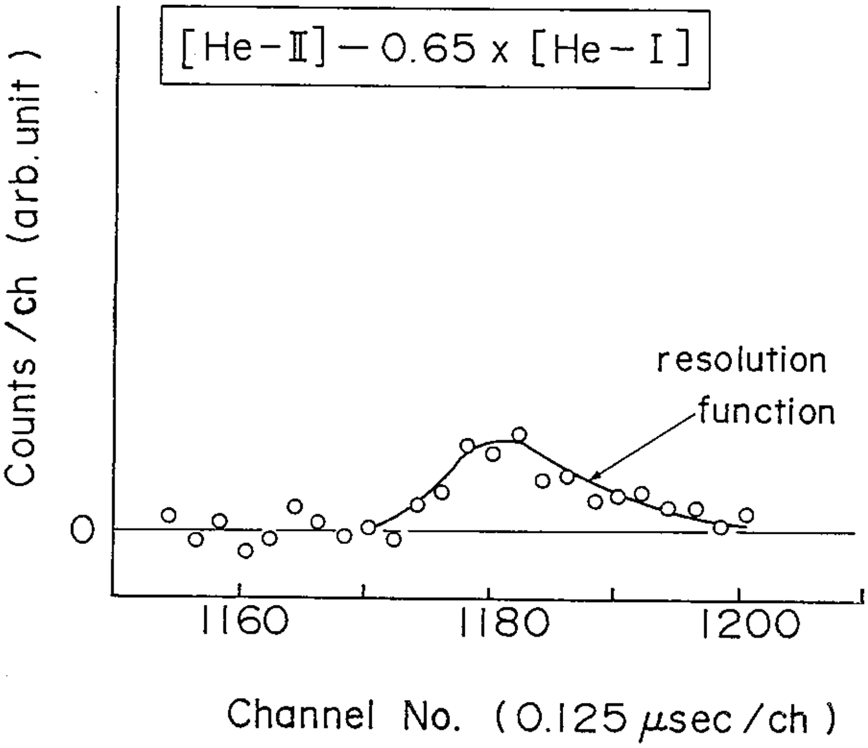

Fig. 2 Subtracted spectrum with a coefficient indicated in the figure. Solid line is calculated instrumental resolution.

If we determine the condensate fraction simply from this result, we have a surprisingly large value of ρ_0 about 35 %, which is much larger than the recent experimental values (12 $\sim$ 15 %) measured at the medium Q range (< 15 A^{-1}) as well as the theoretical values (8 $\sim$ 13 %). The counting statistics in the present measurement is rather poor, but the maximum absolute error in ρ_0 is estimated to be less than 5 %. At this moment, we are not necessarily asserting that the condensate fraction in superfluid ^{4}He is not 12 $\sim$ 15 %, but about 35 %. However, at least, we can say that at such high Q ($\sim$ 150 A^{-1}) the neutron spectrum from He-II is observed as if the conensate fraction is about 35 %.

Neutron scattering spectra have also been analyzed to determine an effective temperature T_{eff} of liquid He-I. For a system in which $n(\vec{p})$ has the Maxwellian form, the scattering function at large Q (equation (1) in the preceding paper) reduces to $^{2)}$,

$$S_{IA}(Q, \omega) = \frac{1}{\sqrt{2\pi}\sigma_R} e^{-(\omega - R)^2/2\sigma_R^2} (1 + h(Q, \omega)),$$

with

$$\sigma_R = \sqrt{2Rk_BT_{eff}}, \tag{2}$$

$$k_BT_{eff} = \frac{2}{3} \langle KE \rangle = \frac{1}{2}\int_0^\infty E \coth(E/2T) f(E) dE,$$

where k_B is the Boltzman constant, T the temperature of the system, f(E) the state density distribution and <KE> the average kinetic energy per atom. h(Q, ω) is higher order correction term which can be expressed as series expansion in powers of $(k_BT_{eff}/R)^{1/2}$ with Hermitian polynominals as coefficients. At very large Q, $S_{IA}(Q, \omega)$ can be given as a simple Gaussian function since $(k_BT_{eff}/R)^{1/2}$ is very small (in the present case, recoil energy R is very large ($\sim$ 11 eV), while T_{eff} is at largest about 20 K). Neutron spectrum of He-I was calculated by simple Gaussian and compared with the measured spectrum in Fig. 3. The best value for T_{eff} is about 21 K, which is larger than the reported values of about 10 K$^{3)}$. In the figure a calculated spectrum with T_{eff} = 10 K is also depicted for comparison (broken line in the figure). The value of 21 K might correspond to the existence of two roton resonances at energies near twice the single roton energy$^{4)}$.

In conclusion, we have presented momentum distributions $n(\vec{p})$ for liquid ^{4}He at 1.2 and 2.5 K based on new neutron inelastic scattering measurements at very high Q ($\sim$ 150 A^{-1}). The condensate fraction is observed like ρ_0 $\sim$

35 % in such a large momentum transfer region. Furthermore the effective temperature for liquid He-I (or the normal component of liquid He-II) obtained in the present experiment is about 21 K, which is also much larger than the reported value of about 10 K. We recognize, of course, that further measurements with better statistics and improved resolution are necessary to confirm our results. We also believe that measurements not only at this Q range with a different technique, but also in the region $15 < Q < 150$ Å^{-1} and $Q >> 150$ Å^{-1} will be important in understanding the very large momentum transfer neutron scattering from liquid ^{4}He.

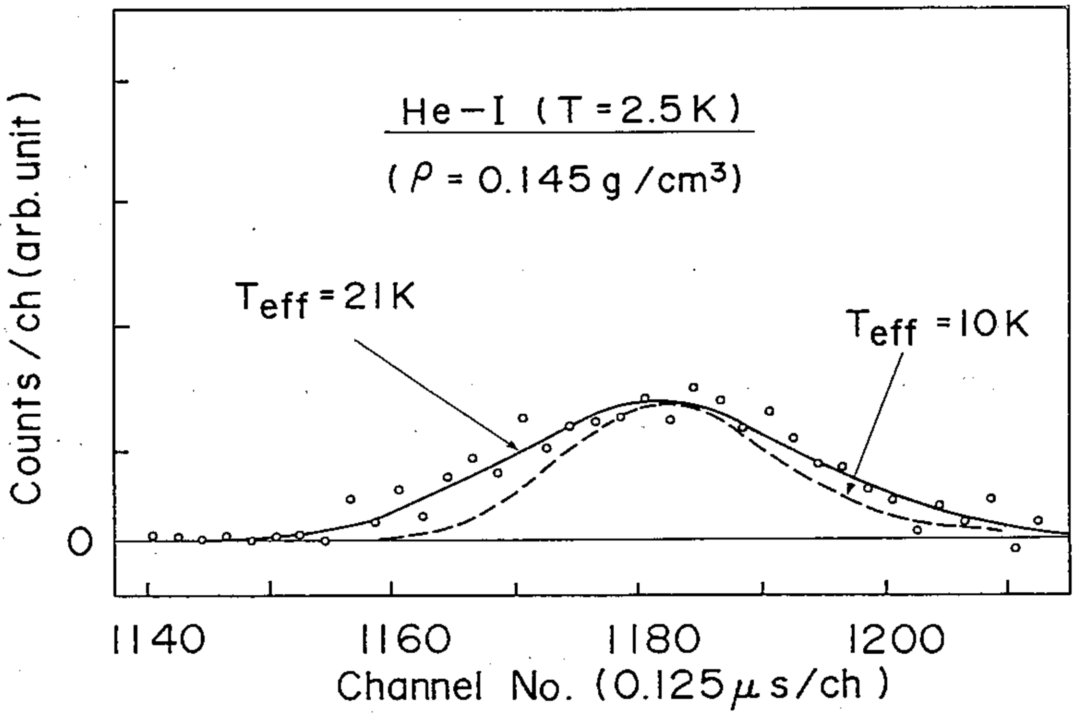

Fig. 3 Calculated neutron spectrum of ^{4}He-I compared with measured one. Silid line: T_{eff} = 21 K, broken line T_{eff} = 10 K.

References

1) J. M. Carpenter and N. Watanabe, Nucl. Instr. Meth. 213 (1983) 311.

2) M. S. Nelkin and D. E. Parks, Phys. Rev. 119 (1960) 1060.

3) A. D. B. Woods and V. F. Sears, J. Phys. C: Solid State Phys. 10 (1977) L341.

4) J. Ruvalds and Zawadowski, Phy. Rev. Lett. 25 (1970) 333.

Polarized Neutron Diffraction from Fe-V, Mg ASF.

Kenji KAWAGUCHI, Ryoichi YAMAMOTO, *Yasuo ENDOH
Nobuyodhi HOSOITO and Teruya SHINJO

Institute for Chemical Reseearch, Kyoto University, Uji, Kyoto 611
*Department of Physics, Tohoku University, Sendai 980

Magnetic properties near the interface layers of Fe-V Multilayered films with artificial superstructure films (we abbreviated as ASF) have been continuously elucidated on TOP spectrometer. The principle of the method was established[2) and therefore we are now applying the technique to different ASF materials.

The distribution of the magnetization density in Fe layers is estimated from the results. When we take a simple model of the clean interface boundary, which gives an assumption of the stepwise density distribution, we can postulate a structure that the top interface atom layer of Fe has a reduced magnetization but others have the bulk magnetization. Furthermore the reduction was derived to be 30%, which is also very consistent with the results of Mössbauer measurements. Further discussions on this matter are described in our full report[3).

Next we have studied the temperature dependence of the flipping ratio using a sample of FMG-3; $(Fe_8Mg_{24})_{100}$, which means that ASF consists of 100 multilayers of 8A Fe and 24A Mg. Samples are obtained by the evaporation method. Our primary concern was the different result of the temperature dependence between the magnetization and Mössbauer measurements. We are also interested in the fact that Fe and Mg are not missible each other. We have observed appreciable diffraction peaks in the small angle diffraction patterns, which clearly indicates the establishment of ASF. The flipping ratio of the 1st satellite was then observed to exhibit the rapid temperature dependence near 120 K, where the internal field disappears. On the contrary the magnetization drops near 30 K and has a long tail above it as shown in Fig. 1. Therefore the discrepancy may arise in the dynamics of the magnetic moments. Note that the characteristic frequency of neutrons is ~ 10^{12} sec^{-1}, and that of Mossbauer is ~ 10^{8} sec^{-1}. However diffraction peaks correspond to the fact that coherence length must exceeds more than 100A in space. Thus we can envision such a magnetic environment that the magnetic moments in each domain which seems to be more than 100A in diameter, fluctuate temporally at the rate of slower than about 10^{-8}sec.

References

1) The work was partly supported by the Grant in Aid for Special Distinguished Research from the Ministry of Education, Science and Culture.

2) Y. Endoh, J. de Physique C, 7 159 (1982)

3) N. Hosoito, K. Kawaguchi, T. Shinjo, T. Takada and Y. Endoh, J. Phys. Soc.. Jpn 53 (1984) 2659.

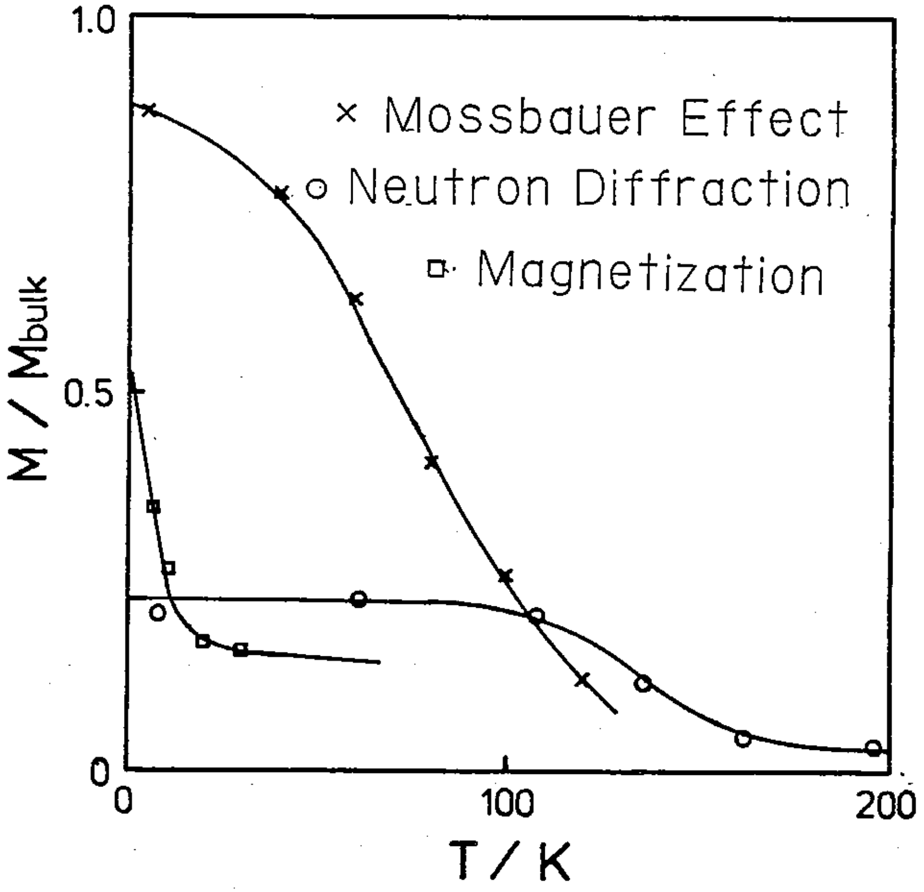

Fig. 1 Temperature dependence of Magnetization, Internal field and Flipping ratio from FeMg ASF.

Neutron depolarization on Metallic Spin Glass

Setsuo MITSUDA, Hiroyuki FUJIMOTO, Yasuo ENDOH and Susumu IKEDA*

Department of Physics, Tohoku Univeristy, Sendai 980
*National Laboratory for High Energy Physics, Ohomachi, Tsukuba-gun, Ibaraki 305

We have continuously studied the remarkable features of the wave length dependence of depolarization of transmitted neutrons through the metallic spin glass such as $Fe_{0.22}Cr_{0.78}$, $Fe_{0.7}Al_{0.3}$ and so forth.

we have been concentrated in the new results of oscillations in polarization with respect to the neutron wave length besides the change of depolarization behaviors associated with the phase transitions in these spin glasses. As was reportedd in KENS IV of the last year's issue$^{1)}$, we have observed the similar oscillations with respect to the neutron wave length, but in more beautiful manners from an $Fe_{0.7}Al_{0.3}$ spin glass. We illustrate the results in Fig. 1. Although we believe that this remarkable wave length dependence of depolarization arises in the dynamical effect of the macroscopic inhomogeneity, we have carefully examined by changing thickness of the sample, applied field and temperature as well.

In the case of the $Fe_{0.7}Al_{0.3}$ spin glass, the oscillation behaviors are observable in the ferromagnetic phase between ~ 200 K and ~ 400 K. Oscillations appear from about 50 Oe of the external field at our experimental condition. The experimental curves were well fitted to the empirical form of $P(\lambda) = P_1(\lambda) + Ae^{-B}\cos(C\lambda + D)$, where the first term in the right hand side represents the average depolarization and the second term corresponds to the oscillation amplitude. This empirical form was derived from the above mentioned dynamical model as was shown in the previous report$^{1)}$.

Alternately we have studied a possible case that the oscillations might occur due to the domain distribution in the ferromagnetic phase. It turned out that the results require a peculiar domain distribution with a regular size of each domain, which connects with each other by a certain angle. This specific domain distribution is unlikely.

Nevertheless we have observed that the wave length dependence of depolarization of transmitted neutrons through the spin glass alloy exhibits entirely different behaviors in the different magnetic phases. Then we emphasize that the depolarization measurements in particualr its wave length dependence can provide a novel information which could not be accessed by the conventional neutron scattering experiments. More details will be described in the full paper submitted to the regular journal[2].

References

1) S. Mitsuda, Y. Endoh and S. Ikeda, KENS RPT IV 189 (1983)
KEK Internal 83-4, ed. Y. Ishikawa et al.
2) Y. Endoh, S. Mitsuda and S. Ikeda, submitted to phys. Rev. Lett.

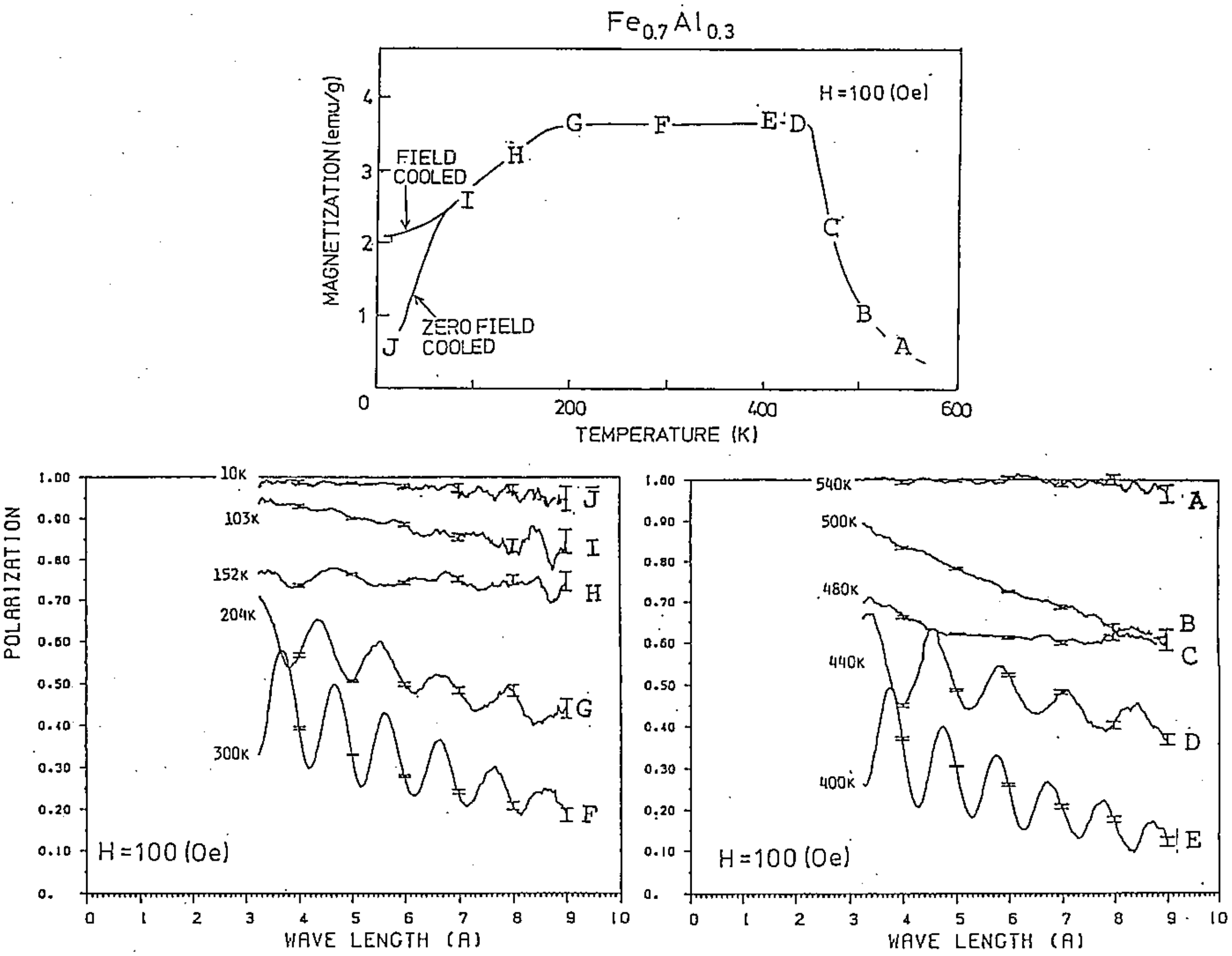

Fig. 1 Magnetization as well as depolarization curves from $Fe_{0.7}Al_{0.3}$ spin glass.

Neutron Depolarization Study on Domain Structure in Amorphous $(Co_{0.94}Fe_{0.06})_{74.5}Si_{13.5}B_{12}$ Alloy

E. Torikai, A. Ito*, S. Mitsuda** and Y. Endoh**

Doctral Research Center in Human Culture, Ochanomizu University, Tokyo 112

* Department of Physics, Ochanomizu University, Tokyo 112, Japan

** Physics Department, Tohoku University, Sendai 980 Japan

In order to investigate the bulk domain structure in amorphous $(Co_{0.94}Fe_{0.06})_{74.5}Si_{13.5}B_{12}$ alloy whose domain structure is difficult to observe by conventional methods, we performed the depolarization measurement of the polarized neutron transmitted through the specimen using the TOP spectrometer. The motivation of the study and the experimental method are described in the KENS report IV (1983, P191). From the preliminary results reported previously, it is found that the depolarization spectrum was drastically changed under magnetic fields below 20 Oe. In the present study, we concentrated into the experiment under magnetic fields between 1 Oe and 20 Oe. The magnetic fields were applied parallel to the initial spin axis of polarized neutron (z-axis).

The sample was prepared by the single-roller-quench method in the form of long ribbon (width 5 mm, thickness 23 μm on an average). The status of samples provided for measurements is as follows; (a) as prepared, (b) annealed for releasing the internal stress and (c) annealed in a magnetic field along the ribbon direction for inducing the magnetic anisotropy.

The neutron depolarization measurements were done at room temperature. Figure 1 shows the remaining polarization of neutrons (σ_z) after transmission through the samples (a), (b) and (c) as a function of wavelength of neutrons (solid lines). A magnetic field of 1 Oe along the ribbon's width was applied to hold the neutron polarization. The sinusoidal oscillation of σ_z is clearly observed though a whole period does not appear in the range of neutron's wavelength. The net magnetic flux density along the neutron's path ($\tilde{B}$) is deduced from the period of rotation. The estimated values of $\tilde{B}$ are (a) 0.59 T, (b) 0.55 T and (c) 0.58 T, which correspond to 79 %, 73 % and 77 % of the saturation magnetic flux density (0.75 T measured by SQUID).

It would be reasonable to attribute the reduction of $\tilde{B}$ compared with the saturated value to local magnetization in thin layers near the surfaces. The amplitude of the rotation reflects the directional distribution of the local magnetization axes. In case of the sample (c) the minimum value of σ_z attains to almost -1, indicating that the local magnetization axes align parallel to the ribbon direction. The smaller amplitude in the sample (a) and (b) compared with the sample (c) suggests that the local magnetization in the sample (a) and (b) has larger z-component. The directional distribution of the local magnetization axes had been also measured using the Mössbauer spectroscopy. The results are as follows; (a) local magnetization axes lie in the ribbon plane and distribute widely around the ribbon direction preferentially, (b) most of local magnetization axes also lie in the ribbon plane but distribute randomly in the plane, (c) almost all of the local magnetization axes are aligned in the ribbon direction. The change of neutron polarization expected from the result of the Mössbauer measurement is also shown in Fig. 1 for each sample by a broken line. The period of rotation was taken as same as that of the solid line because this kind of information is scarecely obtained by the other methods. The result of neutron and the Mössbauer measurements are in good agreement qualitatively with each other. Thus the simple model shown in Fig. 2 is suggested as the domain structure along the ribbon's thickness.

The magnetization process was also studied by observing the change of the neutron depolarization. Figure 3 shows the change of the σ_z after neutrons pass through the sample (c) in the various magnetic fields along the ribbon's width which is the magnetic hard axis in the ribbon plane. In order to increase the thickness of the specimen along the neutron path, the ribbon plane was set at 45 deg. to the neutron beam. The period of rotation becomes longer above 9 Oe but it undulates clearly even at 11 Oe. The reduced net magnetic flux density ($\tilde{B}/B_s$) deduced from the period is shown in Fig. 4. The decrease of $\tilde{B}/B_s$ above 9 Oe indicates that local magnetization axes along the neutron path start to rotate out of phase with one another. But it is noticeable that $\tilde{B}/B_s$ is still kept about 50 % even at 11 Oe; magnetic moments along the ribbon's thickness rotate rather coherently toward the direction of magnetic field. The result for the sample (b) is also shown in Fig. 4.

Figure 5 shows the change of σ_z measured for the sample (a) in the various magnetic fields along the ribbon direction which is the easy axis macroscopically. The periodic oscillation is remarkable even at 20 Oe. This means that the average local magnetization axes are still deviated from the direction (z) of applied fields. The period becomes shorter with increasing the field contrary to the results with the magnetic fields along the hard axis. The value of $\tilde{B}/B_s$ shown in Fig. 6 reaches to almost unity above 15 Oe. This means that the magnetization axes along the neutron's path are arranged in the same direction though they incline from z-axis yet as mentioned above.

The change of the amplitude and the monotonic decay of polarization superposed on the sinusoidal oscillation may give further information about the domain structure. But unfortunately the detail analysis for getting these parameters is difficult because the ribbon's thickness is too thin to rotate neutron spins at least twice in the range of the neutron's wavelength.

To conclude the coherency of the local magnetization axes along the thickness of the ribbon becomes clear. The coherent characteristic is kept even in the magnetization process. The directional distribution of the local magnetization axes is consistent with the result of the Mössbauer measurement.

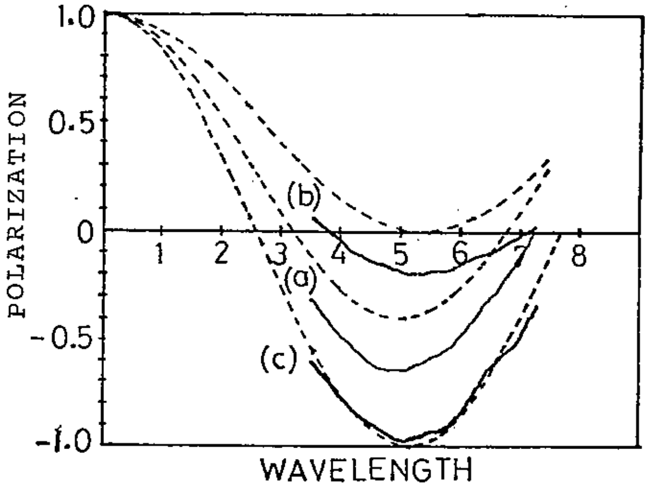

Fig. 1 Remaining polarization of polarized neutron after transmission through samples; (a) as prepared, (b) annealed for releasing internal stress and (c) annealed for inducing magnetic anisotropy along ribbon direction (solid lines). Ribbon's width // z-axis. Dashed lines represent the calculation based on the result of Mössbauer measurement.

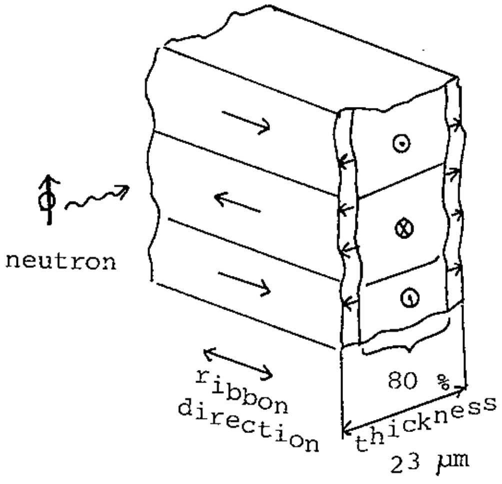

Fig. 2 The model of domain structure along the ribbon's thickness. The direction of magnetization in the sample (c) is described.

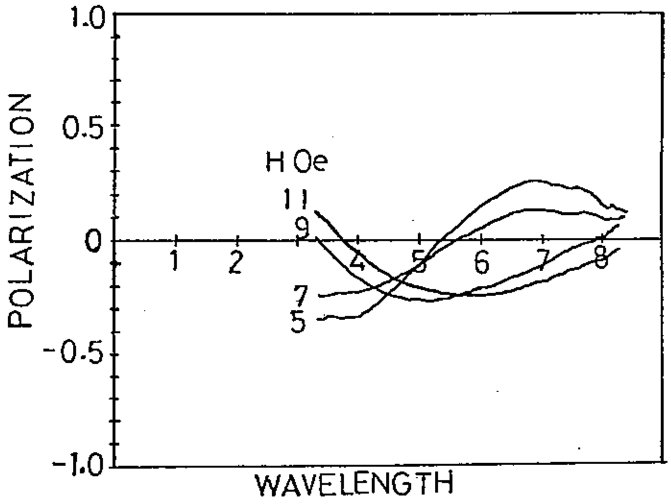

Fig. 3 Remaining polarization of polarized neutron after transmission through the sample (c) in various magnetic fields along the ribbon's width. The ribbon plane was set at 45 deg. to neutron beam.

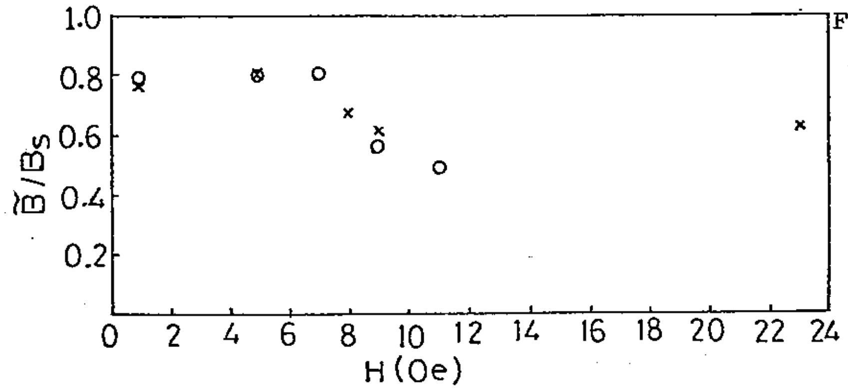

Fig. 4 Change of reduced magnetic flux density ($\tilde{B}/B_s$).

Open circles: sample (c).

Crosses: sample (b).

H // ribbon's width (hard axis).

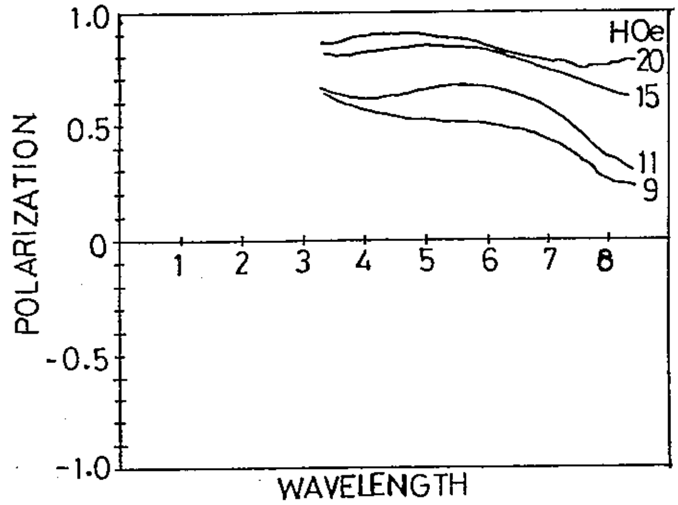

Fig. 5 Remaining polarization of polarized neutron after transmission through the sample (a) in various magnetic fields along the ribbon direction. The ribbon plane was set at 45 deg. to neutron beam.

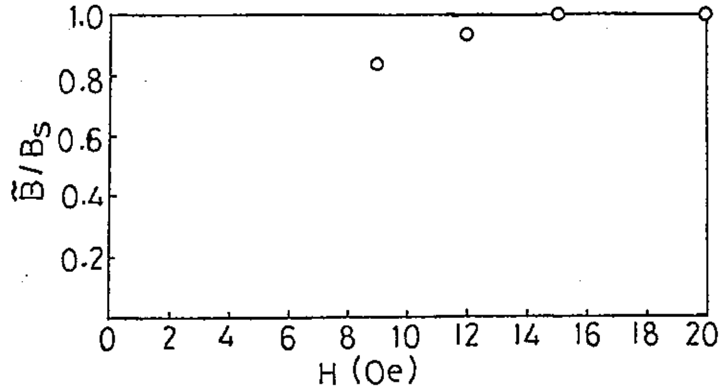

Fig. 6 Change of reduced net magnetic flux density ($\tilde{B}/B_s$) of the sample (a).

H // ribbon direction (easy axis).

Neutron Depolarization Study of the Re-entrant Spin-glass Transition in $Rb_2Mn_{(1-x)}Cr_xCl_4$

Koichi KATSUMATA, Yasuo ENDOH* and Setsuo MITSUDA*

Research Institute of Applied Electricity,
Hokkaido University, Sapporo 060, Japan

*Department of Physics, Tohoku University,
Sendai 980, Japan

The measurements of the depolarization of a polarized neutron beam after passing through magnetic materials have been used to study the ordered phases and the phase transitions of ferromagnets 1-4) and spin-glasses. 4) We have used this technique to clarify the nature of the disordering transition observed in the random mixture, $Rb_2Mn_{(1-x)}Cr_xCl_4$ of an insulating antiferromagnet and an insulating ferromagnet. The concentration versus transition temperature phase diagram of this mixed system obtained from ac susceptibility measurements by one of the authors(K.K.) is presented in Fig. 1. We have two transitions for a given concentration; a transition from the paramagnetic to ferromagnetic phase followed by that from the ferromagnetic to disordered phase upon decreasing temperature. This kind of transition occurring in a random system with competing ferromagnetic and antiferromagnetic exchange interactions is called a re-entrant spin=glass one.

We have made a neutron depolarization measurement on this mixed system by using the TOP spectrometer. The result for the x=0.52 sample is shown in Fig. 2. The polarization decreases with increasing the wave length of the neutrons for all the temperatures measured. If we plot the polarization, for a given wave length of the neutrons, against temperature for the ZFC case, we see drastic changes in the polarization at the two transition temperatures. At the paramagnetic to ferromagnetic transition temperature, the polarization decreases sharply. The polarization then begins to increase around 10K, where the disordering transition has been observed in the susceptibility measurement.

The following two interpretations for the temperature dependence of

Fig. 1.

Concentration versus transition temperature phase diagram in the Cr-rich regions of $Rb_2Mn_{(1-x)}Cr_xCl_4$ obtained from the susceptibility measurements.

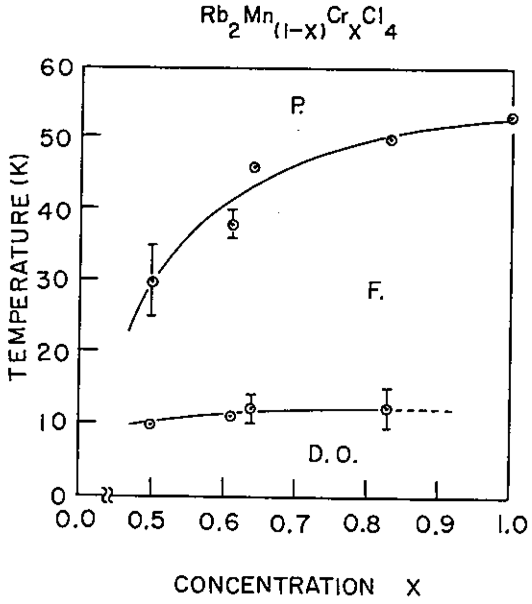

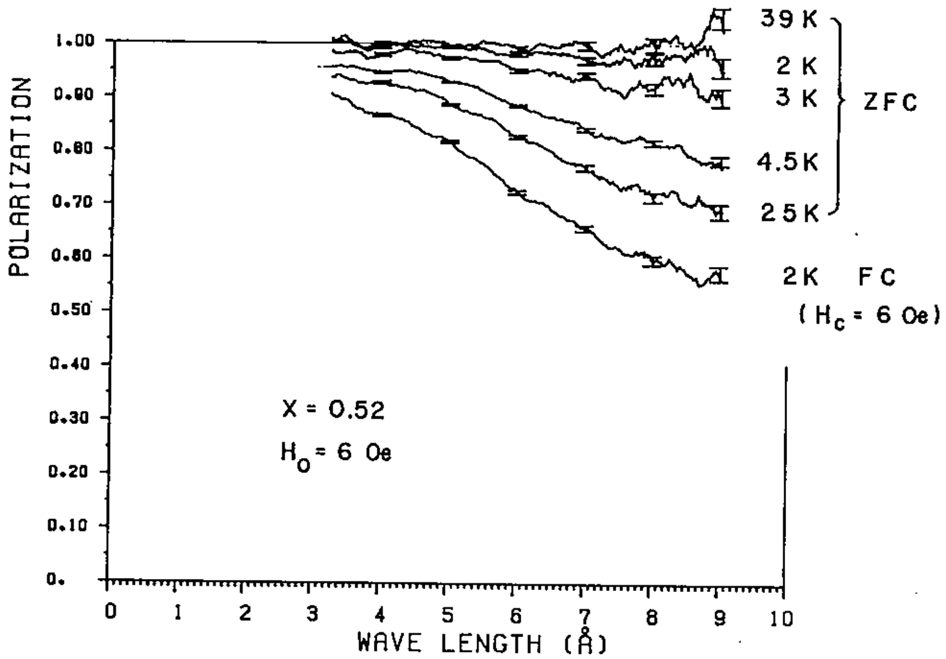

Fig. 2. Polarization of the neutron beam transmitted through thin plate of $Rb_2Mn_{0.48}Cr_{0.52}Cl_4$ is plotted against the wave length of the neutrons for several temperatures. The sample was cooled from the paramagnetic phase to the respective temperature shown in the figure without the external magnetic field(ZFC) or with the external field(FC). In order to maintain the magnetization of the sample, the external field of 6 Oe was applied after cooling the sample in ZFC case.

the polarization are possible. One is that based on a phase transition model, and the other is that based on the model proposed by Aeppli et al.5) The temperature dependence of the polarization is explained by the phase transition model as follows; above the Curie point the spins of the system fluctuate faster than the Larmor period of the neutrons and thus no depolarization of the neutron spins occurs. With decreasing temperature the fluctuation of the system becomes slow and the depolarization of the neutrons results. Since the re-entrant spin-glass phase is different from the ferromagnetic one and we expect that the spins fluctuate in the re-entrant phase faster than in the ferromagnetic one, the polarization increases below the re-entrance temperature. The temperature dependence of the polarization is explained by the Aeppli model as follows; the re-entrant phase in the Aeppli model is composed of ferromagnetic and spin-glass like networks. The increase of the polarization below the re-entrance temperature means that the sizes of the ferromagnetic networks become small, due probably to random field effects.

Details will be reported elsewhere.6)

References

1) O. Halpern and T. Holstein: Phys. Rev. 59 (1941) 960.

2) G. M. Drabkin, E. I. Zabidarov, Ya. A. Kasman and A. I. Okorokov: Soviet Phys. JETP 29 (1969) 261.

3) M. Th. Rekveldt: Z. Phys. 259 (1973) 391.

4) Y. Endoh, Y. Sasaki, H. Ono, S. Mitsuda and S. Ikeda: Physica 120B (1983) 45.

5) G. Aeppli, S. M. Shapiro, R. J. Birgeneau and H. S. Chen: Phys. Rev. B28 (1983) 5160.

6) K. Katsumata, Y. Endoh, S. Mitsuda and M. Tanimoto: preprint.

Long Period Helical Spin Structure in $Fe_{1-x}Co_xSi$

Kenichi Ishimoto, Yasuo Yamaguchi,
Setsuo Mitsuda*, Masayoshi Ishida* and Yasuo Endoh*

The Research Institute for Iron,Steel and Other Metals,
Tohoku University, Sendai 980
*Department of Physics, Tohoku University, Sendai 980

A long periodic helical order in B20 compounds was firstly found in MnSi[1)]. The system of $Fe_{1-x}Co_xSi$ has been known as an itinerant electron magnet system with the same crystal structure[2)]. The long periodic helical spin structure was also observed for $0.05<x<0.8$ in this system by small - angle neutron diffraction measurement on polycrystalline samples[3),4)]. These helical spin structures are thought to be due to non-centrosymmetry of the B20 structure in which the Dzyaloshinsky-Moriya interaction survives[5)].

In this investigation we studied the magnetic field dependence of the long periodic helical structure by polarized neutron diffraction in order to clarify the character of the anisotropic exchange interaction of this system. Experiments were made by using TOP polarized neutron diffractometer installed at the cold neutron guide. We measured the satellites of (000) Bragg reflection for $Fe_{0.8}Co_{0.2}Si$ at 23 K. The magnetic field was applied antiparallel to the scattering vector and the polarization of the neutron was parallel or antiparallel to the scattering vector, as shown in Fig. 1.

Before applying the magnetic field to the sample (virgin state) both clockwise and counterclockwise helix were observed, as shown in Fig. 2. Furthermore in virgin state the satellite was found in any direction around (000). Though satellites were observed at any directions, the intensity peak at <001> direction is thought to be due to the field cooling effect by the residual field of the electromagnet. Then the satellite is thought to be distributed homogeneously on the sphere around (000) in virgin state.

Once high field (≃2 kOe) was applied and removed, the helix with the propagation vector being parallel to the field direction was stabilized, and the winding of the helix was counterclockwise, as shown in Fig. 4. The stability of the helix is thought to be equal in any direction since the width of the rocking curve are same of $(00\bar{\delta})$ and $(\delta\delta\delta)$ reflection^{+}. (Fig. 5)

We investigated the behavior of the helix with respect to the magnetic field. After the helix was stabilized along $[11\bar{1}]$ direction by the operation mentioned above, we observed field dependence of the $(\delta\delta\delta)$ reflection. The result is shown in Fig. 6. We regard this result as following. With increasing field, the propagation vector of the helix is changed to the field direction and helix becomes helical cone with ferromagnetic component. At last all spins are aligned along the magnetic field (ferromagnetic) under the higher field. In the path of decreasing field, the cone angle is increasing and helical spin structure is stabilized along the magnetic field.

These experimental results are very interesting in comparison with those of MnSi. The crystal structure is the same for $Fe_{1-x}Co_xSi$ and MnSi, and the long periodic helical structure of this type was firstly found in MnSi$^{1)}$. The helix in MnSi is reported to be clockwise$^{6)}$ and to be stable in <111> direction.$^{1)}$ The propagation vector of the helix is rotated by the applied magnetic field as in $Fe_{1-x}Co_xSi$, but the propagation vector comes back to <111> direction with decreasing field.$^{1)}$ In the case of $Fe_{1-x}Co_xSi$, the propagation vector of the helix seems to be difficult to rotate under the low magnetic fields. This is thought to come from two respects. One is an intrinsic character of the system. Nakanishi et al.$^{5)}$ obtained the free energy expression of helical spin structure F_H as

$$F_H = -\frac{1}{4\gamma\chi(0)^2}\left\{[1+(\frac{3K_1}{4\gamma}) - 4|D|\chi(0)Q + 2(C + A_1 - A_3)\chi(0)Q^2] + [(\frac{3K_1}{4\gamma}) + 2(A_3-3A_1)\chi(0)Q^2](\beta_1^4+\beta_2^4+\beta_3^4)\right\},$$

where $\vec{Q}$ is propagation vector of helix and βi's are direction cosines of $\vec{Q}$. The last term of right side defines the direction of helix axis. If the second [ ] is positive, $\vec{Q}$ points in <111> direction. If, on the other hand, it is negative, $\vec{Q}$ points in <100> direction. In $Fe_{0.8}Co_{0.2}Si$ this term seems to be very small, so the helix could not change the direction of its propagation vector. The other is inhomogeneity due to the mixed crystal.

+ We use the term "$(00\bar{\delta})$" for the satellite of $[00\bar{1}]$ direction of (000).

The local fluctuation of magnetization in the mixed system might also prevent the propagation vector from moving. In virgin state the propagation vector of helix distributes widely in length, direction and winding. There seems to be local fluctuation of the coefficient of the D-M interaction in this system.

References

1) Y. Ishikawa, K. Tajima, D. Bloch and M. Roth: Sol. Stat. Commun. 19 (1976) 525.
2) W.B. Pearson: Handbook of Lattice Spacing and Structure of Metal (Pergamon Press, Oxford, 1967) Vol. 2.
3) J. Beille, J. Voiron, F. Towfiq, M. Roth and Z.Y. Zhang: J. Phys. F: Metal Phys. 11 (1981) 2153.
4) J. Beille, J. Voiron and M. Roth: Sol. Stat. Commun. 47 (1983) 399.
5) O. Nakanishi, A. Yanase, A. Hasegawa and M. Kataoka: Sol. Stat. Commun. 35 (1980) 995.
6) M. Ishida, Y. Endoh, S. Mitsuda and Y. Ishikawa: KENS REPORT-IV (1983) 198.

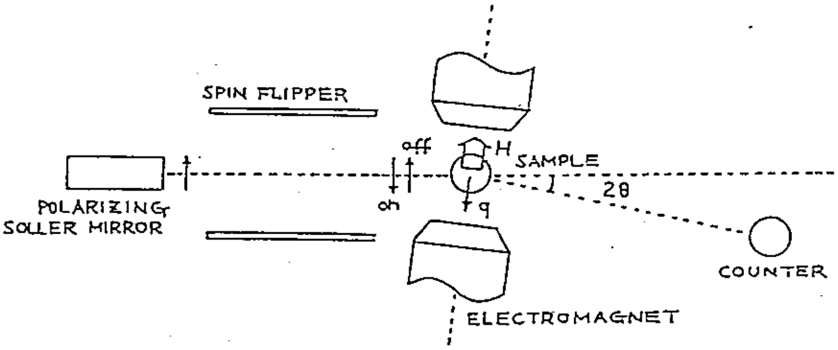

Fig. 1 Schematic arrangement of TOP in this experiment. $2\theta = 0.901°$

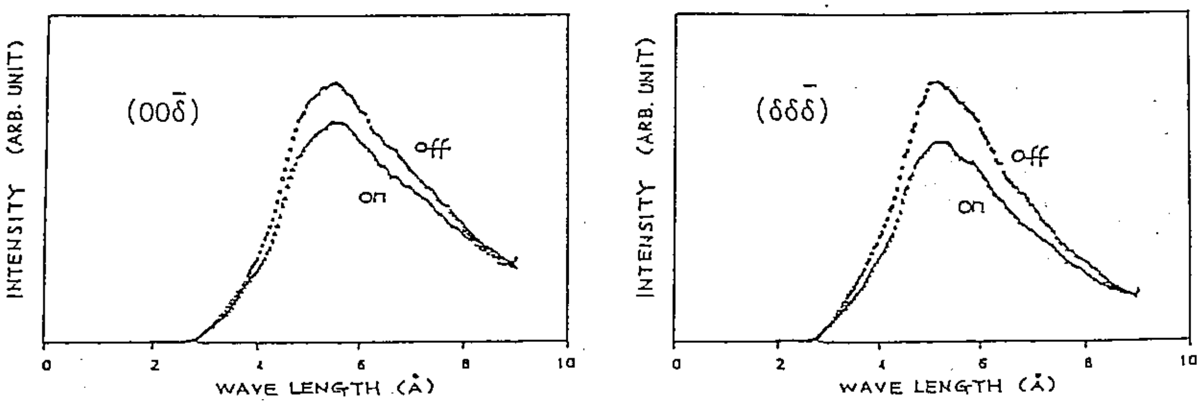

Fig. 2 The intensity of $(00\bar{\delta})$ and $(\delta\delta\bar{\delta})$ reflections, with spin flipper on and off, in virgin state.

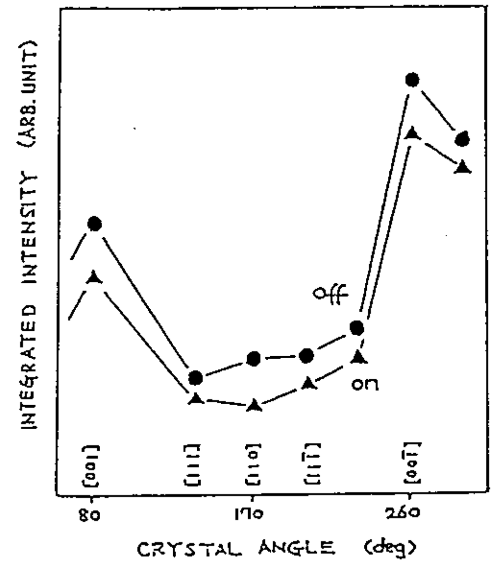

Fig. 3 The distribution of the integrated intensity of the satellites.

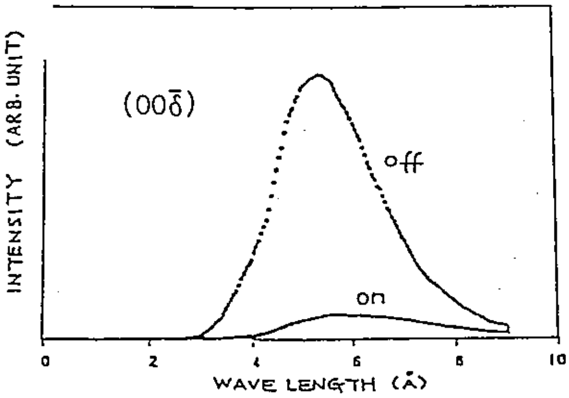

Fig. 4 The intensity of (00$\bar{\delta}$) reflection after high field was applied and removed.

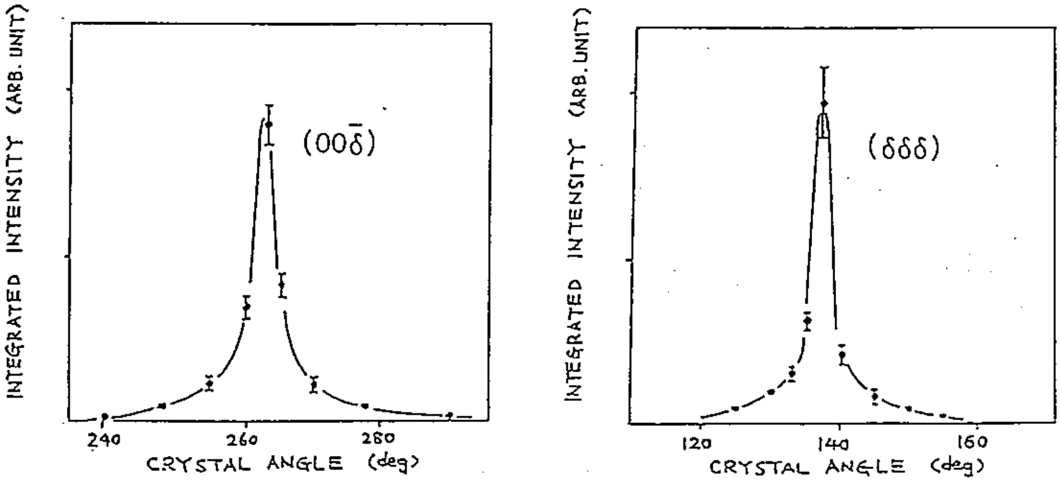

Fig. 5 The rocking curves of (00$\bar{\delta}$) and (δδδ) reflections.

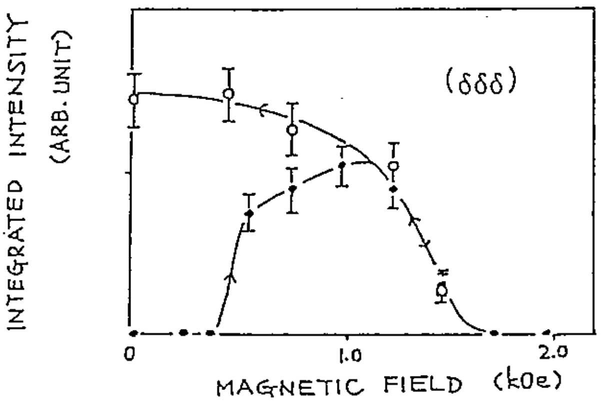

Fig. 6 The field dependence of integrated intensity of (δδδ) reflection after the helix was stabilized along [11$\bar{1}$] direction.

Small-Angle Scattering of Polarized Neutrons from $Fe_{65}{}^{62}Ni_{35}$ Invar Alloy

S. Komura, T. Takeda and Y. Endoh*

Faculty of Integrated Arts & Sciences, Hiroshima University,
Hiroshima 730, Japan
*Department of Physics, Tohoku University, Sendai 980, Japan

Our previous experiment by means of neutron small angle scattering from $Fe_{65}Ni_{35}$ invar alloy[1,2] has established that there is a magnetic inhomogeneous structure inherent to this alloy. In order to accout this fact we have proposed a model[3] in which local fluctuation of chemical composition gives rise to the magnetic inhomogeneous structure; Ni-rich local regions tend to be ferromagnetic and Fe-rich local regions paramagnetic. Although this model explains well the structure function of the alloy, there is no direct evidence which supports the correlation of local chemical composition to the magnetic ordering or disordering.

Small-angle scattering experiment using polarized neutrons offers a possibility to check this correlation, since we can measure the Fourier transform $S_{bp}(\vec{k})$ of the space-correlation function $G_{bp}(\vec{r})$ of nuclear and magnetic scattering amplitude density $\rho_b(\vec{r})$ and $\rho_p(\vec{r})$. These functions are related to one another by

$$G_{bp}(\vec{r}) = \frac{1}{v} \int \{\rho_b(\vec{r}\,') - \bar{\rho}_b\}\{\rho_p(\vec{r}+\vec{r}\,') - \bar{\rho}_p\}\, d\vec{r}\,' \qquad (1)$$

and

$$S_{bp}(k) = 4\pi \int_0^\infty G_{bp}(r)\, \frac{\sin kr}{kr}\, r^2 dr \qquad (2)$$

if $G_{bp}(r)$ is spherical.

We have prepared two $Fe_{65}Ni_{35}$ samples using either natural nickel or isotope ${}^{62}Ni$. Since $b_{Fe} = 0.951 \times 10^{-12}$ cm and $b_{Ni(nat)} = 1.03 \times 10^{-12}$ cm, we expect that in $Fe_{65}{}^{nat}Ni_{35}$ $\rho_b(r) - \bar{\rho}_b$ at Fe-rich regions are negative and that at Ni-rich regions positive. However since $b_{Ni(62)} = -0.87 \times 10^{-12}$ cm, we expect that in $Fe_{65}{}^{62}Ni_{35}$ $\rho_b(r) - \bar{\rho}_b$ at Fe-rich regions is positive and that at Ni-rich regions is negative. Since in our model we assume that Ni-rich regions are ferromagnetic ($p_{Fe} = 0.76 \times 10^{-12}$ cm, $p_{Ni} = 0.16 \times 10^{-12}$ cm) and Fe-rich regions paramagnetic $p_{Fe} = p_{Ni} = 0$, it follows that $\rho_p(r) - \bar{\rho}_p > 0$

at Ni-rich regions and $\rho_p(r) - \bar{\rho}_p < 0$ at Fe-rich regions. These spatial relations are shown schematically in Fig. 1 for $Fe_{65}{}^{nat}Ni_{35}$ and $Fe_{65}{}^{62}Ni_{35}$. Thus for $Fe_{65}{}^{nat}Ni_{35}$ we expect that $G_{bp}(r) > 0$ for small r and $G_{bp}(r) \simeq 0$ for large r due to the irregularity of the shape of either Fe- or Ni-rich regions. Therefore we expect that $S_{bp}(k) > 0$ for small k in $Fe_{65}{}^{nat}Ni_{35}$. However in contrast we expect that in $Fe_{65}{}^{62}Ni_{35}$ $G_{bp}(r) < 0$ for small r and $S_{bp}(k) < 0$ for small k.

In this experiment we used a time-of flight polarized neutron spectrometer TOP$^{4)}$ at KENS and measured the small-angle scattering cross section $d\Sigma/d\Omega(k)$ from either $Fe_{65}{}^{nat}Ni_{35}$ or $Fe_{65}{}^{62}Ni_{35}$ with neutron spin up (↑) and down (↓) and sample magnetization parallel ($\|$) or perpedicular ($\perp$) to the scattering vector k. From these cross sections we obtained the following quantities:

$$\left(\frac{d\Sigma}{d\Omega}\right)_{sum} \equiv \frac{1}{2}\left\{\left(\frac{d\Sigma}{d\Omega}\right)_{\uparrow\perp} + \left(\frac{d\Sigma}{d\Omega}\right)_{\downarrow\perp}\right\} = \left(\frac{d\Sigma}{d\Omega}\right)_{diff} + S_{bb}(k) + S_{pp}(k) \qquad (3)$$

$$\left(\frac{d\Sigma}{d\Omega}\right)_{sub} \equiv \frac{1}{2}\left\{\left(\frac{d\Sigma}{d\Omega}\right)_{\uparrow\perp} - \left(\frac{d\Sigma}{d\Omega}\right)_{\downarrow\perp}\right\} = 2\, S_{bp}(k) \qquad (4)$$

$$\left(\frac{d\Sigma}{d\Omega}\right)_{\|} \equiv \left(\frac{d\Sigma}{d\Omega}\right)_{\uparrow\|} = \left(\frac{d\Sigma}{d\Omega}\right)_{\downarrow\|} = \left(\frac{d\Sigma}{d\Omega}\right)_{diff} + S_{bb}(k) \qquad (5)$$

where $(d\Sigma/d\Omega)_{diff}$ is the contribution from the diffuse scatering, $S_{bb}(k)$ and $S_{pp}(k)$ are nuclear and magnetic structure function, respectively, defined similarly to (2) and (1).

Fig. 2 and 3 show the results of the experiments at room temperature for $Fe_{65}{}^{nat}Ni_{35}$ and $Fe_{65}{}^{62}Ni_{35}$, respectively. There is a severe depolarization of polarized neutrons in the sample. But no corrections for the depolarization has been made. We see that $(d\Sigma/d\Omega)_{sum}$ for both $Fe_{65}{}^{nat}Ni_{35}$ and $Fe_{65}{}^{62}Ni_{35}$ are positive and nearly same to each other, whereas $(d\Sigma/d\Omega)_{sub}$ for $Fe_{65}{}^{nat}Ni_{35}$ are positive and very close to zero and $(d\Sigma/d\Omega)_{sub}$ for $Fe_{65}{}^{62}Ni_{35}$ are negative. This result clearly demonstrates the validity of our model of magnetic inhomogeneous structure for $Fe_{65}Ni_{35}$ alloy, at least qualitatively.

References

1) S. Komura, G. Lippmann and W. Schmatz, J. Appl. Cryst., 7, 233 (1974)

2) S. Komura, G. Lippmann and W. Schmatz, J. Magnetism Mag. Materials, 5, 123 (1977)

3) S. Komura and T. Takeda, J. Magnetism Mag. Materials, 10, 191 (1979)

4) Y. Endoh and Y. Ishikawa, KENS Report I, p.149, KEK Internal 80-1, May 1980, I/B

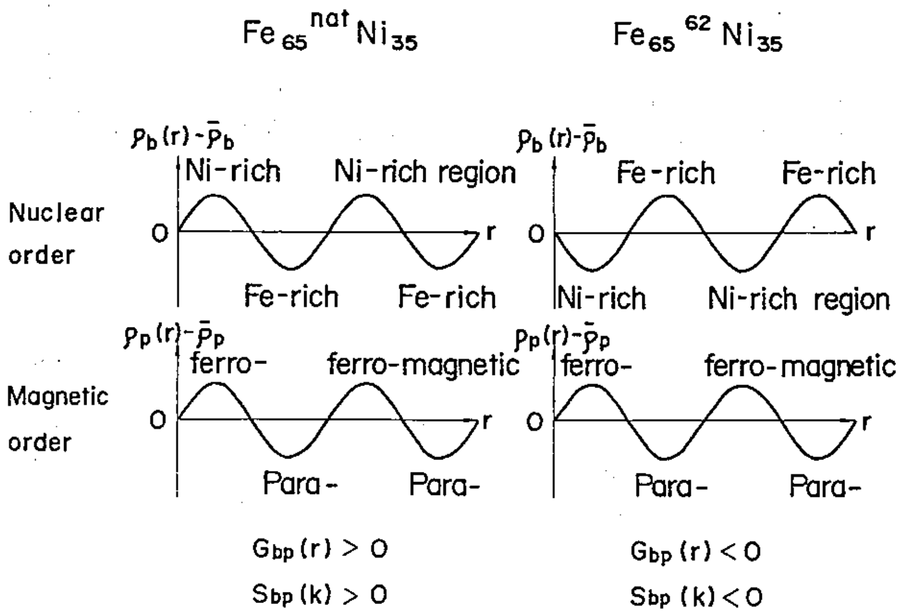

Fig. 1 Schematic pictures of the magnetic inhomogeneous structures correlated with the chemical inhomogenous structures in $Fe_{65}\ {}^{nat}Ni_{35}$ and $Fe_{65}\ {}^{62}Ni_{35}$ expressed in terms of the deviation from the mean scattering amplitude density $\overline{\rho}$.

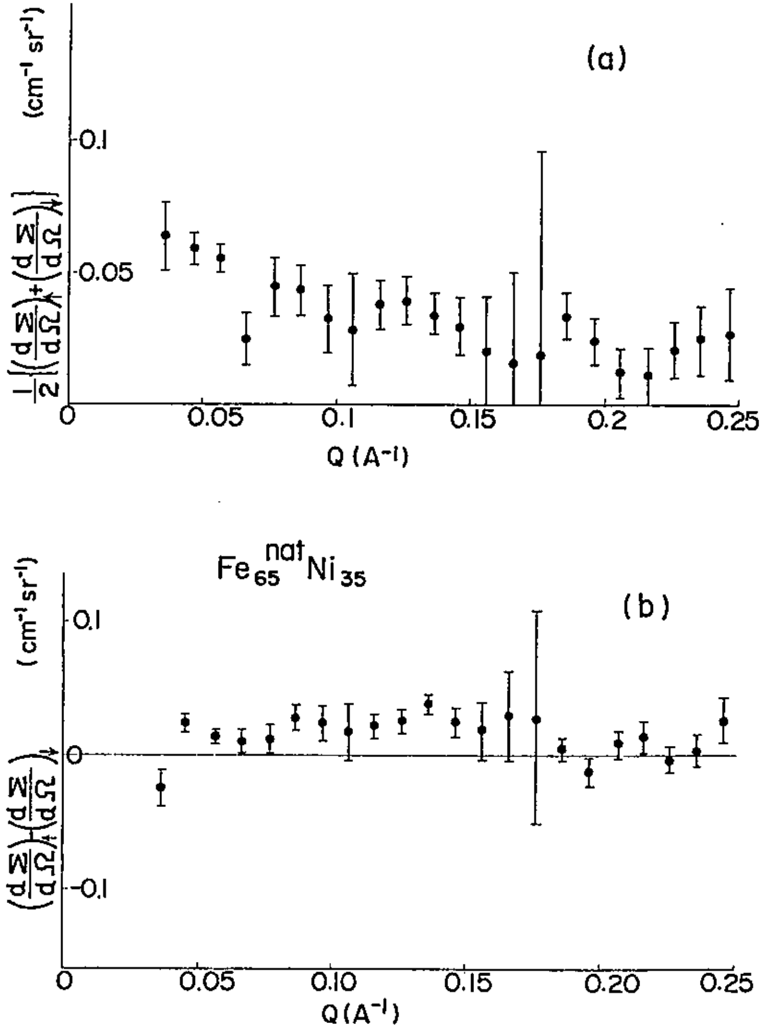

Fig. 2 Scattering cross section (a) $(d\Sigma/d\Omega)_{sum}$ and (b) $(d\Sigma/d\Omega)_{sub}$ for Fe_{65} $^{nat}Ni_{35}$ as a function of scattering vector Q.

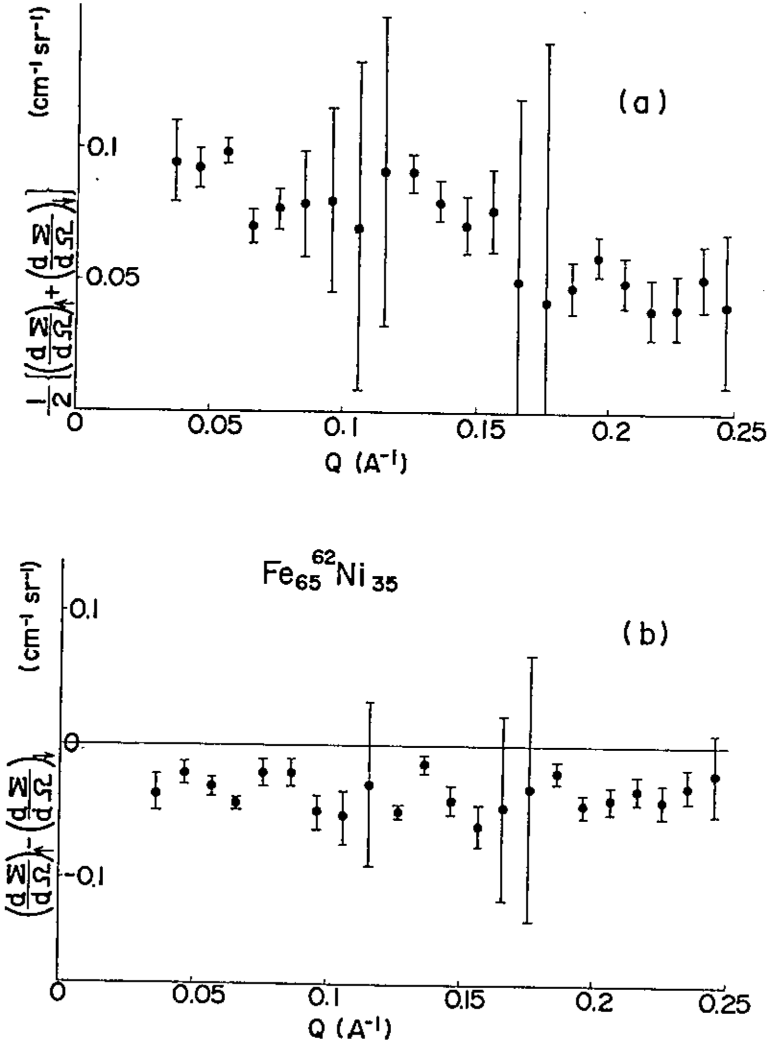

Fig. 3 Same as Fig. 2 for Fe_{65} $^{62}Ni_{35}$.

Setup of neutron spin echo spectrometer and the improvement of the polarizers

Hiroyuki FUJIMOTO, Setsuo MITSUDA, Mitsugu ONODERA,
*Susumu IKEDA and Yasuo ENDOH

Department of Physics, Tohoku University, Sendai 980,
*National Laboratory for High Energy Physics, Oho-machi, Tsukuba, Ibaraki 311

Neutron Spin Echo spectrometer is now under construction. We have designed all of the components necessary for NSE, such as precession coils. Figure 1 shows an overview of our present setup. We examined one of the important components of the spectrometer, the π-turner, which is Mezei-type spin turner. The principle of Mezei-type spin turner is now well understood. Neutrons precess around the direction of applied field. The angular frequency of precession is;

$$\omega=\gamma H, \tag{1}$$

where γ is the gyromagnetic ratio of neutron and H is the applied field. When neutrons of wave length λ pass through the magnetic field of length L(m), the precession angle of neutron is expressed as follows,

$$\begin{aligned}\phi&=\omega t,\\ t&=L/v,\\ v&=3956/\lambda.\end{aligned} \tag{2}$$

where v is the velocity and λ is the wave length of neutron. Therefore the magnetic field H in π-turner must be driven by wave length dependent current with a fixed magnetic field direction, so that neutron spin precesses in the field by just π rad. Figure 2 shows the flipping efficiency of π-turner coil, driven by (a) wave length dependent drive current, (b) constant current. Compared with (b), (a) shows that neutron precesses nearly π rad., through necessary wave length range of 3-9A. We are encouraged by this result, because we will be able to achieve highest efficiency by fine tuning.

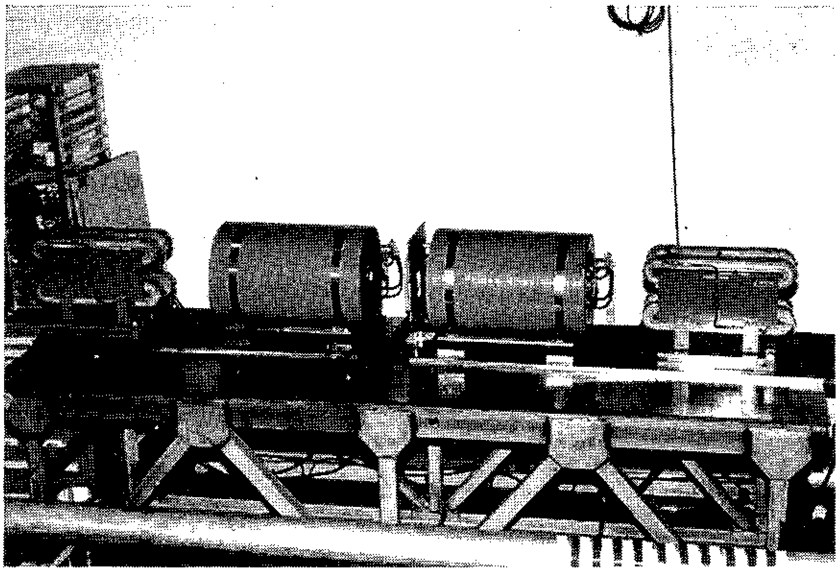

Fig. 1 Setup of NSE spectrometer.

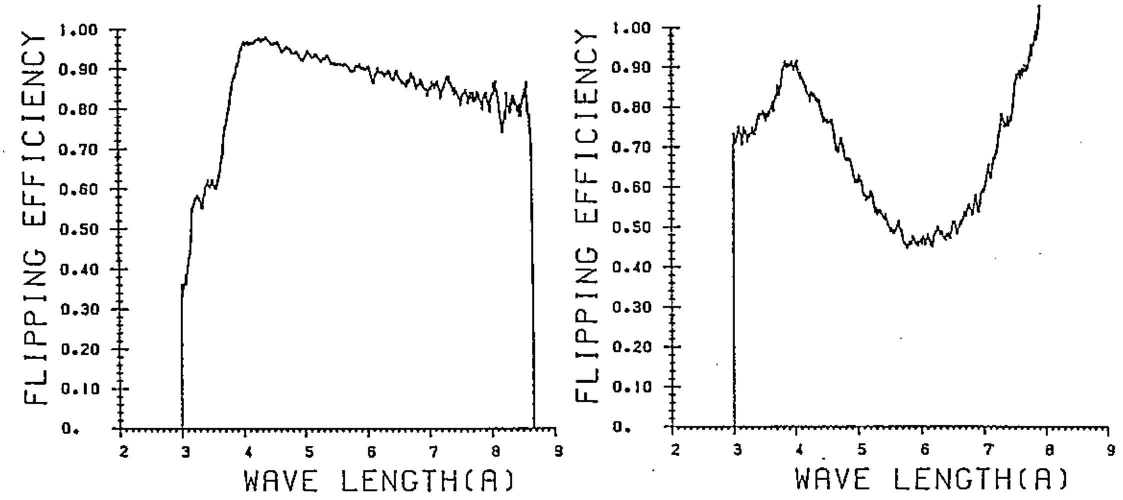

(a)

(b)

Fig. 2 Flipping efficiency of π-turner.
(a) Driven by 1/t current,
(b) driven by constant current.

During this period we have continuously made an effort to provide polarizers. We have then compared the polarizing efficiency of three polarizers. One of them is the newly made polarizer whose alloy concentration of $Co_{67.5}Fe_{32.5}$ is determined, according to the results of test polarizers$^{1)}$. The others are presently installed at TOP spectrometer. Assuming that f=1, beam polarization with polarizer and analyzer is expressed in the following simple relation.

$$P=p_a p_p. \tag{3}$$

We can calculate the polarizing efficiency of each polarizer by means of three combinations of three polarizers (Fig.3). We see immediately the considerable improvement of the polarizability in the longer wave length, similar to the test polarizer$^{1)}$. We confirmed that the alloy concentration seems to be optimal.

At the same time we have examined the multilayered polarizer, which consists of thin films of Fe and Ge alternately evaporated on glass substrate$^{2)}$. As shown in Fig.4 characteristics is relatively of wide peak shape and of good polarizability at the peak point. We are aware that the peak of polarizing efficiency just corresponds to that of beam profile displayed under the polarization curve.

For refernce we show the beam profile and polarizability reflected by a supermirror$^{3)}$ in Fig.5. Polarizing efficiency is constant through the wave length range 3 to 7A, but the supermirror has several disadvantages for our experiments, and discussion is in the previous report$^{1)}$ in detail.

We thank to Mr. H. Ishida (Tohoku Univ.) for his effort to make polarizers. We acknowledge to Prof. Y. Ito (ISSP, Univ. of Tokyo) and Dr. F. Mezei (ILL) for their kind arrangements.

References

1) Y. Endoh, S. Mitsuda, S. Ikeda and M. Onodera: KENS REPORT-IV (1983) 200.

2) Loan from Prof. Ito of ISSP.

3) Loan from Dr. Mezei of ILL.

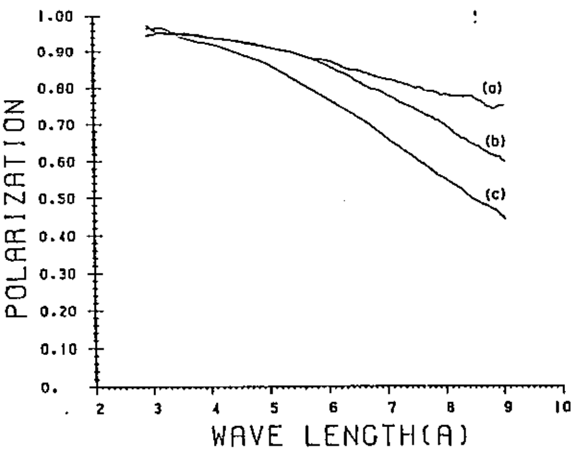

Fig. 3 Polarizability of FeCo Soller type magnetic mirrors.

(a) Newly made polarizer,

(b) currently used at TOP,

(c) currently used at TOP.

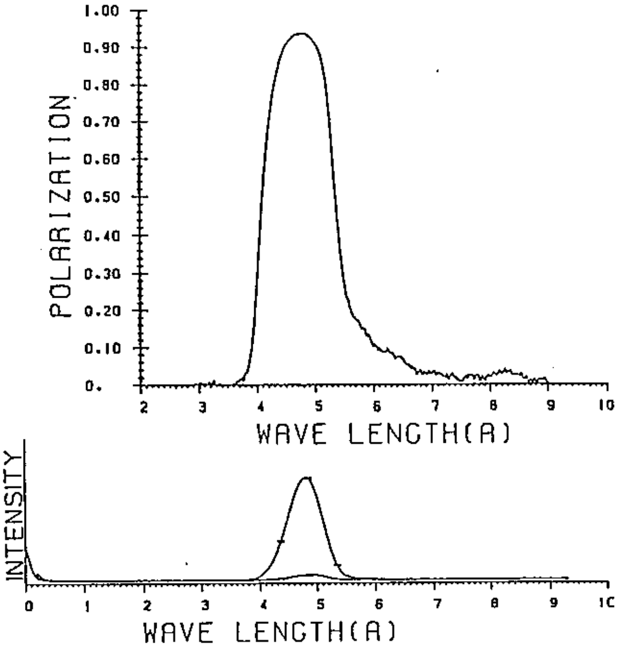

Fig. 4 Polarizing efficiency and beam spectrum of Multilayer.

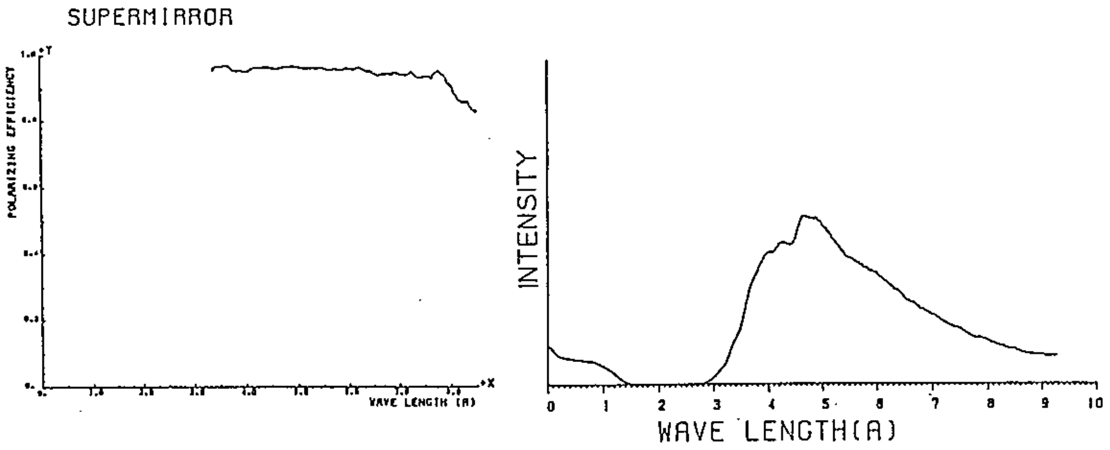

Fig. 5 Polarizing efficiency and beam spectrum of AgFe Supermirrors.

Production of Polarized Epithermal White Neutron Beam by Use of Dynamically Polarized Protons

Masayoshi ISHIDA, Yasuhiro MASUDA[*], Masahumi KOHGI, Yuji KANNO,
Shigenori HIRAMATSU[*], Yoshikazu ISHIKAWA, Akira MASAIKE[*+]
and Kimio MORIMOTO[*]

Physics Department, Tohoku University,
Sendai 980, Japan

[*]National Laboratory for High Energy Physics
Oho-machi, Tsukuba-gun, Ibaraki-ken, 305, Japan

Research and development for the Polarized Epithermal Neutron (PEN) spectrometer[1)] at KENS have been continued. In the present paper, we describe an improvement in neutron polarizations produced by a neutron spin filter of dynamically polarized protons. A compromise between the following conflicted demands was essential in the improvement. The proton polarization increases with the decrease of the filter material temperature. Therefore the filter material should be made small in size and directly immersed in the coolant of liquid ^{3}He for a good thermal contact. On the other hand, ^{3}He nuclei must be removed from the neutron beam path, because the neutron absorption cross section of ^{3}He is very large. In the present work, we

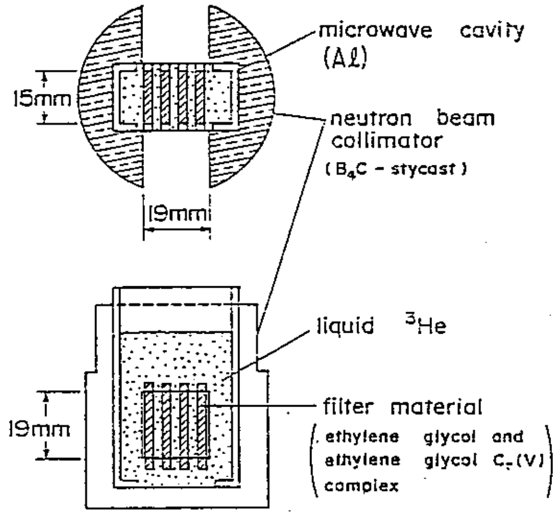

Fig. 1 Neutron spin filter. Filter cells are immersed in the liquid ^{3}He container which is also used as a microwave cavity. The cavity is set in the neutron beam collimator which has windows of 19 mm x 19 mm in the center of the beam.

[+] Present address: Physics Department, Kyoto University, Kyoto 606.

succeeded in eliminating the above mentioned difficulty and in producing highly polarized neutron beam.

The principle of producing polarized neutron beam was already described in the previous papers$^{2), 3)}$. The neutron spin filter which we employed in the present work is schematically shown in Fig. 1. The filter material was a mixture of ethylene glycol and ethylene-glycol Cr(V) complex, which was filled in four separated cells of 2.4 mm width x 20 mm height x 15 mm thickness. The filter thickness was decided by the optimization of the produced neutron polarization and the transmitted beam intensity. The filter cells were immersed in a liquid ^{3}He container which was also a part of a microwave cavity. Spaces of 2.4 mm width were left between the cells for good coolant convection around the filter material. The filter was inserted into a ^{3}He cryostat, set in the center of a superconducting magnet of 25 KG, and cooled down to about 0.5 K. By use of this filter configuration, the maximum proton polarization of (83 ± 5) % was realized, which was determined by the comparison of the enhanced NMR signal with the thermal equilibrium signal. In the continuous operation the polarization was kept more than 70 %. This result is satisfactory in the condition of the magnetic field and the coolant temperature. The neutron beam was collimated so as to be transmitted only through the filter. The experimental arrangement for the determination of the neutron polarization produced by the filter was almost the same as the previous one$^{2)}$ except the neutron spin flipper. The schematic view is shown in Fig. 2. The relative direction of neutron spins to the magnetic field is reversed by the non-adiabatic passage through the boundary where the direction of the magnetic field is reversed. In the present experiment, a superconducting Nb sheet was set in the neutron spin holding field in order to decouple the magnetic fields on the both sides of the sheet. The neutron spin is flipped when the direction of the downstream field was reversed. The flipping ratios of the neutron counting due to the (200) Bragg scattering from a Fe_8Co_{92} single crystal were measured for the determination of the neutron polarization. The flipper efficiency was found to be 0.93. Neutron transmission through the filter was simultaneously measured for the determination of the polarization at the filter. The transmission measurement was also used for monitoring the liquid ^{3}He level in the container. If the level is within the neutron beam path, unpolarized beam directly mixes with the polarized beam. The lowering of the liquid ^{3}He level also causes an anomalous increase in the neutron counting for the

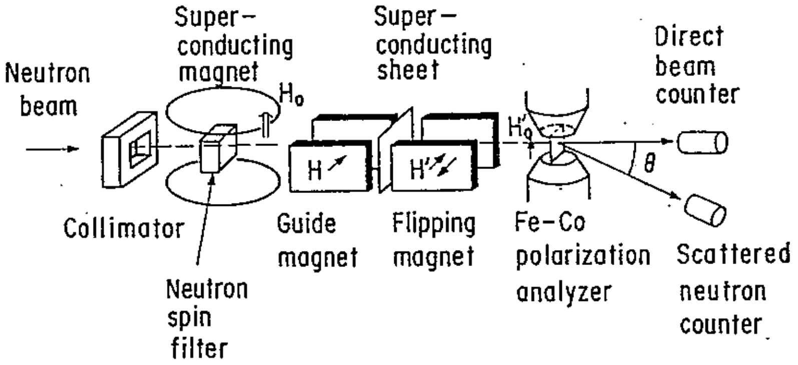

Fig. 2 Experimental arrangement for the determination of the neutron polarization. Neutron beam is collimated to a size of 20 mm x 20 mm before the transmission through the filter. The neutron beam is polarized by passing through the filter set in the center of a superconducting magnet. Neutron spins are hold and reversed in a neutron spin flipper after the passage and before the scattering by a Fe_8Co_{92} single crystal. The direct beam and the scattered beam are detected by a transmission counter and a scattered neutron counter, respectively.

transmission measurement. The level is easily controlled in a vertically arranged ^{3}He cryostat by use of the level monitoring, because the level is very stable in the vertical cryostat. During the present experiment the level was always above the neutron beam path.

The transmission measurement at neutron energy of 1.5 eV gave the average proton polarization in the filter. A typical value was (66.8 ± 0.5) %. The polarization determined by the NMR signal enhancement was (73 ± 4) % at that time. Since the NMR signal enhancement gives the polarization of protons in the neighborhood of the NMR coil, the difference due probably to the locality of the proton polarization in the filter material. Typical results of the neutron polarization are shown in Fig. 3. The closed circles in Fig. 3 are polarizations determined by the transmission measurement. Solid curve is a calculated value by use of the cross section data by Lushchikov et al.[4)] and the proton polarization of 67 %. A good agreement is seen between these results. The values obtained by the transmission measurement give the neutron polarizations at the filter and are found to be the highest polarizations that have ever been achieved for the epithermal white neutron beam. The open circles are the polarizations determined by the Fe_8Co_{92} Bragg scattering. The polarizations are systematically smaller than the values by the transmission. Most of the difference is explained by the depolarization in the neutron flight path after the filter.

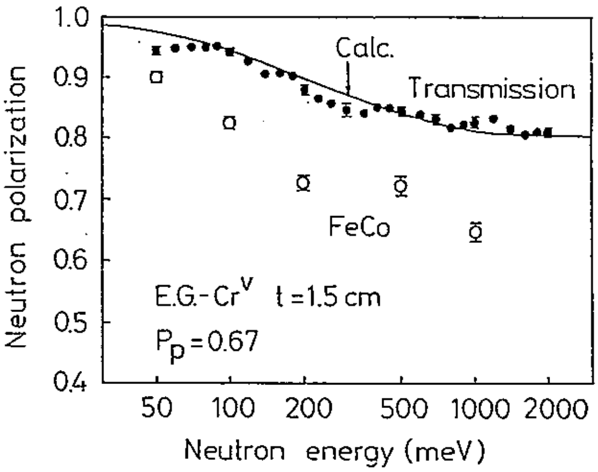

Fig. 3 Polarization of the neutron beam. Solid line is the calculated polarization by use of the cross section data by Lushchikov et al.[4)] and the proton polarization of 67 %. Closed circles are the polarizations determined from the neutron transmission enhancement at the proton polarization of 67 %. Open circles are the polarizations obtained by the scattering from the Fe_8Co_{92} single crystal.

The present values of the neutron polarizations produced by the filter are sufficient for the neutron scattering experiments. Further tuning of the magnetic field along the neutron flight path should be required in order to increase the neutron polarization at the sample position for the scattering experiments up to the values obtained by the transmission measurement. For the further improvement in the neutron counting statistics a new type of neutron spin filter is under development. The effective area for the neutron beam is enlarged by the complete removement of the liquid ^3He from the neutron beam path. Liquid ^4He is used as the coolant for the filter and the liquid ^4He is cooled down by liquid ^3He by use of a heat exchanger.

References

1) M. Ishida, M. Kohgi, Y. Masuda, S. Hiramatsu, S. Isagawa, Y. Ishikawa, S. Ishimoto, A. Masaike, K. Morimoto and T. Nakajima: KENS Report-IV, KEK Internal 83-4 (1983) 202.

2) J. M. Newsam, M. Ishida, S. Isagawa, Y. Ishikawa, S. Ishimoto, M. Kohgi, A. Masaike, Y. Masuda, K. Morimoto and T. Nakajima: KENS Report-III, KEK Internal 82-5 (1982) 123.

3) S. Hiramatsu, S. Isagawa, S. Ishimoto, A. Masaike, K. Morimoto, S. Funahashi, Y. Hamaguchi, N. Minakawa and Y. Yamaguchi: J. Phys. Soc. Japan 45 (1978) 949.

4) V. I. Lushchikov, Yu. V. Taran and F. L. Shapiro: Sov. J. Nucl. Phys. 10 (1970) 669.

Neutron Scattering from Dynamically Polarized Materials

Masayoshi ISHIDA, Yasuhiro MASUDA[*], Yuji KANNO, Masahumi KOHGI,
Yoshikazu ISHIKAWA and Akira MASAIKE[*+]

Physics Department, Tohoku University
Sendai, 980, Japan

[*]National Laboratory for High Energy Physics
Oho-machi, Tsukuba-gun, Ibaraki-ken, 305, Japan

One unique application of the Polarized Epithermal Neutron Spectrometer PEN, which utilizes the dynamical nuclear polarization (DNP) technique, is to investigate the process of the DNP itself[1, 2]. The DNP method is well established to obtain highly polarized nuclei. However, its microscopic mechanism has not been clearly understood yet. Though the spin diffusion is considered to play an important role in the realization of DNP, no direct observation has ever been performed. The aim of the present work is to observe directly the spatial distribution of the proton polarization in the DNP process. We report below some results of the preliminary experiments.

We measured small angle scattering from three different materials in their polarized and unpolarized states. They were deuterated propanediol ($C_3D_8O_2$) doped with EHBA-Cr^V (Na^+ $C_{12}H_{20}O_7Cr^V$), deuterated propanediol doped with EHBA-Cr^V and dicyclohexyl-18-crown-6 ($C_{20}H_{36}O_6$), and partially deuterated propanediol ($C_3D_6H_2O_2$) doped with EHBA-Cr^V. When the protons in these samples are polarized, increase of coherent scattering, which contains the direct information on the distribution of the polarized protons, as well as supression of the incoherent scattering is expected.

The sample container was composed of seven layers separated by 1 mm thick ^{3}He coolant layers as shown in Fig. 1. The size of each layer was 2 mm in width, 4 mm in thickness (along neutron beam direction) and 20 mm in height. The scattering angle was 2°. The Q-range covered at this scattering angle was about 0.07 - 0.4 Å^{-1}. The horizontally convergent type Soller collimator with 0.2° divergence was used to focus the incident beam

---

[+] Present address: Physics Department, Kyoto University, Kyoto 606.

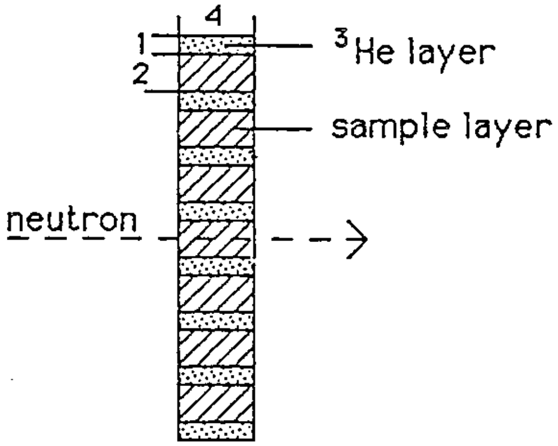

Fig. 1 Configuration of the sample container (horizontal cross section). The height of sample layers is 20 mm.

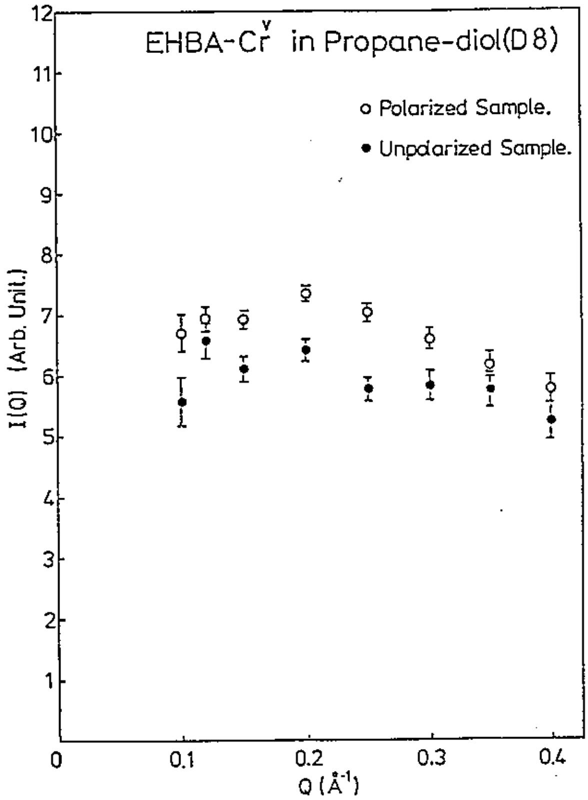

Fig. 2 Scattering function of deuterated propanediol doped with 4 x 10^{20} molecules/cm^3 EHBA-Cr^V. Open and solid circles correspond to the polarized and unpolarized samples, respectively.

at the detector plane, which was 4.5 m downstream from the sample position$^{2)}$. In all experiments sample temperatures were 0.5 - 0.6 K. The experiments for the polarized samples were carried out in the steady state of the DNP.

The experimental results are as follows.

(a) Deuterated propanediol ($C_3D_8O_2$) doped with 4 x 10^{20} molecules/cm^3 EHBA-Cr^V: The observed total scattering functions I(Q) are shown in Fig. 2 for the polarized and unpolarized samples. The scattering functions show only weak Q-dependence in the Q-range shown in the figure. This is a reasonable result if the chemical structure of EHBA-Cr^V is considered. Since the hydrogen atoms are localized on four ethyl radicals in EHBA-Cr^V which are separated together by 3 - 7 Å and the size of each ethyl radical is about 3 Å,$^{4)}$ the scattering functions should show very weak Q-dependence for Q < 0.5 Å^{-1}. Though the observed scattering function for the polarized sample is greater than that for the unpolarized sample, it is difficult to discuss quantitatively this intensity enhancement because the evaluation of the proton polarization in EHBA-Cr^V by means of the NMR technique was unsuccessful.

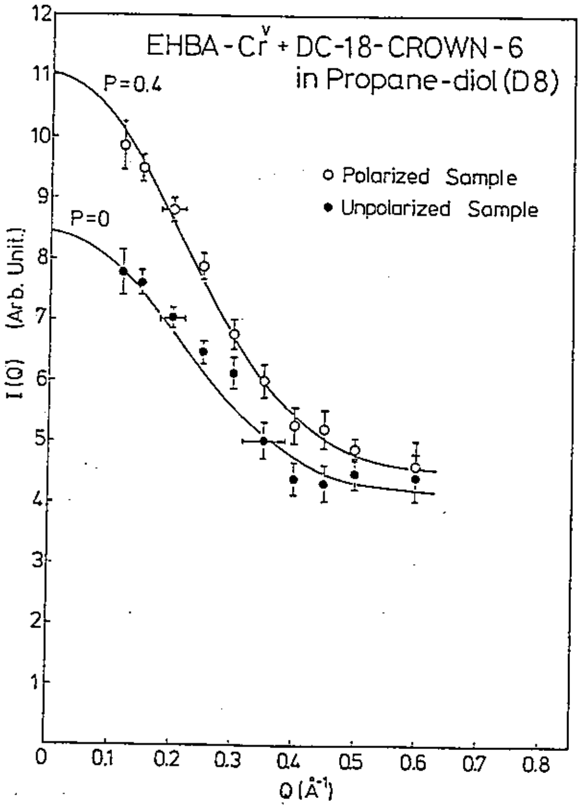

Fig. 3 Scattering function of deuterated propanediol doped with 1 x 10^{20} molecules/cm^3 EHBA-Cr^V and 1 x 10^{20} molecules/cm^3 dicyclohexyl-18-crown-6. Open and solid circles correspond to the polarized and unpolarized samples, respectively. Solid curves are the calculated ones (see text).

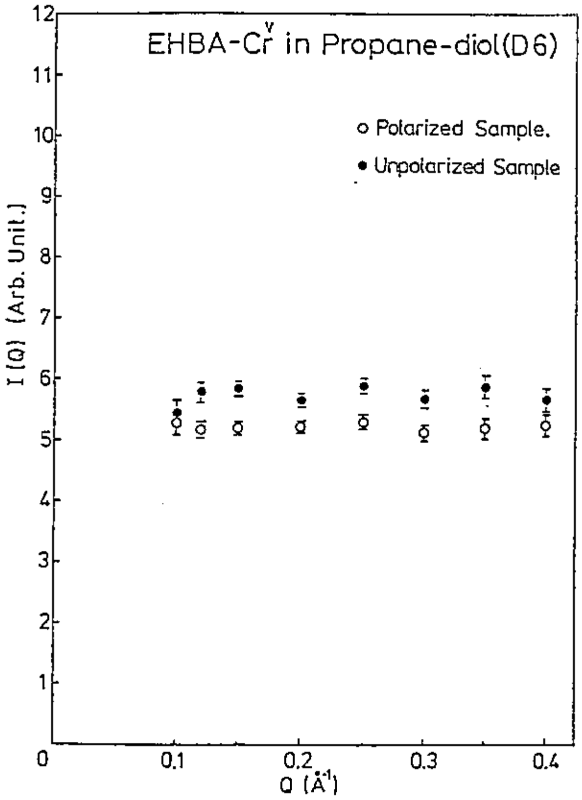

Fig. 4 Scattering function of partially deuterated propanediol doped with 1 x 10^{20} molecules/cm^3 EHBA-Cr^V. Open and solid circles correspond to the polarized and unpolarized samples, respectively.

(b) Deuterated propanediol ($C_3D_8O_2$) doped with 1 x 10^{20} molecules/cm^3 EHBA-Cr^V and 1 x 10^{20} molecules/cm^3 dicyclohexyl-18-crown-6: The experimental results are shown in Fig. 3. Both of the scattering functions for the polarized and unpolarized samples show the typical Q-dependence of the small angle scattering from large clusters. To analyze the data a simple model calculation was carried out, where the directional average of the scattering function of dicyclohexyl-18-crown-6 molecules in a uniform medium of deuterated propanediol was calculated. The calculated best fit scattering functions are shown by the solid curves in the figure. The volume of a dicyclohexyl-18-crown-6 molecule was determined to be 400 Å^3 from the best fit procedure for the unpolarized sample. This value is a reasonable one, considering the chemical structure of dicyclohexyl-18-crown-6 determined by the X-ray diffraction$^{5)}$. The proton polarization determined from the best fit to the polarized sample data was 0.4. This value is twice as large as that determined by the NMR technique. Though the reason of the discrepancy is not well known at this stage, we can nonetheless conclude that, if there exist clusters of polarized protons with the size of roughly 5 - 20 Å, the enhanced small angle scattering must be observed.

(c) Partially deuterated propanediol ($C_3D_6H_2O$) doped with 1 x 10^{20} molecules/cm^3 EHBA-Cr^V: The experimental results are shown in Fig. 4. The scattering functions are nearly flat for both of the unpolarized and polarized samples. Suppression of the scattering intensities is seen for the polarized sample. In this case of the sample, the amount of EHBA-Cr^V molecules was one fourth of the first case (a), however, total amount of hydrogen atoms was about twice as large. In addition to these facts, the contrast of the EHBA-Cr^V molecules to the solvent would be weaker because the hydrogen atoms were distributed also in the solvent. Therefore, in the unpolarized case, the incoherent scattering would be dominant compared with the coherent scattering, and result in the nearly constant scattering intensities. This agrees with the observation. The fact that the scattering in the polarized case is also constant and weaker than that in the unpolarized case demonstrates that the size of the clustering of the proton polarization, if any, is much greater than the order of 10 Å. Supposing the uniform proton polarization, we estimate the suppression of the intensities to be about 5 % by using the value of the proton polarization, which was 0.4, obtained by the NMR technique. This is compatible with the observation.

We are now planning to extend this work to the investigation of the time dependence of the nuclear polarization distribution in the build-up and relaxation stages of the dynamical polarization by utilizing the distinctive features of the KENS neutron source.

References

1) J. M. Newsam, M. Ishida, S. Isagawa, Y. Ishikawa, S. Ishimoto, M. Kohgi, A. Masaike, Y. Masuda, K. Morimoto and T. Nakajima: KENS Report III, KEK Internal 82-5 (1982) 123.
2) M. Ishida, M. Kohgi, Y. Masuda, S. Hiramatsu, S. Isagawa, Y. Ishikawa, S. Ishimoto, A. Masaike, K. Morimoto and T. Nakajima: KENS Report IV, KEK Internal 83-4 (1983) 202.
3) R. I. Schermer and M. Blume: Phys. Rev. 166 (1968) 554.
4) M. Krumpolc, B. G. DeBoer and J. Roček: J. Am. Chem. Soc. 100 (1978) 145.
5) M. Mercer and M. R. Truter: J. C. S. Dalton (1973) 2215.

Operation of a Superthermal Ultra-Cold Neutron Converter

H. Yoshiki
KEK, National Laboratory for High Energy Physics
Tsukuba, Ibaraki-Ken, 305, Japan

An apparatus to produce ultra-cold neutrons by superthermal helium was put into test and 1.5 l purified liquid He^4 was cooled down to 0.55K by means of He^3 refrigeration for more than 60 hours. This model has a built-in superleak which automatically removes He^3 impurity in the commercial liquid helium, while the UCN cavity is being filled with the purified helium. It took two hours to fill the 1.5 l cavity with the purified helium (He^4), as only several liters of ordinary liquid helium was needed to do this. After the cavity liquid reached at the desired temperature, the system was put into a stationary state, so called "continuous operation", with the ordinary 4.2K liquid helium supplied as needed to the system from an external vessel manually.

We show a sketch of this model in Fig.1. Its features are as follows: 1)in order to study the effects of wall material of the UCN cavity on the UCN storage its replacement can be worked out readily, 2) to assure the tightness to UCN leak, the valve used for UCN confinement is carefully fitted to and well pressed against an orfice made at the cavity and it is driven through a vertical stainless steel rod by means of compressed air piston at the top of the cryostat, 3) to assure the cleanness of the UCN cavity, the cavity and its system were designed to comply with the high vacuum specifications, 4) He^3 removal is done inside the system continuously, resulting in high removal efficiency in time and volume, as already mentioned.

It requires about four days to start up the system, including miscellaneous jobs and tests. On the first day one starts the evacuation of 1) the UCN cavity and its related system, 2) 1K, 4.2K baths, 3) the cryostat and 4) He^3 circulation system, independently. While all evacuation is being continued on the second day, about 500 l of liquid helium and 600 l of liquid nitrogen are prepared. Checks on thermal elements and electronics are done on this day. The liquid nitrogen is filled in the outer jacket of the cryostat. On the third day, after certain necessary works of several hours, nitrogen gas is introduced to the cryostat vacuum up to 1 atm, followed by liquid nitrogen filled up to the inner shoulder of the cryostat, submerging the most of the cryoelements. This precooling is continued till the next day. On the fourth day the liquid nitrogen is retrieved and the cryostat is evacuated very slowly. When its vacuum reaches 10^{-6} Torr (after 5 hours), the transfer of liquid helium to 4.2K bath of the cryostat is started. The liquid helium flows to 1K bath below as well in this occasion since the valve connecting 1K and 4.2K bath is kept open. When both baths are filled about five hours later, 1K bath is pumped down. This results in the superthermalisation of the liquid helium in 1K bath and it flows into UCN cavity through the superleak. Up to this point, the temperature of the UCN cavity has been at that of liquid nitrogen. But now it has the helium gas to conduct the heat to 1K and 4.2K bath, the cavity temperature lowers to the helium temperature in 7 hours. This completes the precooling. Works of filling the cavity with the purified liquid helium and cooling it below 0.6K are to follow. The 1K bath is pumped once more and the He^3 circulation starts. While several liters of liquid helium in 1K bath are consumed, the cavity is filled with the purified He^4 liquid about in two hours. Up to this point a total of 160 l of liquid helium must be supplied to the whole system. By continuing the He^3 circulation, the temperature of the liquid in the cavity reaches 0.55K in 20 hours.

This cryostat (as most of cryostats) has not been designed to make much use of the cooling power of evaporated helium and how much enthalpy contributes to the actual cooling is unknown. The total heat quantity from 77K to 4.2K of 4.2K bath, 1K bath and UCN cavity is 153 kJ and 55 l of liquid helium would be required if the latent heat only contributed in the cooling. Adding the physical volumes of baths and cavity, and the natural evaporation in 30 hours to this, one expects that 143 l of liquid helium would have been necessary. The actual consumption was 160 l. Assuming the transfer loss about 30%, about 20% of the total heat was removed by the helium gas after evaporation. In Fig.2, we show a helium consumption curve against time. The first 30 hours up to A is the precooling period. A stand-by period (from A to B), where He^3 circulation was off, is followed by a period after B, where the neutron beam arrived and the He^3 circulation was turned on. The helium consumption rate in this period is 3.2 l/hr.

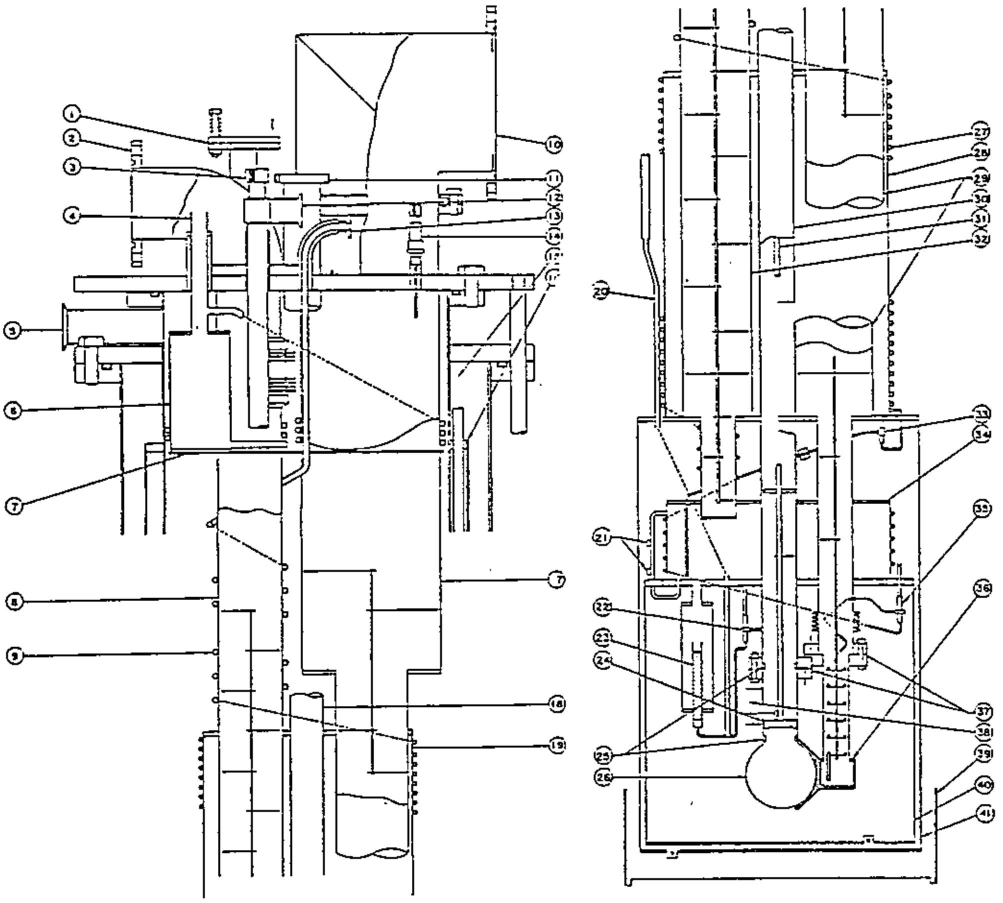

Fig. 1 The inside view of the cryostat.

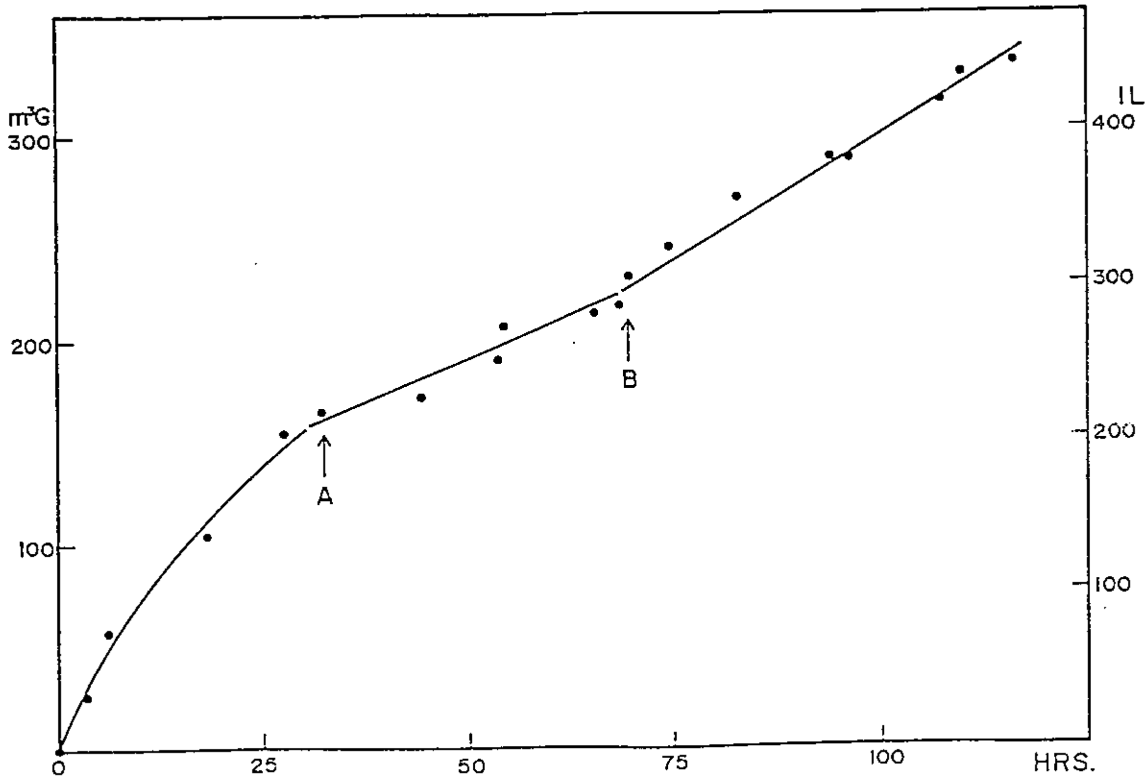

Fig. 2 Helium consumption against time.